



# **Development of a magnetically levitated axial field brushless DC motor**

by

**Markus Raab**

Submitted to the Department of

**Mechatronics**

In partial fulfilment of the requirement for the degree of

**Master of Engineering (M.Eng.)**

at

**Aalen University**

**of Applied Sciences**

**Supervising Professors:**

**Prof. Kazi (Aalen University)**

**Prof. Trumper (MIT)**



## **Certification of Thesis**

I certify that the ideas, experimental work, results, analyses, software and conclusions reported in this thesis are entirely my effort, except where otherwise acknowledged. I also certify that the work is original and has not been previously submitted for any other award, expect where otherwise acknowledged.

---

Date

---

Signature of Candidate

## Acknowledgments

I would sincerely like to thank and acknowledge the following people for their assistance, guidance and support throughout the duration of this thesis project.

First of all I would like to thank my supervisors Prof. Kazi from Aalen University and Prof. Trumper from MIT. Both helped me a lot during the work of this thesis.

Prof. Trumper offered me to stay in his Precision Motion Control lab at MIT as a visiting student for one semester. During my stay I learned a lot about the design and control of mechatronic systems. Especially in the 2.737 mechatronics course where I could help as a teaching assistant I could improve my knowledge about the interaction of mechanical, electrical and control systems. In many discussions Prof. Trumper supported my work with a lot of good ideas about the conception and control of the motor design and encouraged me to work eagerly on my project. Thank you very much for the opportunity to stay in your lab and your help.

I also want to thank Prof. Kazi who supervised the second part of my thesis. In all meetings he improved my design with good ideas and helped me to get the whole concept working. I also want to thank him, for the support in different other student project during my studies.

Thanks a lot to Laura Zaganjori who helped me organizing my stay at MIT and was always there to make things working.

I am also grateful to all of my labmates from the Precision Motion Control Lab of MIT and the Actuator and Sensors Lab of the University Aalen for the support, interest and assistance in this thesis project. Especially I want to thank Alex Adrien who was with me at MIT as a visiting student. Together we could tackle all the difficulties when we arrived in Cambridge. I had good discussions during my work with him. I also want to thank Lei Zhou and Jun Young Yoon which have helped me a lot with different questions regarding technical questions and my stay in the Lab. Also I want to thank Minkyun Noh, Phillip Daniel and Maria Pina Piccolo which worked with me in the Precision Motion Control Lab. Back in Germany, Klaus Wintermayr worked with me in the Actuator and Sensors Lab where we had good dialogues about different technical questions.

I want to thank the German National Academic Foundation who supported me during my studies and my stay in the USA.

Finally I want to thank my fiancée and family which supported me during my whole studies.

## **Abstract**

Brushless DC (BLDC) motors are often used in industrial applications because of their robustness and their low maintenance. On the other hand reluctance actuators are also used in a wide range of industry starting with simple binary actuators up to high precision applications. For this reason it is important to teach students about the design, calculation and control of these devices.

In this thesis, a modular brushless DC motor with a reluctance based magnetically levitated rotor is developed, as a teaching tool for universities. Because of its simple design, it is possible to build this system using standard manufacturing techniques available in most workshops. The low costs approach of the setup features the National Instrument myRIO board.

The modular concept allows the use of the system in different levels of teaching. In its basic configuration, the commutation of BLDC motors as well as the design of position controllers by using model based design can be demonstrated. The next step focuses on the teaching of the magnetically levitation of a disc, in this step forces of reluctance actuators, couplings between different axes and the control of nonlinear system can be explained. In the final step, the motor can be run magnetically levitated and in six degrees of freedom controlled.

In this thesis all the necessary files and algorithms are presented, which are to needed build and run the system.

## **Kurzfassung**

Bürstenlose Gleichstrommotoren erfreuen sich aufgrund ihrer Robustheit sowie ihres wartungsarmen Betriebes zunehmender Beliebtheit in industriellen Anwendungen. Ein weiteres weit verbreitetes Aktuator Prinzip sind Reluktanzaktuatoren, welche binär angesteuerten für einfache Schaltanwendungen bis hin zum Hochpräzisionsbereich Anwendung finden. Aus diesem Grund ist es wichtig, Fachleute in der Auslegung, Berechnung sowie der Regelung dieser Geräte auszubilden.

Im Rahmen dieser Arbeit wird ein modular aufgebauter mit Reluktanzaktuatoren magnetisch gelagerter bürstenloser Gleichstrommotor (BLDC) entwickelt, welcher in der Lehre an Universitäten und Hochschulen eingesetzt werden kann. Durch einen einfachen Aufbau ist es möglich, das System mit standartmäßigen Herstellungsverfahren und geringen Kosten zu fertigen. Als Echtzeit System wird das von National Instruments vertriebene System NI-myRIO verwendet.

Durch den modularen Aufbau ist es möglich, das System in verschiedenen Ausbildungsstufen einzusetzen. In der Grundstufe kann die Kommutierung von BLDC Motoren, sowie das Erstellen von Positionsregelungen auf Basis der modellbasierten Funktionsentwicklung gelehrt werden. In der nächsten Stufe wird eine Stahlscheibe magnetisch gelagert. Hierbei können die Kräfte und das Verhalten von Reluktanzaktuatoren erklärt werden, des Weiteren kann die Entkopplung und Regelung von nichtlinearen Systemen vermittelt werden. In der finalen Stufe wird der Motor in sechs Freiheitsgraden magnetisch gelagert betrieben.

Diese Arbeit umfasst alle benötigten Dokumente und Algorithmen die für den Bau und Betrieb des Systems benötigt werden.

## Contents

Certification of Thesis .....	3
Acknowledgments .....	4
Abstract .....	5
Kurzfassung.....	6
Contents .....	7
List of Figures.....	11
List of Tables .....	15
1 Introduction.....	16
2 Conceptual design .....	18
2.1 Overview brushless DC motors.....	18
2.1.1 Basics of DC motors .....	18
2.1.2 Commutation.....	18
2.1.3 Types of brushless DC motors .....	20
2.2 Overview magnetic bearings .....	21
2.2.1 Reluctance actuators in magnetic levitation .....	21
2.2.2 Magnetic bearings .....	22
2.3 Actuation concept.....	23
2.3.1 Vertical actuation .....	23
2.3.2 Horizontal actuation .....	24
2.4 Sensor concept.....	26
2.4.1 Sensing of the motor angle .....	26
2.4.2 Position sensing for magnetic bearings.....	27
2.5 Rotor concept .....	28
2.6 Concept for a Maglev BLDC motor .....	29
2.6.1 BLDC motor.....	29
2.6.2 Magnetic levitation.....	30
2.6.3 Magnetically levitated BLDC motor .....	31
3 Axial field brushless DC motor.....	32
3.1 Coil design.....	32

## Contents

3.1.1	Winding structure.....	32
3.1.2	Coil Design .....	36
3.2	Rotor design.....	38
3.2.1	Magnetic material .....	38
3.2.2	Flexible magnet rotor .....	39
3.2.3	NeFdB magnet rotor .....	42
3.2.4	Comparison of the rotor configurations.....	43
3.3	Position sensor.....	44
3.4	Parameter calculation.....	46
3.4.1	Torque constant .....	46
3.4.2	Back EMF .....	48
3.4.3	Coil Resistance .....	49
3.4.4	Coil current calculation.....	50
3.4.5	Coil Inductance .....	50
3.4.6	Moment of inertia .....	51
3.4.7	Summary of the motor Parameters .....	51
3.5	Motor design.....	51
3.5.1	Bearing design .....	51
3.5.2	Electronics design .....	52
3.5.3	LabVIEW implementation.....	54
3.5.4	Design summary .....	54
3.6	Motor parameter measurement .....	56
3.6.1	Sine/cosine encoder reading test.....	56
3.6.2	Coil characterization .....	60
3.6.3	Back EMF measurement.....	62
3.6.4	Damping estimation .....	64
3.7	Modelling and control of a brushless DC motor.....	67
3.7.1	Commutation.....	67
3.7.2	Motor characteristics .....	68
3.7.3	Linearized model .....	70
3.7.4	Controller design .....	71
3.7.5	Trajectory based positioning .....	72



## Contents

3.8	Model and control verification .....	76
3.8.1	Open loop speed step.....	76
3.8.2	System frequency response measurement.....	76
3.8.3	Return ratio measurement.....	77
3.8.4	Step response closed loop.....	79
3.8.5	Trajectory based step response closed loop .....	79
4	Three axis magnetic bearing.....	81
4.1	Magnetic bearing design.....	81
4.2	Position sensing .....	82
4.2.1	Sensor selection.....	82
4.2.2	Sensor electronics.....	83
4.2.3	Sensor calibration .....	84
4.3	Actuators.....	85
4.3.1	Actuator design .....	85
4.3.2	Actuator test.....	89
4.3.3	Electronics design .....	90
4.4	Modelling and control.....	95
4.4.1	System model .....	95
4.4.2	Controller design .....	98
4.4.3	Controller tuning .....	107
4.4.4	Measurement of the system behavior for different axes .....	111
4.5	LabVIEW implementation .....	113
5	Magnetic bearing for two additional axes .....	114
5.1	Detailed design horizontal axes bearing.....	114
5.2	Detailed rotor design for magnetic bearing .....	115
5.3	Actuators.....	117
5.3.1	Actuator design .....	117
5.3.2	Actuator test.....	119
5.3.3	Electronics design .....	120
5.4	Modelling and control.....	121
5.4.1	System model .....	121
5.4.2	Controller design .....	125

## Contents

5.4.3	Controller tuning .....	129
5.4.4	Measurement of the system behavior for different axes .....	130
6	BLDC motor with magnetic bearing .....	132
6.1	System response of the magnetic bearing .....	132
6.2	Motor frequency response .....	134
6.3	Motor speed .....	134
7	Conclusion and further work .....	136
8	Bibliography.....	139
9	Appendix Motor.....	144
9.1	Comparison of permanent magnet materials .....	144
9.2	Mechanical design .....	145
9.3	Test specifications.....	148
9.4	Matlab.....	157
9.4.1	Script for PCB coil printing.....	157
9.4.2	Motormodell parameter script.....	164
10	Appendix magnetic bearing.....	165
10.1	Mechanical design .....	165
10.2	Test specifications.....	172
10.3	DSA Tool Test .....	175
10.4	Simulink model .....	176

## List of Figures

Figure 1 Schematic drawing of brushless and brushed DC motors.....	18
Figure 2 brushed DC motor commutation taken from [3, p. 80] .....	19
Figure 3 Bock commutation and Sine commutation .....	19
Figure 4 Radial field and axial field motors .....	20
Figure 5 Disassembled floppy disc axial field motor .....	20
Figure 6 Schematic view of a reluctance actuator based magnetic levitation system .....	21
Figure 7 Motor with magnetic bearings picture taken from [12, p. 3] .....	22
Figure 8 Actuator concept for Z, Pitch and Roll.....	23
Figure 9 Actuation concept for the X and Y axis.....	24
Figure 10 Optical quadrature encoder, picture taken from [13] .....	26
Figure 11 Encoder signals of quadrature and sine/cosine encoders .....	27
Figure 12 Sensor concept of the magnetic bearing.....	28
Figure 13 Rotor concept .....	29
Figure 14 Motor with and without back iron .....	29
Figure 15 Schematic drawing of the motor concept.....	30
Figure 16 Concept of the magnetic levitated brushless DC motor .....	31
Figure 17 Overlapping winding structure.....	33
Figure 18 Layers per Coil .....	34
Figure 19 Through hole and not through hole connection .....	34
Figure 20 Schematic view of non-overlapping windings.....	35
Figure 21 Lorentz forces in a coil.....	36
Figure 22 Rhomboidal coil, coil with parallel active sections, picture taken from [17, p. 2] ...	36
Figure 23 Coil structure for different layers, picture taken from [17, p. 2] .....	37
Figure 24 Coils with straight lines and arc structure .....	38
Figure 25 magnetic circuit of a motor with back iron .....	39
Figure 26 CAD Magnetizing tool .....	40
Figure 27 magnetizing a flexible magnet rotor .....	41
Figure 28 Self magnetized flexible magnet rotor .....	41
Figure 29 CAD drawing of a NeFdB magnet .....	42
Figure 30 Expected magnetic field in the coils .....	42
Figure 31 2D Magnetic field simulation of the motor without back iron .....	43
Figure 32 NdFeB magnet placement tool and NdFeB rotor .....	43
Figure 33 Sine/cosine encoder reading .....	44
Figure 34 Simulated min/max flux densities in the Hall sensors .....	45
Figure 35 Description of the air gap flux density, picture taken from [19, p. 2] .....	47
Figure 36 Coil and area which is in magnetic field .....	48
Figure 37 Bearing bore .....	52
Figure 38 Power electronics of the Motor .....	53

## List of Figures

Figure 39 Sensor reading electronics .....	53
Figure 40 Designed BLDC motor with electronics and real time target.....	54
Figure 41 PCB Setup.....	55
Figure 42 Designed PCB board .....	55
Figure 43 Comparison between measured and desired Hall sensor signal .....	56
Figure 44 Error between measured and simulated angle.....	57
Figure 45 Error curve of the measured angle and FFT analysis of the error signal .....	57
Figure 46 Results of the fitted error fitting .....	58
Figure 47 Measurement of the Angle error for different speed .....	59
Figure 48 Measured and expected step response of the coil .....	60
Figure 49 Measured and fitted step response of the coil .....	61
Figure 50 Back EMF signal .....	62
Figure 51 Comparison of motor speed and back EMF, (A) speed signal and back EMF signal, (B) speed signal vs back EMF.....	63
Figure 52 Back EMF shape .....	64
Figure 53 Measured and simulated friction for decreasing speed .....	65
Figure 54 Simulation for friction simulation.....	65
Figure 55 estimated Friction function .....	66
Figure 56 Top level of the BLDC motor model .....	67
Figure 57 Simulink based BLDC commutation.....	68
Figure 58 Simulink implementation of the voltage to torque behaviour of one coil .....	69
Figure 59 Simulink implementation of the motor torque to speed/angle .....	70
Figure 60 Simulated frequency response of the motor .....	71
Figure 61 Controller structure .....	72
Figure 62 Simulated loop return ratio and controller bode plot .....	72
Figure 63 Acceleration reduced path planning .....	73
Figure 64 State machine for trajectory generation .....	73
Figure 65 Comparison of measured on modeled open loop speed steps .....	76
Figure 66 Comparison between measured and simulated frequency response of the motor .....	77
Figure 67 Measured return ratio.....	78
Figure 68 Closed loop step response.....	79
Figure 69 Trajectory based positioning for 1 mrad and 1 rad.....	79
Figure 70 Trajectory based positioning for one rotation and 10 rotations.....	80
Figure 71 Magnetic bearing for Z, Pitch and Roll axis .....	81
Figure 72 QTR-1A picture taken from [29] .....	82
Figure 73 Sensing circuit.....	83
Figure 74 Sensor calibration .....	84
Figure 75 Schematic of a reluctance actuator .....	85
Figure 76 Measured and fitted inductance of a coil .....	88
Figure 77 Actuator test, using electrical current vs. distance .....	89
Figure 78 Current control schematic.....	90

## List of Figures

Figure 79 Bode plot $U \rightarrow I$ coil .....	92
Figure 80 Bode plot current controller.....	93
Figure 81 Bode plot return ratio current control .....	93
Figure 82 Measured and modeled step response of the current control.....	94
Figure 83 Model of the vertical axes .....	95
Figure 84 Placement of the reluctance actuators and sensors in the system .....	95
Figure 85 Distance caused by angle calculation .....	97
Figure 86 System representation for linearization of the Z-axis .....	99
Figure 88 Linearized system including current control .....	100
Figure 89 Linearized bode plot of the Z-axis .....	101
Figure 90 System representation for linearization of the Pitch axis .....	102
Figure 91 System representation for linearization of the Roll axis .....	102
Figure 92 Linearized bode plot for rotary axis .....	103
Figure 93 DSA system response measurement.....	104
Figure 94 Z-Axis measured and calculated frequency response.....	105
Figure 95 Pitch-Axis measured and calculated frequency response.....	105
Figure 96 Roll-Axis measured and calculated frequency response.....	106
Figure 97 Return Ratio Z-axis.....	107
Figure 98 DSA return ratio measurement .....	108
Figure 99 Measured frequency response of the Z-axis .....	108
Figure 100 Return Ratio rotary axis.....	109
Figure 101 Measured frequency response of the Pitch axis .....	110
Figure 102 Measured frequency response of the Roll axis .....	110
Figure 103 Frequency response measurement for decoupling verification .....	111
Figure 104 Control efforts for changes in the Z axis .....	112
Figure 105 Control efforts for changes in the Pitch axis .....	112
Figure 106 Control efforts for changes in the Roll axis .....	113
Figure 107 Actuators and forces of a 5 DOF bearing .....	114
Figure 108 Detailed rotor design concepts .....	115
Figure 109 Rotor design for low coupling .....	115
Figure 110 Rotor with 3D printed ring for a constant surface .....	116
Figure 111 Final motor and bearing design.....	116
Figure 112 Figure of the final motor setup .....	117
Figure 113 X, Y axis actuator .....	118
Figure 114 Actuator test setup.....	119
Figure 115 X,Y actuator design verification.....	119
Figure 116 Sensor and power electronics .....	120
Figure 117 Modeled of the horizontal axes .....	121
Figure 118 Forces in X and Y axis.....	121
Figure 119 Sensor positions of the horizontal axes .....	122
Figure 120 Coupling between X, Y and Z, Roll, Pitch axis.....	124

## List of Figures

Figure 121 decoupling and trigonometric functions of the X axis .....	126
Figure 122 Linearized bode plot of the X-axis .....	127
Figure 123 X Axis measured and calculated frequency response .....	128
Figure 124 Y Axis measured and calculated frequency response .....	128
Figure 125 Measurement return ratio X axis .....	129
Figure 126 Measurement return ratio Y axis .....	130
Figure 127 Control effort of the X axis .....	131
Figure 128 Control effort of the Y axis .....	131
Figure 129 Five axes magnetic bearing measurement in time domain (without rotation) ...	132
Figure 130 Five axes magnetic bearing measurement in time domain (2000 rpm) .....	133
Figure 131 Frequency response measurement of the motor with magnetic bearing.....	134
Figure 132 Open loop speed step of the maglev BLDC motor .....	135
Figure 133 CAD drawing motor / bore .....	145
Figure 134 CAD drawing motor / rotor iron .....	146
Figure 135 CAD drawing motor / rotor shaft .....	147
Figure 136 Schematic of the inductance measurement circuit .....	149
Figure 137 CAD drawing bearing / reluctance actuator Z core .....	165
Figure 138 CAD drawing bearing / reluctance actuator X-Y core.....	166
Figure 139 CAD drawing bearing / X-Y part for actuator .....	167
Figure 140 CAD drawing bearing / XY part for actuator 2.....	168
Figure 141 CAD drawing bearing / middle iron .....	169
Figure 142 CAD drawing bearing / return iron .....	170
Figure 143 CAD drawing bearing / rotor iron .....	171
Figure 144 Implementation DSA tool test.....	175
Figure 145 DSA tool test .....	175
Figure 146 Simulink model top view .....	176
Figure 147 Simulink model Z, Pitch and Roll axis .....	177
Figure 148 Simlink model of the X and Y axis.....	178
Figure 149 Simulink model current control.....	179

## List of Tables

Table 1 Parameter setup for overlapping windings .....	33
Table 2 Parameter setup for overlapping windings .....	35
Table 3 Summary of the calculated motor behavior .....	51
Table 4 Components current control .....	94
Table 5 Comparison of magnetic materials .....	144
Table 6 Sine/cosine encoder test specification of the motor .....	148
Table 7 Coil characterization of the motor .....	149
Table 8 Back EMF measurement of the motor .....	150
Table 9 friction estimation of the motor .....	151
Table 10 Open loop speed step of the motor .....	152
Table 11 System frequency response of the motor .....	153
Table 12 Return ratio measurement of the motor .....	154
Table 13 Step response closed loop of the motor .....	155
Table 14 Trajectory based positioning of the motor .....	156
Table 15 System frequency response magnetic bearing .....	172
Table 16 Decoupling verification magnetic bearing .....	173
Table 17 Return ratio measurement magnetic bearing .....	174

## 1 Introduction

Brushless DC (BLDC) motors are widely used in many industrial applications due to their robustness and low maintenance compared to conventional (brushed) DC motors. In addition their efficiency is very high, which makes these motors interesting in times where a responsible use of resources becomes more and more important. Due to their stiff and compact design, very high control bandwidths can be achieved. Hence, this motor is often used in positioning applications.

A second group of actuators which is widely used in industry are reluctance actuators. These actuators are often used as simple “binary” actuators like solenoid. However they offer linear movement, high force densities and high control bandwidth. As these actuators do not require a connection between stator and moving part, they are a perfect candidate for high precision positioning application.

It is important to incorporate both BLDC motors based on the Lorentz principle as well as reluctance actuators in universities. Students should understand the fundamentals of the design, building and adjustment of these devices. Brushless DC motors and reluctance actuators are good examples for mechatronic systems due to their close interaction of mechanics, electronics and control. Using these systems the model based design of mechatronic application can be taught. This includes the following details:

- Design of BLDC motors including their pole and winding structure
- Commutation of BLDC motors including different commutation techniques
- Design of reluctance actuators by analyzing the magnetic circuit, as well as calculating the flux densities and forces in the air gap
- System and parameter identification as well as model validation
- Loop shaping design of PID controllers

Systems where brushless DC motors and reluctance actuators work in combination are electro motors with magnetic bearings. Unfortunately, there are no existing solutions of a magnetically levitated BLDC motor which can be used for teaching, as commercial systems do not have access to all the required signals and algorithms. In addition industrial systems are very price intensive which makes it hard to equip a full lab with such setups.

The goal of this thesis is to develop a modular low cost brushless DC motor with a magnetically levitated rotor. This system should provide access to all the signals, which are needed to drive, identify and control the motor and the levitation system. The system shall be used in different levels of teaching, so the various parts need to run separately.

In the design of this system, it is very important to keep the costs low, that universities can afford this system. The motor has to be produced with standard manufacturing techniques and low effort like 3D printing. The real-time target NI myRIO will be used as it is cost and power efficient and can be easily programmed via LabVIEW.



Standard industrial motors use pulse with modulation (PWM) because of their high power efficiency. The downside of this method for teaching is that it is hard to measure and understand the signals in the motor. For the understanding of brushless DC motors, students have to be able to measure the signals of the motor by using an oscilloscope, so analog circuits and signals have to be used. As the focus of this project is set on teaching, the lower power efficiency of analog amplifiers is less important.

To teach students about BLDC motors, the motor has to have access to all the signals and algorithms. Block commutation of BLDC motor has to be necessarily possible. In addition the use of more advanced commutation techniques like sine commutation is desired.

The whole system will be used to teach students about model based design of mechatronic systems and controllers. Therefore a low design complexity is desired, that it is possible for students to model the system accurately. In addition there should be a good comparability between the model prediction and the actual measurement.

One goal of this thesis is to teach students about controller design. The different parameters of a PID controller can be felt if the torque created by the motor is high enough. A torque of  $> 5 \text{ mNm}$  should be achieved as a minimum. The speed of the motor is less important, but should reach a value which is similar to commercial motors which is well above 1000 rpm.

The system has to be designed modular, that it can be used in different levels of studying. This results in a system which starts with the basics of BLDC motors as the first step, up to the control of nonlinear MIMO systems in magnetic levitation for graduate level teaching.

The thesis is structured in the following pattern.

In **chapter 2**, the concept of the brushless DC motor including its magnetic levitation system is developed. Different concepts of actuation and sensing for the BLDC motor as well as for magnetic levitation are evaluated. **Chapter 3** focuses on the development of an axial field brushless DC motor. The design of a winding and pole structure is explained and the relevant motor parameters are calculated. A dynamic model of the motor is created, which is verified in a number of different tests.

In **chapter 4**, a three axis magnetic bearing for controlling the Z, Pitch and Roll axis is developed. Different sensing principles are described. Actuators and power electronics are designed. A dynamic model of the magnetic bearing including position control is created. This model is verified on the setup by measuring the system behavior.

**Chapter 5** describes the design of a magnetic bearing for the two remaining horizontal axes. A model of the magnetic bearing including all controlled axes is built. Based on the model, different controllers are tuned. In different tests, the model is verified. In **Chapter 6** the functionality of the full system is validated. Different tests to show the functionality of the spinning rotor with magnetic levitation are performed. **Chapter 7** summarizes the work which is done in this thesis and gives suggestions for follow-up projects.

## 2 Conceptual design

In this chapter, the concept of a BLDC motor with a magnetically levitated rotor is developed. The defined features from chapter 1 are compared to existing solutions in the field of brushless DC motors (section 2.1) and magnetic bearings (section 2.2). Section 2.3 compares different actuator concepts with respect to their applicability and modularity. In section 2.4, solutions for sensing the rotor position are presented. Section 2.6 presents the overall concept of the motor, to be developed and tested in this thesis.

### 2.1 Overview brushless DC motors

#### 2.1.1 Basics of DC motors

In conventional (brushed) DC motors permanent magnets are mounted at the stator and coils are attached to the rotor. This requires a transmission of electric current from the stationary part of the motor to the rotor which is usually done by brushes. The limited lifetime of the brushes is the major drawback of conventional DC motors.

In brushless DC motors the permanent magnet and coil configuration is mirrored. A schematic drawing of both types of motor is shown in Figure 1. The electric terminals are connected to the windings on the stator, so there are no mechanical connections to transmit electrical power to the rotor required. This increases the lifetime of this motors significantly compared to brushed DC motors. The torque in this motor is created by the Lorentz force [1] [2].

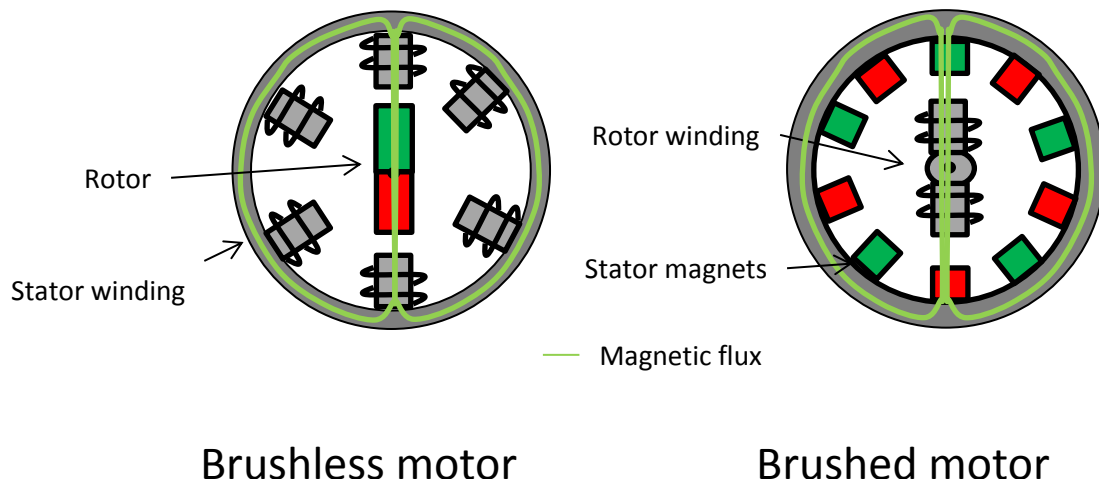


Figure 1 Schematic drawing of brushless and brushed DC motors

#### 2.1.2 Commutation

Commutation i.e. changing the direction of the electric current is necessary in order to achieve a continuous unidirectional torque. This is done by changing the direction of current in the coils, according to the magnetic field of the rotor. In brushed DC motors this is realized with the commutator, which changes the direction of the electrical current in the coils mechanically as shown in the following figure.

## Conceptual design

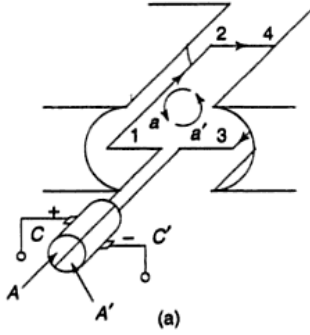


Figure 2 brushed DC motor commutation taken from [3, p. 80]

Using brushless DC motors, the commutation has to be done by motor electronics. The current in the stator coils has to be aligned to the magnetic field of the rotor. If this is done correctly, the electric field rotates in the same speed than the magnetic field of the rotor. To align the electric current in the coils to the rotor angle, a measurement of the rotor angle is required [4, p. 4]. This is usually done by Hall sensors, which measure the magnetic field of the rotor.

Different commutation methods can be chosen to run a BLDC motor. The simplest commutation mode is block commutation. The rotor angle is measured by Hall sensors which generate binary signals for the motor controller. The controller switches the current through the motor coils on and off based on these signals (Figure 3 A). Advantage of this method are that there are low costs for sensing the magnetic angle and the motor software is not complex.

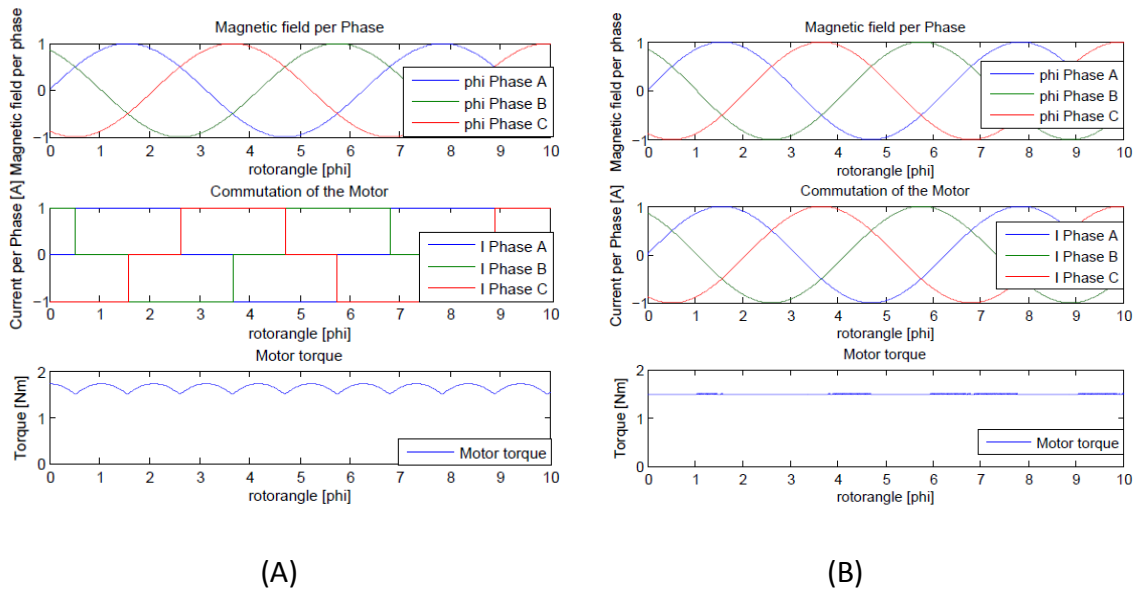


Figure 3 Block commutation and Sine commutation

The switching of the current generates torque ripples in the motor. These torque ripples can be reduced by the use of sine commutation. When sine commutation is used, the rotor angle has to be measured accurately. The current through the coils is adjusted precisely to the magnetic field of the rotor to create torque with little torque ripple (Figure 3 B).

### 2.1.3 Types of brushless DC motors

Brushless DC motors can be separated in different subgroups. The most common types of motors are radial field motors. A schematic drawing of a radial field motor is shown in Figure 2. It can be seen that the magnetic field lines leave the rotor in radial direction.

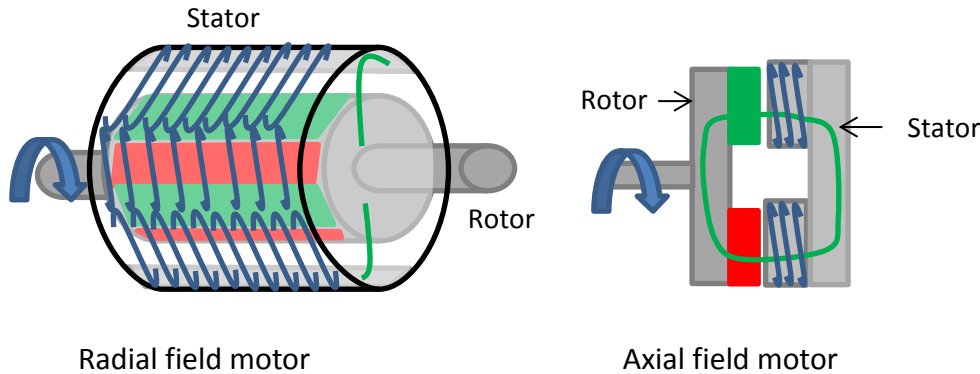


Figure 4 Radial field and axial field motors

The second main group of BLDC motors is axial field motors. In these motors the magnetic field is created in axial direction by a permanent magnet with different poles. The coils are placed in the stationary part of the motor. The advantage of this motor configuration is that the motor can be build flat compared to radial field motors. That's why they are often used in floppy disc drives or hard disc drives. The following pictures shows a disassembled floppy disc axial field brushless DC motor.

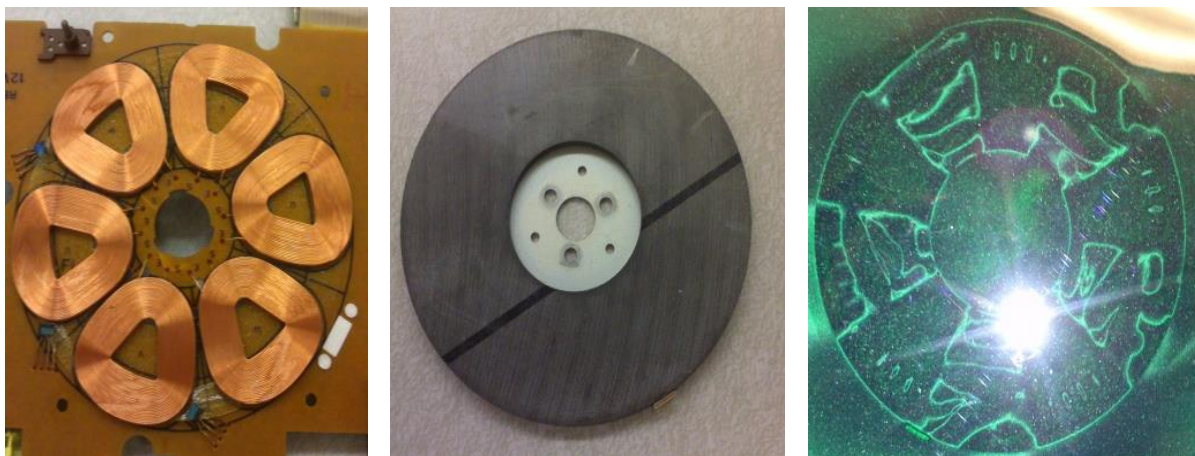


Figure 5 Disassembled floppy disc axial field motor

The design of the rotor can be achieved without big manufacturing effort. Problematic is the winding of the coils of these motors, as this requires special machines to wind the coils in the desired shape. [5], [6] suggest printing coils on a PCB board, because of the high flexibility for the design of the coils. The board can be bought from different vendors after designing it in PCB design software. Using PCB boards for the windings of the motor is well suited for the use in a teaching motor, as the effort and costs to buy such a board are rather low. Power and sensing electronics can be integrated with the coils on the PCB board.

## 2.2 Overview magnetic bearings

### 2.2.1 Reluctance actuators in magnetic levitation

Magnetically levitated systems based on reluctance actuators are often used in universities as a mechatronic example of magnetic actuators and controller design for nonlinear systems. The aim of these teaching projects is to levitate a ball in a constant distance to an actuator. Teaching applications of magnetic levitation using this physical principle of applying forces against gravity are [7], [8], [9] or [10]. A schematic example is shown in the following figure.

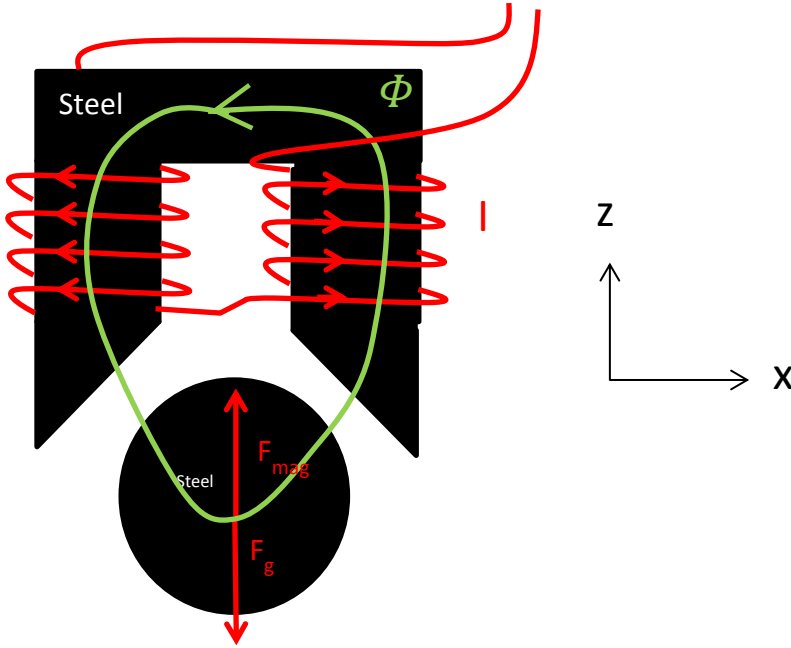


Figure 6 Schematic view of a reluctance actuator based magnetic levitation system

By applying a current  $I$  through a coil which is wound around iron core a magnetic flux  $\Phi$  in the actuator is created. This results in a flux density  $B$  and a force  $F_{mag}$  in the air gap between actuator and mover (steel ball). The current through the actuator is controlled based on the measured position of the steel ball. The position is often measured by optical sensors.

The force characteristic of this actuator can be described with the following equation, where  $x$  represents the distance between actuator and steel ball and  $k$  a geometry specific constant.

$$F_{mag} = k \cdot \frac{I^2}{x^2} \quad \text{Equation 2-1}$$

By the use of one reluctance actuator, only attraction forces between stator and mover (steel ball) can be applied. In the above configuration the negative forces are generated due to gravity. Using this concept the steel ball can be actively controlled in one degree of freedom. If more DOF have to be controlled, as it is the case in this thesis, more reluctance actuators can be used. The University Saarland [11] developed a magnetically levitated plate,

where four reluctance actuators are placed at the edges of the plate. Using these actuators the Z, Pitch and Roll axis can be controlled and the gravity is compensated. This approach seems interesting for the levitation of the horizontal axes of the rotor.

### 2.2.2 Magnetic bearings

Electric motors with magnetic bearings can be separated in two main groups. The first group comprises motors with magnetic bearings. The magnetic bearing is independent from the motor windings itself. A second group is called bearingless motors in which the generation of torque and radial forces is combined [12]. Bearingless motors will not be considered in this thesis as they do not allow a modular design concept of the system.

Figure 7 shows a typical structure of a motor system with conventional magnetic bearings. The motor itself is placed between two radial magnetic bearings. The force created by each radial bearing is perpendicular to the shaft position. This way the rotor can be centered in the middle. The position of the Z axis is regulated by a thrust magnetic bearing.

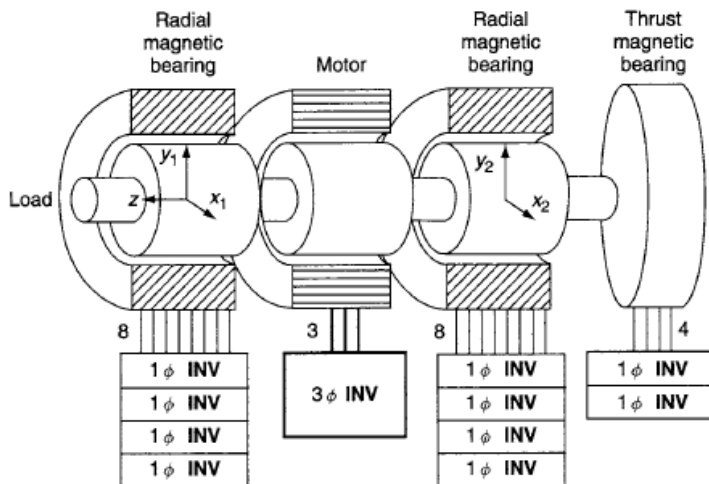


Figure 7 Motor with magnetic bearings picture taken from [12, p. 3]

Typically each radial magnetic bearing has four coils around the stator, two in the X axis and two in the Y axis working in an antagonistic arrangement. So it is possible to create forces in the positive and negative direction of each axis to keep the rotor in its position. This is especially positive when there is no gravity force to readjust the system in negative direction. The motor itself can be used and controlled as a conventional electric motor without any magnetic bearings.

The antagonistic arrangement of the actuators is reasonable for axis, where there are no readjusting gravity force is in the system. For the case of an axial field motor, this configuration has to be preferred for horizontal axis.

## 2.3 Actuation concept

With the defined features and considerations about brushless DC motors and magnetic bearings, different concepts of BLDC motors with magnetic bearings are developed in order to achieve a good overall design.

An axial field brushless DC motor on a PCB board as suggested in [5] is chosen because the windings are the critical part in building the motor. This can cleverly be solved by printing them on a PCB board in combination with the rest of the electronics.

Reluctance actuators above the rotor as advised in [11] will be used to control the vertical axis of the rotor, working against gravity. For the horizontal axis, where no gravity force can be used, an antagonistic arrangement as suggested in [12] is developed.

### 2.3.1 Vertical actuation

The actuation of the Z, Pitch and Roll axis can be done similar to the levitation of a plate in 2.2.1 by mounting reluctance actuators above the rotor. Because of the gravity force of the rotor, only one direction of actuation is required. For the control of the three axes, only three actuators are needed which fits to the limited D/A channels of the myRIO. Also the amount of power electronics can be reduced with this configuration.

Actuator designs which can control these three axes of the rotor are described in Figure 8. All concepts use three reluctance actuators which are mounted above the rotor in an angle of 120°. The magnetic flux created by these actuators is indicated with green lines.

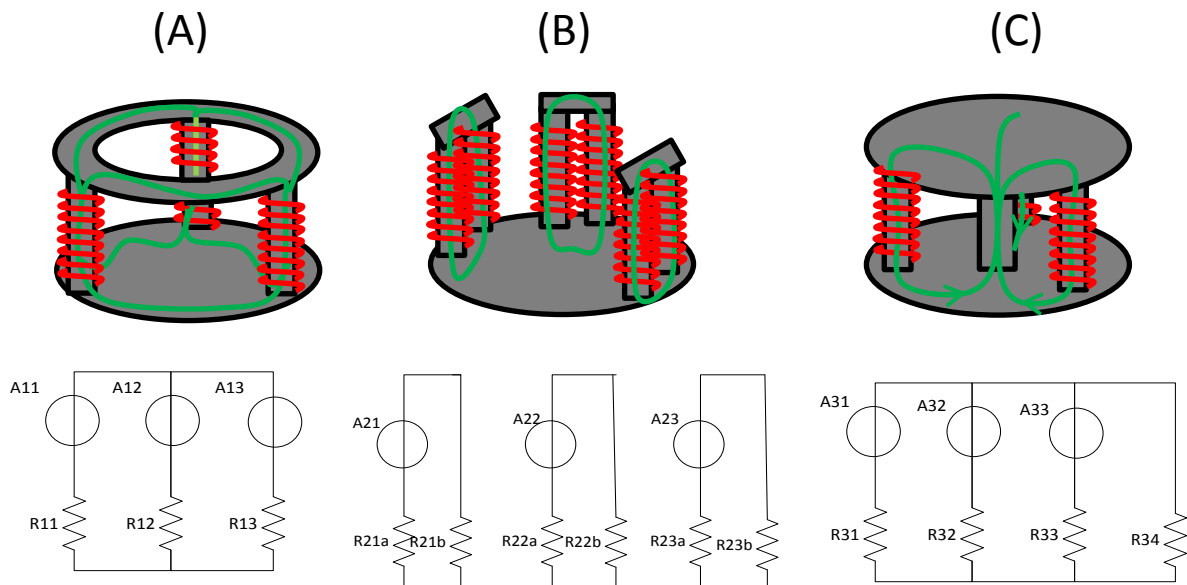


Figure 8 Actuator concept for Z, Pitch and Roll

In (A) three reluctance actuators are mounted above the rotor which are connected via a return path above the other actuators. This results in a simple design. Negative in this actuator configuration is, that there are strong couplings between the actuators. When the cur-

rent in one actuator is increased, the magnetic flux and force increases in all three actuators. This makes this configuration hard to control.

(B) shows a concept where the three reluctance actuators are separated from each other. Couplings in the magnetic flux between the actuators are avoided. The disadvantage in this concept is that each actuator has two points where a force is created at the outer radius which is not wanted. When the rotor tips or tilts, the force generated by one actuator moves between the two stator coils of the actuator, as the resistances changes unequally. This results in an additional nonlinear behavior.

In configuration (C) a feedback path ( $R_{34}$ ) in the middle of the rotor is added. During a normal operation, the magnetic flux created by each actuator is over the feedback path in the middle. So the actuators can be driven mostly independent from each other.

By comparing these three actuator principles it can be seen, that concept (C) offers the most advantages for controlling the Z, Pitch and Roll axis, as the couplings between the actuators are low. In addition the points of force generation are constant.

### 2.3.2 Horizontal actuation

For the control of the X and Y axis additional actuators have to be added. As there is no gravity force in the X-Y plane, an antagonistic actuator principle has to be chosen as it is proposed in 2.2.2 to be able to apply positive and negative forces to the rotor. [12] suggests using two reluctance actuators in each axis to achieve an antagonistic actuation, which results in four actuators for the X-Y plane. Problematic for the use of four actuators is the limitation of D/A channels on the myRIO. So actuator principles using three actuators for the X-Y plane actuation are developed.

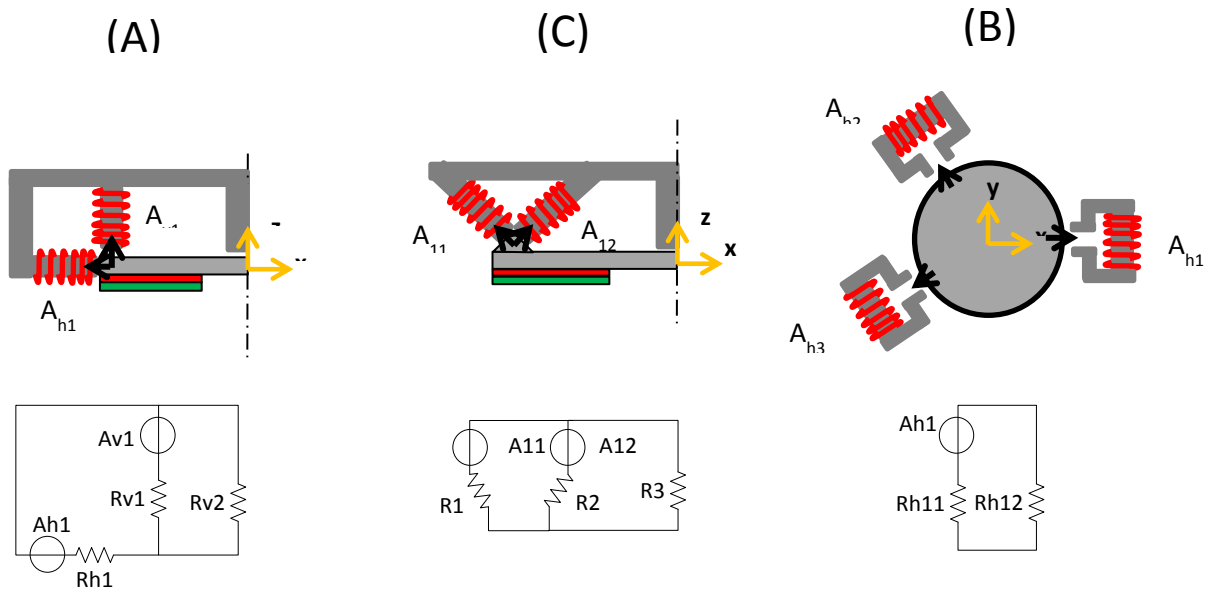


Figure 9 Actuation concept for the X and Y axis



To achieve forces which are distributed equally in the X-Y plane the three additional reluctance actuators are also mounted in an angle of  $120^\circ$  around the rotor. Figure 9 shows three different concepts for controlling the X and Y axis.

The first concept (A) adds a reluctance actuator in the X-Y plane next to each Z axis actuator. By changing the current through this actuator  $A_{h1}$  the rotor can be controlled in X and Y. As the magnetic circuit of the horizontal axis actuator is designed to be over the feedback path ( $R_{V2}$ ) in the middle of the rotor, also a force in the Z axis is created, which needs to be compensated. In addition there is a coupling between the horizontal axis actuators and the vertical axis actuators in the magnetic flux.

Concept (B) shows a more integrated version for the control of the X-Y plane. Two actuators are mounted in an angle of  $45^\circ$  above the rotor where a triangular shaped ring is added. With changing the current in these actuators antagonistically positive and negative forces in the X and Y axis can be applied. By changing the current through both actuators in parallel, a force in the Z axis as well as a torque at the rotor is applied. This can be used to control the Z, Pitch and Roll axis. Negative in this concept is, that the magnetic flux created by the actuators can be shortened. When the rotor turns out of its middle position and the resistance  $R2$  becomes lower than  $R3$  which results in a force mainly in Z direction. Then a creation of forces in the X and Y axis by changing the current antagonistically is not possible and more complex algorithms have to be used.

In concept (C) three reluctance actuators are mounted around the rotor. By applying a current through one actuator ( $A_{h1} - A_{h3}$ ), a force in its direction is created. Because of the angle of  $120^\circ$  between the actuators, positive and negative forces in X and Y can be generated. To keep the point of actuation for each actuator centered, the distance between both force creating parts of one actuator is set to be small. Positive in using this concept is that the X and Y actuators can be used separately from the vertical actuators, which results in a higher possibility of modularization as well as in easier control algorithms. In this concept two points of forces are created by each actuator. The distance between these two points is set to be low, to reduce the effect of the varying center of force per actuator.

For the purpose of this thesis concept (C) offers the most advantages because the couplings between the vertical and horizontal axis are low as it would be the case in concept (A). Also there is no possibility to shorten the magnetic flux as it would be the case in concept (B).

## 2.4 Sensor concept

### 2.4.1 Sensing of the motor angle

In the basic configuration of the motor, commutation as well as position control has to be possible. Because of the modular design of the motor, a contactless measurement of the rotor position needs to be done.

The position sensing of the rotor in BLDC motors is often done by using quadrature encoders. An example of an optical based encoder is shown in Figure 10. On the rotor a disc with different slots is mounted. Via a LED and light receiving elements, quadrature signals are generated when the rotor is rotating.

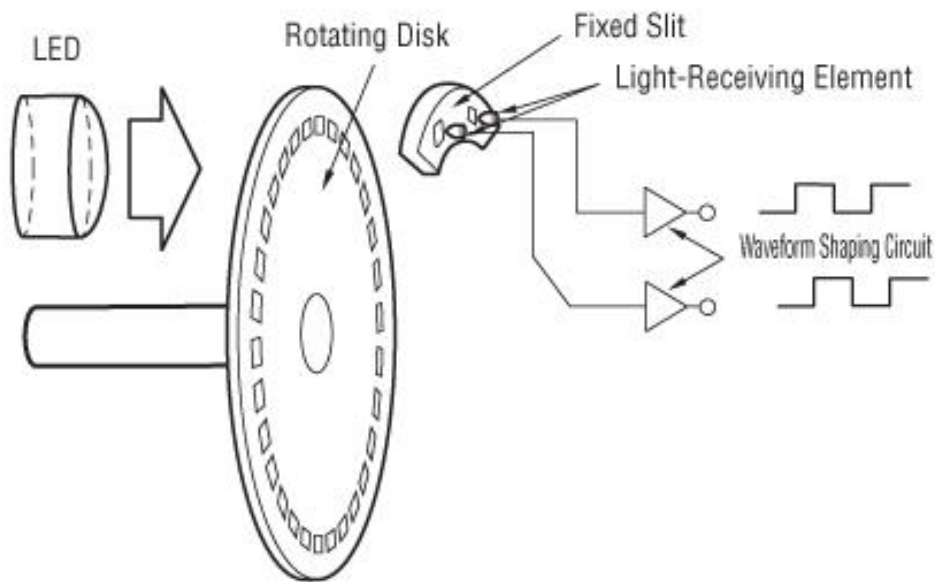


Figure 10 Optical quadrature encoder, picture taken from [13]

The resolution of the encoder is based on the amount of slots on the encoder disc. To increase the resolution of the encoder, analog sine/cosine encoders can be used where the position between each slot is interpolated. The signals of both types of encoder are shown in Figure 11.

For the design of position controllers with a sufficiently high control bandwidth as well as for system identification it is required to measure small angle changes of the rotor ( $< 1^\circ$ ). When a quadrature encoder is used, this results in more than 90 segments of the encoder disc. This high amount of slots in a disc is hard to produce with standard manufacturing techniques. When a sine/cosine encoder is used, which interpolates the values between each segment, the number of segments to achieve a high resolution encoder can be reduced significantly and the encoder disc becomes much easier to manufacture.

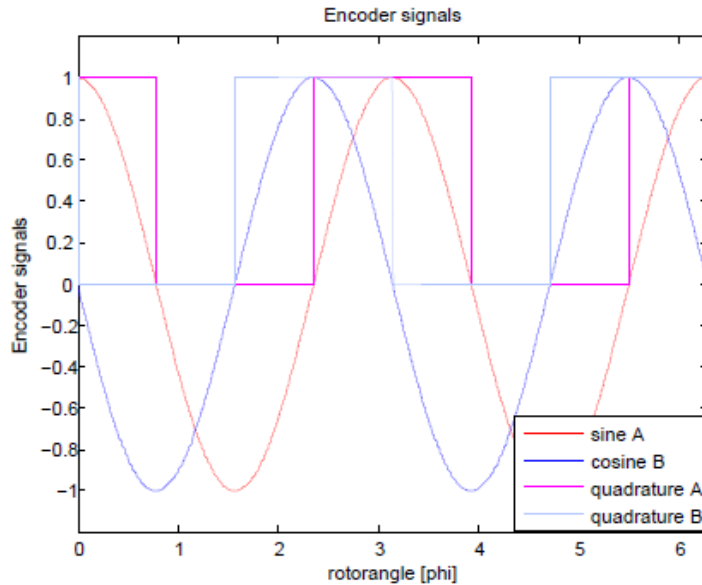


Figure 11 Encoder signals of quadrature and sine/cosine encoders

As the encoder is also used for commutation of the BLDC motor a reference signal of the magnetic angle of the rotor has to be measured and both signals have to be aligned in order to get a good commutation. In industrial application the measurement of the magnetic angle is usually done by three Hall sensors which measure the magnetic field for each phase and generate binary values for the real-time target.

[14] suggests to use permanent magnets and Hall sensors to build an incremental encoder for measuring the rotor position. When the magnetic field of the motor magnets is used to create a sine/cosine encoder, the measurement of the magnetic angle and the rotor position can be combined. Also no additional cost for creating an encoder disc is required. Using this combination a cheap and accurate sensor for both cases of application can be built.

### 2.4.2 Position sensing for magnetic bearings

The magnetic bearing works with closed loop control, that's why an accurate measurement of each axis needs to be done. Because of the different stages of modularization, two sets of sensors should be used to measure the vertical and horizontal axes independently. Sensors which are not sensitive to magnetic fields should be used to avoid disturbances caused by the magnetic fields of the rotor and the reluctance actuators.

The sensors of the Z, Pitch and Roll axes are placed above the rotor close to the actuators as it is shown in Figure 12. Using this configuration the height of the rotor is measured at three points. This makes it possible to control each actuator individually with the measured distance between actuator and sensor. A second option is to transform the measured distances into Cartesian coordinates and to control the different axes.

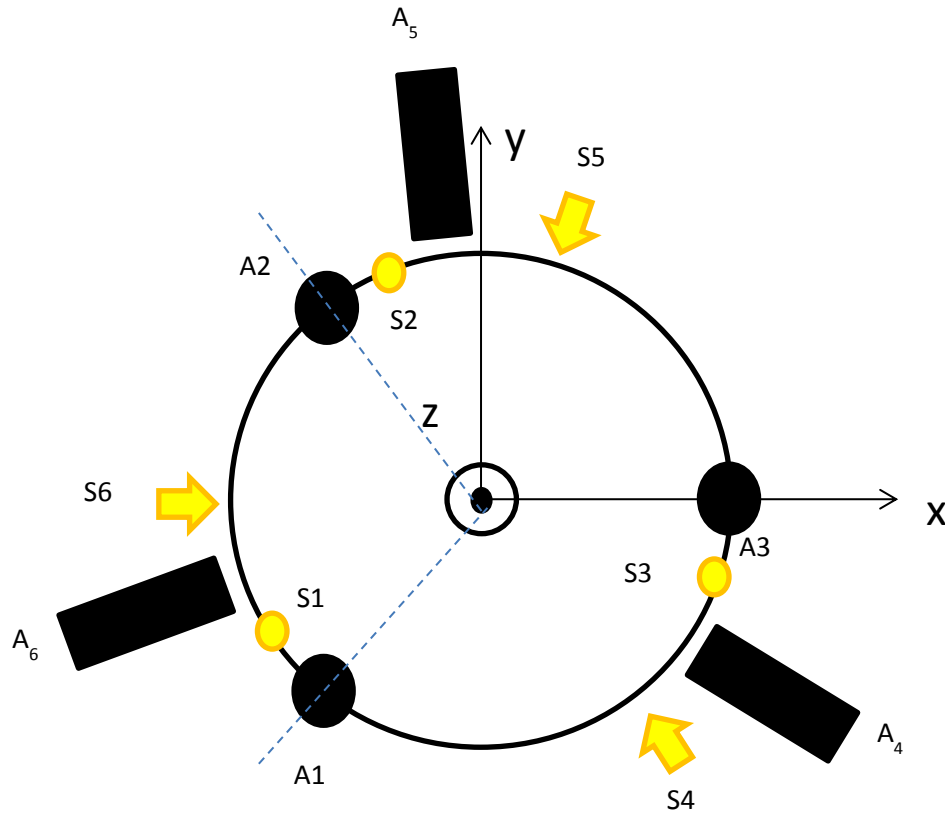


Figure 12 Sensor concept of the magnetic bearing

For the placement of the sensors of measuring the position in X and Y the same approach is chosen. The sensors S4 – S6 are placed next to the actuators and measures the distance between actuator and rotor. So a control of each actuator independently via the measured distance between actuator and rotor is possible. In addition the sensors value can be transformed in Cartesian (X, Y) coordinate. When this is done three the sensors offers a higher accuracy because only two sensors are required to measure these axes. The third sensor acts redundant.

## 2.5 Rotor concept

The rotor of the BLDC motor has to be designed, that permanent magnets can be glued onto the bottom. Therefore a smooth surface between rotor iron an magnets is required in order to reduce the magnetic flux in these points. To achieve high dynamics with the motor, as well as to reduce the bias current to levitate the rotor, a mass of the rotor has to be low.

For levitating the rotor in its desired position, the ferromagnetic surface of the rotor, which interacts with the reluctance actuators, has to be big enough, that no additional resistance between in the magnetic circuits appear. In addition a material with a high permeability has to be chosen.

## Conceptual design

As the vertical and horizontal axes have to be used independently, the couplings between these axis has to be low. This can be achieved, when the horizontal axis actuators are acting in the center of gravity.

The reluctance actuator of the horizontal axes has to be placed close the permanent magnets of the rotor. Nevertheless the rotor has to be designed, that the cogging torque between rotor magnets and actuators is low. In the following figure, the requirements in the rotor design are shown.

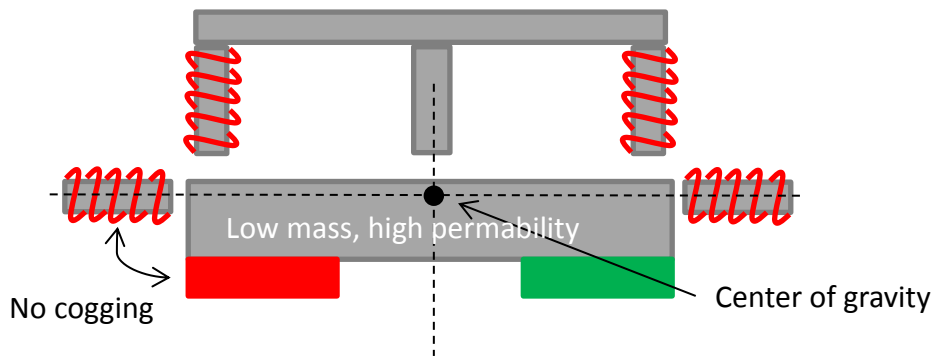


Figure 13 Rotor concept

## 2.6 Concept for a Maglev BLDC motor

### 2.6.1 BLDC motor

An axial field motor is designed with all the electronics and windings placed on a PCB board. The rotor consists of a round steel disc with glued on permanent magnets. To measure the rotor position accurately for control and commutation a Hall sensor based sine/cosine encoder is implemented on the board.

In this step of modularization different commutation techniques of BLDC motors can be shown. Also the processing of sensor signals can be explained. The motor characteristic parameters can be measured and compared to calculated values which have been used the model based design approach. Finally a position control of the rotor axis can be designed and tested.

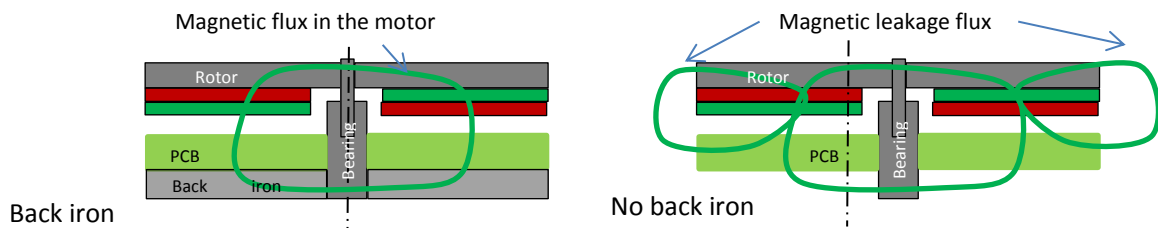


Figure 14 Motor with and without back iron

Because of the modular design it is required to replace the rotor with conventional bearing to the rotor with magnetic bearings. This has to be done without a big effort, which results in a motor without back iron which is described in Figure 14 . The attraction forces between rotor and back iron would make it had to replace the rotor and would increase the force to levitate the rotor significantly. On the other hand the torque generated by the motor is lower because of the high leakage flux and the bigger magnetic resistance. The following figure shows the desired design of the BLDC motor on a PCB board and an easy connection to the myRIO real-time target.

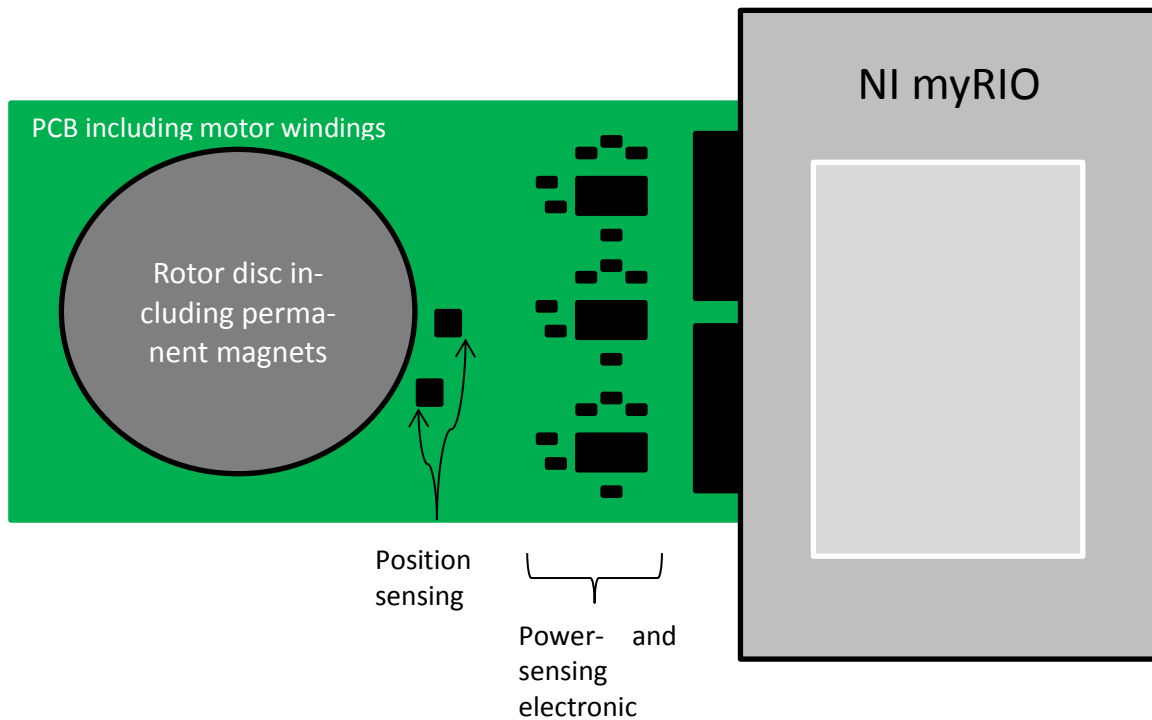


Figure 15 Schematic drawing of the motor concept

### 2.6.2 Magnetic levitation

The second goal of this project is to make the rotor disc levitating using reluctance actuators. In this configuration it is possible to levitate the rotor in up to five degrees of freedom (X, Y, Z, Pitch and Roll). Different control algorithms and interactions between different axes can be observed and algorithms to prevent these effects can be explained.

This is realized by adding three actuators above the rotor in an angle of  $120^\circ$ . These actuators take off the gravity and control the Z, Pitch and Roll axis as it is described in 2.3. A concept for sensing the rotor position is developed in 2.4.2. The placement in the setup is shown in Figure 16.

To stabilize the X and Y axis, three more actuators and sensors are added around the rotor as it can be seen in Figure 16. In this configuration the position in the X and Y plane can be adjusted and imbalances of the spinning rotor can be compensated. With this configuration it is possible to control the rotor disc in five DOF using the magnetic bearing.

### 2.6.3 Magnetically levitated BLDC motor

In the final step the BLDC motor with magnetic bearing can be used. So the motor can be driven magnetically levitated and in six axes controlled. Different effects, like sensor noise because of the rotating rotor and gyroscopic effects can be seen.

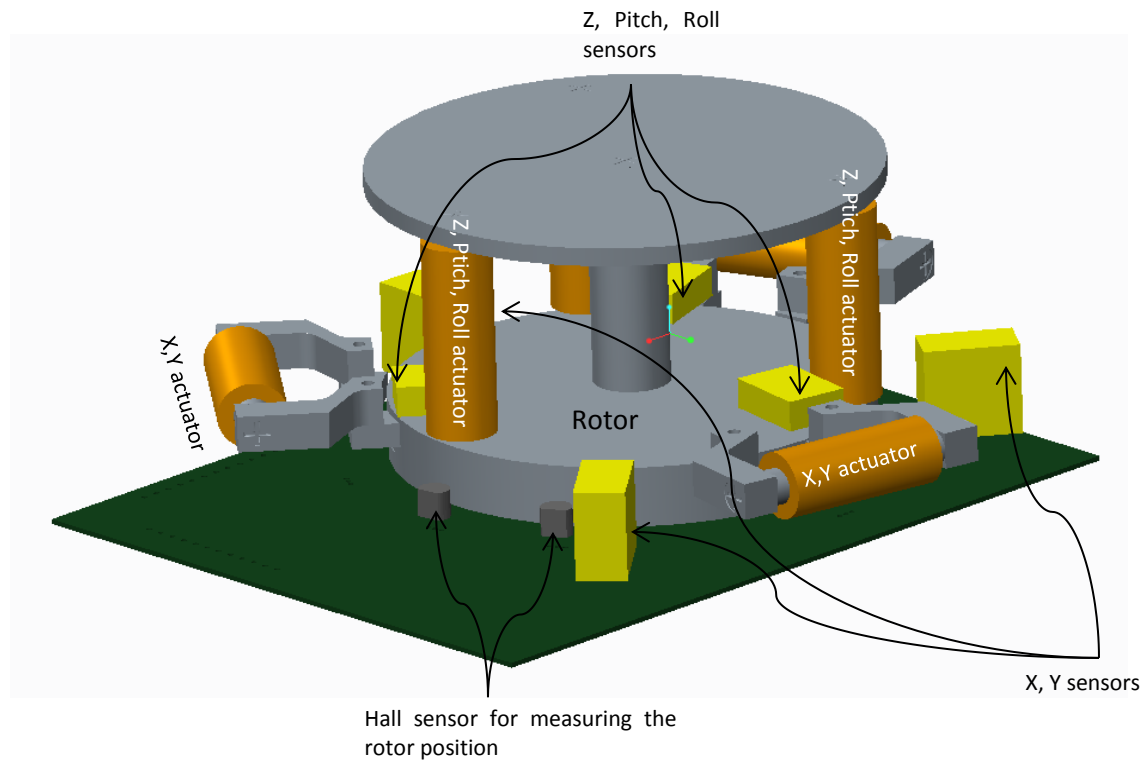


Figure 16 Concept of the magnetic levitated brushless DC motor

### **3 Axial field brushless DC motor**

This chapter describes the design, modeling and testing of an axial field brushless DC motor. Section 3.1 focuses on the coil design of axial field brushless DC motors. Different winding structures are compared and rated regarding their usability in PCB motors. In section 3.2 the rotor of the BLDC motor is developed. Different types of permanent magnets and their use in axial field motors is compared.

The accurate sensing of the rotor position using Hall sensors is explained in section 3.3. For a model based design approach, the motor characteristic parameters are calculated in 3.4 in order to predict the relevant motor behavior.

In section 3.5 the motor is designed including electronics and LabVIEW implementation. With the designed motor, the estimated motor parameters are verified in section 3.6.

For the design of position controllers a dynamic model of the BLDC motor is developed and linearized in section 3.7. A position controller is designed and the implementation of a trajectory based positioning developed. In section 3.8 the model and controller is validated.

#### **3.1 Coil design**

The following section compares different winding structures of brushless DC motors. These structures are compared regarding their use in PCB motors. For the chosen winding structure, coils are designed which offer a high torque capability.

##### **3.1.1 Winding structure**

The winding structures of BLDC motors can be separated in two groups, overlapping and non-overlapping windings. The two different structures are described and compared for the use in PCB motors.

###### ***3.1.1.1 Overlapping winding***

The overlapping winding is the most common winding structure in standard synchronous motors, as the magnetic field in the air gap of the motor is nearly sinusoidal [15, p. 2]. In this type of winding the coils of the different phases are overlapping. So the coils of the different phases have to be separated to different layers on the PCB board. An example of an overlapping winding with four coils per layer is given in the following figure.



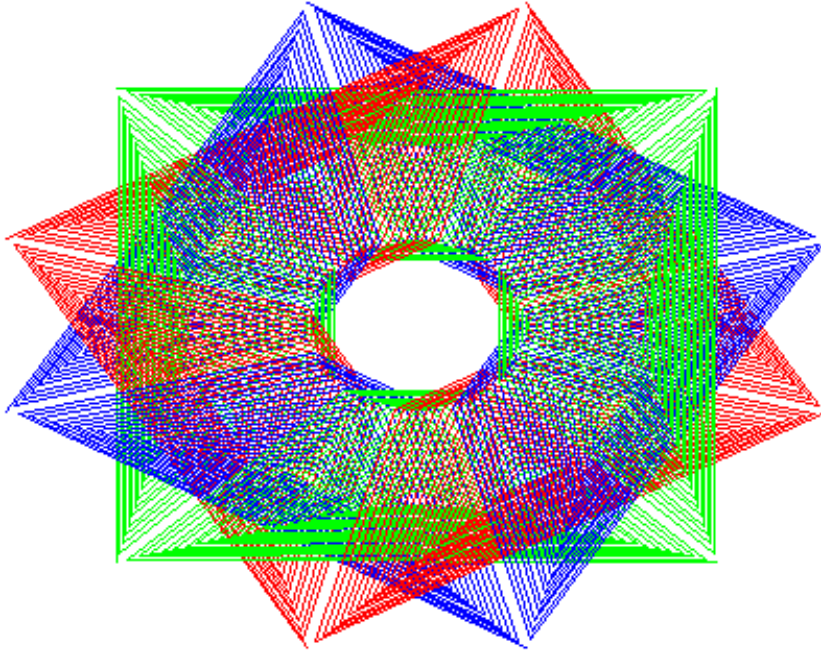


Figure 17 Overlapping winding structure

In the overlapping winding structure the number of coils per phase  $N_{coilperphase}$  is equal to the number of poles at the rotor  $N_{poles}$  as displayed in Equation 3-1. The total amount of coils of the motor is calculated by number of coils per phase multiplied with the number of phases.

$$N_{coilperphase} = N_{poles} \quad \text{Equation 3-1}$$

The difference between electrical speed  $\omega_{el}$  and mechanical speed of the motor  $\omega_{mech}$  is represented in the following equation.

$$\omega_{mech} = \frac{\omega_{el} \cdot 2}{p} \quad \text{Equation 3-2}$$

The variable  $p$  is the number of poles at the rotor. The following table shows the number of poles, the resulting coils and the ratio between mechanical and electrical speed for a three phase motor.

Table 1 Parameter setup for overlapping windings

Poles	Coils	Ratio $\omega_{el}/\omega_{mech}$
2	6	1
4	12	0.5
6	18	0.33
8	24	0.25
10	30	0.2

For the design of brushless DC motors on PCB boards it has to be taken into account, that every coil must have an even number of layers, to have a connection through the lead cables from the outside of the coil. Otherwise an extra connecting layer is needed. This is shown in the figure below. This results in a minimum of six layers of the PCB board for a three phase motor.

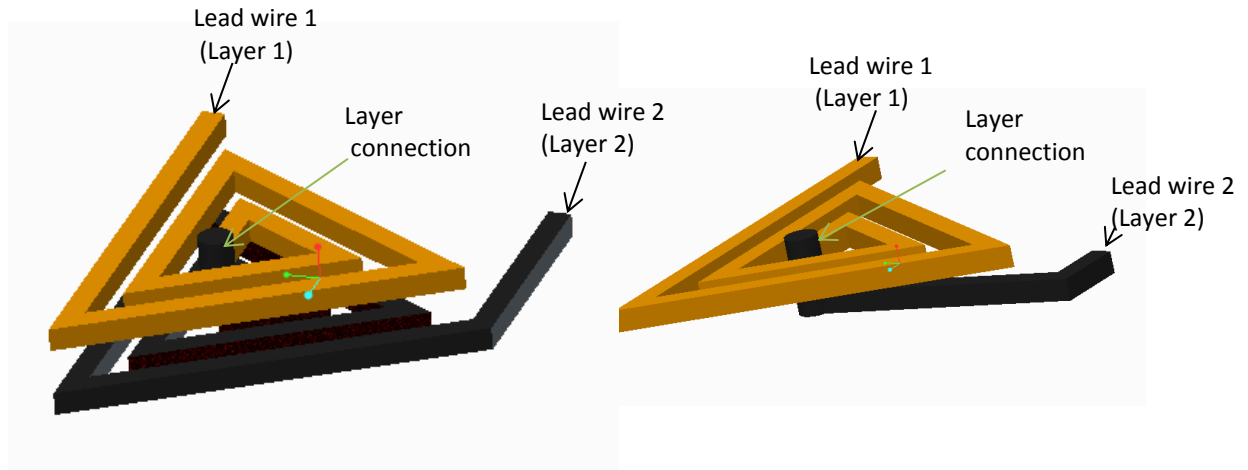


**Figure 18 Layers per Coil**

As the coils of the different phases are overlapping, the connection between the different layers is difficult. It can either be done by using “not through hole connections”, which are expensive to manufacture, or by leaving enough space in the other coils to use standard “through hole connections” which lowers the amount of turns of a winding. Differences between both connection types are shown in the figure below.

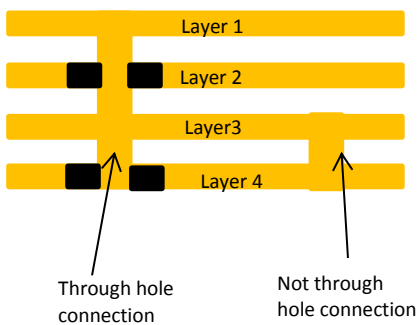


**Figure 19 Through hole and not through hole connection**

### **3.1.1.2 Non Overlapping winding**

In comparison to the overlapping winding structure the coils are separate in the non-overlapping winding structure. This winding structure is a common structure in linear motors and for the building of low speed torque motors [16]. The following figure shows a schematic view of a non-overlapping winding. It can be seen, that every coil is independent from the other coils.

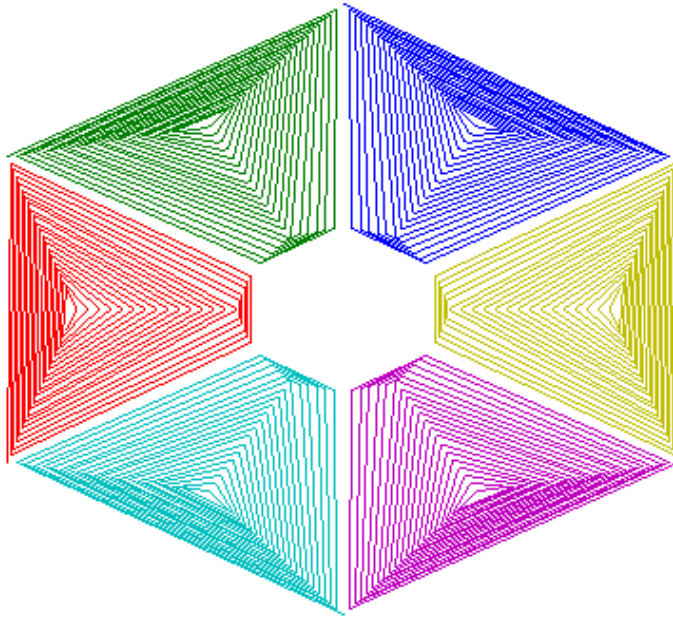


Figure 20 Schematic view of non-overlapping windings

The relation between the electrical and the mechanical speed in Equation 3-2 still holds. Common coil and pole arrangements for non-overlapping windings structures are three coils to four poles or three coils to five poles configurations and their multiples. The following table gives an example of common distributions and their ratio between electrical and mechanical speed.

Table 2 Parameter setup for overlapping windings

Poles	Coils	Ratio $\omega_{el}/\omega_{mech}$
4	3	0.5
8	6	0.25
10	6	0.2

The advantage of a non-overlapping winding structure in the design of an axial field PCB motor is the high design flexibility in designing the coils. For the amount of layers on the PCB board only an even value has to be chosen because of the lead cables. So the torque constant of the motor can be adjusted better by adding or removing two layers on the board. The connection between the different layers on the board can be done by “through hole connections” which makes the board less expensive.

### 3.1.1.3 Winding comparison

By the use of a non-overlapping winding structure there is more flexibility in designing coils. This way the layers of the board can be adjusted freely and the number of turns can be adjusted to the maximum allowable resistance of the coil. In addition the costs for producing the boards are lower because of the possible “through hole connection”. For this reasons a non-overlapping winding structure has been chosen for the design of the motor.

### 3.1.2 Coil Design

To achieve a high torque capability in the motor using little mechanical space, it is important to design coil which are effective in respect of their shape. To maximize the torque crated by each coil, the length  $l$  of wires in radial direction to the rotating axis has to be maximized. These wires create the motor torque via the Lorentz force  $F$  when a magnetic field  $B$  is applied. The following figure shows a simplified coil structure and the forces due to current and magnetic field.

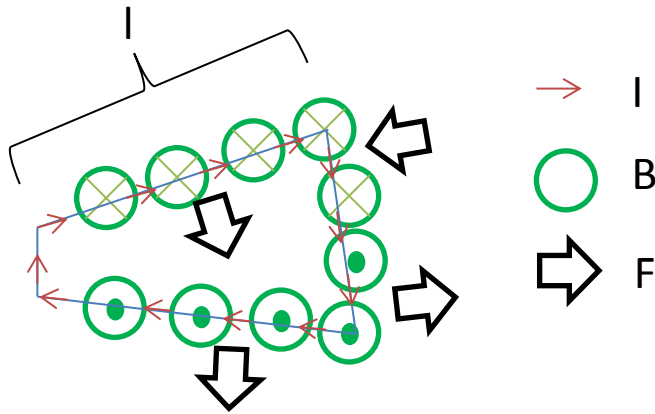


Figure 21 Lorentz forces in a coil

One approach in the design of coils with high torque is the use of rhomboidal turns (Figure 22 A) in the coils. This way the length of wire in the magnetic field can be maximized. On the other hand the  $R \cdot I^2$  losses in the coils are very high, as there is only half of the coil in the magnetic field [5, p. 40]. Also this coil structure needs a lot of space on the PCB board, which makes it inefficient in respect of space.

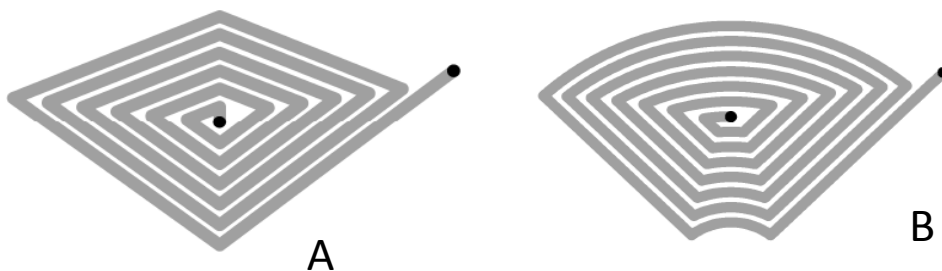


Figure 22 Rhomboidal coil, coil with parallel active sections, picture taken from [17, p. 2]

A second approach is the use of coils with parallel active sections (Figure 22 B). In comparison of the maximum achievable torque under a magnetic field, the torque created by the Lorentz force is lower. But on the other hand a higher torque constant in relation to the used space on the PCB board and to the resistance of the coil can be achieved, which makes this shape attractive.

For the design of the PCB motor the coils with parallel active sections are chosen, as this coil arrangement is more efficient in relation of space and copper losses.

An important design parameter of the coil is the number of turns which can fit on one coil. This parameter is estimated by using the following equation [17, p. 4]:

$$N = \frac{R_o - R_i}{2 \cdot (w + c)} \quad \text{Equation 3-3}$$

The variables  $R_o$  and  $R_i$  represents the outer and inner radius of the coil. N is the total amount of turns at one layer. With a track width of 5 mil and a clearance of 6 mil on the PCB board, an outer diameter of 75 mm and an inner diameter of 20 mm of the coils, each layer of the coil is estimated to have 49 turns.

To achieve a higher torque more layers of coils have to be used and the coils of the different layers have to be connected in series. In order to have the electrical current in the same direction in each coil, the coils of the different layers have to be designed as the following figure indicates.

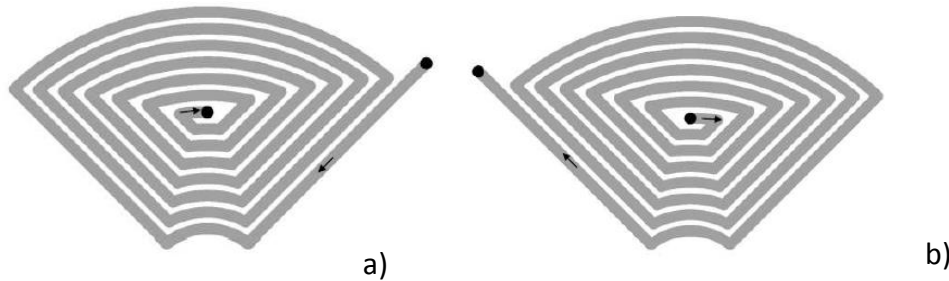


Figure 23 Coil structure for different layers, picture taken from [17, p. 2]

With the first approximation of the coil parameters and the consideration about connecting different layers, a more detailed coil version has been created. A Matlab script for the design of coils is written which is attached at the appendix. This script is interfaced to the PCB design software Altium where the needed Gerber files and the rest of the electronics are designed.

It turned out, that a maximum amount of 35 turns can be placed on one coil and one layer. By using a four layer PCB board 140 turns can be achieved on one coil. The torque constant of each coil can be calculated using Equation 3-18.

To achieve the maximum torque constant in relation to the needed space, different variations of coils with parallel active sections have been calculated. It turned out, that the maximum torque of the motor can be increased by 17 % using coils with an arc structure at the outer radius compared to coils with only straight lines at the outer radius. This is because the maximum length of the tracks parallel to the rotating axis can be enlarged using the arc structure. This can be seen in Figure 24.

That's why coils with parallel active sections and an arc structure at the outer radius have been chosen in the coil design of the motor.

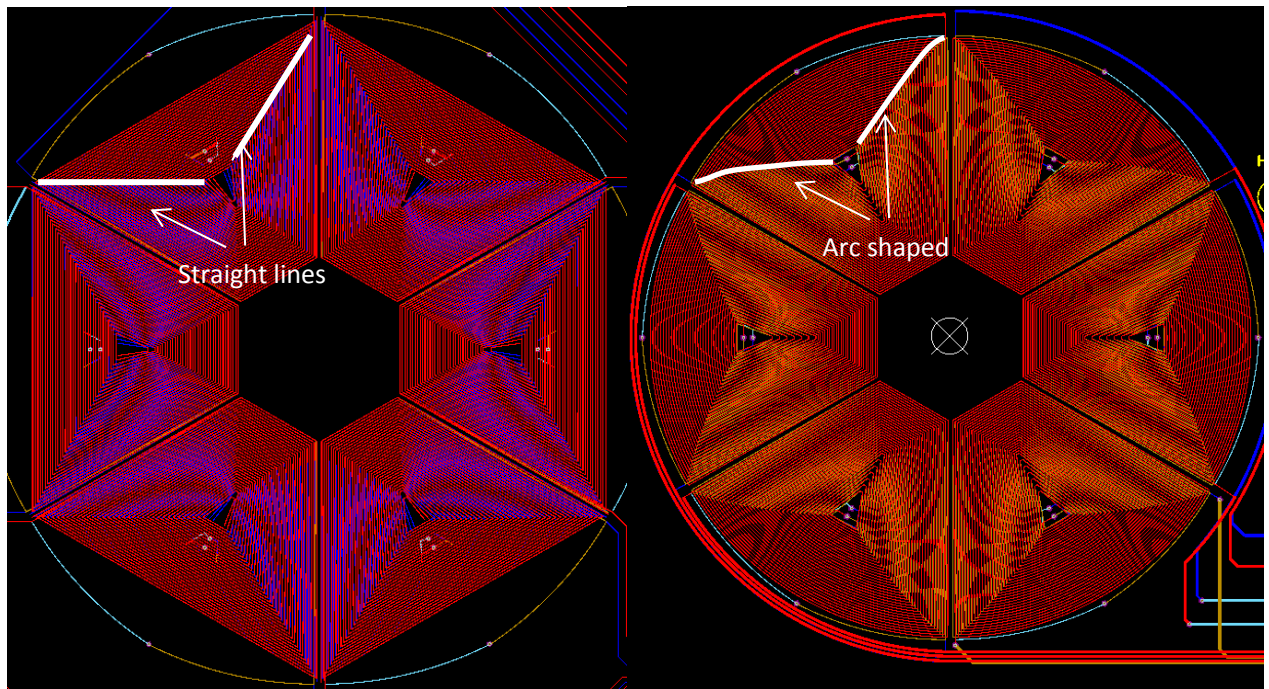


Figure 24 Coils with straight lines and arc structure

## 3.2 Rotor design

After designing the coil structure of the motor a rotor is designed to get a motor with a high torque capability and easy manufacturing. Therefore different magnetic materials are compared and tested. The most promising design is chosen.

### 3.2.1 Magnetic material

To achieve a motor with adequate torque, different magnetic materials are compared. The main requirements for the design of the rotor are that the magnets can be either bought as a standard magnet, or that the permanent magnet material can be magnetized and machined with adequate effort. Also the magnetic field created by the magnets has to be sufficiently high. Table 5 in the appendix shows different magnetic materials and their main properties.

It can be seen, that NdFeB magnets offer the highest energy product, but on the other hand they are hard to machine and remagnetize. This means, that this type of magnetic material can only be used if the suitable shape of NdFeB magnets is available of the shelf. Fortunately there is a wide range of different shapes of NdFeB magnets, which can be bought from different vendors.

Ferrite magnets would be a good solution for the use in rotors for axial field machines, as they can be remagnetized rather easy, and still offer a high magnetic field. Unfortunately no ferrite ring magnet with the right dimensions could be found.

NdFeB flexible magnets and NdFeB bonded magnets are also not the best choice for the design of a prototype of an axial field rotor, as even if they can be machined it is hard to magnetize the rotor in the desired pattern. On the other hand, if a larger amount of motors is planned to be built, bonded NdFeB magnets could be a good choice, as they can be bought machined and magnetized from different vendors. For large amounts of motors this kind of magnet offers high energy product as well as customized shapes.

A flexible ferrite magnet offers the lowest energy product, but they can be machined and magnetized very easy for prototyping of different shapes and magnetic patterns. Because of this features, this material becomes interesting for the use in prototypes of an axial field brushless DC motor.

It can be seen, that NdFeB magnets and ferrite flexible magnets offers the most advantages for a first prototype of an axial field brushless DC motor. Rotor configurations of these two rotor systems will be discussed in the next steps.

### 3.2.2 Flexible magnet rotor

For building a flexible magnet rotor a sheet of flexible magnetic material has been ordered. With a magnetic material listed in Table 5 and a given thickness the magnetic flux density in the PCB board of the motor can be calculated. The magnetic circuit of the motor with a back iron behind the rotor can be represented as the schematic shown in Figure 25.

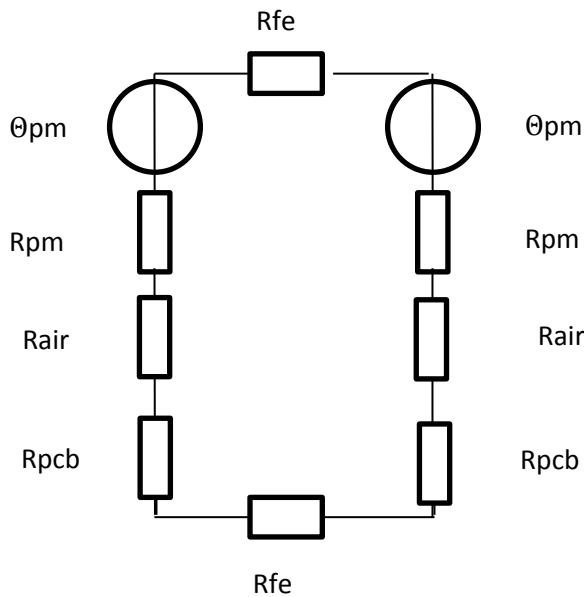


Figure 25 magnetic circuit of a motor with back iron

The magnetomotive force  $\Theta$  created by the permanent magnets can be calculated using the following equation.

$$\Theta = H_{pm} \cdot l_{pm} \quad \text{Equation 3-4}$$



The variable  $H$  represents the magnetic flux intensity of the permanent magnet and  $l$  the length of the magnet. The magnetic resistance  $R_m$  of the different elements in the magnetic circuit can be expressed as:

$$R_m = \frac{l}{\mu_0 \cdot \mu_r \cdot A} \quad \text{Equation 3-5}$$

Where  $\mu_0$  is the magnetic permeability on vacuum,  $\mu_r$  is the magnetic permeability of the material and  $A$  the cross section. With the sum of the resistances and the magnetomotive force, the magnetic flux  $\Phi$  can be calculated.

$$\Phi = \frac{\Theta}{R_{mtot}} \quad \text{Equation 3-6}$$

The flux density  $B$  in the PCB board can be determined as:

$$B = \frac{\Phi}{A} \quad \text{Equation 3-7}$$

The variable  $A$  represents the cross section in the PCB board in the magnetic field. According to these calculations a flux density of 0.08 T can be achieved using a flexible magnet disc with a length of 3 mm.

In order to magnetize the rotor in the desired magnetic pattern a magnetization tool using NdFeB permanent magnets has been developed which is shown in the figure below.

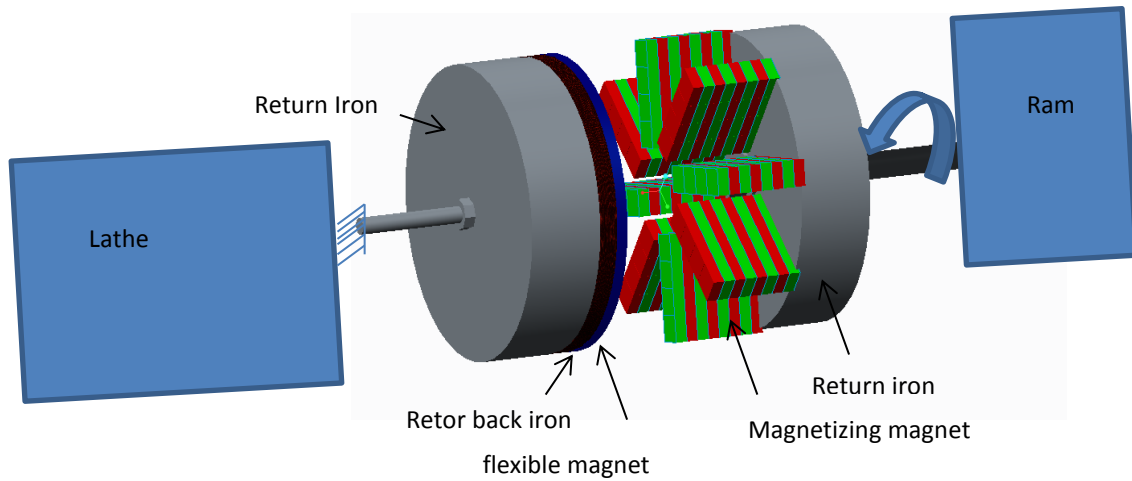


**Figure 26 CAD Magnetizing tool**

Using this tool a pole structure of eight poles can be placed on the sheet of flexible permanent magnets. To magnetize the flexible magnets, the rotor will be clamped in a lathe. On the ram of the lathe the magnetizing tool is clamped. To magnetize the rotor the following steps have to be performed:



## Axial field brushless DC motor

- Lowering the distance between the flexible magnet and the magnetizing tool, until both sides almost touch
- Turning the spindle of the lathe at least  $45^\circ$  by hand (the spindle has to be turned clockwise)
- Increasing the distance between the two sides till the magnetic field between the two parts is negligible
- Removing the rotor from the lathe

The magnetization process is shown in the following figures.

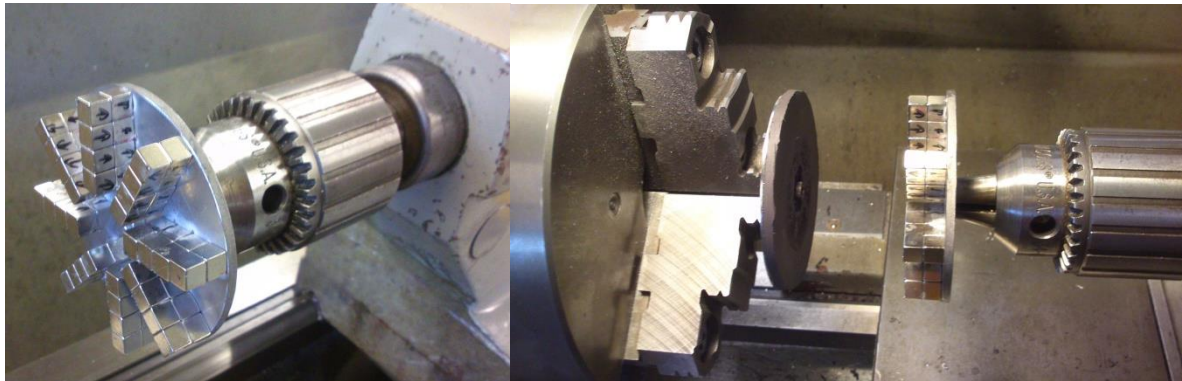


**Figure 27 magnetizing a flexible magnet rotor**

To calculate the needed magnets in the magnetization tool Equation 3-4 to Equation 3-7 have been used. According to these calculations a NeFdB magnet with a length of at least 12 mm has to be used to generate a magnetic field higher than 1.0 T which is desired to achieve full remagnetization in the flexible magnet.

To validate the magnetic patterns on the rotor a magnetic foil has been used, which shows the different magnetic field lines. In Figure 28 it can be clearly seen, that the rotor has the desired pole distribution of 8 poles.



**Figure 28 Self magnetized flexible magnet rotor**

### 3.2.3 NeFdB magnet rotor

The second design approach for a low cost rotor with off the shelf material is done by using NeFdB disc magnets which are glued on a ferromagnetic steel disc. NeFdB magnets have been chosen for this purpose as they can be bought from many vendors.

Different disc magnet configurations have been calculated to achieve the maximum amount of magnets on a rotor disc with a diameter of 75 mm. It turned out, that a magnet configuration of round magnets with a diameter of 13/16" gives the highest density of permanent magnets, without using too many magnets. The following figure shows the CAD drawing of the designed magnet.

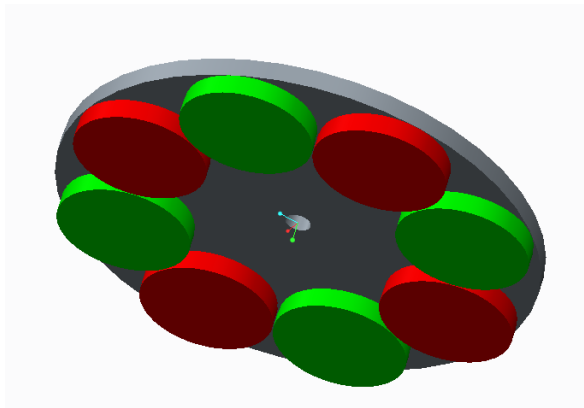


Figure 29 CAD drawing of a NeFdB magnet

Round magnets have the additional advantage, that the magnetic field of a rotation rotor is expected to be more sinusoidal, than by the use of rectangular magnets. This is indicated in the following figure where the magnetic field for one turn of the windings is estimated.

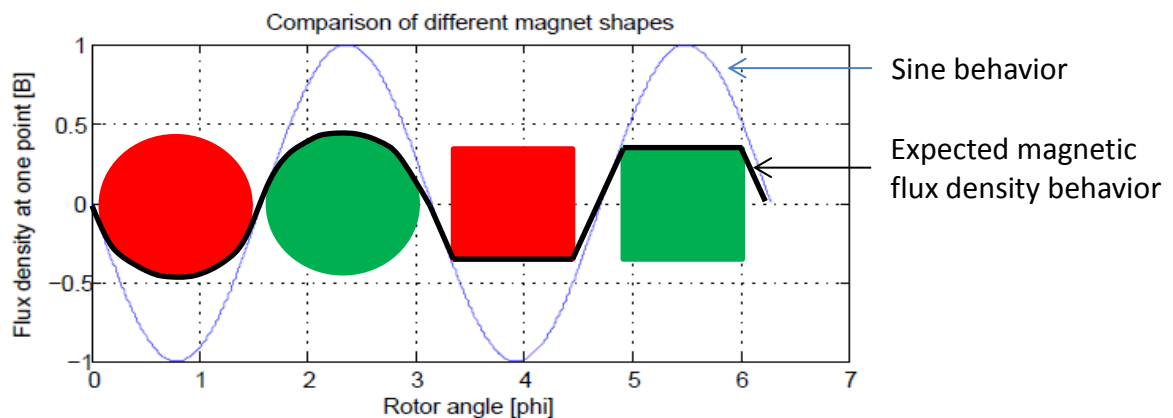


Figure 30 Expected magnetic field in the coils

As the magnetic field of this rotor is strong enough to be used as a motor with and without back iron, the magnetic flux density for both cases has been calculated. According to Equation 3-4 to Equation 3-7 the magnetic field in the PCB board is 0.6 T using a back iron and NeFdB magnets with a length of 3 mm.

For calculation of the magnetic field in the PCB board using no back iron the 2D FEM simulation program FEMM is used. In this software a 2D model of the rotor is created. According to this simulation the magnetic field in the PCB board is averaged at 0.23 T. A figure of the simulated magnetic field is shown in Figure 31

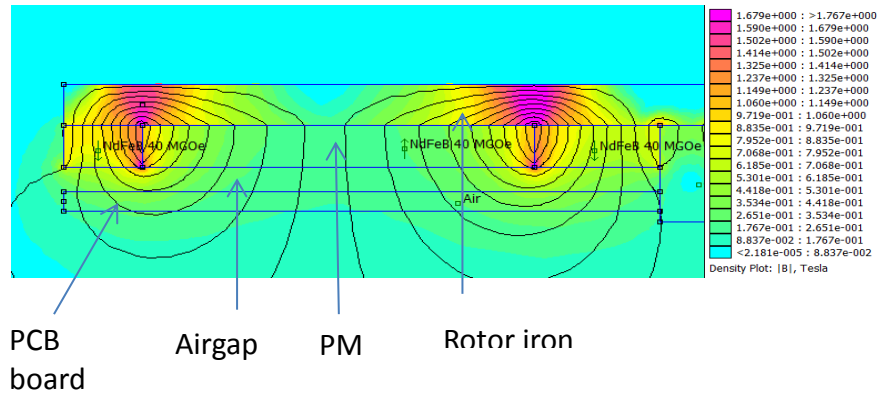


Figure 31 2D Magnetic field simulation of the motor without back iron

When building a rotor with glued on permanent magnets it turned out, that it is very important that the magnets are placed correctly. Variations on the placement will affect the Hall sensor reading negatively and create imbalances on the rotor. For an accurate placement of the magnets on the rotor iron, a mounting tool has been designed and 3D printed. A picture of the placement tool and the designed rotor is shown in the following figure.



Figure 32 NdFeB magnet placement tool and NdFeB rotor

The rotor has been manufactured according to the CAD files attached in the appendix.

### 3.2.4 Comparison of the rotor configurations

Two different rotor configurations have been designed. Depending on the purpose of the motor application it can be decided, which meets the specifications better. For a teaching motor, it is suggested to use NdFeB magnet, as this type of rotor offers a higher torque capability, even if it is used without a back iron under the PCB board.

### 3.3 Position sensor

For commutation of the motor current as well as for position control of the motor, a position sensor has to be implemented, as it is described in chapter 2.4.

Two hall sensors are measuring the magnetic field which is exposed by the permanent magnets of the rotor. The Hall sensors are placed in a  $22.5^\circ$  angle mechanically, which is an angle of  $90^\circ$  in magnetic field.

When the rotor is spinning, the magnetic field should change in sinusoidal shape. The frequency of the magnetic field is four times the mechanical rotor frequency because of the eight poles (four pole pairs) on the rotor. This way one mechanical rotation of the motor angle  $\varphi$  results in four rotations in magnetic angle  $\varphi_{mag}$  as it is shown in the following equation.

$$\varphi = \frac{\varphi_{mag}}{p/2} \quad \text{Equation 3-8}$$

The following figure shows the rotor with the different poles and the desired signal sensor curve.

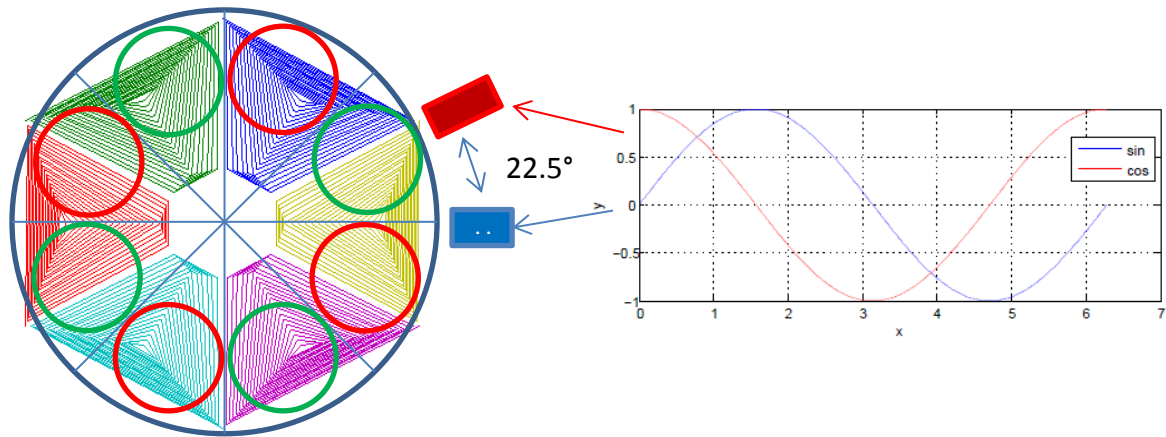


Figure 33 Sine/cosine encoder reading

To calculate the magnetic angle of the rotor, the arctan between the sine signal (A) and the cosine signal (B) has to be build.

$$\varphi_{mag} = \tan^{-1}\left(\frac{A}{B}\right) \quad \text{Equation 3-9}$$

For efficiency reasons, the atan2 function is used, as this function takes care of the four quadrants of the signal.

$$\varphi_{mag} = \text{atan2}(A, B) \quad \text{Equation 3-10}$$

The value range of the atan2 function is  $-\pi$  to  $\pi$ . To measure the total magnetic rotation of the rotor the numbers of rotations have to be counted and added to the previous value.

For the placement of the sensors, they have to be in the magnetic field of the permanent magnets, but not in the field of the coils, as this would disturb the measurement of the rotor angle. So the sensors are placed outside the coils as shown in Figure 33.

When the sensor is placed at a distance of 3 mm next to the rotor, the magnetic flux density in the sensors changes between +0.13 T to -0.13 T according to the FEMM simulation which is shown in Figure 34. This results in a change of the output voltage of the Hall sensors of more than 3 V [18].

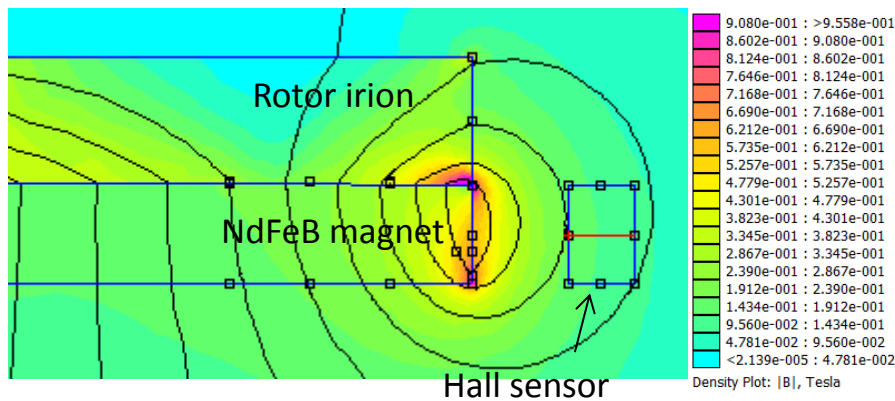


**Figure 34 Simulated min/max flux densities in the Hall sensors**

The voltage change is sensed by the 12 bit A/D channels of the myRIO system. Caused by the quantization of the real-time target, one magnetic rotation can be sensed with roughly 2500 steps. If the sine behavior is ideal, and there is no noise on the signal, this results in a sensor resolution of  $0.04^\circ$  which shows, that the position can be sensed using this concept with high resolution. Because of non-linearity in the sine behavior and sensor noise, the accuracy will be lower.

The processing of these sensor values is put on the FPGA of the myRIO real-time target, in order to save resources of the microprocessor and to lower time dependencies. Additionally the resolution of the sensing can be increased by oversampling on the FPGA and averaging the signals via a low pass filter.

If a higher accuracy of the rotor position measurement needs to be done, a sine/cosine encoder using photo resistive elements and LED in addition to a 3D printed slotted disc can be added to the rotor. An example of such an encoder is shown in Figure 40.

### 3.4 Parameter calculation

In the design of motors it is very important to know the motor behaviors like maximum torque, maximum speed, current through the coils and different time constants in advance. These data can be calculated with the motor geometry and material specific constants. By knowing about these parameters, the motor which has to be designed can be matched perfectly to the desired application by a model based design approach.

In this section the motor specific parameters of axial field brushless DC motors will be calculated, and the equations for specific parameters are discussed.

#### 3.4.1 Torque constant

To calculate the maximum achievable torque of the motor, the torque constant is calculated. The torque constant represents the relation between applied current and torque of the motor. The torque in the motor is created by the Lorentz force. For the calculation of the total torque, the torque which is created by each wire is calculated and the different values are summarized. The Lorentz force which is created by each wire is calculated based on the following equation.

$$F = I \times B \quad \text{Equation 3-11}$$

If the field is perpendicular to the electric current, the equation can be written as:

$$F = I \cdot B \cdot l \quad \text{Equation 3-12}$$

$F$  is the force which is created by the current  $I$  through a wire with the length  $l$ .  $B$  is the magnetic flux density which is applied at the wire. For the calculation of the torque  $T_{wire}$  which is created, the integral of the force of each wire has to be built. In this equation  $r_o$  represents the outer end of the wire and  $r_i$  the inner end of the wire:

$$T_{wire} = \int_{r_i}^{r_o} I \cdot B \cdot l \, dl \quad \text{Equation 3-13}$$

This results in the following equation:

$$T_{wire} = \frac{1}{2} \cdot I \cdot B \cdot (r_o^2 - r_i^2) \quad \text{Equation 3-14}$$

To get the total torque of one coil  $T_{coil}$ , the torques created by all the wires have to be summed:

$$T_{coil} = \sum_{c=1}^N T_{wire_c} \cdot 2 \quad \text{Equation 3-15}$$

The factor 2 results because only one half of the coil has to be calculated, as the second half can be mirrored

$$T_{coil} = \sum_{c=1}^N \cdot I \cdot B \cdot (r_{oc}^2 - r_{ic}^2) \quad \text{Equation 3-16}$$

The characteristic parameter of a motor is the torque constant  $Kt_{coil\_max}$ . The unit is Nm/A. It can be calculated by dividing the torque with the current, so the torque constant results as:

$$Kt_{coil\_max} = \sum_{c=1}^N \cdot B \cdot (r_{oc}^2 - r_{ic}^2) \quad \text{Equation 3-17}$$

Depending on the position of the rotor, the air gap flux density changes with a sine function [19], which can be seen in the figure below. This is desired in order to get small torque ripples by the use of sine commutation and has already taken into account by the design of the rotor

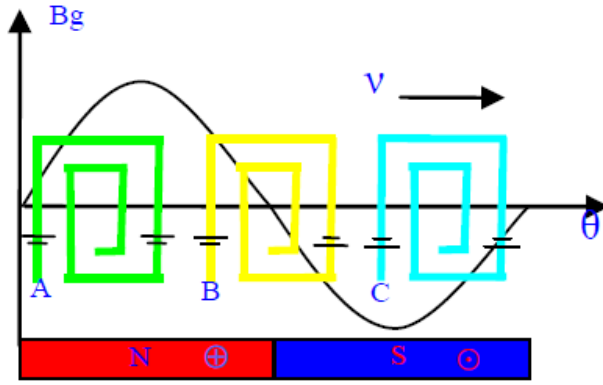


Figure 35 Description of the air gap flux density, picture taken from [19, p. 2]

With this behavior, the torque constant of the motor for one coil can be expressed as:

$$Kt_{coil} = \sum_{i=1}^N \cdot B \cdot (r_{oi}^2 - r_{ii}^2) \cdot \sin(\varphi_{mag}) \quad \text{Equation 3-18}$$

Because the round magnets, which have been chosen for the rotor, do not cover the whole coils, a Matlab file has been written, to detect the areas under a magnet, and calculate the torque constant. The following figure shows an area of a coil. The black circles indicate the magnets and so the area which is under the magnetic field.



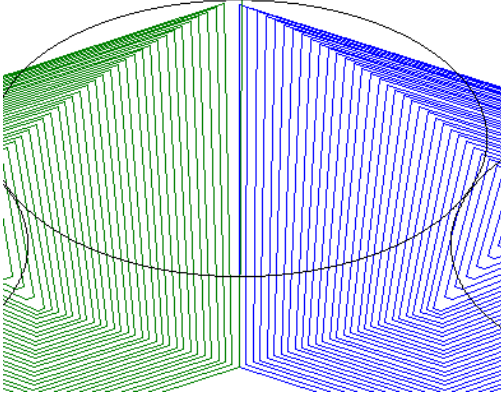


Figure 36 Coil and area which is in magnetic field

Using the calculated track length of the Matlab script for a coil diameter of 75 mm and the simulated flux density of 0.23 T for a rotor assembly without back iron (section 3.2.3), a torque constant with an amplitude of 0.0206 Nm/A is calculated.

### 3.4.2 Back EMF

The back EMF is the voltage which is introduced in the system via electromagnetic induction when the motor is spinning. In the following the calculation of this voltage in relation to the rotor speed is done.

The voltage which is induced can be expressed as:

$$V = v \cdot l \cdot B \quad \text{Equation 3-19}$$

Where U is the voltage and v is the velocity, with which a wire is moving in a constant magnetic field. To calculate the back EMF in a rotary system, the velocity has to be converted in to the angle velocity for the velocity  $\omega$  of a specific point. It can be expressed as:

$$v = 2 \cdot \pi \cdot r = \omega \cdot r \quad \text{Equation 3-20}$$

The velocity is changing with the radius of the wire. Therefore the velocity has to be calculated using the integral of the radius r. Thus the voltage induced by one wire is:

$$V_{wire} = \omega \cdot B \cdot \int_{r_i}^{r_o} l \, dl \quad \text{Equation 3-21}$$

Solving this integral, the voltage induced by one wire is:

$$V_{wire} = \frac{1}{2} \cdot \omega \cdot B \cdot (r_o^2 - r_i^2) \quad \text{Equation 3-22}$$

To get the total induced voltage, the sum of all wires which are in the magnetic field has to be taken. The voltage is only calculated for one half of the coil and the voltage can be doubled, as the system is symmetric. This results in the factor of two in the following equation.



$$V_{coil} = \sum_{i=1}^N U_{wire\_i} \cdot 2 \quad \text{Equation 3-23}$$

So the maximum back EMF can be expressed with:

$$V_{coil\_max} = \sum_{i=1}^N \cdot \omega \cdot B \cdot (ro_i^2 - r_i^2) \quad \text{Equation 3-24}$$

The speed constant  $K\Omega_{coil\_max}$  is the relation between motor speed and voltage. It can be calculated by dividing the back EMF with the speed. This way the speed constant results to:

$$K\Omega_{coil\_max} = \sum_{i=1}^N B \cdot (ro_i^2 - r_i^2) \quad \text{Equation 3-25}$$

As the air gap flux density changes with the position of the rotor (Figure 35), the speed constant and the back EMF shows the same sinusoidal behavior as the torque constant of one coil.

$$K\Omega_{coil} = \sum_{i=1}^N B \cdot (ro_i^2 - r_i^2) \cdot \sin(\varphi_{mag}) \quad \text{Equation 3-26}$$

It can be seen, that the speed constant  $K\Omega$  is equal to the torque constant  $Kt$ . This relation can be used for measuring the torque constant of the motor by measuring the back EMF.

$$K\Omega_{coil} \left[ \frac{V}{\frac{rad}{s}} \right] = Kt_{coil} \left[ \frac{Nm}{A} \right] \quad \text{Equation 3-27}$$

### 3.4.3 Coil Resistance

To calculate the resistance of each coil, the wire length of each coil has to be calculated, this is performed in the Matlab script which calculates the shape of the coils. Each coil has a total length  $l_{coil}$  of 8.48 m. The track width  $w_{coil}$  is chosen to be 5 mil (127e-6 m) in order to get as much turns as possible on a coil. The copper height of the layers  $h_{coil}$  is about 1 mil (1 oz) at the outer layers and 0.5 oz in the inner layers [20]) which is 25.4e-6 m. The resistance of the coil  $R_{coil}$  can be calculated with:

$$R_{coil} = \rho_{cu} \cdot \frac{l_{coil}}{h_{coil} \cdot w_{coil}} \quad \text{Equation 3-28}$$

The resistivity of copper  $\rho_{cu}$  is 1.73e-2 [ $\Omega \cdot \text{mm}^2/\text{m}$ ] [21, p. 232]. Therefore the resistance of each coil is 45  $\Omega$ .

### 3.4.4 Coil current calculation

The coil current can be calculated based on Ohm law.

$$U = I \cdot R_{coil} \quad \text{Equation 3-29}$$

A maximum current of roughly 300 mA can be applied to the PCB board with the designed track widths [22]. This result in a maximum voltage of 13.5 V. Including a safety factor a maximum voltage of 10V has been chosen, which results in 220 mA per coil.

With the calculated torque constant and the current through one coil, the maximum torque of the motor can be calculated with the following equation [23, p. M1.24b].

$$T_{mot} \approx 2 \cdot K_{t\_max} \cdot I \cdot 1.5 \quad \text{Equation 3-30}$$

The factor of two is because there are two coils connected in parallel. The multiplication factor of 1.5 is explained in 3.7. The maximum torque of the motor is estimated to be 15 mNm which is well above the required torque.

### 3.4.5 Coil Inductance

For the calculation of the dynamic behavior of the motor a value for the coil inductance has to be calculated. For a round air coil the inductance  $L_{coil}$  can be calculated using the following term:

$$L_{coil} = \mu \cdot N^2 \cdot \frac{A}{h} \quad \text{Equation 3-31}$$

The variable N is the number of turns of the coil. A is the area of the coil and h is the thickness of the coil. As the area of the coil is changing for each turn, it has been assumed, that the coil has a constant area, which is described as the middle turn of the coils. This can give a first approximation of the inductance. Using this equation an inductance of the coil of 0.62 mH has been calculated.

With the coil resistance and inductance the time constant of the voltage to current behavior can be calculated using following equation.

$$t_{coil} = \frac{L_{coil}}{R_{coil}} \quad \text{Equation 3-32}$$

A time constant of  $t_{coil} = 0.15$  ms is calculated. This indicates, that the time constant of the coil do not affect position controllers which will be built as this time is smaller than the sampling rate of the real-time target. So the motor can be run in voltage mode without integrated current controllers.

### 3.4.6 Moment of inertia

The moment of inertia of the rotor can be approximated with a disc in combination with a ring. A steel disc describes the back iron of the motor. The permanent magnets can be approximated as a ring where the inner diameter is represented with the inner part of the magnets and the outer diameter is represented as the outer part of the magnets. This results in the following equation.

$$J_{rotor} = \frac{1}{2} \cdot m_{backiron} \cdot R_0^2 + \frac{R_{mago}^2 + R_{magi}^2}{2} m_{pm} \quad \text{Equation 3-33}$$

The back iron of the motor has a mass of 95 g and each magnet has a mass of 8 g. With this data a moment of inertia of 115E-6 kgm<sup>2</sup> can be estimated. This estimation fits well to the CAD predicted moment of inertia, which is 114.9E-6 kgm<sup>2</sup>.

### 3.4.7 Summary of the motor Parameters

The following table shows the calculated parameters of the motor which are used for modeling the motor behavior.

Table 3 Summary of the calculated motor behavior

Parameter	Calculated
R <sub>coil</sub>	45 Ω
L <sub>coil</sub>	0.66 mH
M	0.160 kg
J	1.15e-04 kgm <sup>2</sup>
K <sub>t</sub>	0.0206 Nm/A
V <sub>max</sub>	10 V

## 3.5 Motor design

### 3.5.1 Bearing design

To restrict the degrees of freedom of the rotor in its basic configuration, a ball bearing structure has been designed. As a high comparability between model and motor has to be achieved, ball bearings are used because of their low friction. Additionally they can handle high radial forces and moderate axial forces. To keep the costs for bearings low, some standard industrial ball bearings have been chosen.

A bore is designed which can be glued into the PCB board. A figure of the glued in bearings is shown in the following figures.



Figure 37 Bearing bore

### 3.5.2 Electronics design

The electronics of the motor can be divided in two main parts. The power electronics, which is amplifying the output signals of the myRIO control system, and the sensor electronics, which is used for preprocessing the Hall sensor values. In the following both electronic parts are described.

#### 3.5.2.1 Power electronics

The myRIO system provides four D/A converters with an output range of 0 – 5 V. These signals are used for steering the motor. In combination with these D/A converters, linear amplifiers are used.

As power amplifiers Fairchild Semiconductors L272 dual power amplifiers are used. These amplifiers can be bought in a DIP 8 package and provide a maximum output current of 0.7 A [24, p. 1]. To achieve a high enough torque and speed in the motor a 12 V power supply is used.

To apply positive and negative voltages to the coils, the two amplifiers in the package are connected as a bridge amplifier. For the conversion of the input voltage (0 V – 5 V) to the output signal of the amplifier (0 V – 10 V) a gain of two has been chosen for amplifier 1.

The input of the second amplifier is the output of the first amplifier, the gain of this amplifier is one. Because of the unipolar input and bipolar output of this amplifier, an offset signal for both amplifiers has to be provided, to shift the signal in the desired range. This is done by adding a voltage to the non-inverting inputs of the amplifiers. To get constant offset voltages a zener diode with a voltage of 10 V in combination with voltage dividers is used.

The required current to control one amplifier with the myRIO is lower than 0.5 mA, and so this current meets the specifications of the myRIO board [25].

Important are the 0.1  $\mu$ F capacitors between the output of the amplifiers and ground. Without these capacitors the amplifiers becomes unstable. Also 47 pF capacitors should be added between the inverting and non-inverting inputs of the amplifier, to stabilize the opamps.

## Axial field brushless DC motor

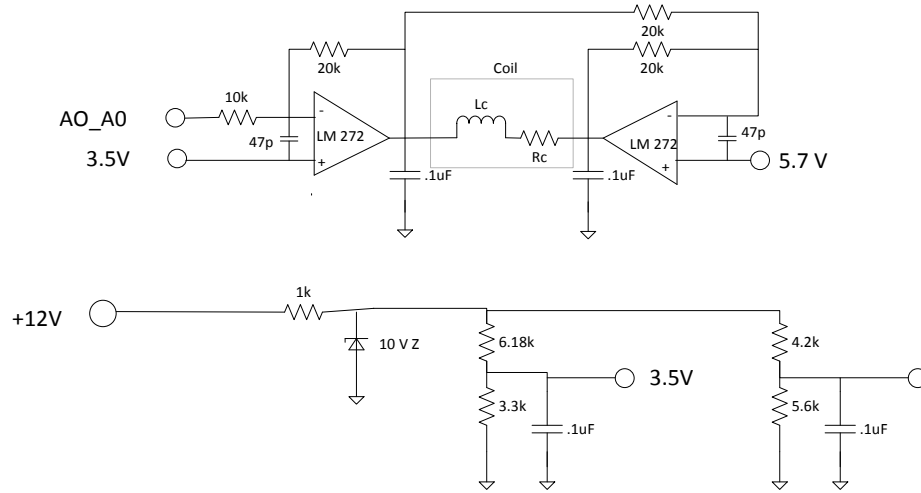


**Figure 38 Power electronics of the Motor**

The test of the electronics shows a maximum temperature of 81 °C on the PCB windings and 49 °C on the power opamps. This indicates that the design is stable against thermal distortion for normal Lab conditions.

### 3.5.2.2 Sensor electronics

For measuring the position of the rotor two SS49E Hall sensors [18] are used. These sensors are connected to the 5 V power supply of the myRIO. The output signal of the Hall sensors is between 1 V and 4 V. This output is connected to the analog input of the myRIO system. As the input impedance of the myRIO is higher than 500 kΩ, the Hall sensors output current is well under the maximum specification [18].

To avoid aliasing in the myRIO, a low pass filter with a break frequency of 4 kHz has been designed. The break frequency of a first order low pass filter is given by:

$$f_{break} = \frac{1}{R \cdot C \cdot 2 \cdot \pi} \quad \text{Equation 3-34}$$

With the given break frequency and a chosen resistance R of 4 kΩ the required capacitor can be calculated to C=0.01 μF. The following figure shows the electronic circuit used for the sensor reading.

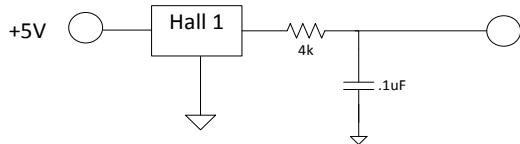


**Figure 39 Sensor reading electronics**

For an easy connection of the motor to the myRIO, a PCB board with all the electronic components is designed. The PCB board can be connected directly to the myRIO.

### 3.5.3 LabVIEW implementation

The algorithms for sensing the rotor position, commutation as well as the position controller including the trajectory based path planning have been implemented on the myRIO board.

Because there is a difference between mechanical and magnetic angle of a factor of four, the measured frequency of the encoder is four times the mechanical rotor speed. Also the commutation frequency is four times the rotor frequency. This effect can be seen in the phase shift of the system. When the sensor reading is done on the microcontroller of the myRIO the phase shift in the system is four times the expected value from the sampling rate.

The higher phase shift can be avoided by putting the sensor reading on the FPGA of the myRIO. The FPGA samples much faster than the microcontroller. This way a higher phase shift in the system can be avoided.

Unfortunately the programming of LabVIEW FPGA has to be done in fixed point arithmetic's. When the FPGA is used, the amount of iterations in testing the code should be reduced as the compilation of code to the system take rather long (up to one hour).

When using the FPGA of the myRIO, the timing in the real-time system becomes important. The sensor reading, signal processing and output writing has to be done in the right order. This can be done with error handling or sequence structures.

### 3.5.4 Design summary

The following picture shows the designed motor with electronics and real-time target. Using this configuration, all the tests of the BLDC motor have been done.

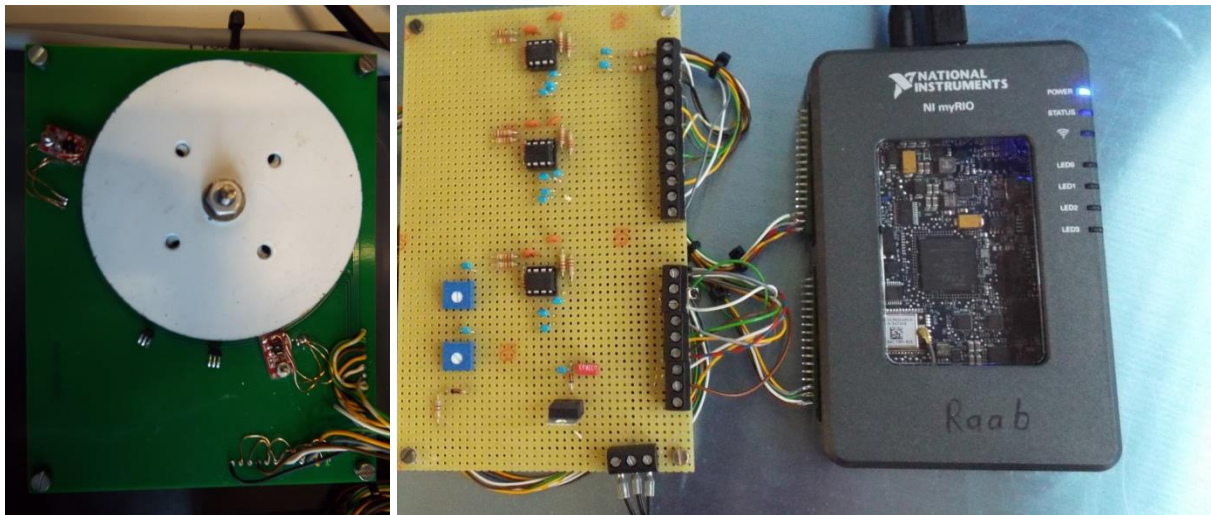


Figure 40 Designed BLDC motor with electronics and real time target

Figure 41 shows the setup on the PCB board with the bore and the bearings are glue in the board. Hall sensors and reflective sensor are place at the outside of the coils.

## Axial field brushless DC motor

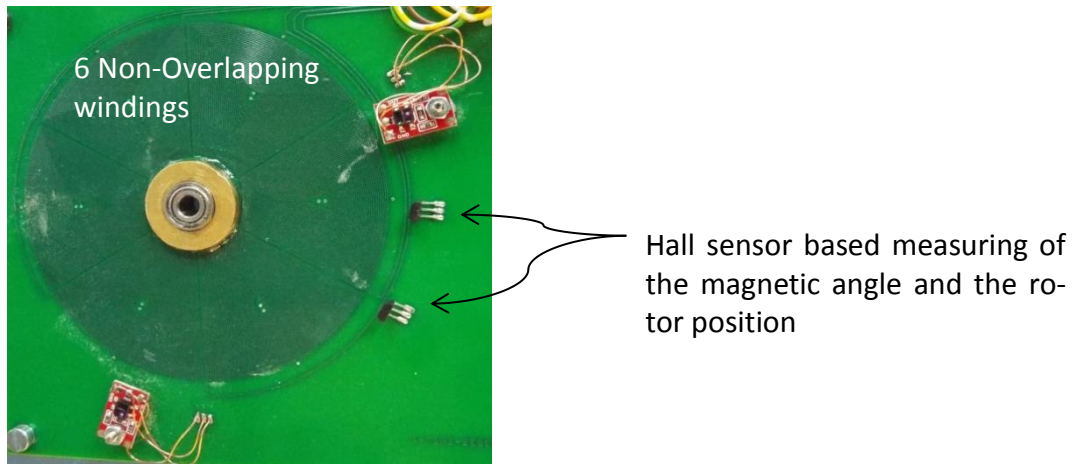


Figure 41 PCB Setup

To have all the electronic parts put together on one board and to ensure an easy connection between myRIO system and motor. All the electronics have been placed on one PCB board. The following figure shows the designed board with electronics and windings.

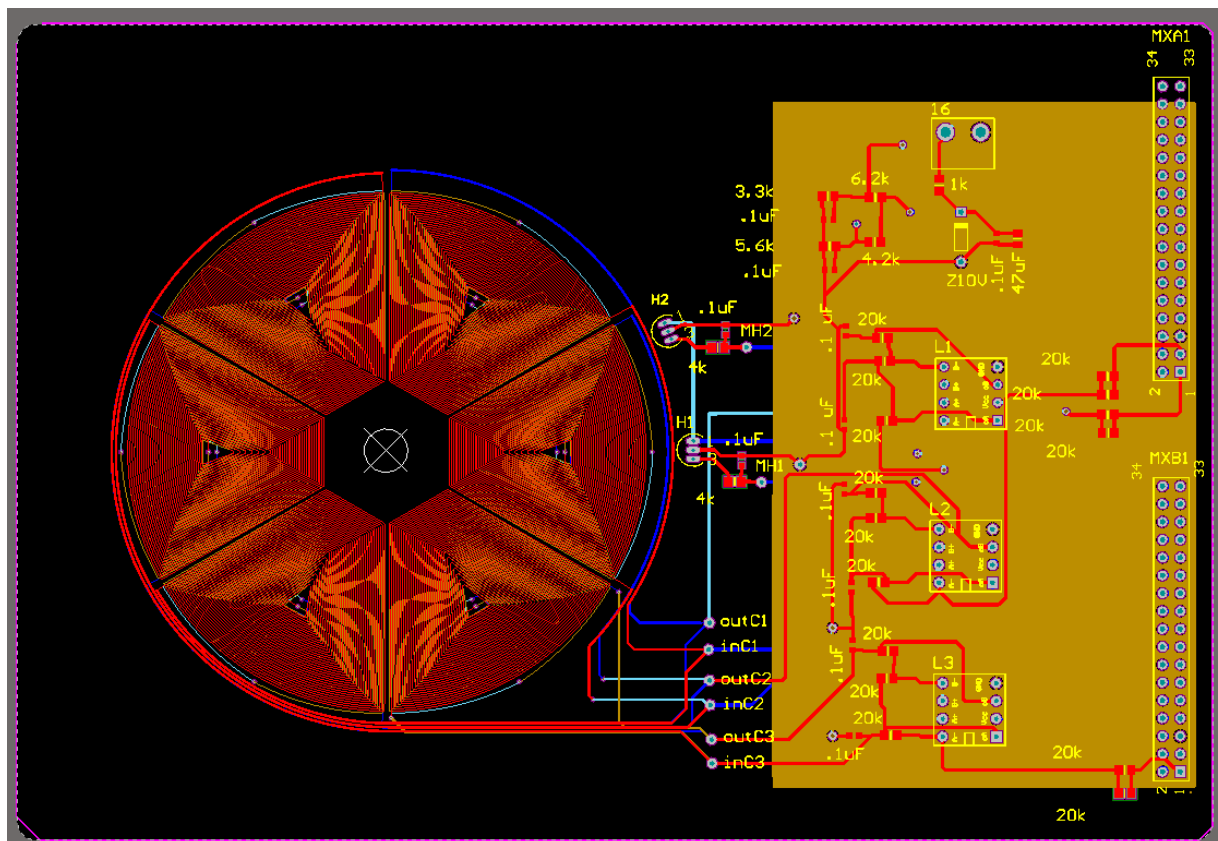


Figure 42 Designed PCB board

### 3.6 Motor parameter measurement

To verify the calculated motor parameters, different experiments are performed. In this part, the planning, processing and analysis of the experiments are described.

#### 3.6.1 Sine/cosine encoder reading test

A working encoder is fundamental for testing the different motor characteristics, as most of the other tests are based on the encoder measurement. For this reason the designed sine/cosine encoder is tested and adjusted first. In a first step the differences between the desired and actual angle signal of the encoder with constant rotor speed are compared and a fitting curve is designed to compensate repeatable angle errors. In a second step the fitted angle curve is compared with a desired angle curve under constant speed. The exact test specification for adjusting the Hall sensor signals to the motor angle as well as for verifying the encoder behavior is described in Table 6 in the appendix.

##### 3.6.1.1 Error fitting

To determine the linearity, accuracy and resolution of the sine/cosine encoder, the raw data from a rotor which is rotating with constant speed has been measured. For a good sine/cosine interpolation, signals with sinusoidal shape are required. The following figure shows the measured signals compared to sine and cosine functions. It can be seen, that the desired signal curve has higher harmonics which results in errors in the encoder reading.

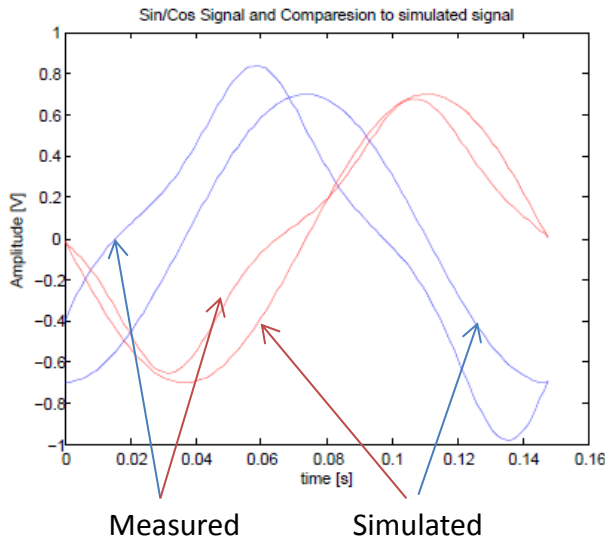
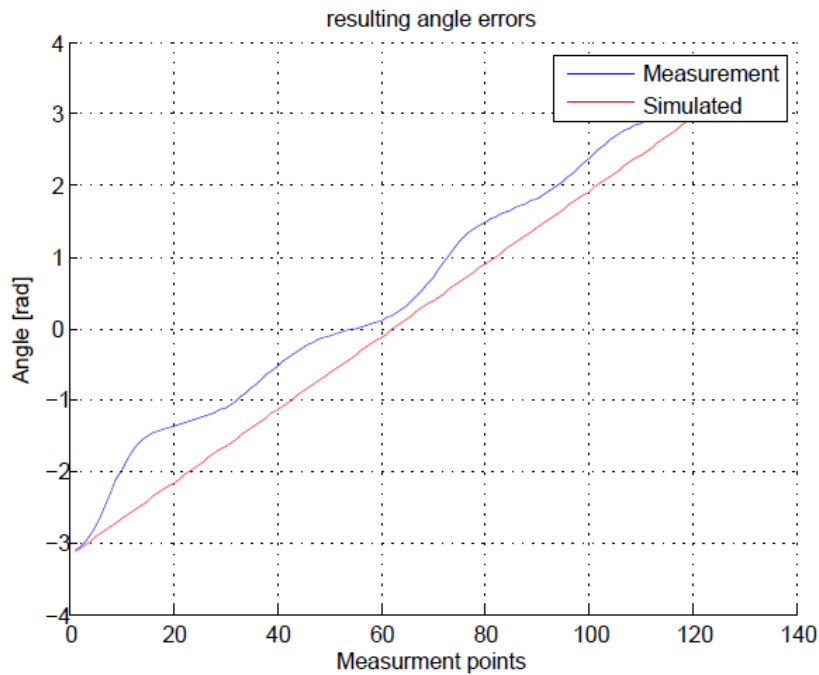


Figure 43 Comparison between measured and desired Hall sensor signal

With the measured signals the magnetic angle of the rotor has been calculated using Equation 3-10. This measured angle has been compared to the calculated angle from the simulated sine/cosine signals. In Figure 44 it can be seen, that the maximum angle error between measured angle and simulated is 0.9 rad in the magnetic angle which is 0.225 rad (12.9°) mechanically. However, this angle error is repeatable and mostly independent from the rotating speed of the rotor. Therefore the error can be fitted to calculate the actual angle in the real-time system.





**Figure 44 Error between measured and simulated angle**

To design a function which describes the angle error per magnetic degree, the error has been plotted versus the measured angle. With this error function an FFT analysis has been done. This analysis shows that the error mainly consists of a DC offset and six higher harmonics. The following figure shows the error per measured angle and the FFT analysis of the error signal.

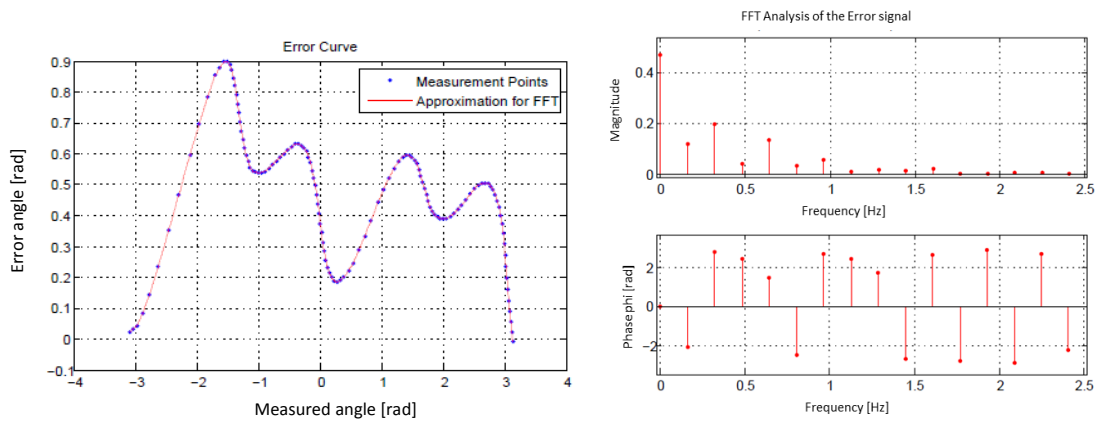


**Figure 45 Error curve of the measured angle and FFT analysis of the error signal**

A fitting function, consisting of a sum of eight sine function, has been created using the Matlab Curve fitting tool. This tool offers a higher accuracy than fitting the error curve based on the FFT analysis. Using this function, the error of the measured signal is reduced to  $\pm 0.045$  rad magnetically and 0.0113 rad ( $0.65^\circ$ ) mechanically. The results are shown in Figure 46 which shows the measured, simulated and fitted angle.

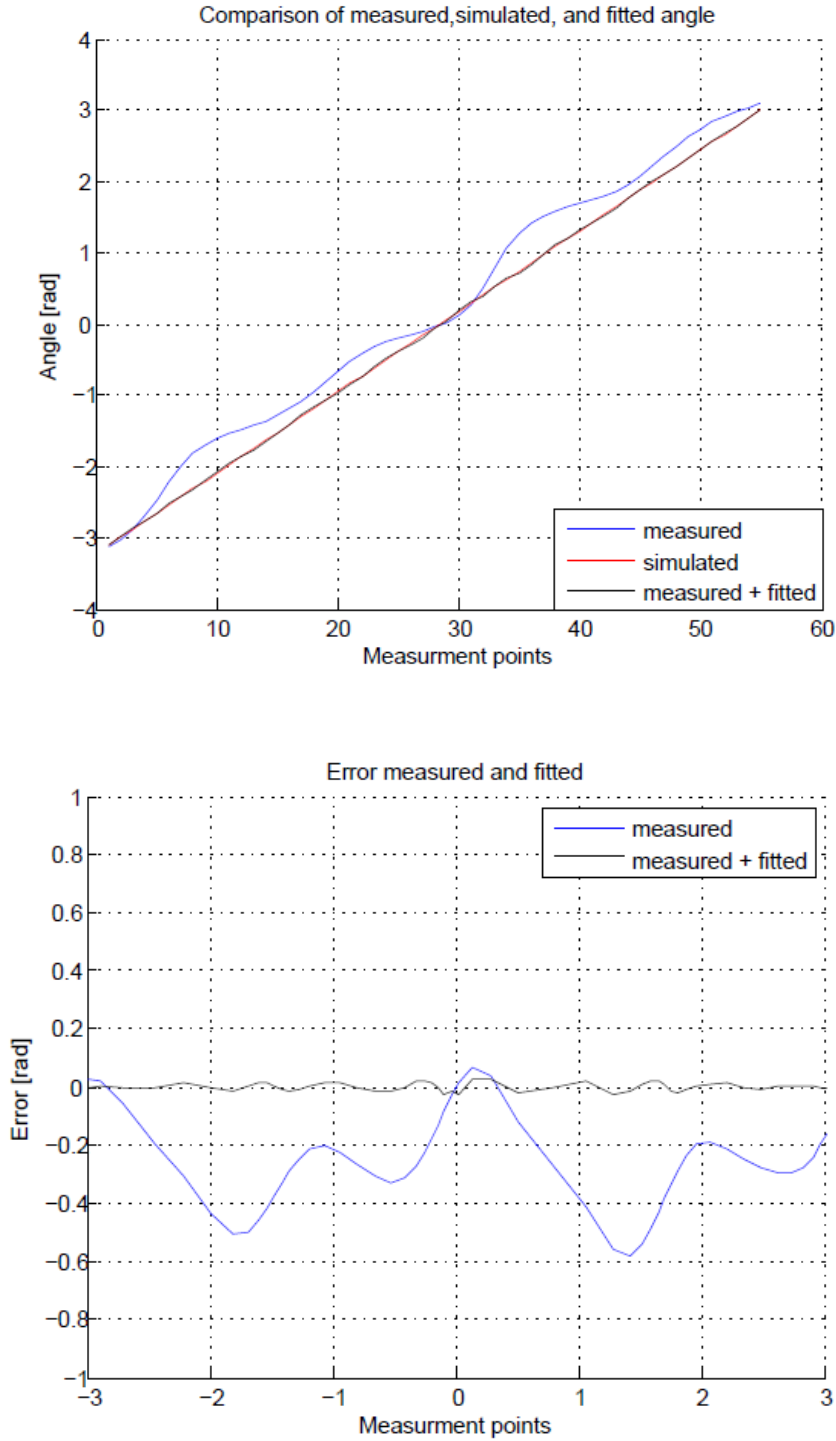
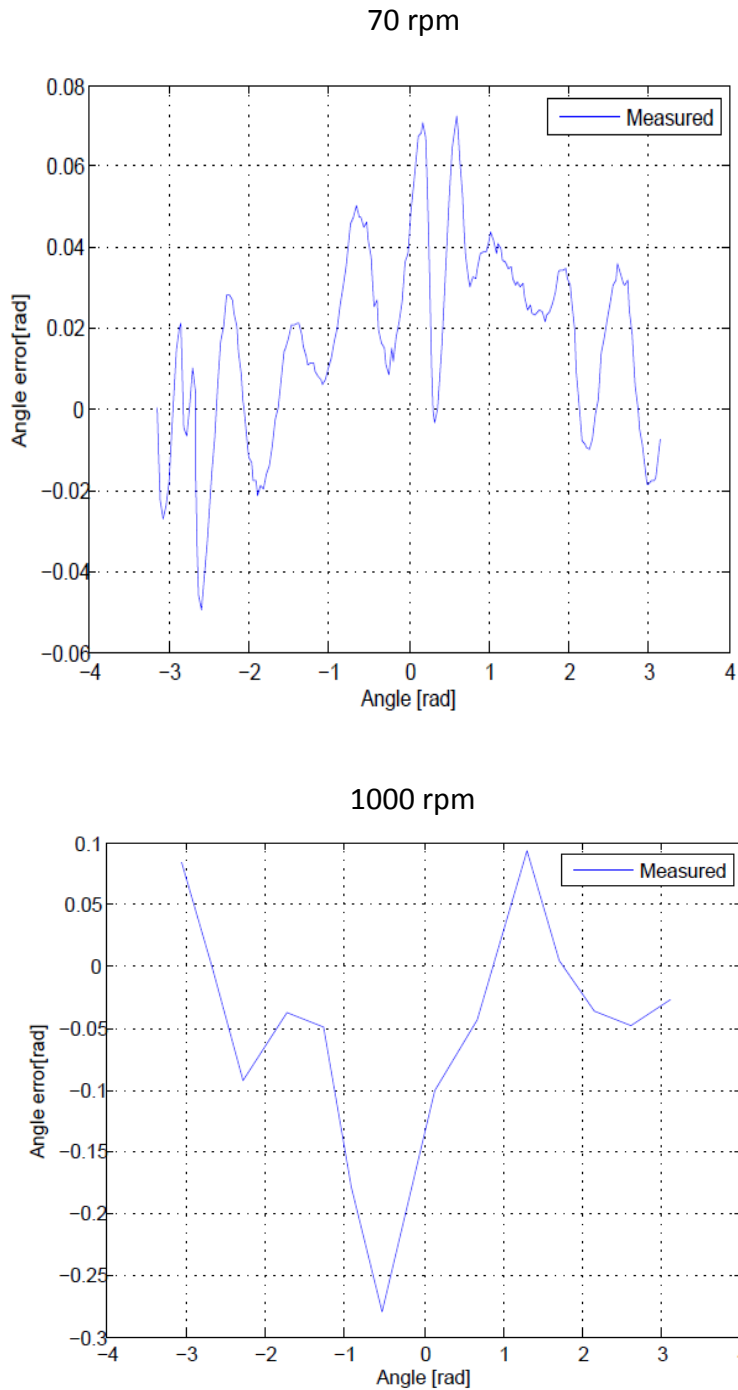


Figure 46 Results of the fitted error fitting

### 3.6.1.2 Test results

With the implemented fitting curve in the NI real-time system the accuracy of the encoder measurement has been verified. The measured angle for different speed levels has been recorded and analyzed regarding its linearity. As it can be seen in Figure 44 the encoder signal has to be a straight line for constant speeds. Changes between the desired straight line and rotor measurement are errors in the measurement. This error is measured by subtract-

ing the measured curve form an ideal curve. The results for 70 rpm and 1000 rpm are shown in the following figures.



**Figure 47 Measurement of the Angle error for different speed**

The measurement shows a maximum error of 0.07 rad which results in  $1^\circ$  mechanically for lower speed, for higher speed, this error increases up to 0.25 rad which is  $3.5^\circ$  mechanically for higher speed. The error between measured and desired angle increases with speed. This is caused by the error not being totally independent of speed. Also there are fewer meas-

urement points which have been taken with higher speed. Therefore also the error because of the sampling rate becomes larger.

It can be seen, that for low frequencies, the accuracy of the encoder is pretty high. The decreasing accuracy with speed mainly effects the commutation of the motor, but this does not affect the motor dynamics much. Positive is, that a resolution smaller than 0.1 mrad can be achieved with this encoder which is important in order to get a good working commutation and position control. When a higher accuracy in the measurement is wanted, the proposed encoder shown in Figure 40 and Figure 41 can additionally be implemented.

### 3.6.2 Coil characterization

For the characterization of the coil, the inductance was measured. The inductance will affect the motors behavior for high frequencies. In a first step, the resistance of the coil has been measured using a handheld multimeter. For measuring the coil inductance an opamp circuit driven by a signal generator was built. The current through the coil is sensed by a sensing resistance and an oscilloscope. To calculate the actual inductance, the step response of the current through the coil is characterized. The used electronic circuit and a more detailed test specification are attached in Table 7 in the appendix. In the coil characterization higher errors between calculation and experiment are expected, as the used equations should only give a first approximation. Also material specific constants have not been exactly known.

The coil resistance was measured to be 59.5  $\Omega$ . Compared to the predicted resistance of each coil (45  $\Omega$ ) calculated in 3.4.3, there is an error of 23 % between calculation and measurement. Possible reasons for the difference are variations between the expected and actual layer height of the PCB board and the conductivity of the used copper.

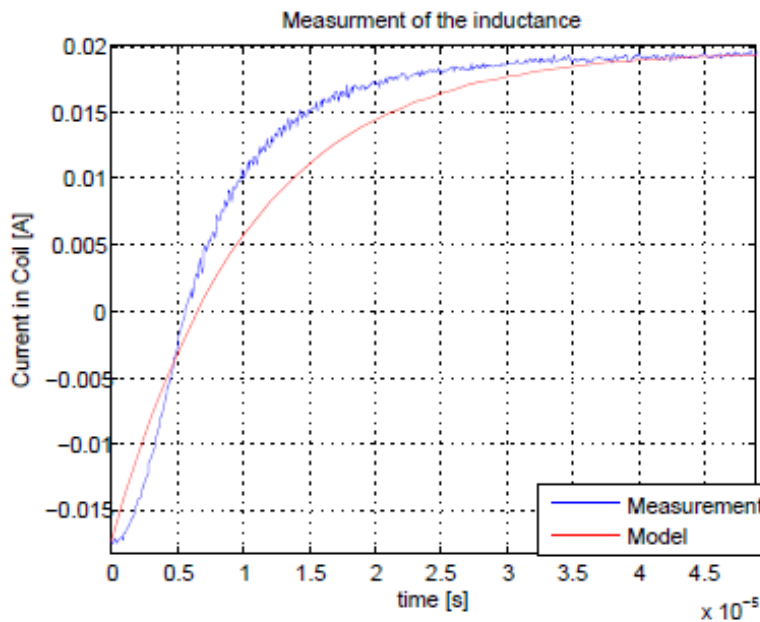


Figure 48 Measured and expected step response of the coil

The measured step response of the coil is shown in Figure 48. The blue line shows the measured curve, and the red line indicates the expected behavior of the coil. It can be seen that both curves fit rather good as the used equation for estimating the inductance is for round coils and therefore does not fit perfect to this application.

To improve the model behavior of the coil, the inductance has been estimated by adjusting a model of the coil which is represented with Equation 3-39. The resistance of the coil and the sensing resistance are given values. In an iterative process the inductance of the model has been adjusted until the model response fits to the measured response. A value of 0.42 mH fits the measured curve well enough for the describing of the coil behavior.

In the measurement of the coil, a higher order behavior of the system can be seen at the starting point of the curve. One possible explanation is a capacity in the coil. This behavior will not be represented in the model as it does not affect the motor behavior.

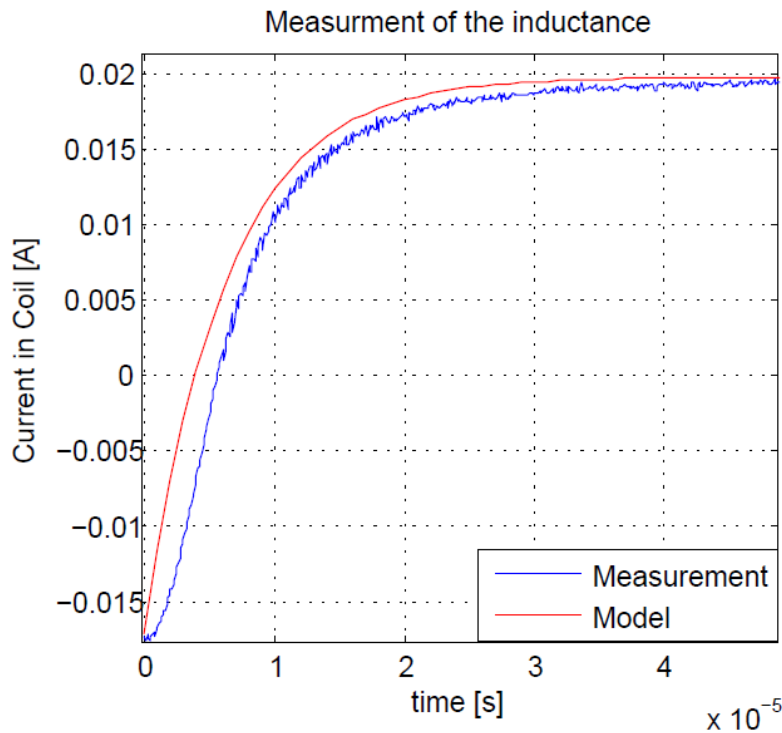


Figure 49 Measured and fitted step response of the coil

Neglecting the higher order behavior, the fitted inductance of the coil (0.42 mH) fits the expected value with 0.62 mH. An error of 47 % between expected and measured value is still a good results for a roughly approximated value.

### 3.6.3 Back EMF measurement

To characterize the behavior of the motor, the torque constant is measured and compared to the calculated value. This is done by measuring the back EMF of a spinning motor and determining the speed constant, which is equal to the torque constant of the motor. Also the shape of the back EMF is discussed, as this has to be fed back to achieve good commutation results.

#### 3.6.3.1 Speed constant

To measure the speed constant, the motor was accelerated by hand. The speed of the rotor, as well as the back EMF has been measured. Using the rotor speed and the back EMF, the speed constant is calculated and compared to the predicted one. The tests for measuring the back EMF of the motor have been done according to the test specification of Table 8 in the appendix.

With spinning the motor by hand a maximum speed of 45 rad/s was achieved. This speed results in an amplitude of the back EMF of 1.1 V. The following figure shows the measured back EMF over the time.

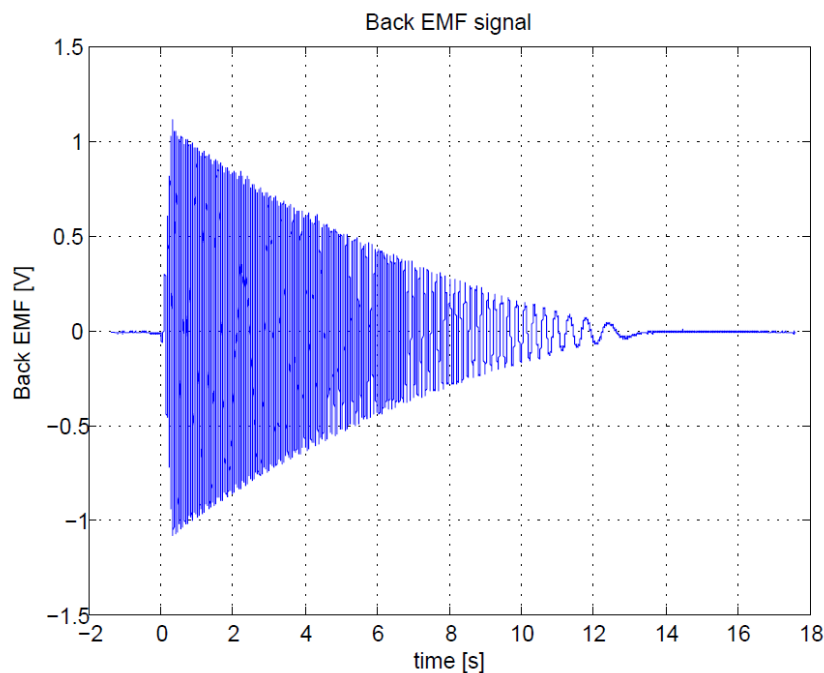
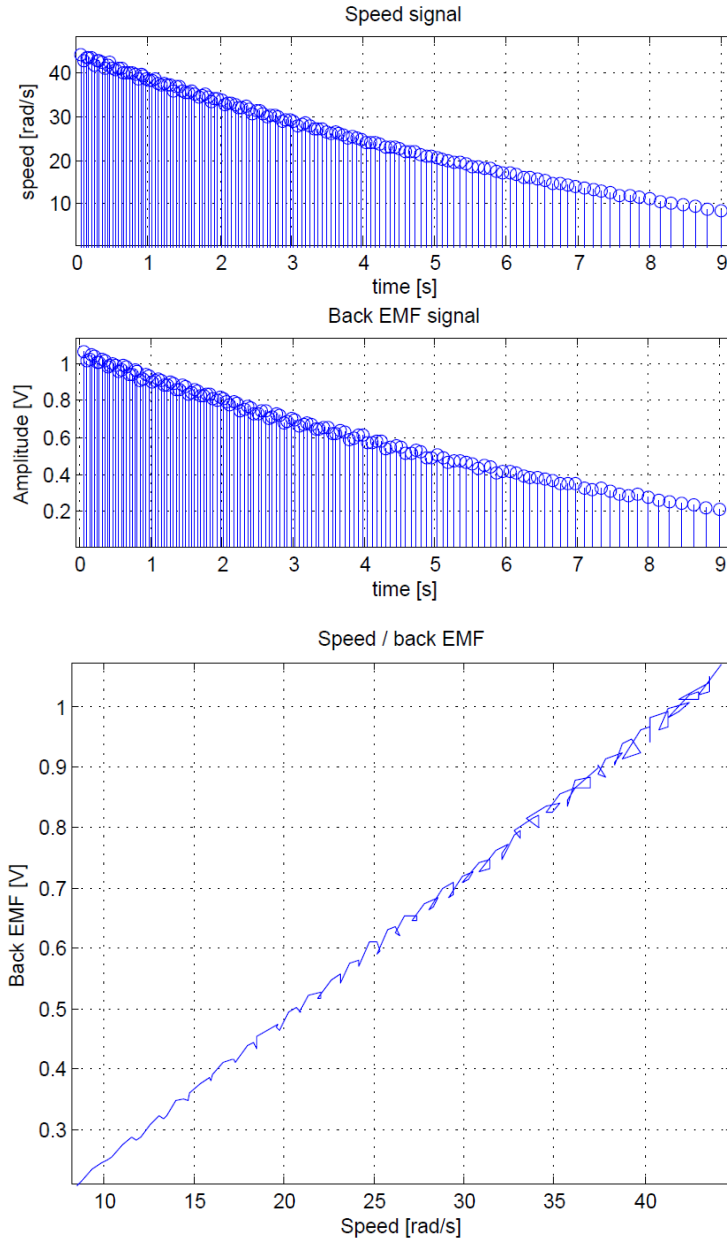


Figure 50 Back EMF signal

It should be noticed, that besides the speed constant and back EMF, also the damping of the motor can be estimated using this curve. Nevertheless the damping measurement will be discussed in a following section, where the shape of the decreasing speed has been measured with higher starting speed to distinguish more clearly between the coulomb friction and viscous friction of the rotor.

Using the measurement from Figure 50 the speed at each point has been calculated and the amplitude of the signal is measured. In Figure 51 it can be seen, that the speed signal and the amplitude of the back EMF signal have proportional behavior.

Figure 51 also shows that the relation between speed and back EMF results in a straight line. To calculate the speed constant of the motor, the back EMF has to be divided by the rotor speed signal according to Equation 3-25. This results in a speed constant (and torque constant) of  $0.0233 \frac{V}{rad/s}$ .



**Figure 51 Comparison of motor speed and back EMF, (A) speed signal and back EMF signal, (B) speed signal vs back EMF**

The comparison between the measured speed constant and the expected speed constant (of  $0.0206 \frac{V}{rad/s}$ ) shows that there is an error between expected and measured value of 11.6 %.

One possible reason that the measured speed constant is higher than the expected one is, that for the calculation of the speed constant only the area of the magnets has been taken into account. As the magnetic field does not end with the magnets, this results in the additional torque. Still both values shows a good comparability

### 3.6.3.2 Back EMF shape

In the motor design it was desired to build a motor with sinusoidal back EMF behavior, as this result in small torque ripples by the use of sine-commutation. The back EMF signal is analyzed to verify, that the motor shows sinusoidal back EMF behavior.

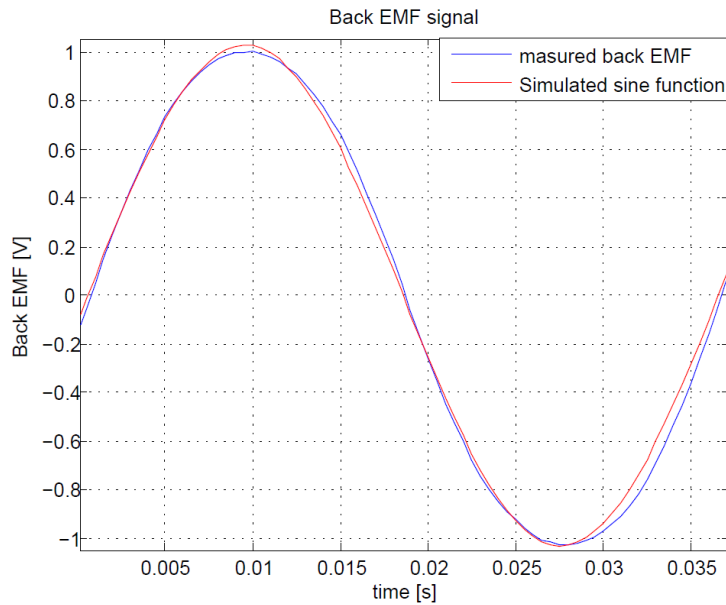


Figure 52 Back EMF shape

Figure 52 shows the shape of the back EMF at a rotating rotor. It can be seen, that the measured function has a good comparability to a simulated sine function (red line), which is even better than the expected curve of Figure 30. Therefore the commutation using a sine function is an effective way of driving the motor.

### 3.6.4 Damping estimation

To characterize the motor behavior the damping in the system has to be measured. The damping values are hard to predict, as there are no friction values given in the datasheet of the bearing.

For the damping characterization the motor is accelerated to maximum speed. Then the power to the amplifiers is switched to 0 V. To make sure, that there is no damping due to back EMF, the cables of the windings are disconnected (in the final design on the PCB this can be done by just switching of the power opamps). The decreasing speed function is recorded. In an iterative process the simulated damping is fitted to the actual curve. A more detailed specification is attached in Table 9 in the appendix.



By performing the test in the described manner the decreasing speed function shown in Figure 53 can be measured. It can be seen, that the curve has a speed depending term as the measurement is not a linear function. This speed dependent behavior can be described with viscous friction.

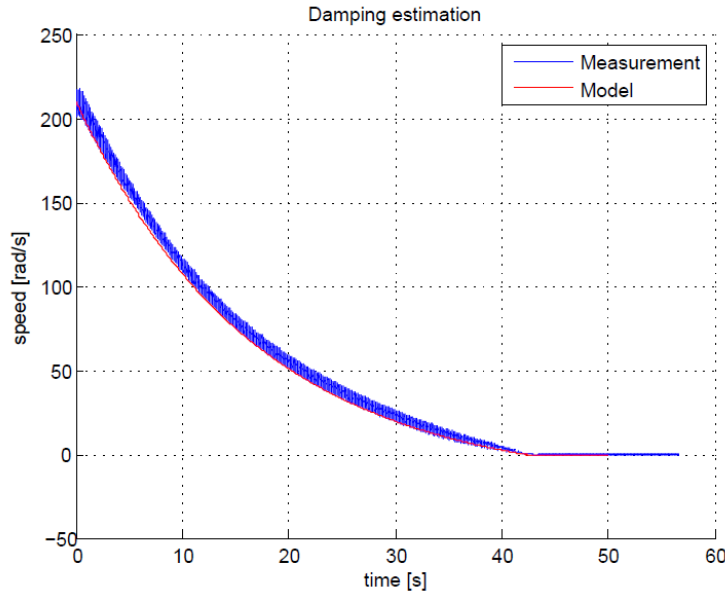


**Figure 53 Measured and simulated friction for decreasing speed**

The curve also shows a linear function for lower speed. This is caused by the coulomb friction in the bearing. To estimate the overall friction of the motor an iterative process has been chosen, where the coulomb friction and the viscous friction have been changed and the simulated results are compared to the measured curve.

In the simulation the moment of inertia, calculated in 3.4.6, and the sum of torques, applied to the motor according to Equation 3-45, are used. The Simulink simulation is shown in the figure below.

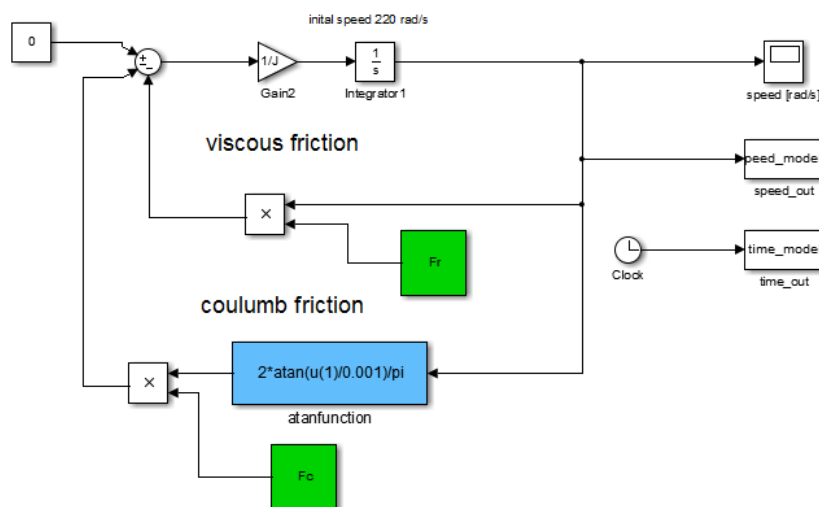


**Figure 54 Simulation for friction simulation**

Using this simulation, a good comparability between model and simulation has been achieved. This can be seen in Figure 53. The fitted friction function is shown in the equation and figure below.

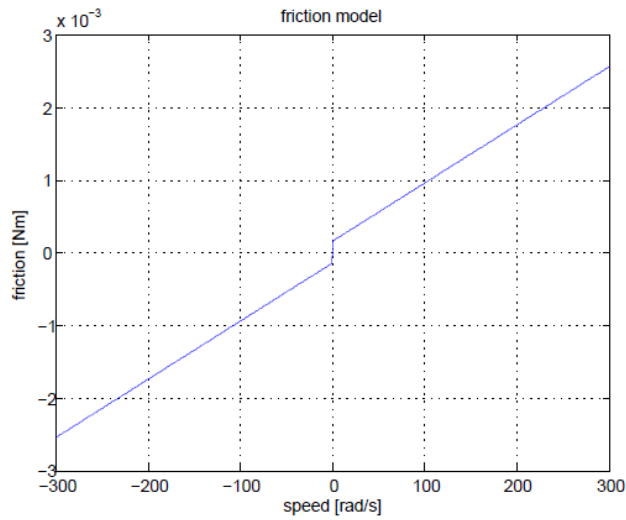


**Figure 55 estimated Friction function**

The friction can be expressed using the following equation and parameters.

$$T_{friction} = F_r \cdot \omega + F_c \cdot \frac{2}{\pi} \cdot \tan^{-1} \left( \frac{\omega}{0.001} \right) \quad \text{Equation 3-35}$$

- $F_r = 8 \cdot 10^{-6} \left[ \frac{Nm \cdot s}{rad} \right]$
- $F_c = 0.15 \cdot 10^{-3} [Nm]$

### 3.7 Modelling and control of a brushless DC motor

For the prediction of the motor behavior and the design of control algorithms of a brushless DC motor, an analytic model is built in this section. This model represents the dynamic as well as the stationary behavior of a brushless DC motor. The modelling of the motor can be separated into two main sections, the commutation which is done in the power electronics and the modelling of the motor behavior including torque generation the friction modelling. These steps are discussed in detail in the following sections. The following figure shows the top-level of the developed model.

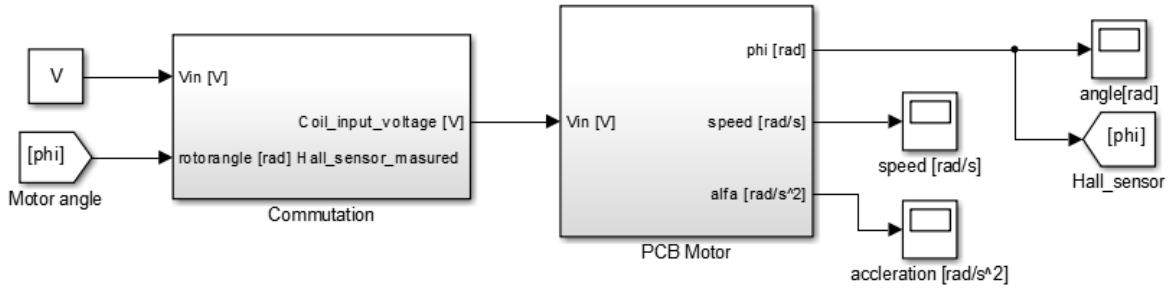


Figure 56 Top level of the BLDC motor model

#### 3.7.1 Commutation

To achieve a constant torque in the motor the current of each winding has to be aligned to the motor position. This is called commutation. The commutation process is described in chapter 2.1.2. In the following the algorithms of a sinusoidal commutation are explained, in order to achieve a dynamic model. These algorithms are also implemented in the setup of the motor.

The aligned electric current values of the motor can be expressed as the following equation where  $\hat{I}$  is the amplitude of the current.

$$\begin{aligned} i_A &= \hat{I} \cdot \sin(\varphi_{mag}) \\ i_B &= \hat{I} \cdot \sin\left(\varphi_{mag} - \frac{2 \cdot \pi}{3}\right) \\ i_C &= \hat{I} \cdot \sin\left(\varphi_{mag} - \frac{4 \cdot \pi}{3}\right) \end{aligned} \quad [23, p. M1.24] \quad \text{Equation 3-36}$$

Because of the small time constant of the coils, the motor can run in voltage mode. The voltages in the coils are controlled by the real-time target. As the dynamics of the voltage to current behavior are high this is a reasonable approach.

A Simulink based model of sine commutation in BLDC motors is shown in the figure below. It has to be noticed, that the electrical angle is four times the mechanical angle according to Table 2.

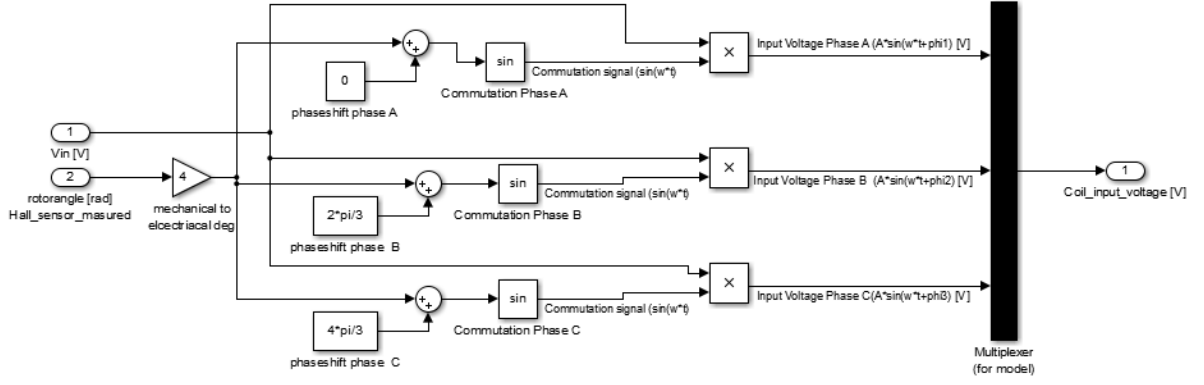


Figure 57 Simulink based BLDC commutation

In real-time systems, a phase shift  $\varphi_{error}$  between the measured angle and the actual angle will appear due to time delay. The phase shift can be seen in a bode plot using the time delay of the real-time system. To keep the angle between rotor and current aligned for higher speed, this error has to be compensated using Equation 3-37.

$$\varphi_{error} = -k \cdot \omega \quad \text{Equation 3-37}$$

The caused phase shift is proportional to the rotor speed, so it can be compensated with a linear function. For a sampling rate of 1 kHz the phase shift is  $k = -0.004 \frac{\text{rad}}{\text{rad/s}}$ .

### 3.7.2 Motor characteristics

The input parameter of the motor is the voltage with the in 3.7.1 described commutation pattern. When the motor is spinning, a back EMF is introduced, which has the opposite sign of the input voltage. So the armature voltage of the motor is:

$$\begin{aligned} V_A &= \hat{V} \cdot \sin(\varphi_{mag}) - K n_{coil\_max} \cdot \omega \cdot \sin(\varphi_{mag}) \\ V_B &= \hat{V} \cdot \sin\left(\varphi_{mag} - \frac{2 \cdot \pi}{3}\right) - K n_{coil\_max} \cdot \omega \cdot \sin\left(\varphi_{mag} - \frac{2 \cdot \pi}{3}\right) \\ V_C &= \hat{V} \cdot \sin\left(\varphi_{mag} - \frac{4 \cdot \pi}{3}\right) - K n_{coil\_max} \cdot \omega \cdot \sin\left(\varphi_{mag} - \frac{4 \cdot \pi}{3}\right) \end{aligned} \quad \text{Equation 3-38}$$

With the voltage at each coil, the current through the coils can be calculated as shown below. Because of the small time constant of the voltage to current behavior, this time dependency is less important for the build BLDC motor.

$$V = i \cdot R + L \cdot \frac{di}{dt} \quad \text{Equation 3-39}$$

To calculate the torque of each coil, the following equations are used [23, p. M1.24b].

$$\begin{aligned} T_A &= i_A \cdot K_t(\varphi_{mag}) = i_A \cdot K_{t\_max} \cdot \sin^2(\varphi_{mag}) \\ T_B &= i_B \cdot K_t(\varphi_{mag}) = i_B \cdot K_{t\_max} \cdot \sin^2\left(\varphi_{mag} - \frac{2 \cdot \pi}{3}\right) \\ T_C &= i_C \cdot K_t(\varphi_{mag}) = i_C \cdot K_{t\_max} \cdot \sin^2\left(\varphi_{mag} - \frac{4 \cdot \pi}{3}\right) \end{aligned} \quad \text{Equation 3-40}$$

According to trigonometric functions, the  $\sin^2$  can be converted as shown below.

$$\sin^2(\varphi_{mag}) = \frac{1}{2} \cdot (1 - \cos(2 \cdot \varphi_{mag})) \quad \text{Equation 3-41}$$

As the total motor torque is the sum of the torque from the three phases, the motor torque can be calculated by adding the torques of the different phases.

$$T_{mot} = K_{t\_max} \cdot I \cdot \left( \frac{3}{2} - \left( \cos(2 \cdot \varphi_{mag}) + \cos\left(2 \cdot \varphi_{mag} - \frac{2 \cdot \pi}{3}\right) + \cos\left(2 \cdot \varphi_{mag} - \frac{4 \cdot \pi}{3}\right) \right) \right) \quad \text{Equation 3-42}$$

When the higher frequency cosine terms which causes torque ripple are neglected, the motor torque is an independent value of the rotor angle. The torque at this point is proportional to the input current  $I$  and is comparable to a brushed DC motor [23, p. M1.24b].

$$T_{mot} \approx K_{t\_max} \cdot I \cdot 1.5 \quad \text{Equation 3-43}$$

The voltage to torque behavior of one coil has been implemented. The implementation can be seen in the figure below. The 3/4 distribution of the winding/pole structure results in a speed difference between mechanical and electrical speed with a factor of four.

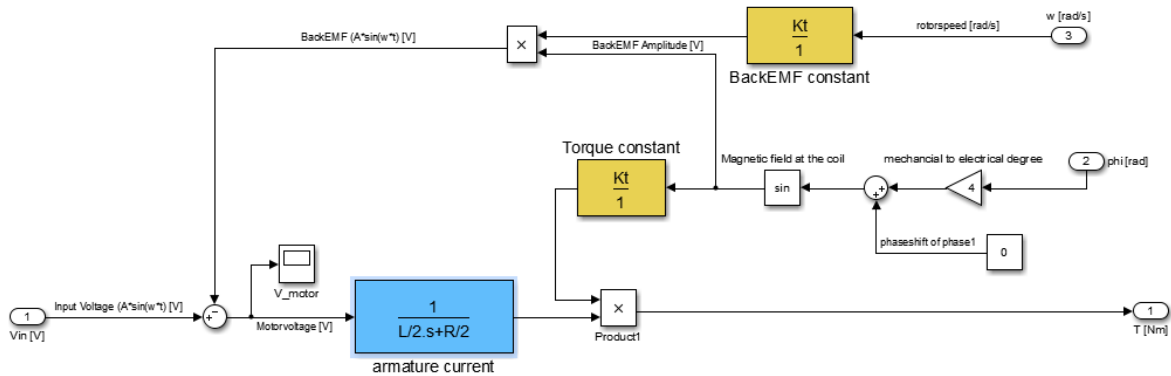


Figure 58 Simulink implementation of the voltage to torque behavior of one coil

For the simulation of the motor, and calculation of the sum of acting torques, the friction in the bearing has been taken into account. To characterize this friction, the experiments in 3.6.4 have been done. The friction of the motor can be modeled as coulomb and viscous friction which are described in the following equations [26].

$$T_c = \frac{2}{\pi} \cdot \tan^{-1} \left( \frac{\omega}{0.01} \right) \cdot F_c \quad \text{Equation 3-44}$$

$$T_v = F_v \cdot \omega$$

The acceleration  $\alpha$  of the motor can be calculated by summing all the acting torques of the motor as shown below.

$$\alpha = \frac{T_{mot} - T_v - T_c}{J_{rotor}} \quad \text{Equation 3-45}$$

The speed of the rotor and the actual angle of the rotor can be determined by integrating the acceleration of the rotor.

$$\omega = \int \alpha$$

$$\theta = \int \int \alpha \quad \text{Equation 3-46}$$

The Simulink implementation of the torque generation and torque to angle behavior is shown in Figure 59.

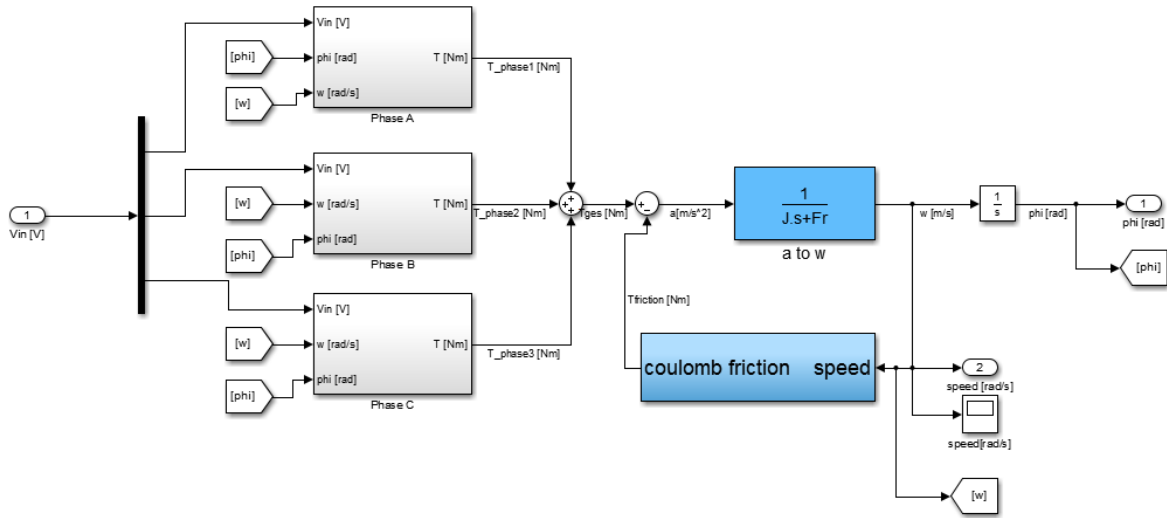


Figure 59 Simulink implementation of the motor torque to speed/angle

### 3.7.3 Linearized model

An easier approach of modelling a brushless DC motor is neglecting the commutation of the motor as well as the angle dependent torque and speed constant of the motor. According to Equation 3-43, a factor of 1.5 multiplied to the measured torque constant has to be used. This linearized model can be used for loop shaping design of PID controllers. For calculating the frequency response of the system, the coulomb friction is neglected as this behavior is nonlinear. By transforming the equations of the motor in state space form, the following matrixes can be calculated.

$$A = \begin{bmatrix} -\frac{R/2}{L/2} & 0 & -\frac{Kt}{L/2} \\ 0 & 0 & 1 \\ \frac{K}{J} & 0 & -\frac{Fr}{J} \end{bmatrix} b = \begin{bmatrix} \frac{cg}{L/2} \\ 0 \\ 0 \end{bmatrix} \quad \text{Equation 3-47}$$

$$c = [0 \quad 1 \quad 0]$$

$$d = 0$$

The constant  $c_g$  specifies the gain factor between the myRIO and the real system. A factor of 1 in the myRIO causes an amplitude of 10 V at the motor. According to Equation 3-43, the motor torque is 1.5 times the torque constant. This results in a gain factor of 15 for  $c_g$ .

For the simulation of the system a time delay of 1 ms has been taken into account, which is the sampling time of the myRIO system. The time delay causes a phase drop in the system, which is one of the main limitations for achieving high bandwidth control on the motor.

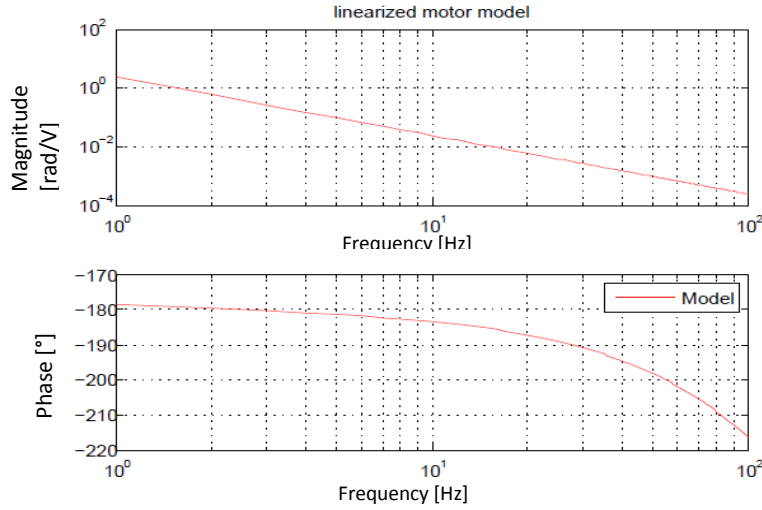


Figure 60 Simulated frequency response of the motor

### 3.7.4 Controller design

For a stable control of the motor a phase margin of at least  $45^\circ$  and a gain margin of 6 dB are desired in the return ratio of the system. A PI controller with a lead-lag compensator is designed for a crossover frequency of 25 Hz. With this frequency a good gain and phase margin can be achieved. On the other hand the system has a good stiffness due to the bandwidth. The equations of the PI controller and the lead-lag compensator are shown below.

Equation 3-48

$$PI = K_p \cdot \left( \frac{1+w_i}{s} \right) \cdot lead$$

Equation 3-49

$$lead = \frac{1/\omega_{lead} \cdot s + 1}{1/\omega_{lag} \cdot s + 1} lead$$

The integrator term of the controller is designed for having a static accuracy. To separate the phase drop caused by the integrator term and the phase lift from the lead-lag compensator, an integrator frequency of 2 Hz which is smaller than on tenth of the desired crossover frequency has been chosen.

The lead-lag compensator is designed to lift the phase by  $60^\circ$  by setting the lead frequency to 7 Hz and the lag frequency to 125 Hz. This way a phase margin of  $45^\circ$  will be achieved in

the system. The gain of the controller has been adjusted based on the simulated return ratio of the system to be 44.5 in order to get a crossover frequency of 25 Hz. The implemented controller is shown in the following figure.

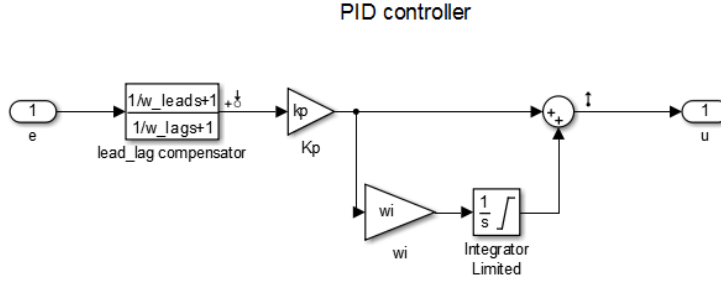


Figure 61 Controller structure

With the designed controller  $G_C$  and the modeled system behavior  $G_{mot}$  shown in Figure 60 the loop return ratio  $G_{RR}$  can be calculated. It can be seen, that a crossover frequency of 25 Hz is achieved with a phase margin of 45°.

$$G_{RR} = G_C \cdot G_{mot} \quad \text{Equation 3-50}$$

The following figure shows the simulated loop return ratio of the BLDC motor

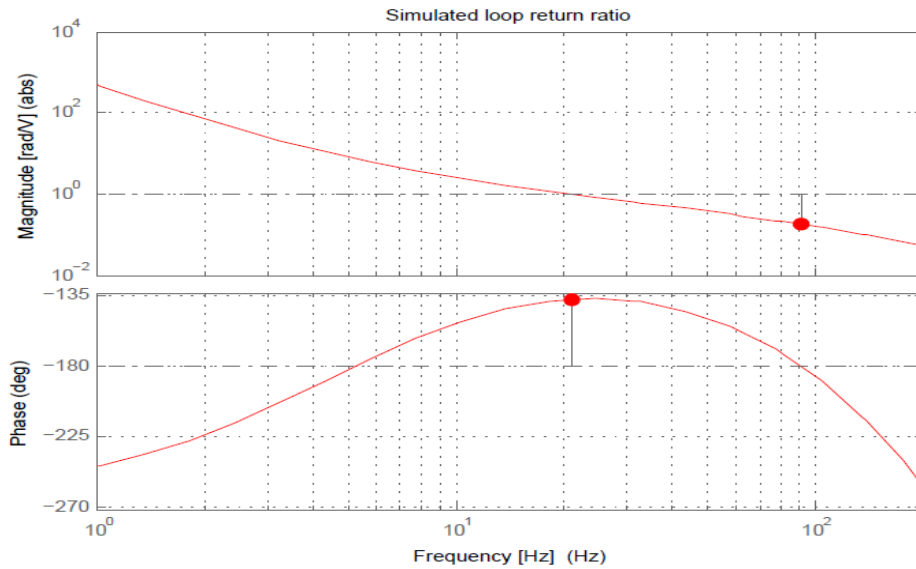


Figure 62 Simulated loop return ratio and controller bode plot

### 3.7.5 Trajectory based positioning

In most applications where position controllers are implemented, overshoots during the positioning process have to be avoided and the time of positioning has to be reduced. This can be done by adding a trajectory based path planning using an acceleration reduced profile. As



it can be seen in Figure 63, the time dependent rotor position is calculated based on the maximum acceleration of the motor [27].

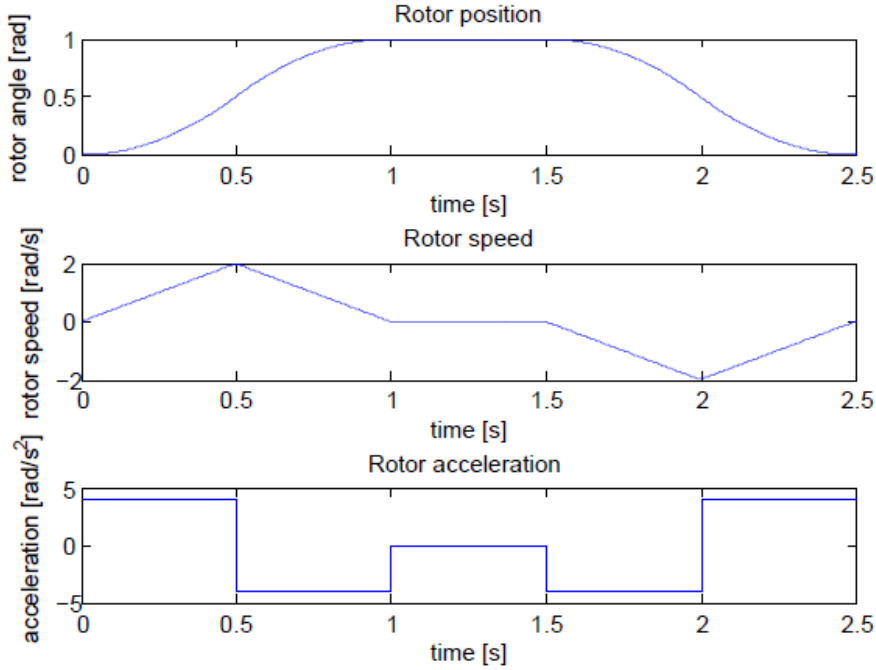


Figure 63 Acceleration reduced path planning

When a change of the position is given to the real-time system, a profile for changing the rotor position, based on the data's of the motor is calculated. The path planning is implemented in a state machine as shown below.

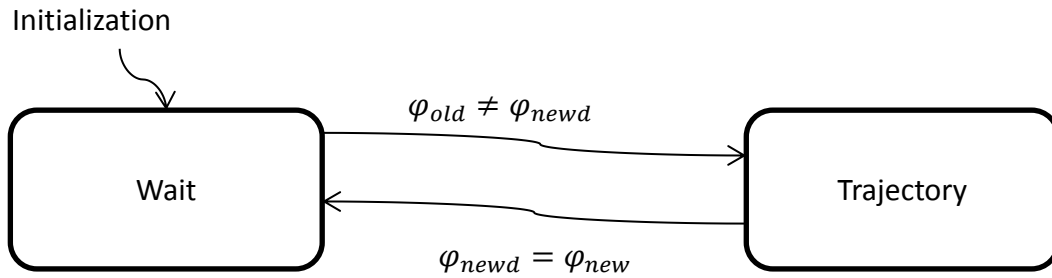


Figure 64 State machine for trajectory generation

When the rotor position changes from an old position  $\varphi_{old}$  to a new position  $\varphi_{newd}$ , the state machine changes to the step "trajectory" until the output value of the trajectory profile  $\varphi_{new}$  is equal to the desired position.

In the trajectory calculation the difference between old and new position is calculated and a direction flag  $f_{dir}$  is set which is 0 for negative directions and 1 for positive directions.

$$\Delta\varphi = |\varphi_{old} - \varphi_{new\_d}| \quad \text{Equation 3-51}$$

The maximum allowable acceleration  $\alpha_{max}$  of the motor as well as the maximum speed  $\omega_{max}$  can be determined with the modeled system behavior. As the acceleration of the motor decreases with increasing speed (the motor is driven in voltage mode) an allowable acceleration of  $20 \frac{rad}{s^2}$  is chosen. The maximum speed is  $450 \frac{rad}{s}$ . For the calculation of the acceleration reduced profile, the time of acceleration  $t_{acc}$  and the angle of rotation during acceleration  $\varphi_{acc}$  are calculated [27].

$$t_{acc} = \frac{\omega_{max}}{\alpha_{max}} \quad \text{Equation 3-52}$$

$$\varphi_{acc} = \frac{1}{2} \cdot \alpha_{max} \cdot t_{acc}^2 \quad \text{Equation 3-53}$$

Using this profile it has to be distinguished between the following two different cases. Long stroke profiles, where the maximum speed is achieved and short stroke profiles where the maximum speed is not achieved [27]. To calculate which case has to be solved, the following equation can be used.

$$\begin{aligned} \text{if } \varphi_{acc} > \Delta\varphi &\rightarrow \text{short stroke} \\ \text{else} &\rightarrow \text{long stroke} \end{aligned} \quad \text{Equation 3-54}$$

When a short stroke profile has to be used, the time of acceleration  $t_1$ , can be calculated using the following term.

$$t_1 = \sqrt{\frac{\Delta\varphi}{\alpha_{max}}} \quad \text{Equation 3-55}$$

Using time  $t_1$ , the acceleration reduced profile can be calculated as shown below where the variable  $t$  represents the time in the positioning process.

$$\begin{aligned} \text{if } t < t_1 & \quad \text{Equation 3-56} \\ \varphi_{des} &= \frac{1}{2} \cdot \alpha_{max} \cdot t^2 \\ \text{else} & \\ \varphi_{des} &= \Delta\varphi - \frac{1}{2} \cdot \alpha_{max} \cdot (2 \cdot t_1 - t)^2 \end{aligned}$$

When a long stroke profile has to be used, the time while the rotor is spinning with maximum speed is calculated as shown below.

$$t_{\omega_c} = \frac{\Delta\varphi - 2 \cdot \varphi_{acc}}{\omega_{max}} \quad \text{Equation 3-57}$$

In a next step, the profile for a long stroke profile is defined in three parts. In a first part, the motor is accelerated to maximum speed, the second part is driving the motor with maximum

speed and the last part is reducing the motor speed. The calculation is shown in the following equation.

$$\begin{aligned}
 & \text{if } t < t_{acc} && \text{Equation 3-58} \\
 & \quad \varphi_{des} = \frac{1}{2} \cdot \alpha_{max} \cdot t^2 \\
 & \text{elseif } (t < t_{acc}) \&\& (t < t_{acc} + t_{\omega_c}) \\
 & \quad \varphi_{des} = \varphi_{acc} + \omega_{max} \cdot (t - t_{acc})^2 \\
 & \text{else} \\
 & \quad \varphi_{des} = \Delta\varphi - \frac{1}{2} \cdot \alpha_{max} \cdot (2 \cdot t_{acc} + t_{\omega_c} - t)^2
 \end{aligned}$$

In a last step of the trajectory planning the time dependent position is added to the value of the old position and the positive and negative direction is set based on the direction flag. This is described in the following equation.

$$\begin{aligned}
 & \text{if } f_{dir} == 1 && \text{Equation 3-59} \\
 & \quad \varphi_{new} = \varphi_{des} + \varphi_{old} \\
 & \text{else} \\
 & \quad \varphi_{new} = -\varphi_{des} + \varphi_{old}
 \end{aligned}$$

After performing the trajectory, the state machine changes from the case trajectory to the case wait and changes and  $\varphi_{old}$  becomes the recent position. The profile has been added in the LabVIEW code. In the following section the functionality of the profile is verified.

### 3.8 Model and control verification

#### 3.8.1 Open loop speed step

To verify the model of the motor that is built in chapter 3.7 and adjusted with the fitted parameters, the open loop steps of the motor for different voltage levels was measured and compared to the model.

The measurement of the changing speed due to open loop voltage steps was measured as in Table 10 (appendix) described. Figure 65 shows the comparison between measured and simulated step responses.

It can be seen, that there is a good comparability between the measurement of the actual system and the simulations (black lines). So it can be concluded, that the mathematical model represents the motor behavior accurately.

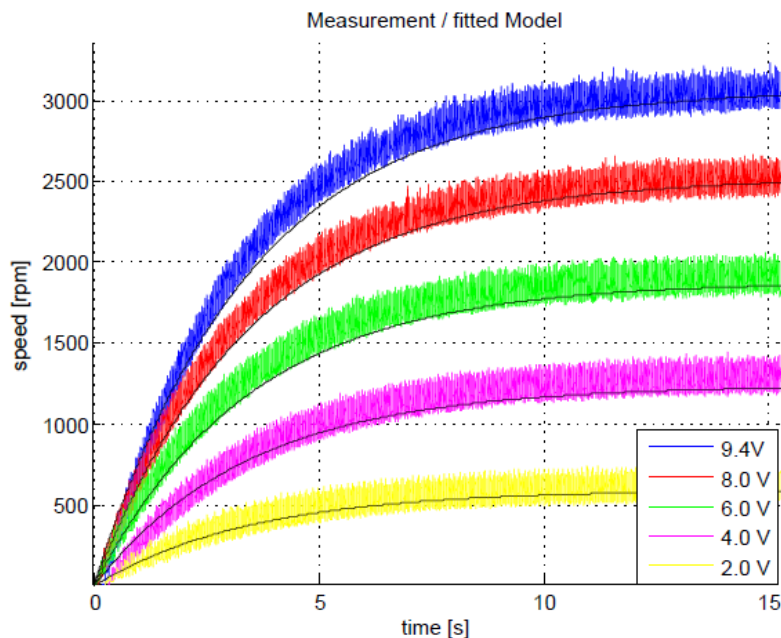


Figure 65 Comparison of measured on modeled open loop speed steps

#### 3.8.2 System frequency response measurement

A second way for verifying the model to the actual design is measuring the frequency response of the system. This is done by implementing sine functions with constant amplitude and different frequencies. The input function and the response of the system are compared in amplitude and phase to calculate the system behavior. The measurement process, as well as the sine signal generation is fully implemented in a LabVIEW based DSA tool, which was written at MIT. The frequency response of the system is measured under closed loop conditions. This way, higher frequencies can be measured more accurately.

The measuring of the frequency response was done according to the specifications in Table 11 in the appendix. The measured frequency response and the comparison to a linear model of the motor are shown in Figure 66.

It can be seen, that the magnitude of the bode plot shows a high comparability between model and measured behavior. For low frequencies there is a difference between the measured and simulated phase of the system. This difference can be explained with the coulomb friction, which is not represented in the linear motor model.

For higher frequencies there is a phase drop in the system. The motor itself would have a constant phase of  $-180^\circ$  for all frequencies. This phase shift has been identified as the sampling time  $t_s=1$  ms.

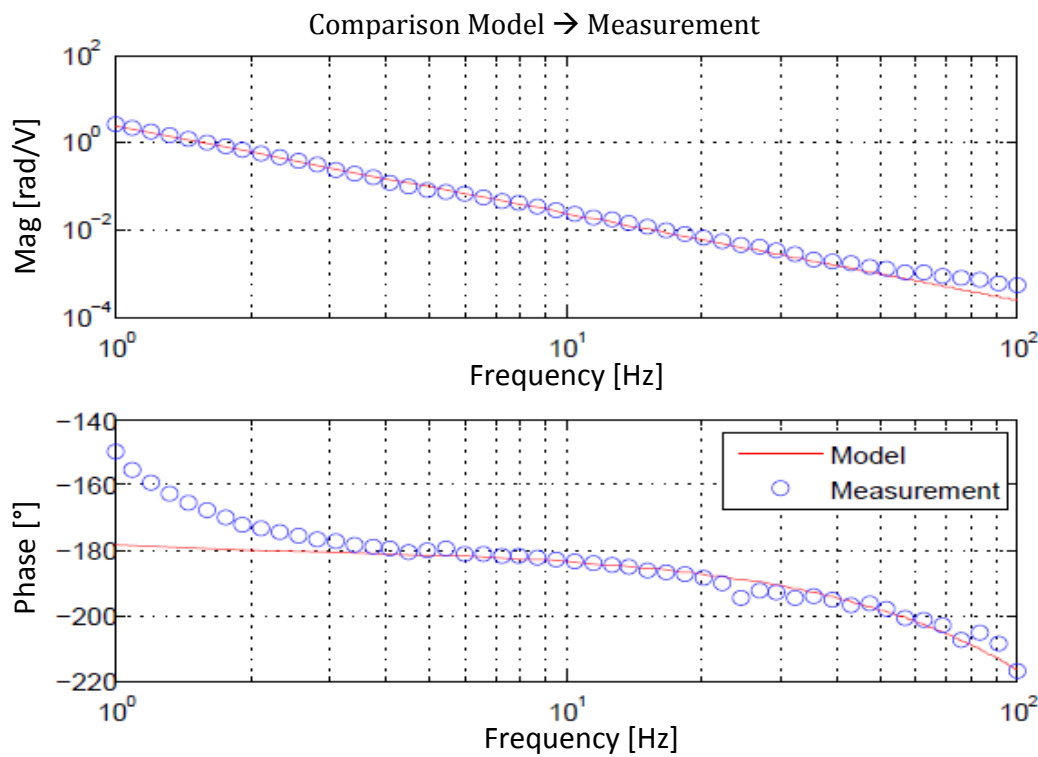


Figure 66 Comparison between measured and simulated frequency response of the motor

Summarizing it can be said, that the measurement and the model have a high comparability. So the modeled motor behavior can be used for a position control design of the motor.

### 3.8.3 Return ratio measurement

To verify the stability of the model based controller from 3.7.4, the return ratio of the system was measured. This was done with a LabVIEW based DSA measurement tool. The return ratio is also measured under closed loop conditions. The specification for this test is attached in Table 12. The measured frequency response and the comparison to a linear model of the motor are shown in Figure 67.

It can be seen, that the desired crossover frequency of 25 Hz can be achieved. Also the magnitude of the plot has a high comparability. The phase of the measured and the simulated system shows a high difference for low frequencies. One reason for this behavior could be the coulomb friction of the motor which results in stiction during the measurement process. Also for higher frequencies there is a difference between the both phase plots, which causes a lower phase margins in the real system. In other measurements it turned out that this error was caused by a wrong connection of the DSA tool in the LabVIEW program of the BLDC motor.

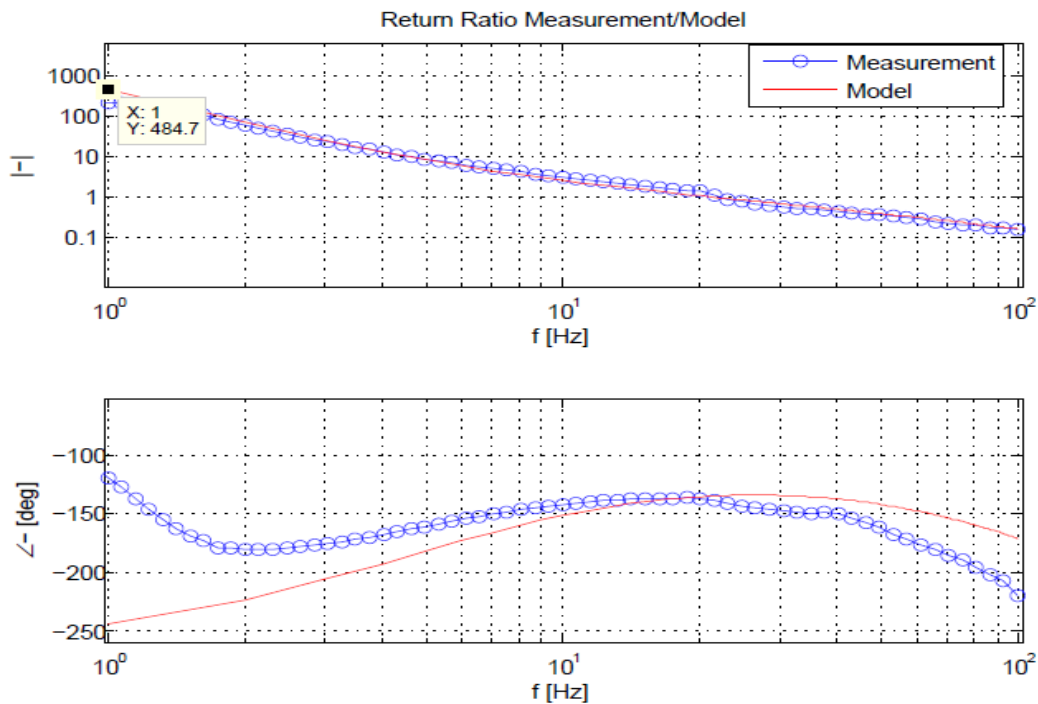


Figure 67 Measured return ratio

### 3.8.4 Step response closed loop

The system response of an input step in closed loop conditions was measured and compared to the model. This way the accuracy of the whole model can be characterized in time domain. The specification for these tests is documented in Table 13 in the appendix.

The measurement results of two exemplar step responses are shown in Figure 68. It can be seen, that both graphs show a high comparability. Thus it can be said, that using the developed model, a good estimation of the actual behavior of the motor can be achieved.

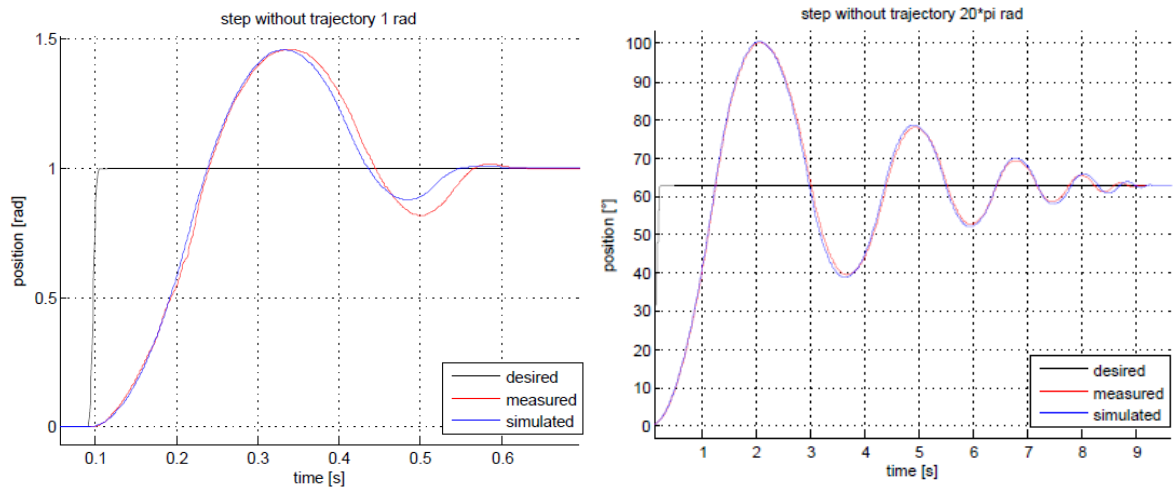


Figure 68 Closed loop step response

### 3.8.5 Trajectory based step response closed loop

To reduce overshoots in the system an acceleration reduced path planning is implemented as it is described in chapter 3.7.5. Using this trajectory, the overshoot by the positioning can be significantly reduced. The specification of this test is shown in Table 14 in the appendix. The results of the trajectory based positioning can be seen below.

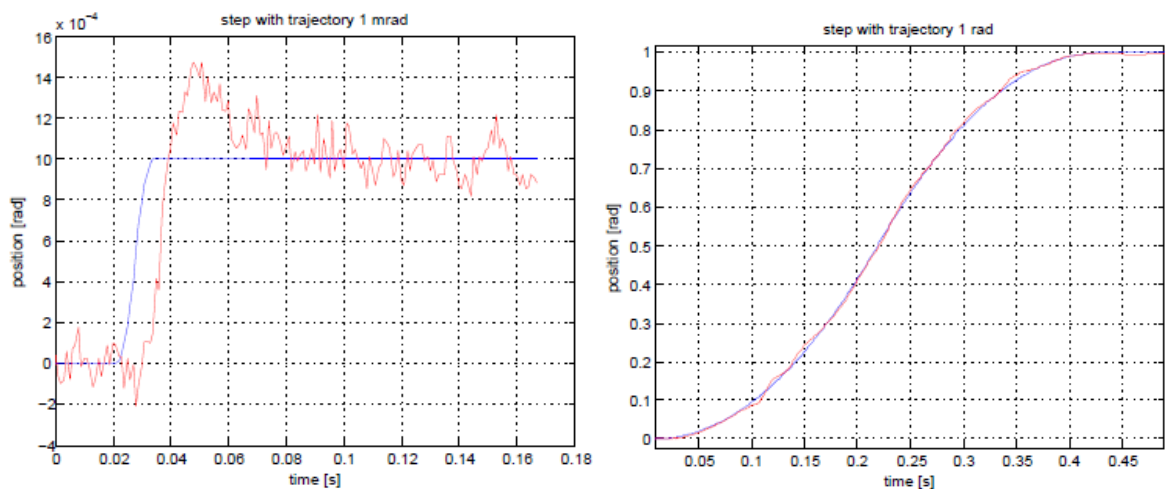
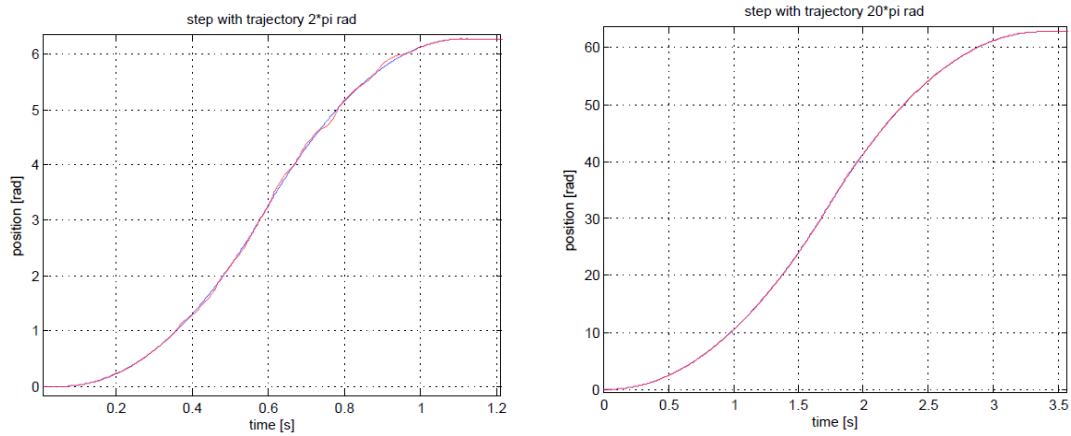


Figure 69 Trajectory based positioning for 1 mrad and 1 rad

## Axial field brushless DC motor



**Figure 70 Trajectory based positioning for one rotation and 10 rotations**

For the positioning of small angles, there are still overshoots in the system. Possible reasons for this could be the coulomb friction in the system. To get rid of this effect, a mathematical compensation of the coulomb friction can be implemented. For larger angles, the motor has a good following behavior of the desired trajectory. Thus it can be concluded, that the overshoot during the positioning of the motor can be significantly reduced by using the trajectory profile, also the positioning time is much shorter than without the trajectory.



## 4 Three axis magnetic bearing

In this chapter a three axis magnetic bearing using reluctance actuators according to the concept of section 2.3 is developed. Section 4.1 focuses on the design of the bearing. In section 4.2 different sensors are compared and rated. The actuators used in the bearing are designed and electronics for the actuators is developed in section 4.3. A dynamic model of the system is created and linearized in order to design position controllers for each axis in section 4.4. Control algorithms for the magnetic bearings are calculated implemented in the system. The functionality of the magnetic bearing is tested and the comparability to the model is verified.

### 4.1 Magnetic bearing design

A magnetic bearing for the Z, Pitch and Roll axis is developed according to the concept of chapter 2.3. For the assembly of the different parts, a 3D printed stage is designed, which can be plugged into the PCB board. On this stage, the reluctance actuators including the return iron for the magnetic flux, as well as the sensors for measuring the rotor position in the three desired axes are attached.

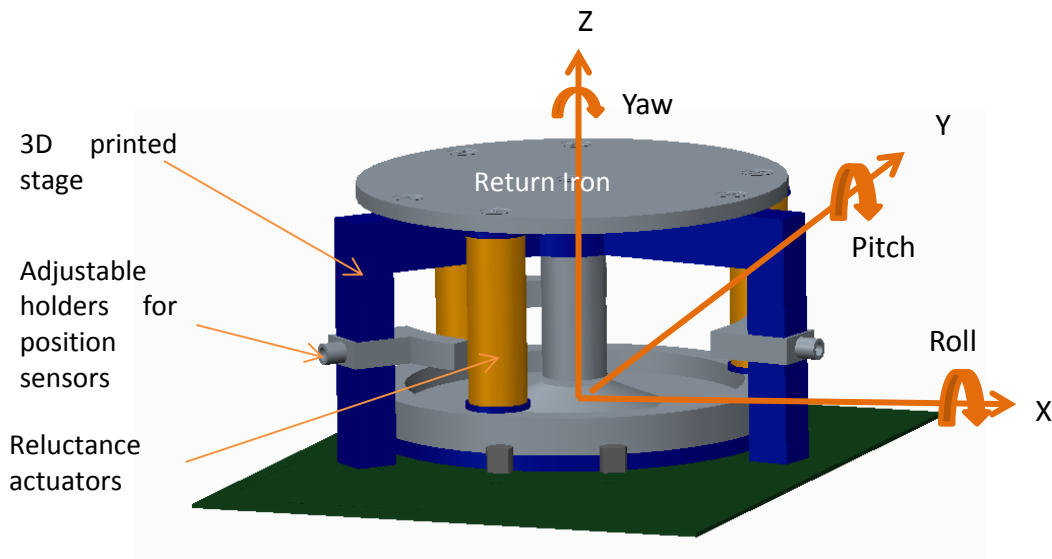


Figure 71 Magnetic bearing for Z, Pitch and Roll axis

The return iron is screwed in the stage to ensure a good positioning and the three reluctance actuators are mounted on the return iron. To lift the rotor out of its starting position a maximum distance of 2 mm between actuator and rotor has been chosen. The holders for the sensors are made to be adjustable, so the distance between rotor and sensor can be adjusted to the required distance.

All the parts are designed to be manufactured with standard manufacturing techniques. The nonmagnetic parts are made using 3D printing. The CAD sheets for manufacturing of the different parts are included in the appendix and the required stl. files are attached on a CD.

The parts in the magnetic circuit are made out of soft magnetic steel which shows a high permeability as well as a small hysteresis. A low carbon steel (C45) has been chosen.

### 4.2 Position sensing

To levitate the rotor of the brushless DC motor, its position needs to be measured according to the concept of chapter 2.4. In this section different sensing principles are compared and rated regarding their usability. The best concept is chosen and the needed electronic interface to the real-time system is designed.

#### 4.2.1 Sensor selection

The rotor can move a maximum distance of 2 mm in Z direction, sensors are needed which measure these distance contactless with a high accuracy. To avoid disturbances in the measurement, sensors which are not sensitive to magnetic fields have to be chosen. Also the sensors should have a small time delay which does not interfere with the phase margin of the control bandwidth. In order to keep the costs of the project low, sensors which are not price intensive (cheaper \$ 5 each) have to be chosen.

A sensor opportunity which is available as a low cost sensing is the LCD1000 inductance to digital chip [28] which can measure distances up to 8 mm depending on the configuration of the sensing coil. Using this sensor, a very high resolution can be achieved for a low price. The disadvantage of this sensor is that the adjustment of this sensor has to be done by adjusting the coil and the converter parameters of the chip. Designing and parametrizing the sensor takes a lot of time. Also the interface between sensors needs to be done via a digital bus signal.

The QTR-1A reflective sensor can be used for measuring distances between 3 mm to 6 mm between sensor and object. The sensor consists of an infrared diode and a photo resistive element [29]. The sensor needs a voltage supply of 5 V. With changing the distance between object and sensor the reflected infrared light changes. This causes changes in the resistance of the photo resistive element. The output voltage changes between zero and five volts. A picture of the reflective sensor can be seen in the following figure.

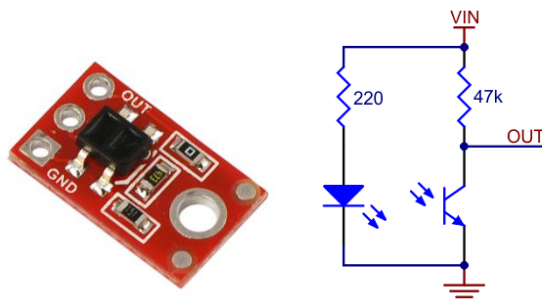


Figure 72 QTR-1A picture taken from [29]

There is a wide range of other sensors which offers non-contact measurement, easy connections to the real-time system and no sensitivity to magnetic field. Examples are capacitive,

inductive or eddy current sensors. Unfortunately sensors based on these principles are much more price intensive.

The reflective sensor offers the most advantages for the measuring of the rotor position because of its low price, and the easy connection to the real-time system via an analog input. Also there are no interference between the actuators and sensors.

### 4.2.2 Sensor electronics

By testing the sensors it turned out, that there are disturbances in the measured sensor signal which are caused by the fluorescent lamp of the laboratory, also the sensor signal changes with different light from the windows. To compensate this effect, an additional sensor which measures to a fixed position is mounted on the test bench. The sensor output of this sensor is only influenced by the disturbing light sources. With an instrumentation amplifier circuit shown in Figure 73 the sensor signal and the compensation signal can be subtracted. This way a huge amount of the disturbances can be eliminated

To reduce the quantization effect of the A/D converter, the full range of the converter should be used. With the gain factor of the LT1167, the output signal of the sensor is adjusted to the A/D range. A gain factor of 3.2 ( $R_g=22k\Omega$ ) has been chosen to adjust the sensor signal to the signal from the A/D converter.

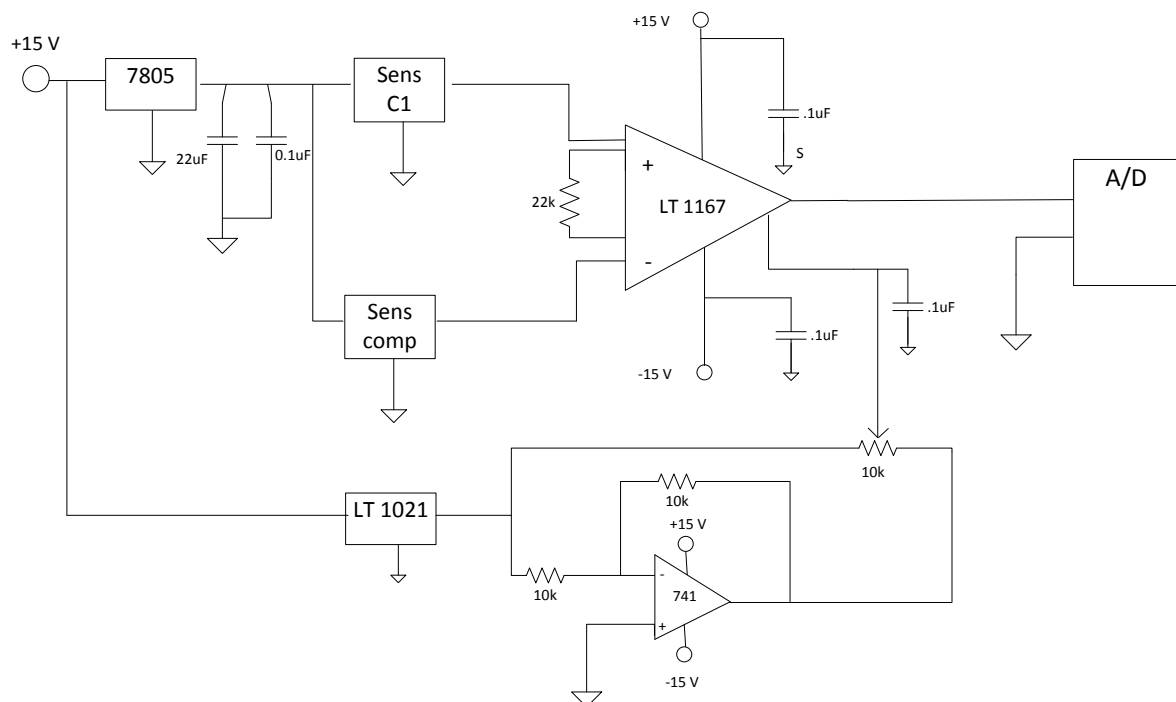


Figure 73 Sensing circuit

The adjustment of the sensor output to the A/D converter range is done with a potentiometer, which is connected to the reference input of the instrumentation amplifier. By changing the potentiometer value the output of the LT1167 can be adjusted in positive and negative direction. To get a voltage at the reference input which is independent from variations of the

voltage source a reference voltage chip LT 1021 in combination with a inverting amplifier with a gain of one is implemented.

### 4.2.3 Sensor calibration

The sensors are calibrated after mounting in the system. The calibration has been done, by changing the distance between sensors and object in steps of 0.2 mm. Therefore gauge blocks with different thicknesses have been used. The measured signal of the output of the instrumentation amplifier is shown in the following figure.

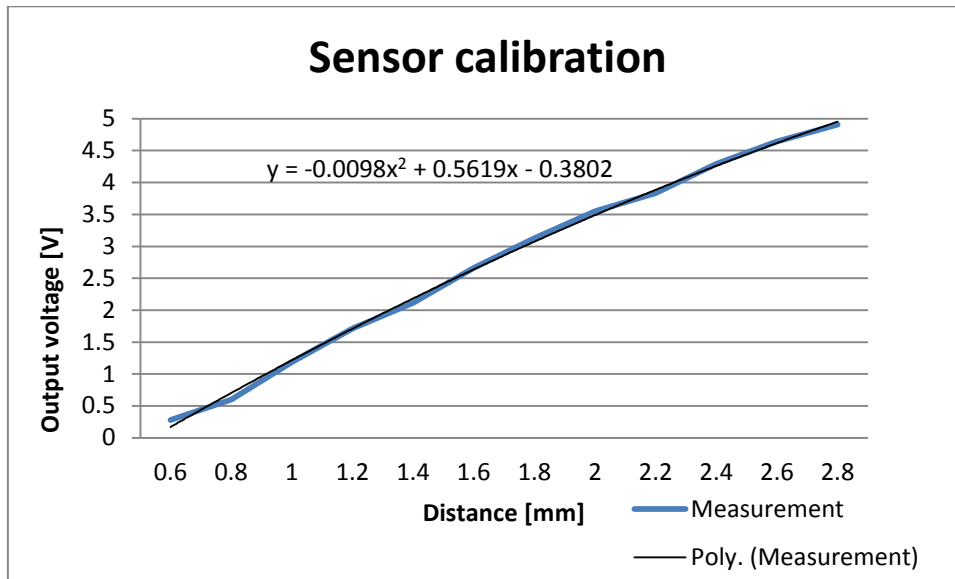


Figure 74 Sensor calibration

It can be seen, that the sensor shows a second order behavior in the used measurement range. The voltage to distance behavior can be described with a second order polynomic function. This function is implemented in the FPGA of the myRIO to convert the input voltage to the actual distance.

An important parameter by the use of these sensors turned out to be the measurement surface of the object. The best results can be achieved by using a matt white surface. The white color reflects the infrared light good, which results in a high measurement range of the rotor. Matt color makes the measurement less angle dependent. In addition the surface should be made out of a material which cannot be scratched when the spinning rotor hits the actuators, which is likely for teaching tool. The best results have been achieved by using electric tape mounted around the rotor.

### 4.3 Actuators

To levitate the rotor disc, reluctance actuators have to be designed. This type of actuator applies forces due to magnetic fields which are created via a current through a coil. In this chapter actuators are designed based on the equations of the magnetic circuit of the actuator. In a second step an operational amplifier based current control loop is designed to keep the dynamic behavior of the actuators high. The design of the actuator and current control is verified in different tests.

#### 4.3.1 Actuator design

##### 4.3.1.1 Force calculation

To levitate the rotor in a distance of 1 mm between rotor and actuators a gravity force of 1.86 N has to be compensated by the three actuators. So each actuator is designed to achieve 0.65 N at a distance between rotor and stage of 1 mm and an electrical current of 0.4 A. The force of the actuator is proportional to the square of the magnetic flux density in the air gap of the magnetic circuit. To calculate the force of the actuator the magnetic circuit of the system is analyzed. A simplified schematic of the magnetic circuit of the actuator can be seen in the following figure.

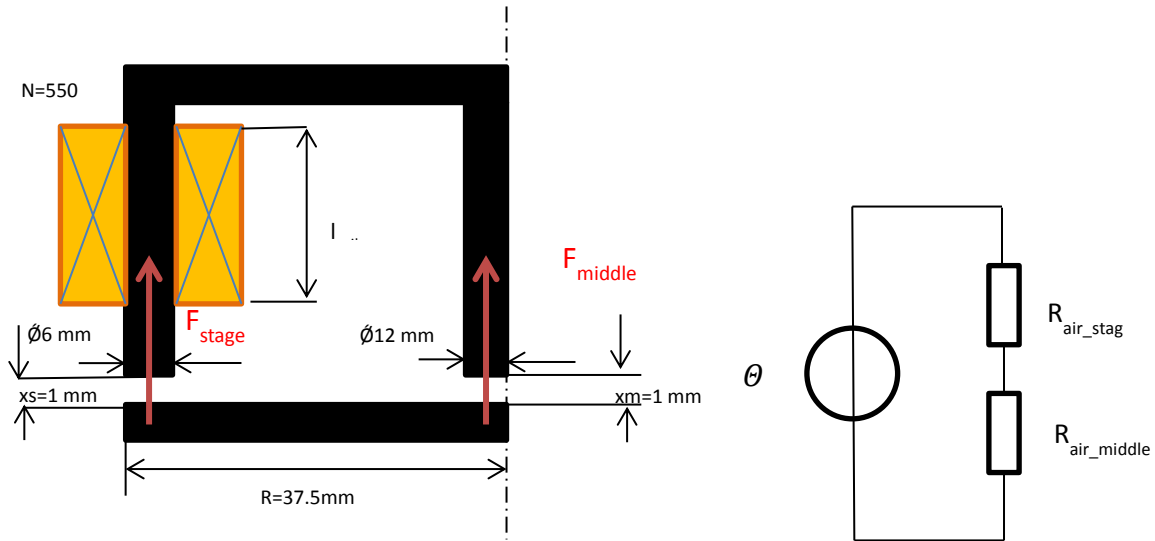


Figure 75 Schematic of a reluctance actuator

In the following the forces created by each actuator are calculated. The magnetomotive force  $\Theta$  of the coils can be calculated as the product of turns  $N$  and the electrical current  $I$ .

$$\Theta = N \cdot I \quad \text{Equation 4-1}$$

Using Equation 3-5 to Equation 3-7 the flux density in the air gap of the actuators can be calculated. The force  $F$  generated by the actuators is calculated by using the flux density in the air gaps and the cross sections of the iron core of the actuators.

$$F = B^2 \cdot \frac{A}{2 \cdot \mu_0} \quad \text{Equation 4-2}$$

### Three axis magnetic bearing

Using this equation to force of the stage part and middle part of the actuator can be expressed as:

$$F_{stage} = \left( \frac{N \cdot I}{\frac{x_{stage}}{\mu_0 \cdot A_{stage}} + \frac{x_{middle}}{\mu_0 \cdot A_{middle}}} \right)^2 \cdot \frac{1}{2 \cdot \mu_0 \cdot A_{stage}}$$

$$F_{middle} = \left( \frac{N \cdot I}{\frac{x_{stage}}{\mu_0 \cdot A_{stage}} + \frac{x_{middle}}{\mu_0 \cdot A_{middle}}} \right)^2 \cdot \frac{1}{2 \cdot \mu_0 \cdot A_{middle}}$$
Equation 4-3

As there are two air gaps in the magnetic circuit of one actuator, the total force due to this actuator can be calculated as the sum of both forces.

$$F_{act} = F_{stage} + F_{middle}$$
Equation 4-4

Caused by the force  $F_{stage}$  a torque  $T_{act}$  is applied on the rotor which can be calculated with the following equation.

$$T_{act} = F_{stage} \cdot (R - D_{actuator}/2)$$
Equation 4-5

Diameters of 6 mm for the stage and 12 mm for the middle cylinder are chosen in order to avoid high flux densities which results in saturation in the iron. With these diameters and 550 turns at the coil a force of 0.65 N can be applied to the rotor when an electrical current of 0.4 A is applied and the distance between actuator and rotor of 1 mm is estimated.

#### 4.3.1.2 Force calculation simplification

For reasons of simplifications it can be assumed, that the distance between the actuator and the rotor is the same on the stage and in the middle of the rotor. This reduces the equation to the following term:

$$F_{stage} = \left( \frac{A_{stage} \cdot A_{middle}^2 \cdot N^2 \cdot \mu_0}{2 \cdot (A_{stage} + A_{middle})^2} + \frac{A_{middle} \cdot A_{stage}^2 \cdot N^2 \cdot \mu_0}{2 \cdot (A_{stage} + A_{middle})^2} \right) \cdot \frac{I^2}{x^2}$$
Equation 4-6

Only  $I$  and  $x$  are variables which can change during the levitation of the rotor. Therefore the rest of the parameters can be pooled as a parameter  $k_z$ .

$$k_z = \frac{A_{stage} \cdot A_{middle}^2 \cdot N^2 \cdot \mu_0}{2 \cdot (A_{stage} + A_{middle})^2} + \frac{A_{middle} \cdot A_{stage}^2 \cdot N^2 \cdot \mu_0}{2 \cdot (A_{stage} + A_{middle})^2}$$
Equation 4-7

The total force of the actuator can now be written as:

$$F_{act} = k_z \cdot \frac{I^2}{x^2}$$
Equation 4-8

The torque created by one actuator can also be simplified. For the torque only the stage part of the actuator is acting. So the can be simplified the following:

$$T_{act} = R \cdot k_t \cdot \frac{I^2}{x^2} \quad \text{Equation 4-9}$$

With

$$k_t = \frac{A_{stage} \cdot A_{middle}^2 \cdot N^2 \cdot \mu_0}{2 \cdot (A_{stage} + A_{middle})^2} \quad \text{Equation 4-10}$$

The actuators have been built according to the calculation. To wind the actuators a small casing has been designed and 3D printed. While winding the coils, the wire has been added with glue to increase the thermal conductivity in the coil. During the winding of the coils it turned out, that 575 turns are more useful for filling the coil length.

#### 4.3.1.3 Coil dimensions calculation

In a next step the needed length of the coils is calculated. These parameters are required to create a CAD model of the actuator and the casings which are 3D printed. For a permanent electric current of 0.4 A, a wire diameter in the coil of 0.4 mm [30] is needed. As the thermal conductivity in the coil is high, a diameter of 0.35 mm is enough.

The turns which fit on the coil can be estimated by using the length of the coil and the diameter of the wire.

$$turns_z = \frac{l_{coil}}{d_{wire}} \quad \text{Equation 4-11}$$

To calculate the thickness of the coil, the total turns of the coil can be divided by turns in Z directions.

$$turns_x = \frac{N}{turns_z} \quad \text{Equation 4-12}$$

For manufacturing the coils, the outer diameter  $d_{coil\_out}$  of the coil is an important parameter. The estimated coil diameter is 10.9 mm.

$$d_{coil\_out} = d_{stage} + 2 \cdot turns_x \cdot d_{wire} \quad \text{Equation 4-13}$$

#### 4.3.1.4 Coil resistance

With the known dimensions of the coil, the electric resistance of the wire in the coil can be calculated. Therefore the middle diameter  $d_{coil\_middle}$  of a turn is calculated.

$$d_{coil\_middle} = d_{stage} + turns_x \cdot d_{wire} \quad \text{Equation 4-14}$$

The total length of the wire can be calculated using the slope of the middle diameter of the coil times the number of turns on the coil.

$$l_{wire\_coil} = d_{coil\_middle} \cdot \pi \cdot N \quad \text{Equation 4-15}$$

The total electric resistance of the coil is determined using Equation 3-28 to be 2.62  $\Omega$ . This result fits with an error of 25 % to the measured resistance of 3.5  $\Omega$  which is an acceptable value.

#### 4.3.1.5 Coil inductance

For designing a current controller the inductance of the coil has to be calculated. The inductance of the coil can be calculated with the number of turns at the coil and the resistance in the magnetic circuit.

$$L_{coil} = \frac{N^2}{R_{tot}} \quad \text{Equation 4-16}$$

An inductance of 8.6 mH is calculated for the coil of the actuator. To verify the calculated value, the inductance is measured in a next step according to Table 7 in the appendix. It has to be mentioned, that for reasons of the measurement setup, a 1  $\Omega$  sensing resistance has been used for measuring the signal. The air gap in the actuator is adjusted to be 1 mm. The measured graph and the comparison to the calculated model are shown in the following figure.

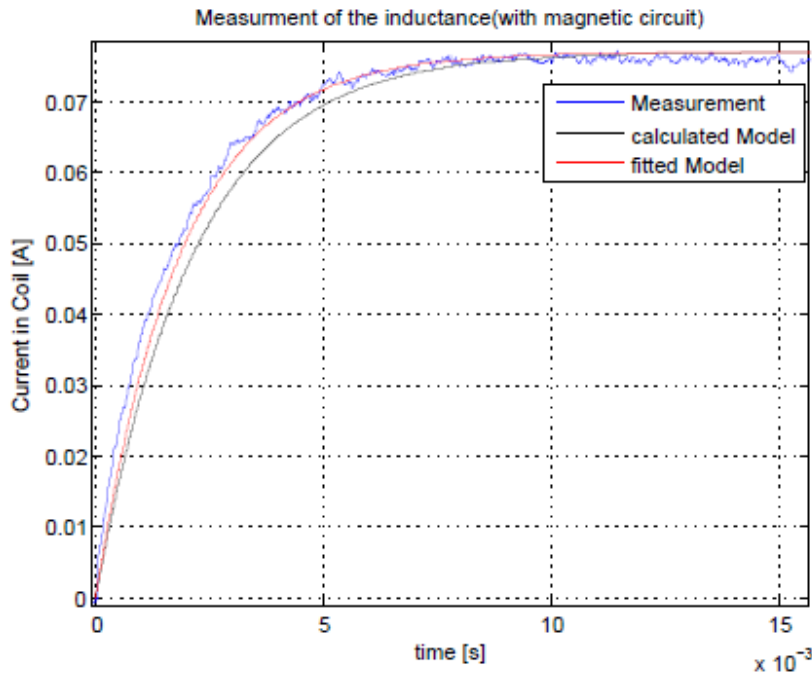


Figure 76 Measured and fitted inductance of a coil



By fitting the parameters it can be seen, that the calculated inductance of 8.6 mH is too large. A better comparability can be seen with a coil inductance of 7.5 mH. So the error between calculations and measurement is 13 %.

### 4.3.2 Actuator test

The force calculated by the actuator has been tested and compared to the estimated parameters to verify this design. This test has been done under closed loop conditions. The distance between rotor and the actuators is measured by reflective sensors. Using a multi-meter the current through the three actuators is measured. In the test process the distance between actuators and rotor is increased in steps of 0.1 mm and the current through the actuators is measured at each distance. The result can be seen in the following figure.

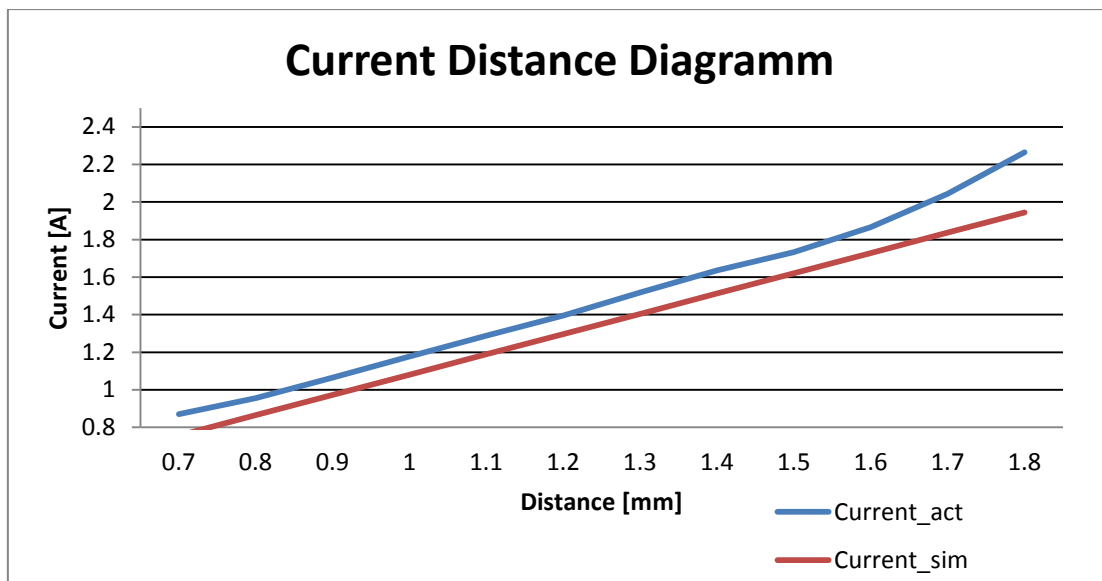


Figure 77 Actuator test, using electrical current vs. distance

The measured currents have been compared to the expected currents which are needed to levitate the rotor at a constant position (red curve). The errors are between 8 % and 16 %. These differences can be explained by the leakage flux and the resistance of the iron which has been neglected in the calculations. At higher currents the error between these two curves becomes bigger. A possible explanation is an increasing leakage flux for higher distances.

### 4.3.3 Electronics design

To achieve a high voltage to current dynamic, an operational amplifier based current controller is build. This is done in order to achieve a high bandwidth with the position controllers which are programmed in the real-time target. The following subchapter focuses on the design of sensing and power amplifiers and the design of an operational amplifier based current controller. In a last step, the functionality of the current controller is verified. The following figure shows the designed electronic circuit.

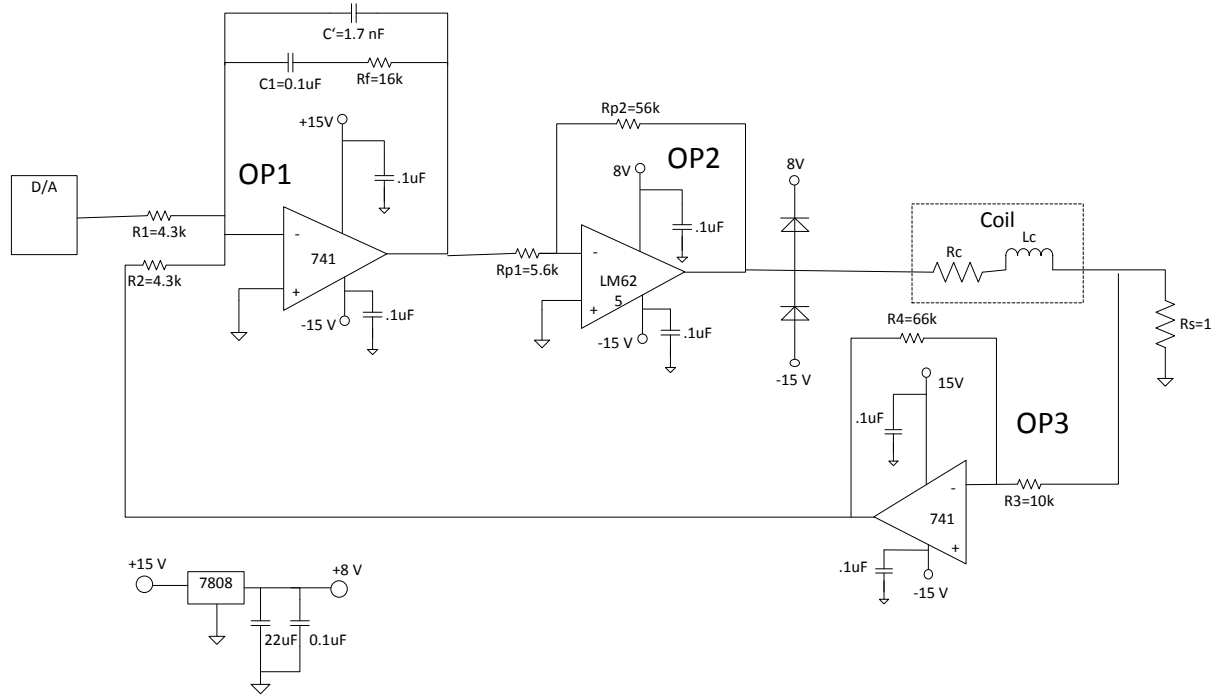


Figure 78 Current control schematic

#### 4.3.3.1 Current sensing amplifier

The actuators are designed, that an electrical current of 0.4 A is needed to achieve a levitation of the rotor. As higher distances as 1 mm has also be possible to lift the rotor, the current controller is designed, that 10 V at the output of the D/A results in 1.5 A in the current. The adjustment of the input voltage to output current is done in OP3 (Figure 78). OP3 is connected as an inverting amplifier. The gain  $G$  of the amplifier is:

$$G = \frac{R_4}{R_3} \quad \text{Equation 4-17}$$

It can be calculated with the maximum output voltage of the D/A converter divided by the desired maximum current. Using these values a gain of 6.67 has to be adjusted. For the current sensing a 1  $\Omega$  aluminum housed resistor which can dissipate up to 5 W [31] has been chosen, as the voltage drop is sufficiently high to be measured and the dissipated power in the resistance is still moderate.

#### 4.3.3.2 Power amplifier design

For the power amplifiers, which drives the current through the coils, the opamp TI LM675 is chosen which can handle up to 3 A. In addition this amplifier has a thermal protection included which makes this operational amplifier good for the use in teaching systems. The power amplifier OP2 is designed to have a gain of 10 [32, p. 1]. This is the minimum gain which is allowed in the specification of the amplifier. The supply voltage of the power opamp has been chosen to be +8 V and -15 V. According to the specifications the amplifier needs at least 16 V to work correctly [32, p. 1]. One goal in designing this circuit is, to avoid high voltage drops inside the amplifier, as this cause heating due to the  $I^2R$  losses inside the amplifier. For this reason the positive supply voltage is lower than the negative one. When 0.75 A are required by the system, the voltage drop by the coil and the sensing resistance is 3 V, this results in a voltage drop of 5 V inside the amplifier. The dissipated energy is 3.75 W according to the following equation.

$$P_{dis} = (U_s - U_{sys}) \cdot I \quad \text{Equation 4-18}$$

To prevent the power amplifier from damage due to introduced voltage from the coil two Schottkey diodes are implemented at the output of the amplifier.

#### 4.3.3.3 Current controller design

According to chapter 4.4.3 the crossover frequency of the levitation system has to be higher than 30 Hz. To get a voltage to current behavior which does not affect this crossover frequency of the position controller, the crossover frequency of the voltage to current behavior is designed to be 1 kHz which is more than ten times higher than the crossover frequency of the position controller.

The transfer function of the voltage to current behavior can be expressed as a first order system consisting of the coil parameters (resistance and inductance) and the sensing resistance.

$$\frac{I}{U} = \frac{1}{L_c \cdot s + (R_c + R_s)} \quad \text{Equation 4-19}$$

With the measured coil parameters from chapter 4.3.1.5, and the sensing resistor (1  $\Omega$ ), the bode plot shown in Figure 79 can be calculated. It can be seen, that a controller gain of 36.6 is needed. As the power amplifier already has a gain of 10, the controller gain of OP 1 adjusted to 3.66.

The integrator frequency of the current controller is set to be 1/10 of the crossover frequency (100 Hz).

$$\omega_i = \frac{1}{R_f \cdot C_1} \quad \text{Equation 4-20}$$

### Three axis magnetic bearing

This way the phase drop due to the integrator does not affect the phase of the crossover frequency. The integrator frequency can be calculated as indicated in the following equation where  $C'$  can be approximated to be infinity.

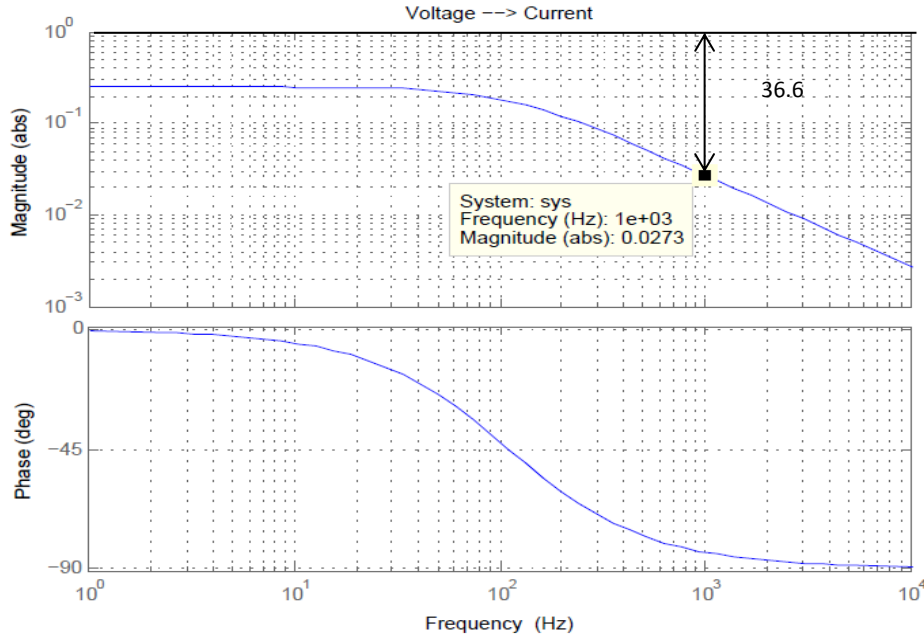


Figure 79 Bode plot U → I coil

To avoid a gain of high frequencies in the controller, the capacitor  $C'$  is implemented in the circuit. The high frequency roll off can be calculated by approximating the circuit as an opamp based low pass. For these frequencies, the capacitor  $C_1$  is acting as a shortcut. The cut off frequency is set to be 10 kHz.

$$\omega_l = \frac{1}{R_f \cdot C'} \quad \text{Equation 4-21}$$

With the resistances  $R_1$  and  $R_2$ , the needed controller gain is adjusted. In the control range of the controller, the opamp acts as an inverting amplifier. The capacitor  $C_1$  is approximated as a shortcut and the capacitor  $C'$  as an infinite resistance. The controller gain is adjusted with the following equation:

$$kp = \frac{R_f}{R_1} \cdot \frac{R_{p2}}{R_{p1}} \quad \text{Equation 4-22}$$

The controller can be desired with the following equation:

$$G_{cc} = kp \cdot \frac{\omega_i \cdot s + 1}{s} \cdot \frac{1}{\omega_l \cdot s + 1} \quad \text{Equation 4-23}$$

$$G_{cc} = \frac{R_f \cdot C_1 \cdot s + 1}{R_2 \cdot C_1 \cdot s} \cdot \frac{1}{R_f \cdot C_2 \cdot s + 1} \cdot \frac{R_{p2}}{R_{p1}}$$

### Three axis magnetic bearing

Using the calculated behavior of the coil and the designed controller the return ratio can be simulated to verify the stability of the designed current controller. The calculated controller as well as the return ratio of the system can be seen in the following figures. The controller fits to the desired crossover frequency of 1 kHz. A phase margin of  $85^\circ$  should be achieved.

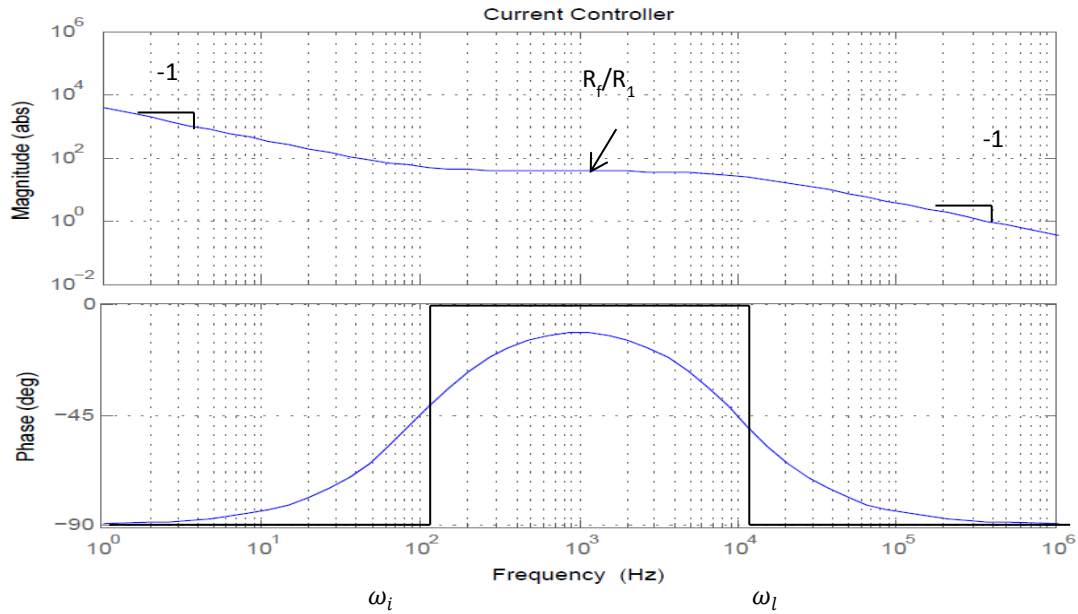


Figure 80 Bode plot current controller

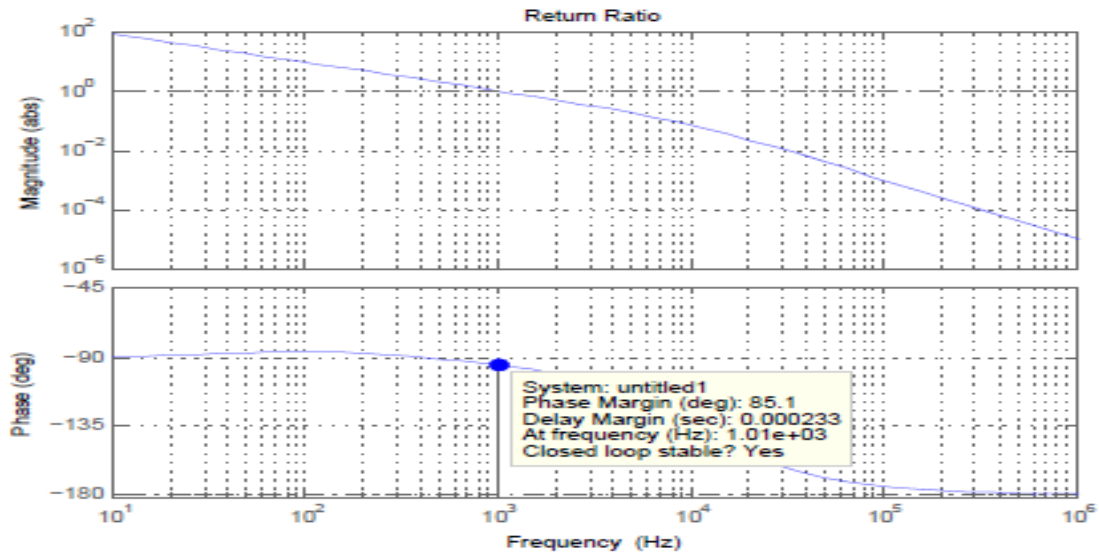


Figure 81 Bode plot return ratio current control

### Three axis magnetic bearing

The calculated parameters for the current control are shown in the following table:

**Table 4 Components current control**

Component	Value
R1	4.3k
R2	4.3k
Rf	16k
C1	0.1uF
C'	1.7nF
Rp1	5.6k
Rp2	56k
R3	10k
R4	66k
Rs	1

For modelling the total system behavior, the closed loop transfer function of the current control has to be used. This can be calculated using the following equation:

$$G_{CL\_currentcontrol} = \frac{G_{cc} \cdot G_{coil}}{1 + G_{cc} \cdot G_{coil}} \quad \text{Equation 4-24}$$

The electronics has been soldered on a pefboard according to the following figure which shows a schematic view of the designed electronics. Every reluctance actuator needs its own current control electronics, so it has to be built three times for the top reluctance actuators.

The current control has been tested by connecting a square wave generator at the input of the current control and measuring the current through the coil (the voltage at  $R_s$ ). In Figure 82 it can be seen, that there is a good comparability between the desired and measured step response.

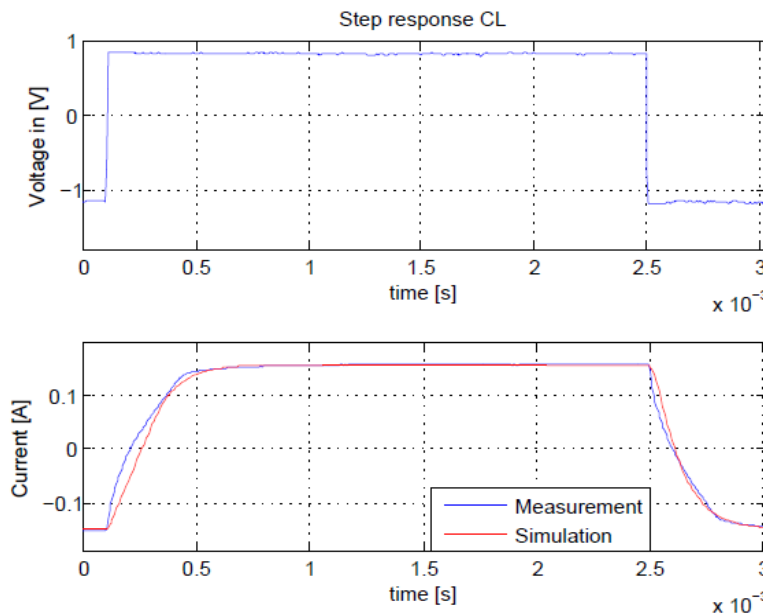


**Figure 82 Measured and modeled step response of the current control**

#### 4.4 Modelling and control

Before building the actual magnetic bearing system, a dynamic model including the different nonlinearities of the system is built. Based on this model a structure for the control of the three Cartesian axes Z, Pitch and Roll is developed. The model is structured in two sections, the system behavior and the control structure. This is indicated in the figure below.

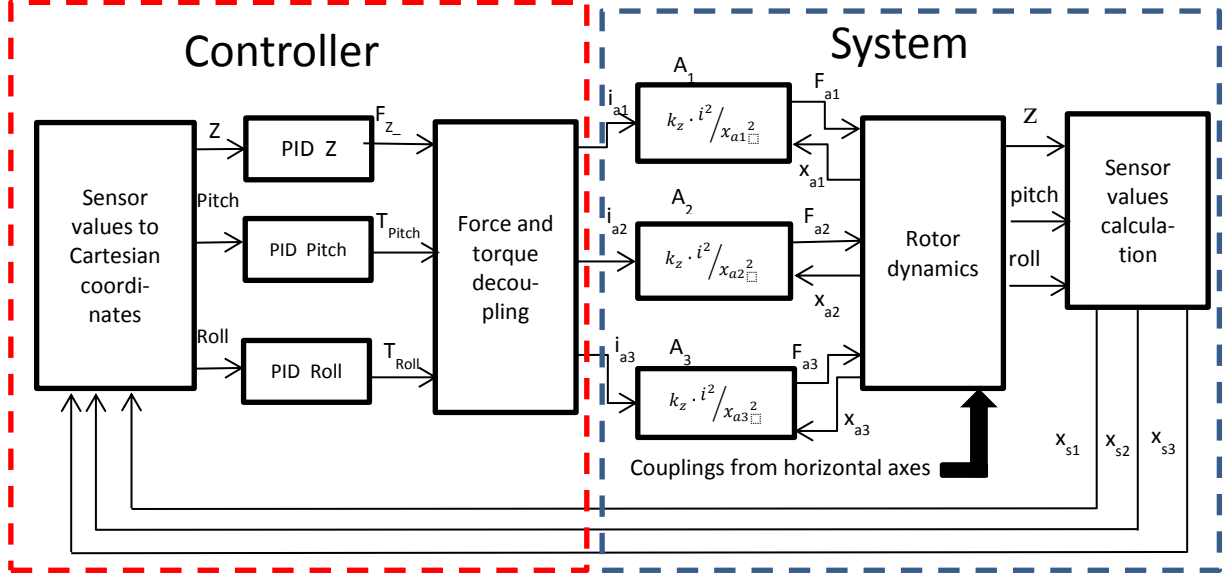


Figure 83 Model of the vertical axes

The modeled system behavior and the designed controller are validated in different tests.

##### 4.4.1 System model

###### 4.4.1.1 Force and dynamics model

For modeling the rotor dynamics in the Z, Pitch and Roll axis, the forces and torques created by each actuator is calculated and analyzed. The forces created by the actuators can be determined using Equation 4-3, Equation 4-5 can be used for calculating the torques of the actuators. The forces which are applied are shown in Figure 84.

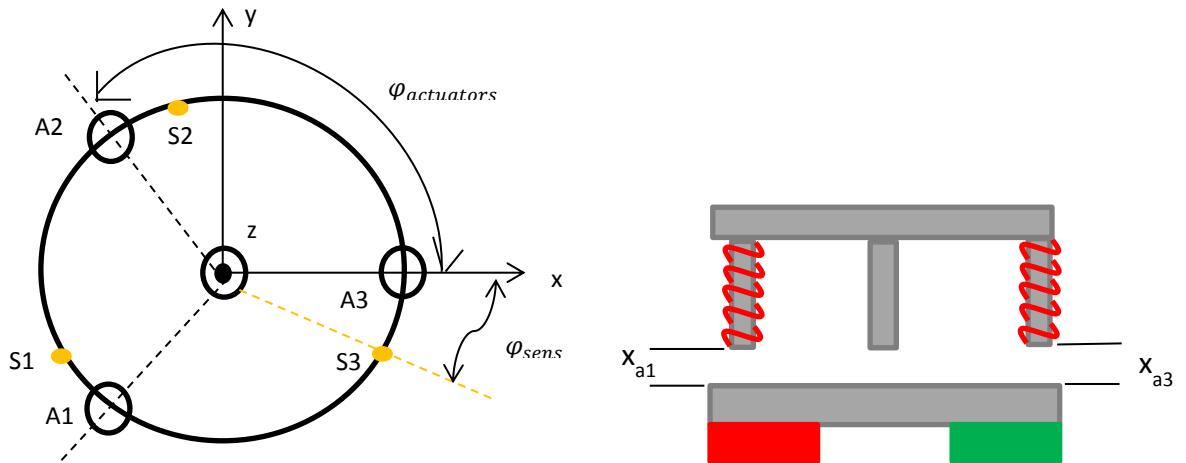


Figure 84 Placement of the reluctance actuators and sensors in the system

### Three axis magnetic bearing

To calculate the forces in the Z axis, the sum of the acting forces has to be built.

$$F_z = F_{A1} + F_{A2} + F_{A3} + F_m - F_G \quad \text{Equation 4-25}$$

The torque created by the reluctance actuators in every axis is calculated by analyzing the trigonometric functions shown in Figure 84. The torque in one axis can be calculated using Equation 4-26. It has to be noticed, that the angle  $\varphi_{coil}$  between each actuator is  $120^\circ$ .

$$\begin{aligned} T_{pitch} &= T_{A1} \cdot \cos(240) + T_{A2} \cdot \cos(120) + T_{A3} \\ T_{roll} &= T_{A1} \cdot \sin(240) + T_{A2} \cdot \sin(120) \end{aligned} \quad \text{Equation 4-26}$$

In the following equation the actuator force and torque behavior is described in matrix notation:

$$\begin{aligned} \mathbf{F}_{axis} &= \mathbf{A}_{actuator to axis} \cdot \mathbf{F}_{Actuator} \\ \begin{bmatrix} F_z \\ F_{pitch} \\ F_{roll} \end{bmatrix} &= \begin{bmatrix} 1 & 1 & 1 \\ -\frac{1}{2} & -\frac{1}{2} & 1 \\ -0.86 & 0.86 & 0 \end{bmatrix} \cdot \begin{bmatrix} F_{A1} \\ F_{A2} \\ F_{A3} \end{bmatrix} \end{aligned} \quad \text{Equation 4-27}$$

The rotor position of each axis can be calculated by using the basic kinetic functions (Equation 4-28). The acting mass of the rotor and the moments of inertia can be estimated using the CAD model. The rotor with the glued on permanent magnets has a mass of 186 g. As the rotor is a symmetric device, the moment of inertia is the same for the Pitch and the Roll axis, based on the CAD model it is estimated to be  $8.088 \times 10^{-5} \text{ kgm}^2$ .

$$\begin{aligned} F_z &= m \cdot \ddot{z} \\ T_{pitch} &= J_{pitch} \cdot \ddot{\varphi}_{pitch} \\ T_{roll} &= J_{roll} \cdot \ddot{\varphi}_{roll} \end{aligned} \quad \text{Equation 4-28}$$

Using these equations and the Laplace transformation, the position in the Z axis and the rotor angles can be calculated.

$$\begin{aligned} \frac{z}{F_z} &= \frac{1}{m \cdot s^2} \\ \frac{\varphi_{pitch}}{T_{pitch}} &= \frac{1}{J_{pitch} \cdot s^2} \\ \frac{\varphi_{roll}}{T_{roll}} &= \frac{1}{J_{roll} \cdot s^2} \end{aligned} \quad \text{Equation 4-29}$$

#### 4.4.1.2 Sensor value calculation

To get a model of the system behavior, the distances between the sensors S1 to S3 and the rotor needs to be calculated. The angle between the reluctance actuators and the sensors for each actuator  $\varphi_{sens}$  is  $16.5^\circ$ . For the identification of the distances the trigonometric behaviors, shown in Figure 84, are used.



### Three axis magnetic bearing

Also the sine behavior by rotating the rotor in the Pitch and Roll axis as it can be seen in Figure 85 is taken into account. The following figure shows the sine dependency when the rotor is rotating in the Pitch or Roll axis.

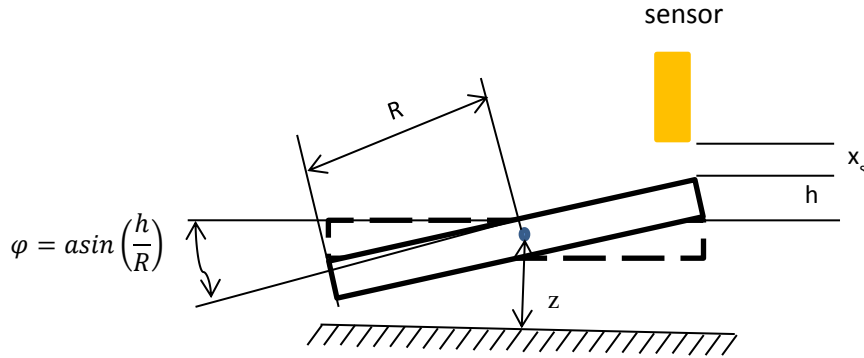


Figure 85 Distance caused by angle calculation

This results in the following behavior between Cartesian coordinates and sensor values.

$$\begin{aligned} x_{s1} &= x_z + R \cdot \sin(\varphi_{pitch}) \cdot \cos(240 - \varphi_{sens}) + R \cdot \sin(\varphi_{roll}) \cdot \sin(240 - \varphi_{sens}) \\ x_{s2} &= x_z + R \cdot \sin(\varphi_{pitch}) \cdot \cos(120 - \varphi_{sens}) + R \cdot \sin(\varphi_{roll}) \cdot \sin(120 - \varphi_{sens}) \\ x_{s3} &= x_z + R \cdot \sin(\varphi_{pitch}) \cdot \cos(-\varphi_{sens}) + R \cdot \sin(\varphi_{roll}) \cdot \sin(-\varphi_{sens}) \end{aligned}$$

Equation 4-30

The equations can be transformed into matrix notation with the following parameters:

$$\begin{aligned} x_1 &= x_z \\ x_2 &= \sin(\varphi_{pitch}) \\ x_3 &= \sin(\varphi_{roll}) \\ a &= R \cdot \cos(240 - \varphi_{sens}); \\ b &= R \cdot \sin(120 - \varphi_{sens}); \\ c &= R \cdot \cos(120 - \varphi_{sens}); \\ d &= R \cdot \sin(120 - \varphi_{sens}) \\ e &= R \cdot \cos(-\varphi_{sens}); \\ f &= R \cdot \sin(-\varphi_{sens}) \end{aligned}$$

Equation 4-31

$$\underbrace{\begin{bmatrix} x_{s1} \\ x_{s2} \\ x_{s3} \end{bmatrix}}_{\mathbf{x}_s} = \underbrace{\begin{bmatrix} 1 & a & b \\ 1 & c & d \\ 1 & e & f \end{bmatrix}}_{\mathbf{A}_{senstoaxis}} \cdot \underbrace{\begin{bmatrix} x_z \\ x_{pitch} \\ x_{roll} \end{bmatrix}}_{\mathbf{x}_{axis}} ;$$

$$\mathbf{x}_s = \mathbf{A}_{senstoaxis} \cdot \mathbf{x}_{axis}$$

As there are only small angles in the Pitch and Roll axis, the sine behavior can be neglected. This is shown in the following equation.

$$\begin{aligned}\varphi_{pitch} &\approx \sin(\varphi_{pitch}) \\ \varphi_{roll} &\approx \sin(\varphi_{roll})\end{aligned}\tag{Equation 4-32}$$

#### 4.4.1.3 Distance between actuators and rotor

The force of the three vertical axes actuators is depending on their distance to the rotor. To get a model which represents the system dynamics, these distances needs to be calculated by using the trigonometric behaviors of Figure 84.

$$\begin{aligned}x_{c1} &= x_z \cdot R \cdot \sin(\varphi_{pitch}) \cdot \cos(240) + R \cdot \sin(\varphi_{roll}) \cdot \sin(240) \\ x_{c2} &= x_z \cdot R \cdot \sin(\varphi_{pitch}) \cdot \cos(120) + R \cdot \sin(\varphi_{roll}) \cdot \sin(120) \\ x_{c3} &= x_z + R \cdot \sin(\varphi_{pitch})\end{aligned}\tag{Equation 4-33}$$

These equations can be transformed to matrix representation. As the angle of the rotor is small, the sine dependency of the Pitch and Roll axis is neglected.

$$\mathbf{x}_{actuator} = \mathbf{A}_{axistoactuator} \cdot \mathbf{x}_{axis}\tag{Equation 4-34}$$

$$\begin{bmatrix} x_{a1} \\ x_{a2} \\ x_{a3} \end{bmatrix} = \begin{bmatrix} 1 & R \cdot \varphi_{pitch} \cdot \cos(240) & R \cdot \varphi_{roll} \cdot \sin(240) \\ 1 & R \cdot \varphi_{pitch} \cdot \cos(120) & R \cdot \varphi_{roll} \cdot \sin(120) \\ 1 & R \cdot \varphi_{pitch} & 0 \end{bmatrix} \cdot \begin{bmatrix} x_z \\ x_{pitch} \\ x_{roll} \end{bmatrix}$$

### 4.4.2 Controller design

#### 4.4.2.1 Sensor values to Cartesian coordinates

Controllers for the three Cartesian coordinates Z, Pitch and Roll have to be built. Therefore the sensor values needs to be transformed into Cartesian coordinates. In the model of the system, the three sensor values (S1 – S3) are calculated out of the Cartesian coordinates by using the regular matrix  $\mathbf{A}_{senstoaxis}$  (Equation 4-31). By inverting this equation, the transformation between sensor values and Cartesian coordinates can be performed as shown below.

$$\mathbf{x}_{axis} = \mathbf{A}_{senstoaxis}^{-1} \cdot \mathbf{x}_s\tag{Equation 4-35}$$

$$\begin{bmatrix} x_z \\ x_{pitch} \\ x_{roll} \end{bmatrix} = \begin{bmatrix} 0.33 & 0.33 & 0.33 \\ -13.8167 & -4.4466 & 18.2632 \\ -13.1115 & 18.5213 & -5.4098 \end{bmatrix} \cdot \begin{bmatrix} x_{s1} \\ x_{s2} \\ x_{s3} \end{bmatrix}$$

#### 4.4.2.2 Force and torque decoupling

For controlling the rotor in the Cartesian coordinates Z, Pitch and Roll the forces and torques created by the actuators needs to be decoupled. When this is done correctly, the system results in three different SISO systems with independent controllers. To decouple the system the geometry shown in Figure 84 is analyzed.

### Three axis magnetic bearing

It can be seen, that for a change in the Z axis, the force due to the actuators A1 – A3 has to change their force in the same way. For changing the torque in the Pitch axis the actuators A1 and A2 have to change their force antagonistically. To change the torque in the Roll axis actuator A3 and the actuators A1 & A2 have to be controlled antagonistically. This can also be seen in Equation 4-27. Thus the following matrix decouples the system.

$$\mathbf{F}_{Actuator} = \mathbf{A}_{actuator to axis}^{-1} \cdot \mathbf{F}_{axis}$$

$$\begin{bmatrix} F_{c1} \\ F_{c2} \\ F_{c3} \end{bmatrix} = \begin{bmatrix} 0.33 & -0.33 & -0.57 \\ 0.33 & -0.33 & 0.57 \\ 0.33 & 0.66 & 0 \end{bmatrix} \cdot \begin{bmatrix} F_z \\ F_{pitch} \\ F_{roll} \end{bmatrix} \quad \text{Equation 4-36}$$

#### 4.4.2.3 System linearization

The modeled dynamics and the forces created by the reluctance actuators of chapter 4.3.1 are linearized to design independent controllers for each axis.

##### 4.4.2.3.1 Linearization of the Z-Axis

For a linear approximation the forces of the actuators can be described with Equation 4-8. The system of three actuators can be considered as shown in the following figure.

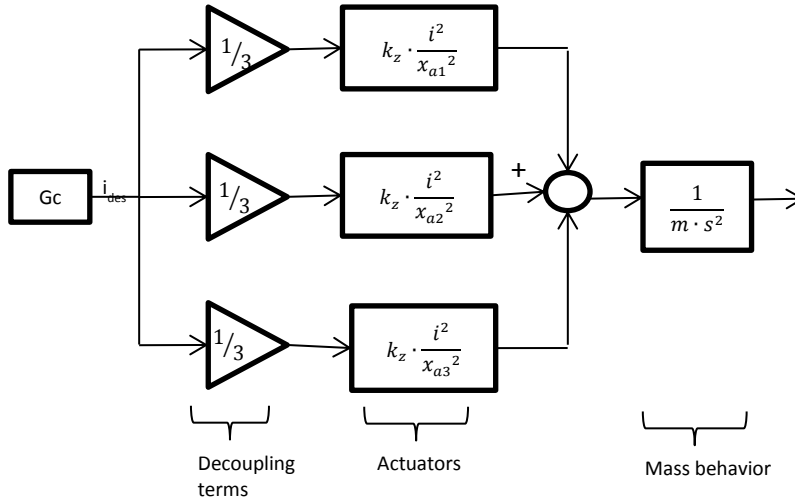


Figure 86 System representation for linearization of the Z-axis

The total force is created by three actuators. Also the decoupling factors have to be taken into account as they multiply the current through each actuator with a factor of 0.33. Using these behaviors, the system can be written in the following representation.

$$m \cdot \ddot{x} = -g \cdot m + 3 \cdot k_z \cdot \frac{\left(\frac{i}{3}\right)^2}{x_a^2} \quad \text{Equation 4-37}$$

In a stationary case, the current through the actuators can be calculated using the following equation:

### Three axis magnetic bearing

$$0 = F_g + 3 \cdot k_c \cdot \frac{\left(\frac{i}{3}\right)^2}{x_a^2} \rightarrow i_0 = 3 \cdot \sqrt{\frac{m \cdot g \cdot x_a^2}{k_c \cdot 3}} \quad \text{Equation 4-38}$$

The current controller is designed to have a ratio  $V_{tol}$  of 1/6.67 between Voltage of the A/D converters and the current (4.3.3.1).

The system is linearized for a distance between rotor and actuators of 1 mm and a speed of 0 m/s. The linearization is calculated in the following equation:

$$F_a = \frac{\partial f}{\partial x} \Big|_{x_0, u_0} \cdot \Delta x + \frac{\partial f}{\partial i} \Big|_{x_0, i_0} \cdot \Delta i \quad \text{Equation 4-39}$$

$$\frac{-2 \cdot k_c \cdot i^2}{3 \cdot x_a^3} \cdot \Delta x + \frac{2 \cdot k_c \cdot i_0}{3 \cdot x_a^2} \cdot V_{tol} \cdot \Delta i = m \cdot \ddot{x}$$

$$G_z = \frac{x}{i} = \frac{\frac{2 \cdot k_c \cdot i_0}{3 \cdot x_a^2} \cdot V_{tol}}{m \cdot s^2 + \frac{2 \cdot k_c \cdot i^2}{3 \cdot x_a^3}}$$

To get a higher accuracy of the model, the voltage to current behavior with the integrated current controller can be taken into account. The closed loop transfer function of the current control (Equation 4-24) can be multiplied to the linearized system. This is represented in the following figure.

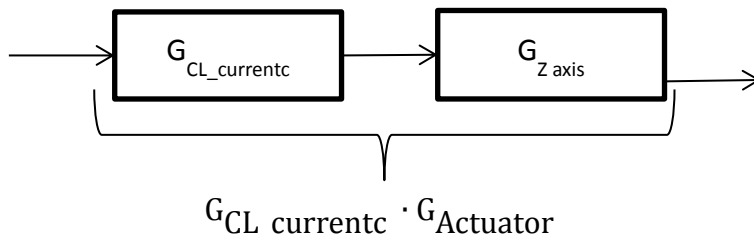


**Figure 87** Linearized system including current control

The linearization of the Z axis results in the bode plot shown in Figure 88. It can be seen, that the system has a negative spring stiffness as up to 10 Hz, the magnitude is constant. Above this point, the magnitude falls with a factor of -2. The phase of the system is  $-180^\circ$ . For higher frequencies, the phase drops due to the time delay in the system caused by the sampling rate of 2 kHz can be seen. A crossover frequency between 30 Hz and 100 Hz has to be achieved in the controller design in order to achieve a good phase and gain margin.

### Three axis magnetic bearing

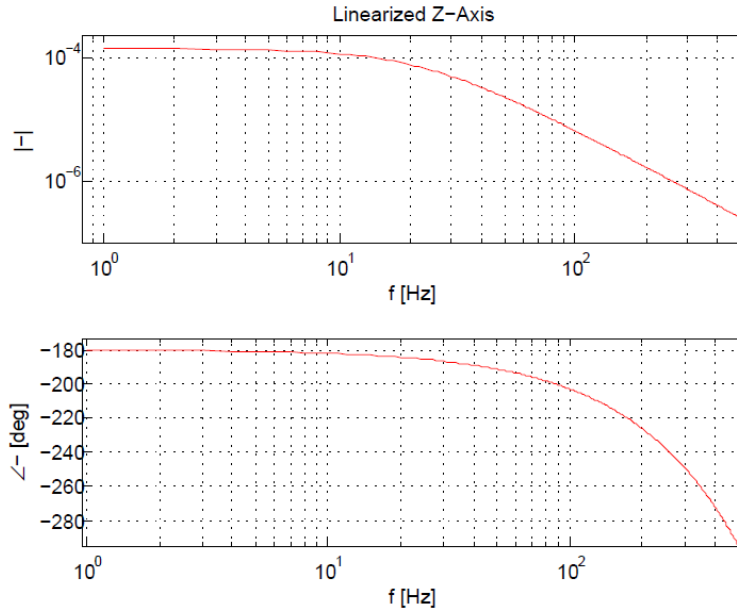


Figure 88 Linearized bode plot of the Z-axis

#### 4.4.2.3.2 Linearization of the rotary axis

To design controllers for the rotary axis, the dynamics for these axes are linearized. The torque created by a reluctance actuator is approximated using the force for a linearization position  $z_0$  plus an additional distance due to angle disturbances. The torque behavior can be expressed with the following equation.

$$T_{act} = k_t \cdot \frac{i^2}{z_0^2 + (\sin(\alpha) \cdot R)^2} \cdot R \quad \text{Equation 4-40}$$

To linearize the system of the rotary axis, the representation shown in Figure 89 and Figure 90 is analyzed. It can be seen, that the desired current (torque) created by the controller is multiplied by the decoupling factors. These figures also indicate that the system for both axes can be represented with the same set of equations.

The actuators in combination with the trigonometric terms of the system create the torque of one axis. With Equation 4-40 and the considerations of Figure 89 and Figure 90 the system can be represented as shown below.

$$J \cdot \ddot{\varphi} = \frac{k_t \cdot R}{J} \cdot \frac{i^2}{z_0^2 + (\sin(\alpha) \cdot R)^2} \cdot 0.55 \quad \text{Equation 4-41}$$

### Three axis magnetic bearing

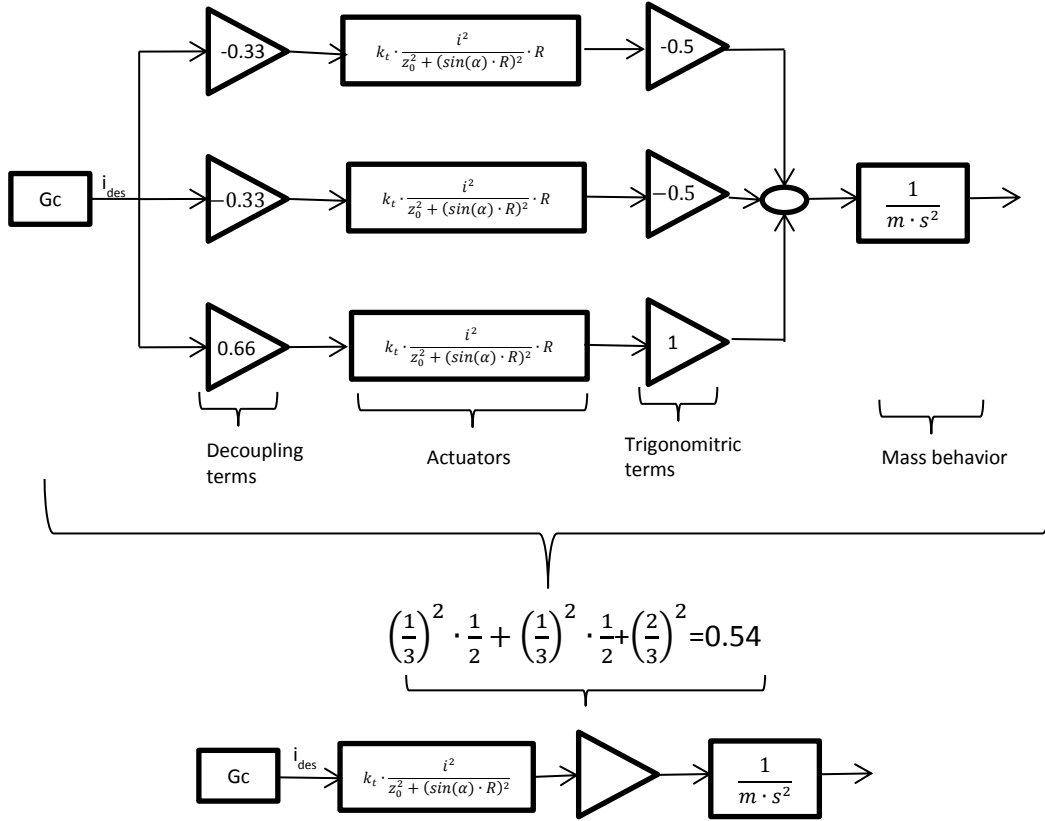


Figure 89 System representation for linearization of the Pitch axis

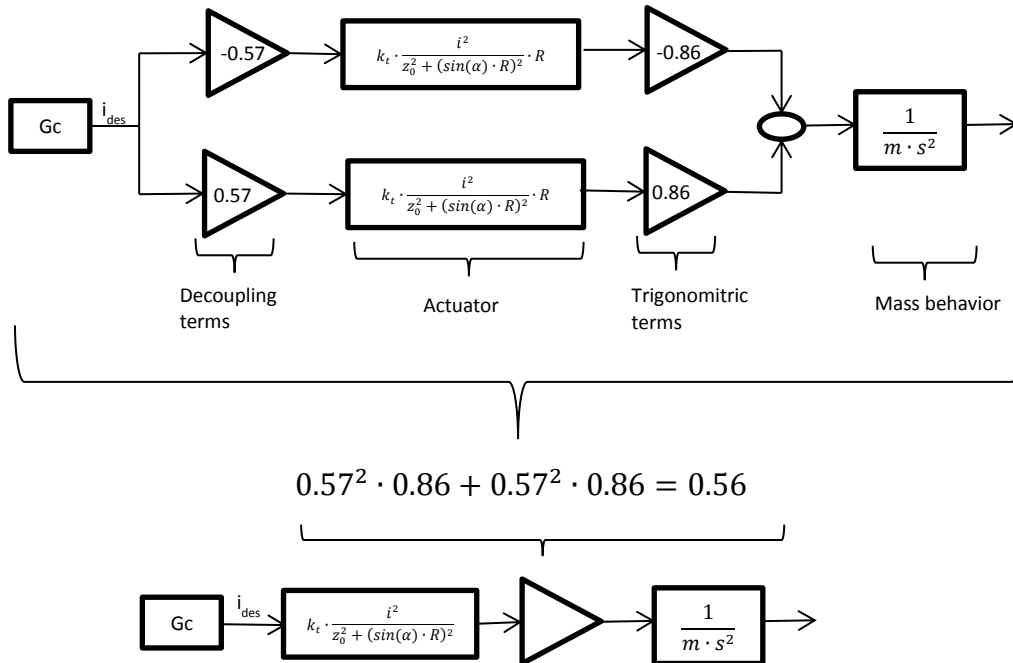


Figure 90 System representation for linearization of the Roll axis

In a stationary case, there is no constant electric current required to keep the rotor in its angle position (Equation 3-35). But as there is a current through the actuators because of the

### Three axis magnetic bearing

Z axis, these values have to be added, which results in the same electrical current used for linearization of the Z axis.

$$0 = k_t \cdot \frac{i^2}{x0^2 + (\sin(\alpha) \cdot R)^2} \rightarrow i_0 = 0 \quad \text{Equation 4-42}$$

The system is linearized for a distance between rotor and actuators of 1 mm and a Pitch and Roll angle of 0°. As described in the linearization of the Z axis the D/A voltage to current factor has to be multiplied for comparison of the measurements to the modeled behavior. The system linearization is shown below.

$$T_a = \frac{\partial f}{\partial \varphi} \bigg|_{\varphi_0, i_0} \cdot \Delta \varphi + \frac{\partial f}{\partial i} \bigg|_{\varphi_0, i_0} \cdot \Delta i$$

$$\frac{-2 \cdot R^3 \cdot k_t \cdot i_0^2 \cdot \cos(\alpha) \cdot \sin(\alpha) \cdot 0.55}{(R^2 \cdot (\sin(\alpha))^2 + z0^2)^2} \cdot \Delta \varphi + \frac{k_t \cdot i_0 \cdot R \cdot 0.55 \cdot Vtol}{z0^2} \cdot \Delta i = J \cdot \ddot{\varphi}$$

$$G_{Pitch} = G_{Roll} = \frac{\varphi}{i} = \frac{\frac{k_t \cdot i_0 \cdot R \cdot 0.55 \cdot Vtol}{z0^2}}{J \cdot s^2 + \frac{2 \cdot R^3 \cdot k_t \cdot i_0^2 \cdot \cos(\alpha) \cdot \sin(\alpha) \cdot 0.55}{(R^2 \cdot (\sin(\alpha))^2 + z0^2)^2}}.$$

$$\text{Equation 4-43}$$

To increase the accuracy of the model the voltage to current behavior of Equation 4-24 is multiplied to the state space representation above. The following figure shows the calculated bode plot of the linearized system.

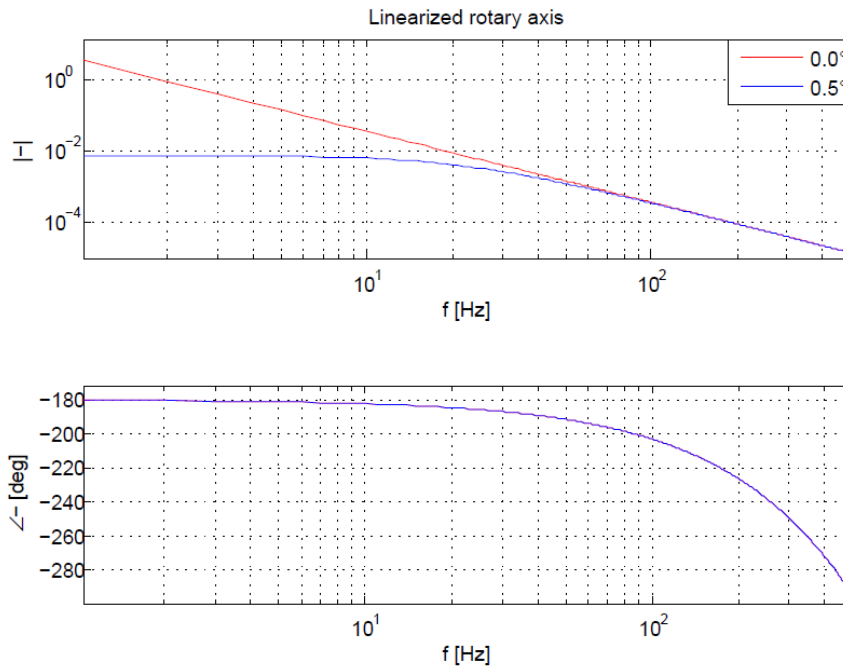


Figure 91 Linearized bode plot for rotary axis

It can be seen, that there is no negative spring stiffness of the system for an angle of  $0^\circ$ . In the real application it has to be taken into account, that angle error due to the accuracy of the sensors and error in the whole setup are likely, which creates spring stiffness in the system. Figure 91 shows a bode plot of the linearized rotary axis for  $0^\circ$  and  $0.5^\circ$  angle in one axis. It can be seen, that the crossover frequency for the controllers in a range between 30 Hz and 100 Hz has to be achieved in order to design a stable system.

### 4.4.2.4 Frequency Response measurement of the System

To verify, that the system behaves like the linearized model, the frequency response of the magnetic bearing is measured for every axis. The measurement is done using the LabVIEW DSA tool written at MIT in the Precision Motion Control Lab.

As the system is open loop unstable, the frequency response has to be measured under closed loop conditions. The DSA tool has to be implemented in LabVIEW as it can be seen in Figure 92. The tests are done according to Table 11 in the appendix.

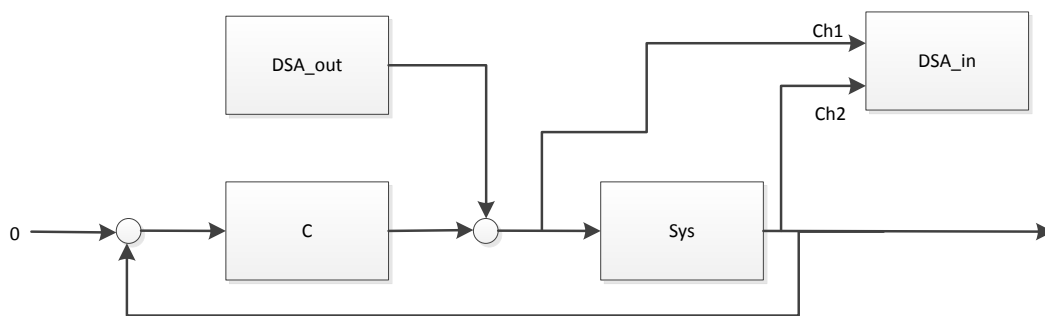


Figure 92 DSA system response measurement

#### 4.4.2.4.1 Z axis

In a first step, the system behavior of the Z axis has been measured and compared to the linearized model of chapter 4.4.2.3.1. Figure 93 shows the modeled and measured system behavior.

It can be seen, that there is a good comparability between the modeled and measured behavior. The calculated spring stiffness is nearly the same than the modeled one. In the measurement a factor of 0.85 between measurement and model can be approximated. This error of 15 % is an good difference between model and setup, as this error is already seen in the qualification of the actuators.

There are differences in the phase delay. As it can be seen in appendix 10.2 there is a phase lag which appears during a DSA measurement. This can describe the measured phase difference. Also the dynamic behavior of the reflective sensors has not been measured.



### Three axis magnetic bearing

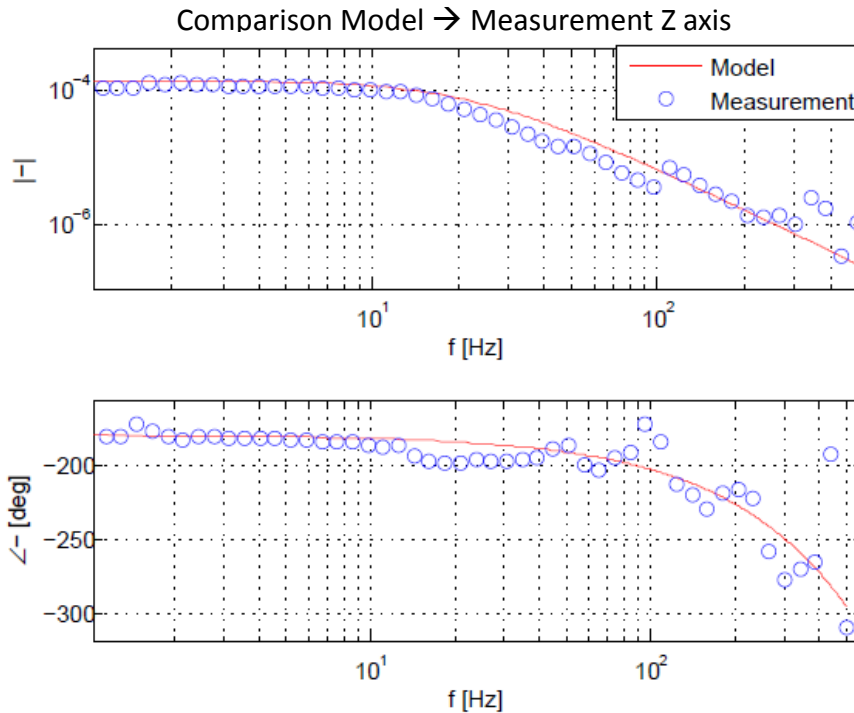


Figure 93 Z-Axis measured and calculated frequency response

#### 4.4.2.4.2 Pitch axis

The frequency response of the Pitch axis has been measured and compared to the linearized model of chapter 4.4.2.3.2. Figure 94 shows the modeled and measured system behavior.

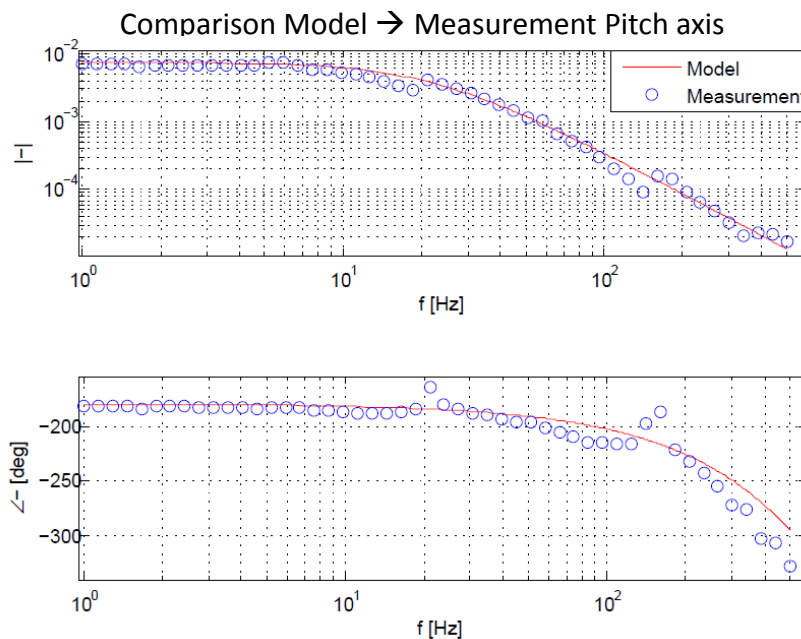


Figure 94 Pitch-Axis measured and calculated frequency response

By comparing the figure, the angle error created by measuring errors of the sensors and angle errors of the whole setup has not been known. This error affects the spring stiffness of

the system, but the mass line remains constant. By iteratively changing the modeled angle error, it turned out, that for an error of  $0.5^\circ$  there is a good comparability between measured and modeled behavior. Still there is a difference of 10 % between the measured behaviors which states a good comparability. Possible reasons are the lower force which has already been measured in the qualification of the actuators.

### 4.4.2.4.3 Roll axis

The frequency response of the Roll axis also has been measured and compared to the linearized model of chapter 4.4.2.4.2. The following figure shows the modeled and measured system behavior.

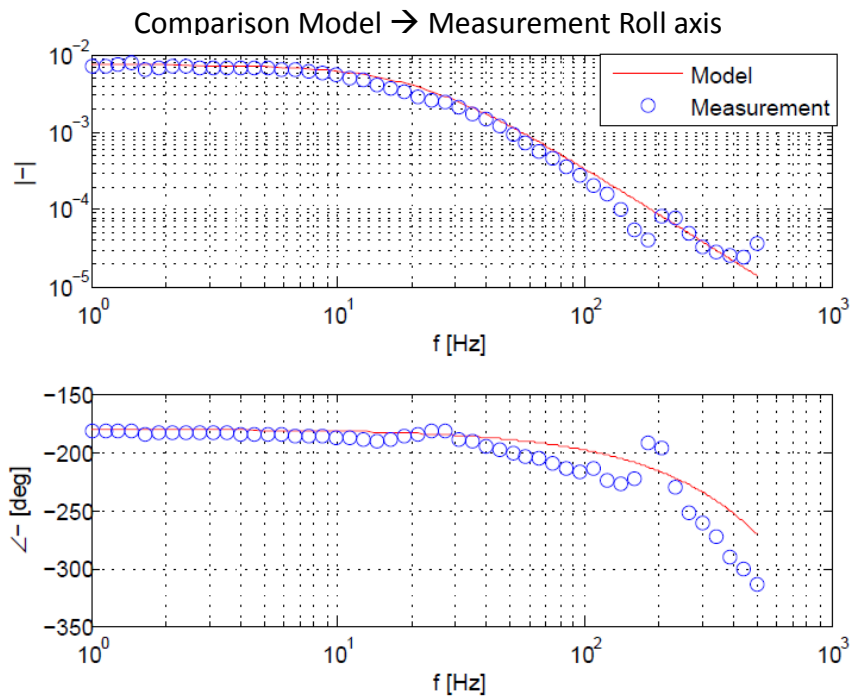


Figure 95 Roll-Axis measured and calculated frequency response

For comparing the two graphs, the modeled rotor angle has been adjusted iteratively as described in the section above. For an angle error of  $0.5^\circ$  a good comparability between modeled behavior and measurement can be seen.

In this measurement a 10 % error between measured and expected behavior can be seen, which states a good comparability between model and measurement.

### 4.4.3 Controller tuning

#### 4.4.3.1 Z axis controller

Based on the modeled and measured system behavior, the Z axis PID controller is designed to achieve a crossover frequency of 60 Hz with a phase margin of 40°.

The integrator frequency is designed to be smaller than 1/10 of the crossover frequency, to avoid a phase drop due to the phase of the integrator term. For  $\omega_i$  a value of 1 Hz is chosen. The integrator term of the controller causes a phase drop of 1° at the crossover frequency and can be neglected. As this system has negative spring stiffness the integral part is required to achieve stationary accuracy on the system.

The factor of the proportion gain  $K_p$  of the controller is adjusted based on the return ratio shown in Figure 96 to be 22000. The equation of a PI controller is shown in Equation 3-48. A lead-lag compensator according to Equation 3-49 is designed to lift the phase in the region of the crossover frequency.

With the two frequencies  $\omega_{lead}$  and  $\omega_{lag}$  the phase lift can be adjusted. The lead compensator is adjusted to have a maximum phase lift at 70 Hz. The lead frequency is set at 20Hz, and the lag frequency at 220 Hz.

Figure 96 shows the bode plot of the return ratio. Also the frequency response of the system is shown. It can be seen, that a crossover frequency of 62 Hz is achieved with a phase margin of 42°. At this frequency a phase drop caused by the sampling rate of the system of 11° has to be compensated.

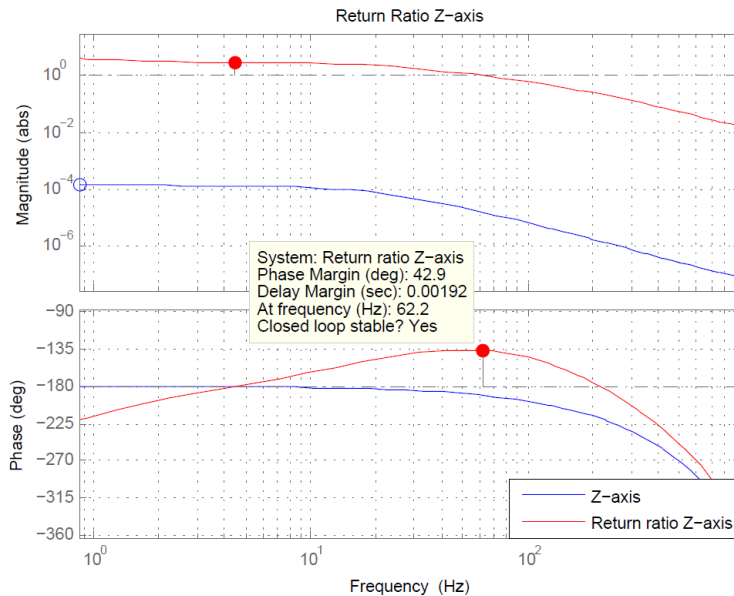


Figure 96 Return Ratio Z-axis

#### 4.4.3.2 Return Ratio measurement of the Z axis controller

To verify the stability of the system in the Z-axis, the return ratio has been measured and analyzed regarding its gain and phase margin. The measurement is done using the already described DSA tool.

For the measurement of the return ratio, the excitation signal of the DSA is added after the controller into the system. The channel Ch1 and Ch2 measures the loop transmission in front and after the excitation signal as shown in Figure 97. A detailed specification of the test can be found in Table 17 in the appendix.

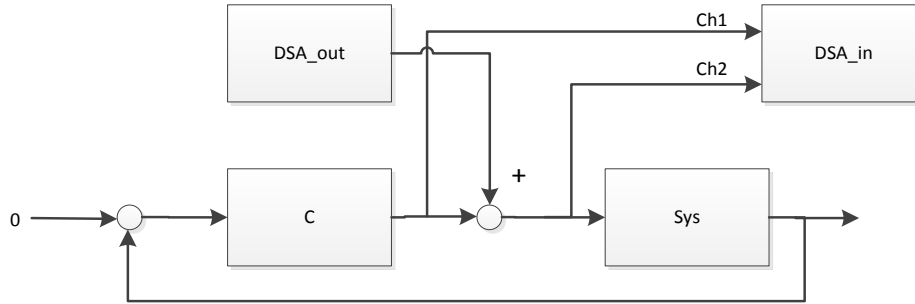


Figure 97 DSA return ratio measurement

By analyzing the measured frequency response shown in Figure 98, it can be seen that a crossover frequency of 35 Hz with a phase margin of 35° is achieved. These values show a stable behavior of the controller even if the desired parameters of 60 Hz crossover frequency and 40° phase margin are not achieved. Between the measurement and the expected model behavior an error of 20 % is measured. As the error in the system measurement has already been 15 % error there is a good comparability between model and setup.

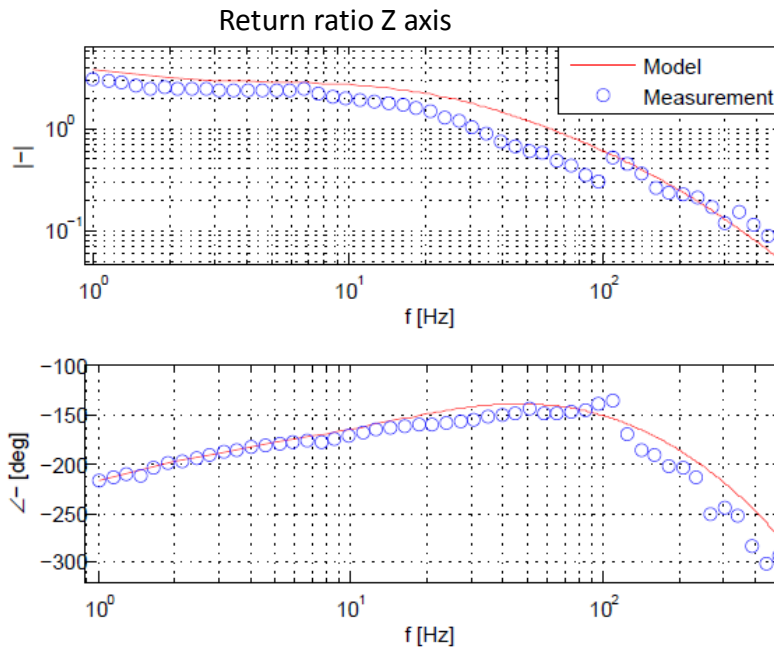


Figure 98 Measured frequency response of the Z-axis

The actual phase of the system is expected to be a bit higher than the measurement due to phase lag caused by the measurement of the DSA tool.

### 4.4.3.3 Rotary axis controller

The controllers for the Pitch and Roll axis have been designed the same way than the Z axis. A PI controller and a lead-lag compensator have been chosen to achieve a phase margin of  $40^\circ$ . The crossover frequency is adjusted to be 50 Hz. The modeled return ratio of the rotary axes is shown in the following figure.

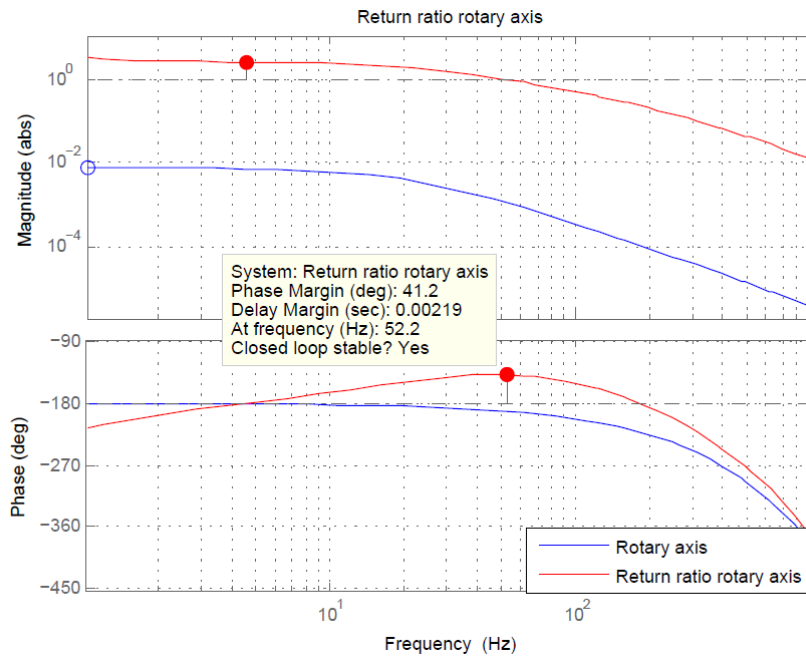


Figure 99 Return Ratio rotary axis

Based on the modeled system behavior, the controller has been adjusted to have the same lead compensator which is used in the Z axis. The integral term is set to be 1 Hz to avoid a phase drop at the crossover frequency. The controller has been adjusted based on the model of the linearized rotary axis using an angle error of  $0.5^\circ$ . Figure 99 shows the expected return ratio of the rotary axis for a gain factor  $K_p$  of 350.

### 4.4.3.4 Return ratio measurement of the Pitch axis controller

The return ratio of the Pitch axis has been measured in the same way, described for the Z axis. As it can be seen in Figure 100, the measurement shows a good comparability between expected behavior and measurement. Nevertheless there is a factor of roughly 0.8 between model and measurement. So the error in this measurement is 10 % higher than in the measurement of the Pitch axis.

## Three axis magnetic bearing

With the designed controller a crossover frequency of 40 Hz with a phase margin of  $30^\circ$  is achieved. This shows that this axis is controlled stable, even if the phase is  $10^\circ$  smaller than expected.

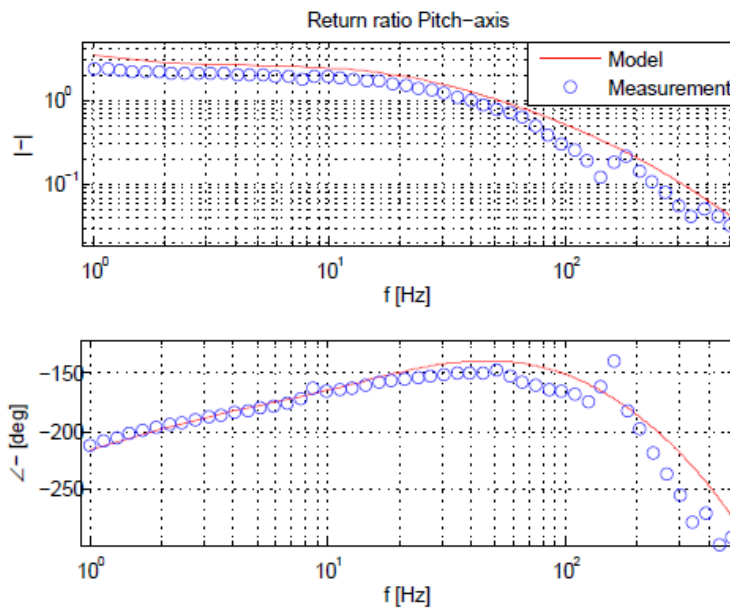


Figure 100 Measured frequency response of the Pitch axis

### 4.4.3.5 Return ratio measurement of the Roll axis controller

Figure 101 shows the frequency response measured for the Roll axis. As in the measurements of the other axis, the system shows a good comparability between expected and modeled behavior. Between model predictions and actual measurement a factor of 0.9 can be measured which is similar to the error of the measurement of the Roll axis. This results in a lower crossover frequency of 40 Hz and a phase margin of  $30^\circ$ .

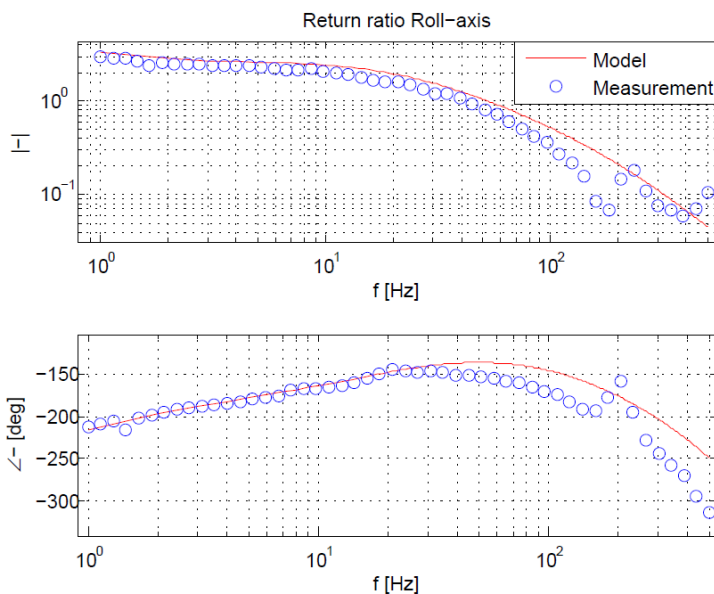


Figure 101 Measured frequency response of the Roll axis

#### 4.4.4 Measurement of the system behavior for different axes

To verify, that the axes can be adjusted separately by using the designed control structure the control efforts of the three controlled axis for a varying position in on axis is measured. If the system work decoupled, the control effort of the unactuated axes is significantly lower than the actuated one.

The test is done by connecting the output of the DSA tool to the desired position of one axis. The DSA tool measures the desired position and the controller effort of this axis as shown in Figure 102. In a second step, the control effort of the two other axes is measured. The test is specified in Table 16 in the appendix.

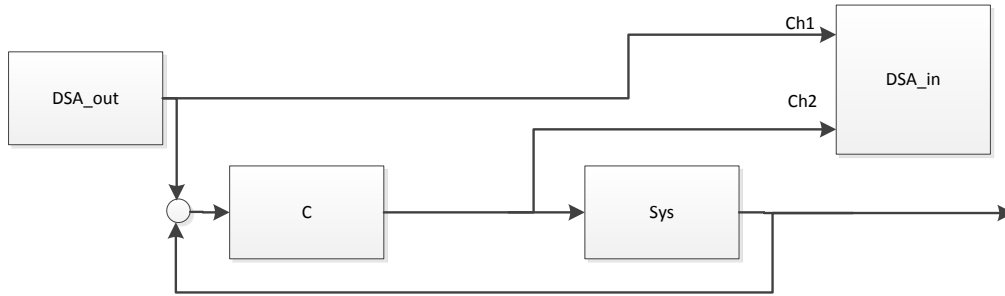


Figure 102 Frequency response measurement for decoupling verification

The measured frequency response of the actuated axis can be described with the following transfer function which is also compared to the measured system behavior:

$$G_{controller} = \frac{C}{1 + C \cdot sys} \quad \text{Equation 4-44}$$

By analyzing the measured bode plots in Figure 103, Figure 104 and Figure 105 the decoupling behavior of the system can be seen. For small frequencies a decoupling with a factor of roughly 50 can be measured. In the region of 20 – 100 Hz the decoupling factor decreases. Reasons for this behavior have not been found yet. For frequencies higher 80 Hz the decoupling between the different axes gets better. This behavior is the same for the measurement of all three axes.

Also the control effort for every axis has been compared to the expect control effort based on the model calculation. It can be seen, that there is a good comparability between the modeled control effort and the measurement. In the region between 20 Hz and 100 Hz there are bigger differences between model and measurement. Reasons can be the decreasing decoupling factor in this range. The phase of the actuated axis shows the same lag behavior which has been seen in the measurement of the system. The phase of the non-actuated axis shows a big phase delay. This behavior has not been studied yet and is not important for the rating of the decoupling.

Three axis magnetic bearing

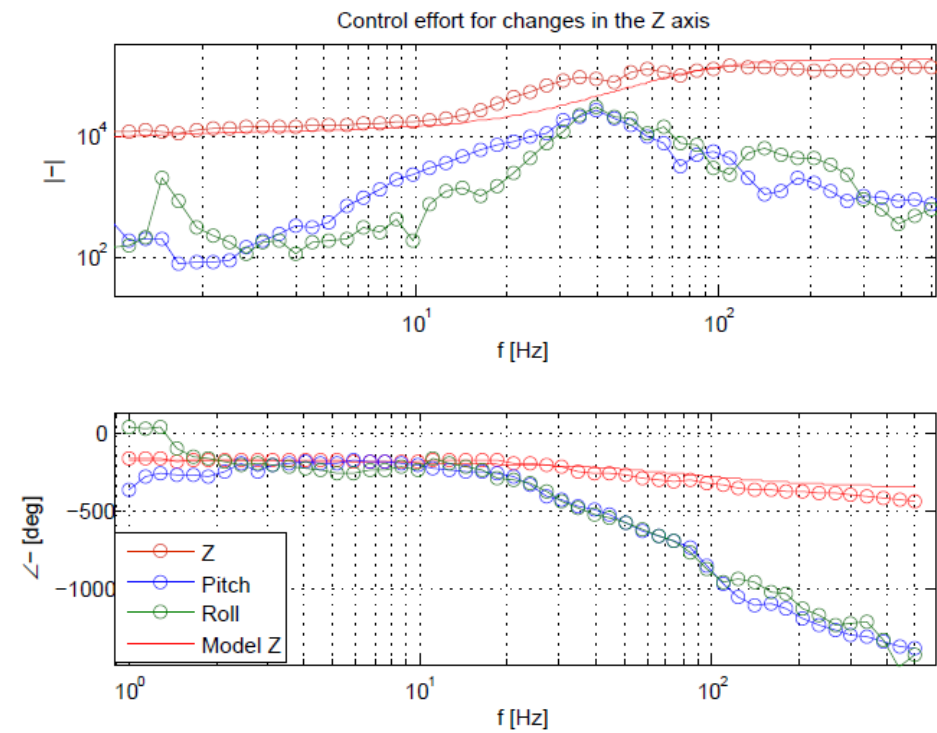


Figure 103 Control efforts for changes in the Z axis

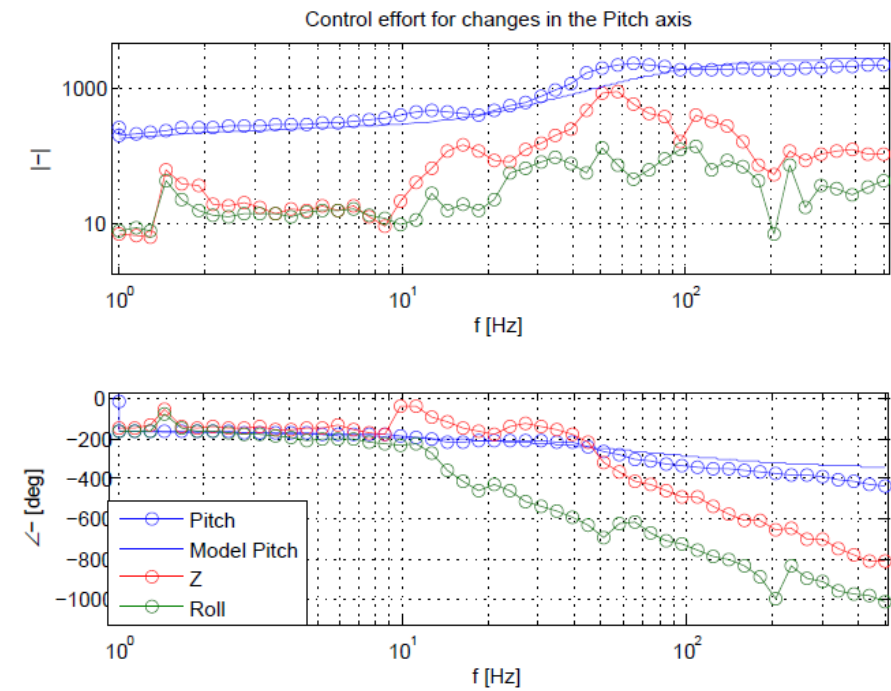


Figure 104 Control efforts for changes in the Pitch axis



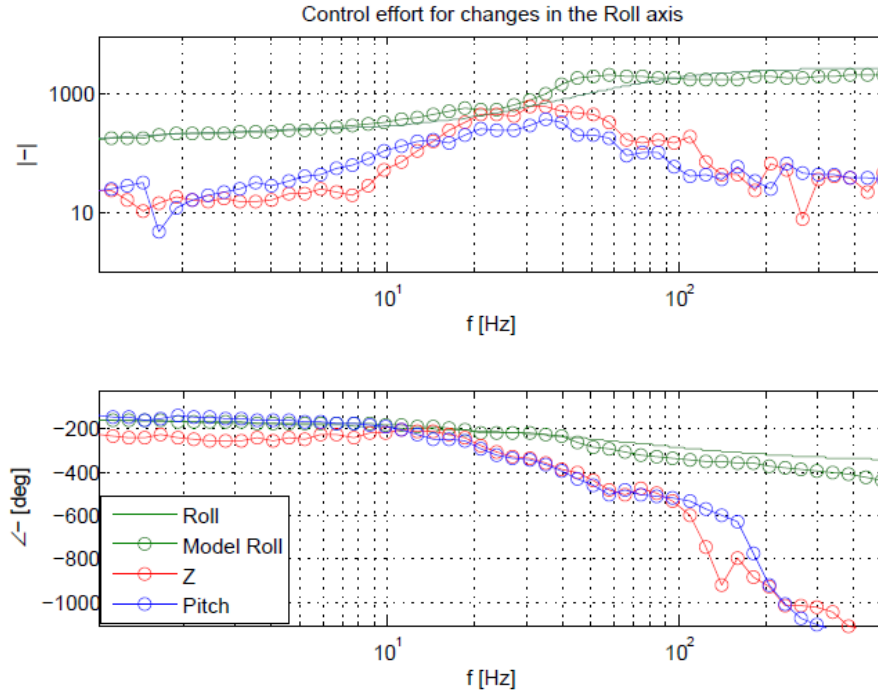


Figure 105 Control efforts for changes in the Roll axis

### 4.5 LabVIEW implementation

The different algorithms and controllers are implemented on the NI myRIO system. By implementing in the real-time system it is very important to keep the performance of the system high in order to have a small phase delay due to sampling.

The sensor signal preprocessing including the sensor reading of the analog values, filtering, calculation of the axis parameters and the decoupling algorithms are implemented on the integrated FPGA. The loop of the FPGA runs with a sampling rate of 100 kHz. This implementation has been done with fixed point arithmetic's. By programming with LabVIEW FPGA it has to be taken into account that the compilation of the code into hardware language takes up to 1.5 h, so the iterations of the program test should be reduced.

The PID controllers for each axis are implemented on the microcontroller of the myRIO system, which runs with a sampling rate of 2 kHz. With this sampling frequency the phase drop in the desired crossover frequency range is low. Also the DSA tool for measuring the frequency responses and return ratios of the system is implemented on the microcontroller.

To avoid higher time delays due to sampling, the program has to be processed in the right order. This is done by error handling and the use of sequences.

## 5 Magnetic bearing for two additional axes

In chapter 4 a model of a three axis controlled active magnetic bearing has been developed and verified. In this chapter, a magnetic bearing for the two remaining additional axes which results in a five DOF magnetic bearing based on the concept of section 2.6 is developed in section 5.1. A rotor based on the requirement for the magnetic bearing is designed in section 5.2. The actuators for the additional bearing are designed (section 5.3). A dynamic model is build, which is used to design a control structure of the horizontal axes (section 5.4). In a final step the functionality of the bearing is verified.

### 5.1 Detailed design horizontal axes bearing

This design adds three additional reluctance actuators around the rotor disc according to concept of chapter 2.3 which work antagonistically. With these actuators, positive and negative forces in the X and Y axis can be applied to keep the rotor in its desired position. A CAD drawing of the five DOF bearing is shown below.

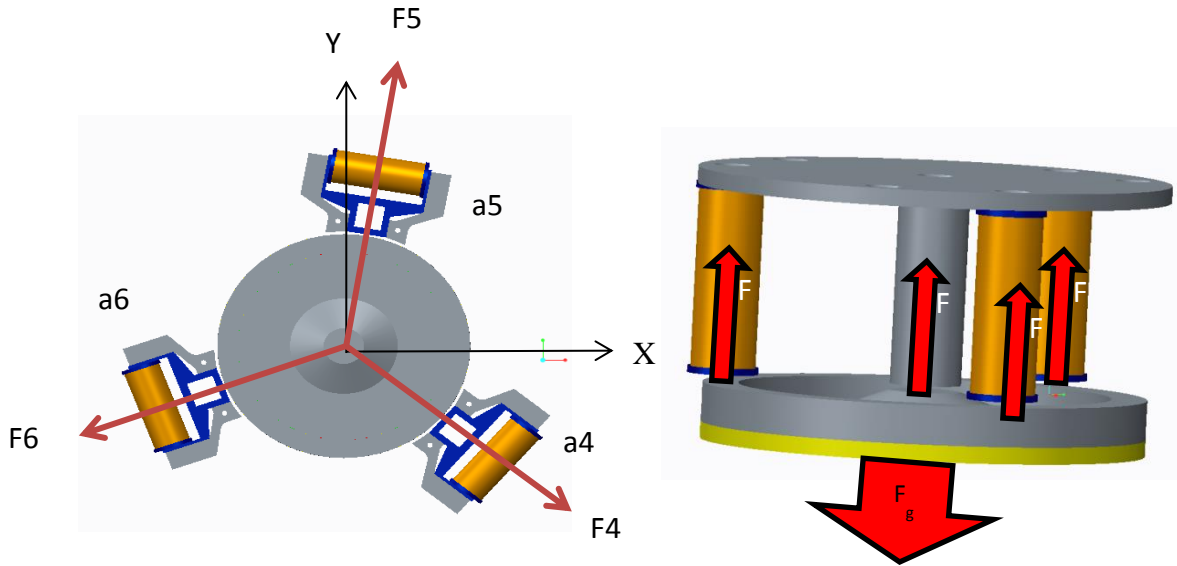


Figure 106 Actuators and forces of a 5 DOF bearing

The actuators are designed the same way than the actuators used in the three axis bearing by analyzing the magnetic flux. For the iron which is used in the magnetic circuit a ferromagnetic material with a high permeability (C45) is chosen. To keep the points of actuation close together, the distances between both force generating part if the actuator is set to be small.

The actuators are attached to the 3D printed staged shown in Figure 71 by a 3D printed casings which can be seen in the figure above. The CAD files for manufacturing the actuators are attached in the appendix.

For controlling the axis of the rotor an accurate measuring of the rotor position is required. As the reflective sensors which are used for testing the three DOF magnetic bearing has

turned out to work accurate, they are used in the same way for measuring the X and Y axis. The sensors are placed according to the concept of 2.4.2.

### 5.2 Detailed rotor design for magnetic bearing

To achieve the defined goals of the rotor design (section 2.5) which are a low mass, a smooth surface between rotor and motor magnets, a big enough surface for interaction with the reluctance actuators, low cogging between actuators and rotor as well as the actuator acting at the center of gravity, a detailed design for the rotor needs to be done. Three different concepts have been developed to achieve these goals.

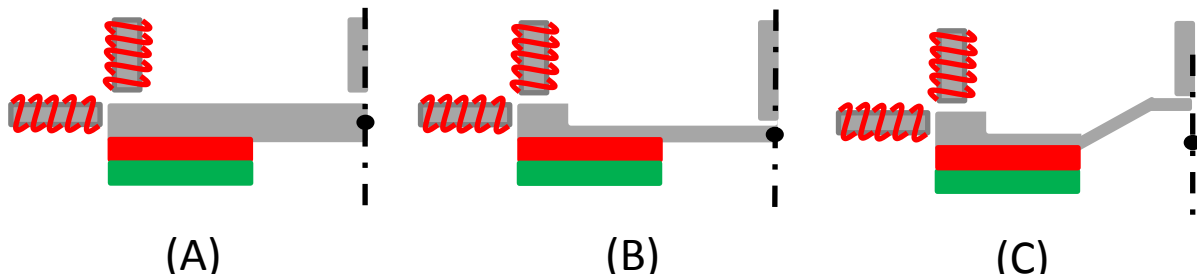


Figure 107 Detailed rotor design concepts

All the developed concepts have a smooth surface for the motor magnets, that there is no additional resistance the magnetic flux of the permanent magnets. The iron of the rotor needs a height which is at least the height of the horizontal axis actuators. Nevertheless a bigger height is desired to reduce a cogging between rotor magnets and horizontal actuators. When an additional distance of 4 mm between magnets and actuators is designed the cogging torque can be reduced by a factor higher than three. In concept (A) these requirements are solved by using a thick steel disc. Unfortunately the weight of the rotor increases significantly with a full metal steel disc. For this reason in concept (B) there is only the outer ring of the rotor built out of solid steel. The downside of this concept is, that the center of gravity is lowered, which increases the coupling between the horizontal and vertical axes. This leads to concept (C) where the center of gravity is lifted by increasing the height in the middle of the rotor.

Concept (C) is chosen to be designed. Figure 108 shows a CAD drawing of the designed rotor. Nevertheless, it is not possible to lift the center of gravity fully into the axis of actuation of the horizontal actuators using this concept. The remaining couplings to the vertical axes are calculated in section 5.4.1.4.

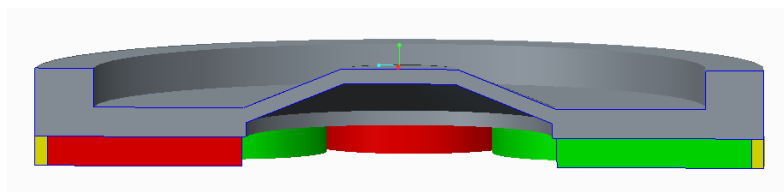


Figure 108 Rotor design for low coupling

## Magnetic bearing for two additional axes

For measuring the rotor position, in the horizontal axes, it is important that the outer side of the rotor has a smooth surface. The measurement of the sensors would be disturbed by the varying distances of the permanent magnets. To get a constant surface at the outer radius of the rotor a plastic disc has been 3D printed which can be mounted around the rotor. This way, the rotors measures against a constant surface.

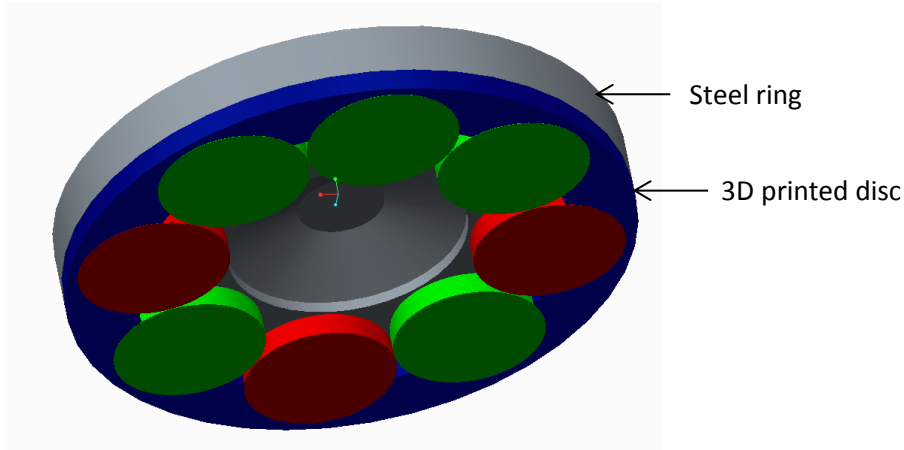


Figure 109 Rotor with 3D printed ring for a constant surface

A picture of the manufactured motor with magnetic bearings is shown in the following picture. The different actuators and their placement on the setup can be seen. The whole setup is mounted on a plastic plate. It is important, that no ground plate with high electric conductivity is used, as this decreases the rotor speed due to eddy currents significantly.

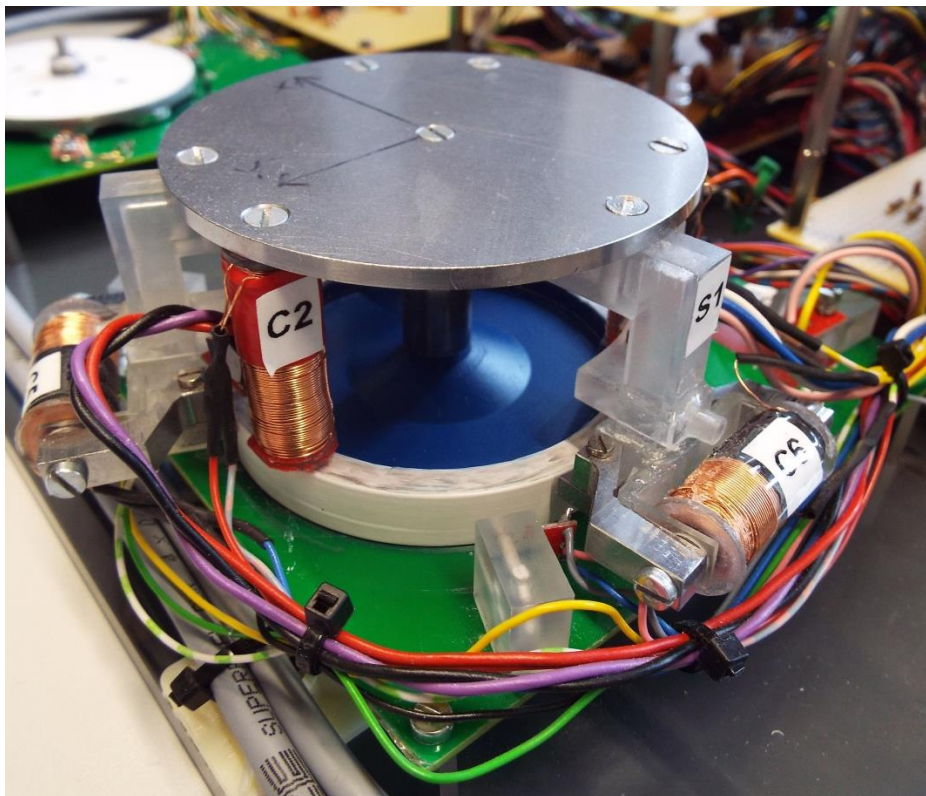


Figure 110 Final motor and bearing design



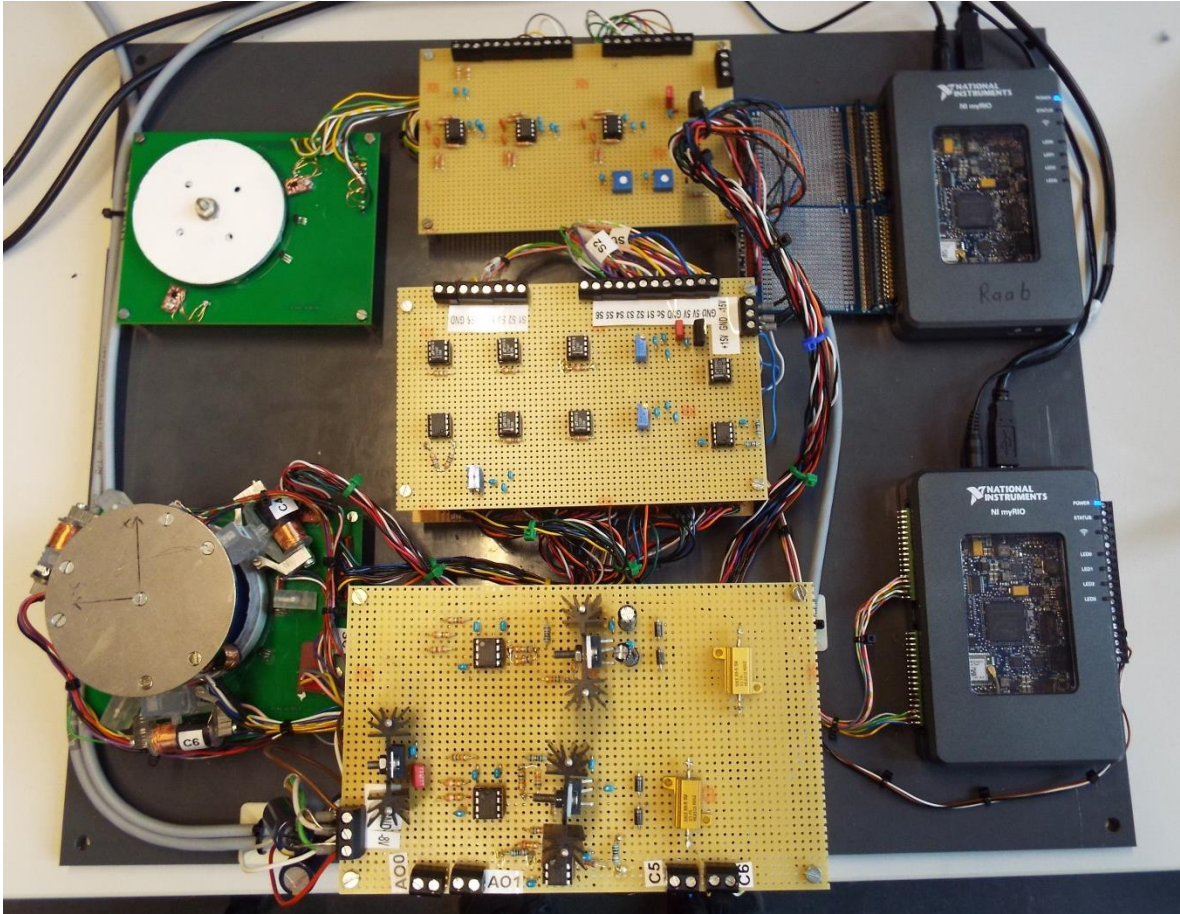


Figure 111 Figure of the final motor setup

### 5.3 Actuators

To keep the rotor in a stable X and Y position, three reluctance actuators are placed around the rotor disc as it can be seen in Figure 106. These actuators work in an antagonistic way. The following subchapter focuses on the design and testing of these actuators.

#### 5.3.1 Actuator design

When the rotor is levitated in its middle position, a distance between rotor and actuators of 1 mm is designed. The actuator forces will be designed for this distance.

Because of manufacturing error, imbalances because of an eccentricity of the center of gravity can appear which causes imbalance forces. The eccentricity of the rotor is estimated to be smaller than 0.02 mm (this is an eccentricity which would apply by adding two grams at the outer radius of the rotor) due to a precise manufacturing of the different parts and the mounting tools. The imbalance forces created by the rotor can be calculated using the following equation [33].

$$F_{\text{imbalance}} = m \cdot e \cdot \omega^2 \quad \text{Equation 5-1}$$

## Magnetic bearing for two additional axes

Using the mass of the rotor and a speed of 3000 rpm (314rad/s) an imbalance force of 0.37 N appears. It can be seen, that this force is in the same range, than the required force of the vertical axes actuators. The actuators are designed to keep the rotor in its middle position with a force of 0.5 N and a current of 0.5 A. Using this current values the same the same power opamps which are used the vertical axes can be used.

The actuators are designed based on the analysis of the magnetic circuit. When analyzing the magnetic circuit to calculate the actuator forces, only the resistances of the air gaps are taken into account. The ferromagnetic materials are estimated with an infinite permeability. The following figure shows the designed actuator.

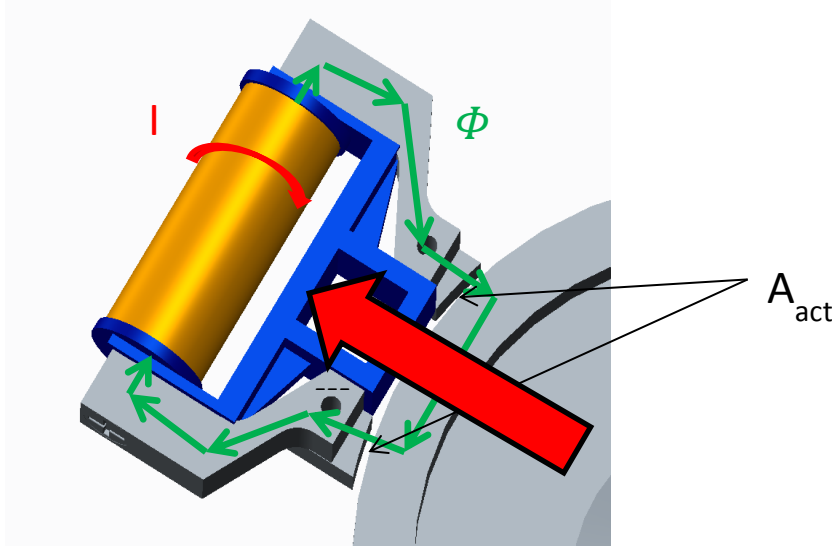


Figure 112 X, Y axis actuator

The cross section  $A_{act}$  is designed to have a high of 4 mm and a length of 6 mm in order to keep the distance between rotor magnets and actuators high and to avoid high flux densities in the actuator

As a simplification it is assumed, that the distance in the air gaps of the actuators are the same. According to 4.3.1.1 the force of the actuator can be calculated with the following equation

$$F_{act} = k_x \cdot \frac{I^2}{x^2} \quad \text{Equation 5-2}$$

The variable  $k_x$  is an actuator specific constant which can be calculated by using Equation 3-5 to Equation 3-7 as well as Equation 4-1 and Equation 4-2. This results to the following factor for  $k_x$ .

$$k_x = \frac{A_{act} \cdot N^2 \cdot \mu_0}{4} \quad \text{Equation 5-3}$$

When  $N=550$  turns are used in the actuator a force of  $0.57\text{ N}$  is created for the specified distance of  $1\text{ mm}$  between actuator and rotor. This leads to a  $k$  value of  $2.28\text{e-}6 \frac{\text{N}\cdot\text{m}^2}{\text{A}^2}$ .

### 5.3.2 Actuator test

The designed actuators have been tested and compared to the expected behavior. As a test, an additional force in X and Y direction has been added as shown in Figure 113. This has been done by connecting a wire with a weight at the other side to the rotor. To create only forces in the X, Y plane and to reduce friction, a deflection pulley is used.

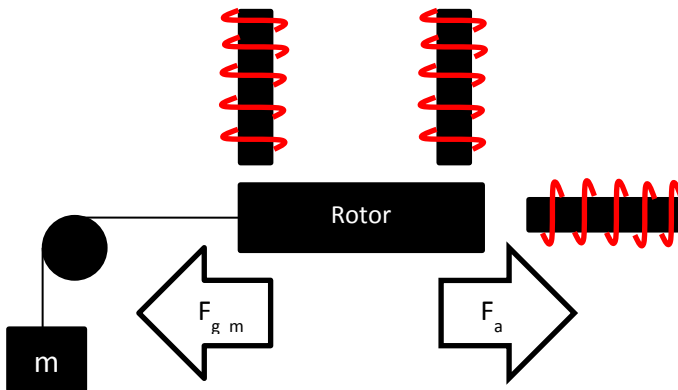


Figure 113 Actuator test setup

The rotor is centered in its middle position of the system by the closed loop control of the magnetic bearings. The distances have not been varied, as the rotor is spinning in the middle position in normal actuation.

By adding different forces to the rotor, the current, through the actuators increases. This increase can be measured with an oscilloscope which is connected at the current sensing resistance of the actuator. This current is compared to the expected values.

The following figure shows the measured and expected behavior of the actuator for a distance of  $1.2\text{ mm}$  between rotor and actuator.

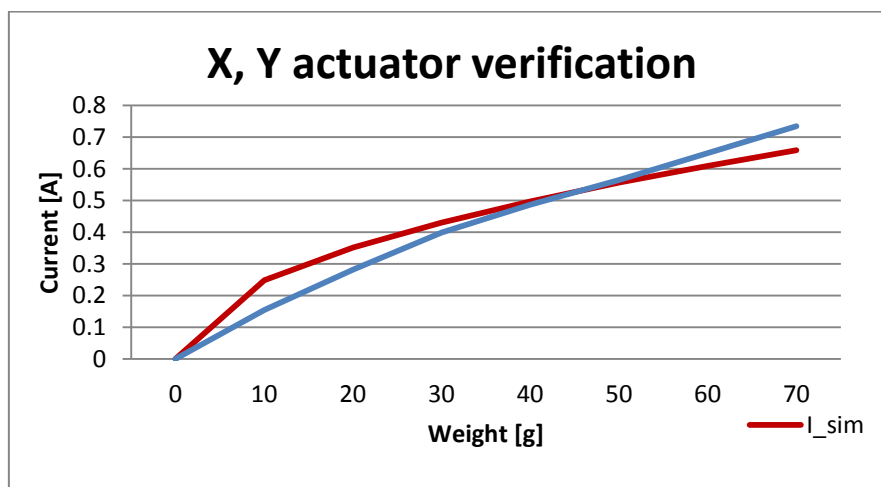


Figure 114 X,Y actuator design verification

## Magnetic bearing for two additional axes

It can be seen, that the currents which are needed to keep the rotor in its position are in the same range than the expected ones. Nevertheless the measured behavior does not totally fit to the expected current function. Reasons for the differences can be friction in the measurement setup. Friction can explain the lower current which is required for small forces.

### 5.3.3 Electronics design

For the horizontal axes, the same power and sensing electronics can be used as for the vertical axis, as the horizontal actuators have nearly the same characteristics than the vertical actuators.

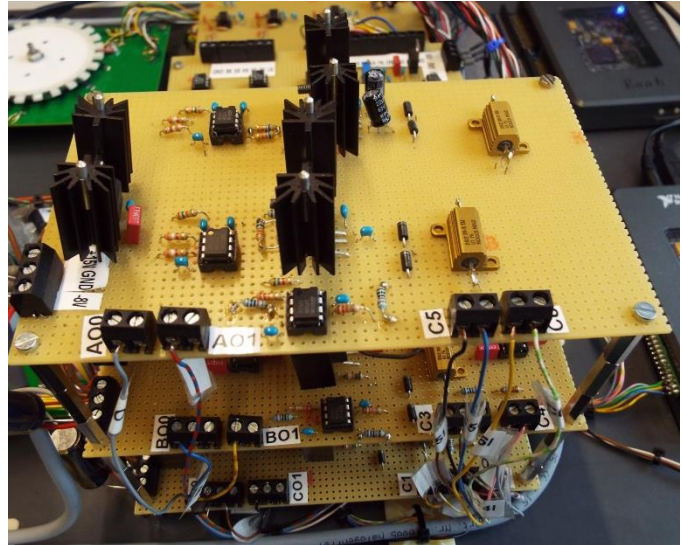
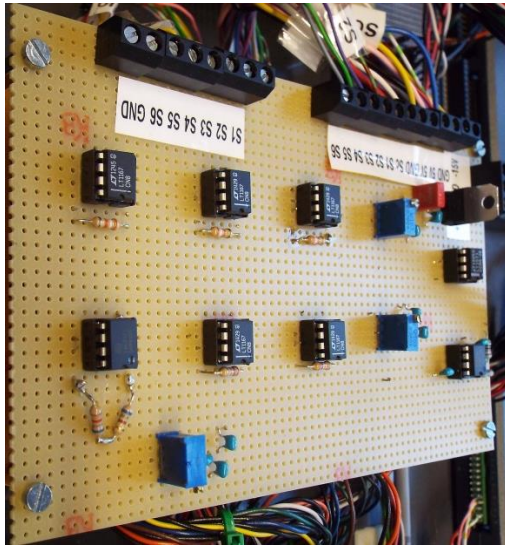


**Figure 115 Sensor and power electronics**



## 5.4 Modelling and control

This chapter focuses on the modelling of the dynamics of the horizontal axes, in order to control of the X and Y position of the rotor. The model is split in two main sections. The modeling of the system behavior is described in a first section, and design of a control structure for Cartesian coordinates in a second section. The top-level of the model it is indicated in the following figure.

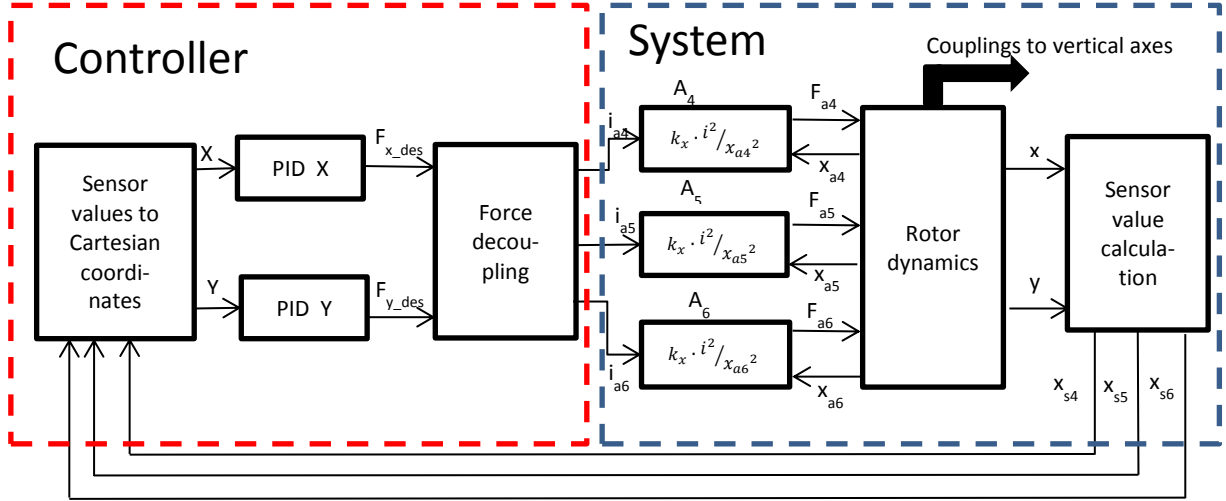


Figure 116 Modeled of the horizontal axes

### 5.4.1 System model

#### 5.4.1.1 Force and dynamics model

For modeling the rotor dynamics in the X and Y axis, the force created by each coil is calculated and analyzed. The forces created by each actuator can be determined using the distance between rotor and actuator and the current in the actuator.

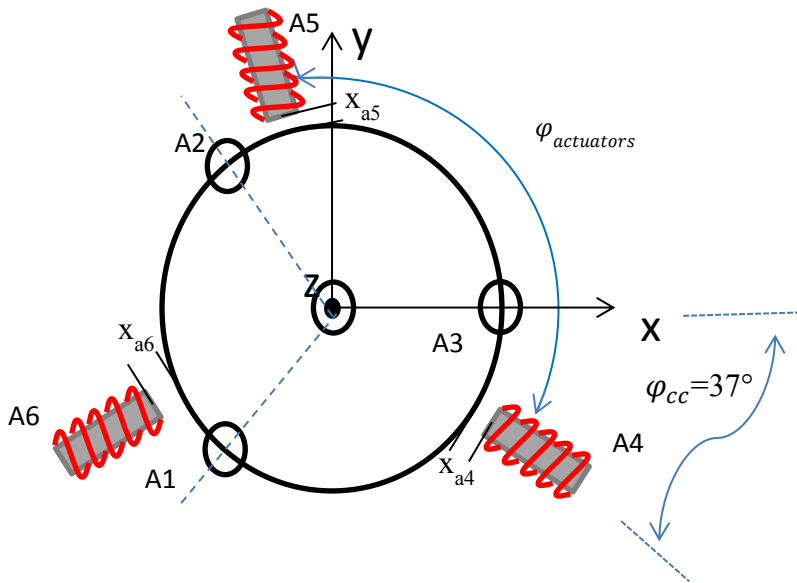


Figure 117 Forces in X and Y axis

## Magnetic bearing for two additional axes

The sum of forces in the X and Y direction yields to the following terms, where  $\varphi_{cc}$  is the angle between the vertical axes actuators and the horizontal actuators.

$$\begin{aligned} F_x &= F_{A4} \cdot \cos(-\varphi_{cc}) + F_{A5} \cdot \cos(120 - \varphi_{cc}) + F_{A6} \cdot \cos(240 - \varphi_{cc}) \\ F_y &= F_{A4} \cdot \sin(-\varphi_{cc}) + F_{A5} \cdot \sin(120 - \varphi_{cc}) + F_{A6} \cdot \sin(240 - \varphi_{cc}) \end{aligned} \quad \text{Equation 5-4}$$

Equation 5-4 can be transformed into matrix notation. This is shown in Equation 5-5

$$\mathbf{F}_{axisxy} = \mathbf{A}_{actuator\ to\ axisxy} \cdot \mathbf{F}_{Actuatorxy} \quad \text{Equation 5-5}$$

$$\begin{bmatrix} F_x \\ F_y \end{bmatrix} = \begin{bmatrix} \cos(-\varphi_{cc}) & \cos(120 - \varphi_{cc}) & \cos(240 - \varphi_{cc}) \\ \sin(-\varphi_{cc}) & \sin(120 - \varphi_{cc}) & \sin(240 - \varphi_{cc}) \end{bmatrix} \cdot \begin{bmatrix} F_{A4} \\ F_{A5} \\ F_{A6} \end{bmatrix}$$

The X, Y dynamic for both axis can be calculated using the kinematic functions (Equation 5-6). The acting mass of the rotor has been measured to be 186 g.

$$\begin{aligned} F_x &= m \cdot \ddot{x} \\ F_y &= m \cdot \ddot{y} \end{aligned} \quad \text{Equation 5-6}$$

Using these equations and the Laplace transformation, the position in the X and Y axis is calculated as shown below.

$$\begin{aligned} \frac{x}{F_x} &= \frac{1}{m \cdot s^2} \\ \frac{y}{F_y} &= \frac{1}{m \cdot s^2} \end{aligned} \quad \text{Equation 5-7}$$

### 5.4.1.2 Sensor value calculation

To get a model which represents the actual setup, the distances between sensors and rotor have to be calculated based on the calculated Cartesian rotor position.

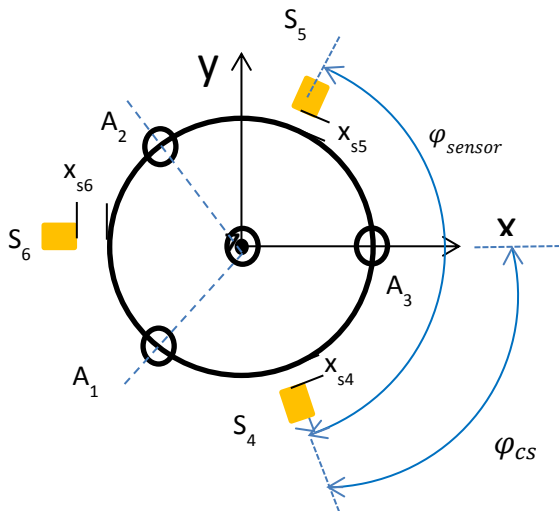


Figure 118 Sensor positions of the horizontal axes

The angle  $\varphi_{sensor}$  between each sensor is  $120^\circ$  and the angle between the reluctance actuators (A4 to A6) and the sensors is  $\varphi_{cs}$  is  $63^\circ$ . Using these angles, the distance between each sensor and the rotor is calculated for with following equation.

$$\begin{aligned} x_{s4} &= x \cdot \cos(-\varphi_{cs}) + y \cdot \sin(-\varphi_{cs}) \\ x_{s5} &= x \cdot \cos(120 - \varphi_{cs}) + y \cdot \sin(120 - \varphi_{cs}) \\ x_{s6} &= x \cdot \cos(240 - \varphi_{cs}) + y \cdot \sin(240 - \varphi_{cs}) \end{aligned} \quad \text{Equation 5-8}$$

The equations can be transformed into matrix notation with the following parameters:

$$\begin{aligned} x_1 &= x \\ x_2 &= y \\ a &= \cos(-\varphi_{cs}) \\ b &= \sin(-\varphi_{cs}) \\ c &= \cos(120 - \varphi_{cs}) \\ d &= \sin(120 - \varphi_{cs}) \\ e &= \cos(240 - \varphi_{cs}); \\ f &= \sin(240 - \varphi_{cs}) \end{aligned} \quad \text{Equation 5-9}$$

$$\begin{bmatrix} x_{s4} \\ x_{s5} \\ x_{s6} \end{bmatrix} = \begin{bmatrix} a & b \\ c & d \\ e & f \end{bmatrix} \cdot \begin{bmatrix} x_1 \\ x_2 \end{bmatrix}$$

$$\mathbf{x}_{sensors} = \mathbf{A}_{axistosensor} \cdot \mathbf{x}_{axisxy}$$

#### 5.4.1.3 Distance between rotor and actuators

The actuator force depends in the current in the actuator and the distance between actuator and rotor. The distance between rotor and actuator can be calculated with the following equations:

$$\begin{aligned} x_{a4} &= x \cdot \cos(-\varphi_{cc}) + y \cdot \sin(-\varphi_{cc}) \\ x_{a5} &= x \cdot \cos(120 - \varphi_{cc}) + y \cdot \sin(120 - \varphi_{cc}) \\ x_{a6} &= x \cdot \cos(240 - \varphi_{cc}) + y \cdot \sin(240 - \varphi_{cc}) \end{aligned} \quad \text{Equation 5-10}$$

This can also be converted into matrix notation:

$$\mathbf{x}_{actuatorxy} = \mathbf{A}_{axistoactuatorxy} \cdot \mathbf{x}_{axisxy} \quad \text{Equation 5-11}$$

$$\begin{bmatrix} x_{a4} \\ x_{a5} \\ x_{a6} \end{bmatrix} = \begin{bmatrix} \cos(-\varphi_{cc}) & \sin(-\varphi_{cc}) \\ \cos(120 - \varphi_{cc}) & \sin(120 - \varphi_{cc}) \\ \cos(240 - \varphi_{cc}) & \sin(240 - \varphi_{cc}) \end{bmatrix} \cdot \begin{bmatrix} x \\ y \end{bmatrix}$$

#### 5.4.1.4 Couplings between horizontal and vertical axes

In section 5.2 it has been shown, that the horizontal actuators will not act at the center of gravity. So an additional torque is applied into the vertical axis. Figure 119 shows the coupling between the different axes.

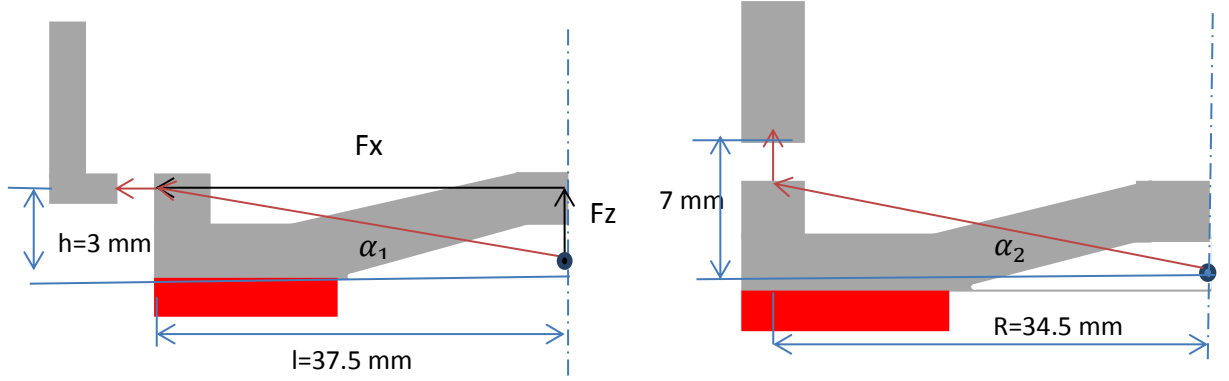


Figure 119 Coupling between X, Y and Z, Roll, Pitch axis

The angle between center of gravity and the actuator force is given by trigonometric functions.

$$\alpha_1 = \text{atan}\left(\frac{l}{h}\right) = \text{atan}\left(\frac{37.5}{3}\right) = 0.0798 = 4.5^\circ \quad \text{Equation 5-12}$$

Thus the forces in the X and Y axis can be calculated as follow.

$$\begin{aligned} F_x &= F \cdot \cos(\alpha_1) = F \cdot 0.9968 \\ F_z &= F \cdot \sin(\alpha_1) = F \cdot 0.0797 \end{aligned} \quad \text{Equation 5-13}$$

It can be seen, that the force created in the Z axis is low compared to the force in the X axis. The couplings between the X and Y axis actuators and rotary axis have to be considered. The torque created by the X and Y actuators is calculated using the following equation.

$$T_{rolldis} = F_x \cdot h = F \cdot 0.003 \quad \text{Equation 5-14}$$

The disturbance torque is compared to a torque, which is created by the Z axis actuators, when the same force is applied.

$$T_{roll} = F_z \cdot R = F \cdot 0.0345 \quad \text{Equation 5-15}$$

By comparing the two torques which are created by the same force, it can be seen, that the disturbance torque is more than a factor of ten smaller than the desired torque. This shows that the axis can be controlled independently without a decoupling in a first step.

$$\frac{T_{dis}}{T} = 8.7 \% \quad \text{Equation 5-16}$$

### 5.4.2 Controller design

In this section the transformation of the sensor values in Cartesian coordinates and the decoupling of the different actuator forces are described. Then the system is linearized in order to calculate PID controllers for the different Cartesian axis.

#### 5.4.2.1 Sensor values to Cartesian coordinates

To control the rotor position in Cartesian coordinates the rotor position needs to be calculated out of the measured rotor position. This can be done by inverting the over-determined system of equations of Equation 5-9. The axes calculation is performed as in the following equation described [34, p. 33].

$$\begin{aligned} A_{axistosensor} \cdot x_{axisxy} &= x_{sensor} \\ A_{axistosensor}^T \cdot A_{axistosensor} \cdot x_{axisxy} &= A_{axistosensor}^T \cdot x_{sensor} \\ x_{axisxy} &= (A_{axistosensor}^T \cdot A_{axistosensor})^{-1} \cdot A_{axistosensor}^T \cdot x_{sensor} \end{aligned} \quad \text{Equation 5-17}$$

This leads to the following system of equations:

$$\begin{aligned} x_{axisxy} &= A_{senstoaxisxy} \cdot x_{sensor} \\ \begin{bmatrix} x \\ y \end{bmatrix} &= \begin{bmatrix} 0.302 & 0.363 & -0.665 \\ -0.594 & -0.591 & 0.0349 \end{bmatrix} \cdot \begin{bmatrix} x_{s4} \\ x_{s5} \\ x_{s6} \end{bmatrix} \end{aligned} \quad \text{Equation 5-18}$$

#### 5.4.2.2 Force decoupling

The forces in the X and Y axes which are controlled by the PID controllers need to be converted into forces of the three actuators. This can be done by analyzing the trigonometric behavior between actuator forces and axes shown in Figure 117. This results in the following equation.

$$\begin{aligned} F_{Actuatorxy} &= A_{axistoactuator} \cdot F_{axisxy} \\ \begin{bmatrix} F_{a4} \\ F_{a5} \\ F_{a6} \end{bmatrix} &= \begin{bmatrix} \cos(-\varphi_{cc}) & \sin(-\varphi_{cc}) \\ \cos(120 - \varphi_{cc}) & \sin(120 - \varphi_{cc}) \\ \cos(240 - \varphi_{cc}) & \sin(240 - \varphi_{cc}) \end{bmatrix} \cdot \begin{bmatrix} F_x \\ F_y \end{bmatrix} \\ \begin{bmatrix} F_{a4} \\ F_{a5} \\ F_{a6} \end{bmatrix} &= \begin{bmatrix} 0.80 & -0.60 \\ 0.12 & 0.99 \\ -0.92 & -0.39 \end{bmatrix} \cdot \begin{bmatrix} F_x \\ F_y \end{bmatrix} \end{aligned} \quad \text{Equation 5-19}$$

#### 5.4.2.3 System linearization

The system in the X and Y axis is linearized the same way as the Z axis described in 4.4.2.3.1 to design decoupled controllers for each axis. To get the system behavior, the decoupling and trigonometric functions have to be taken into account. These functions are shown in the figure below. It can be seen, that the desired force is separated into the different actuators.

## Magnetic bearing for two additional axes

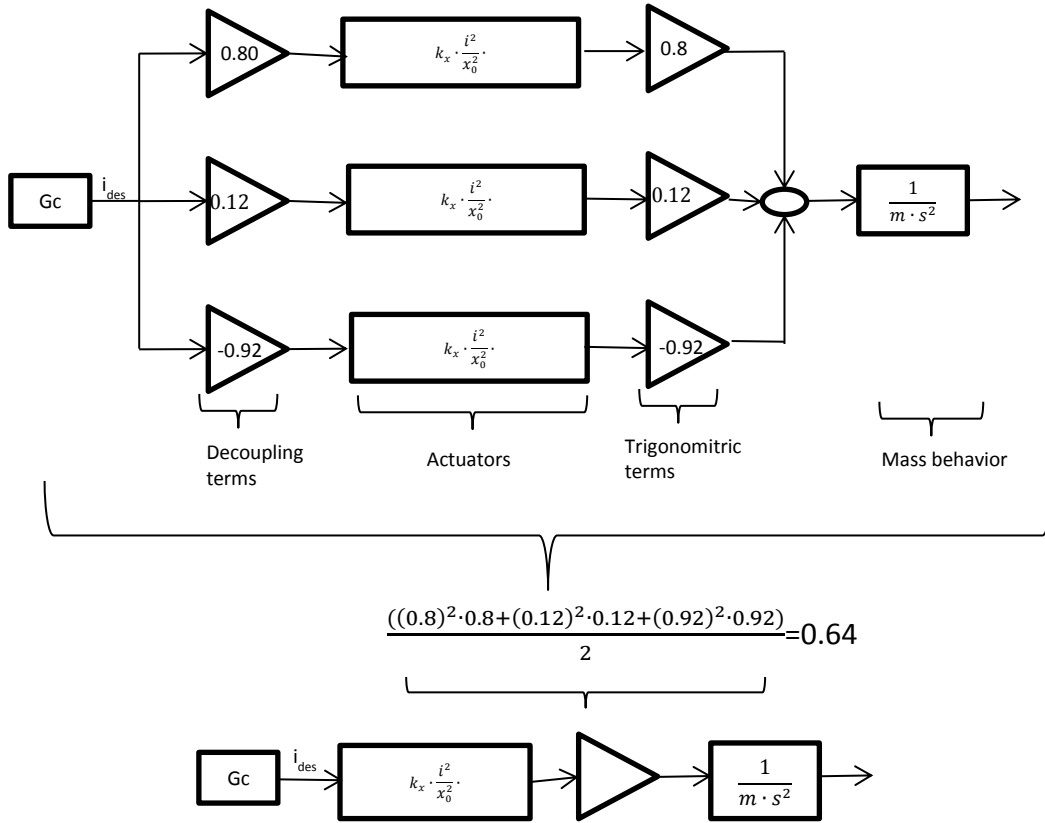


Figure 120 decoupling and trigonometric functions of the X axis

As negative forces created by the actuators are not possible, only 50 % of the force is acting when the rotor turns out of its middle position, this taken into account with the dividing factor of two in the above equation. It can be seen, that a factor of 0.64 has been used for linearizing the X axis. The Y axis has been calculated the same way, and a factor of 0.622 is calculated. This shows that both axes can be linearized in the same way using a factor of 0.63.

The system equation is shown below.

$$m \cdot \ddot{x} = k_x \cdot \frac{i^2}{x_a^2} \cdot 0.63 \quad \text{Equation 5-20}$$

For the linearized system there is no constant current required to keep the rotor in its middle position as it can be seen in Equation 5-21. This is obvious for a stationary case with zero external force and velocity. Nevertheless the system is linearized for a constant current of 0.5 A, which is the maximum desired current in one actuator.

$$0 = k_x \cdot \frac{i}{x^2} \rightarrow i_0 = \frac{0 \cdot x^2}{k_c} \quad \text{Equation 5-21}$$

The system is linearized for a distance between rotor and actuators of 1 mm and a speed of 0 m/s. The linearization is calculated in the following equation:

$$F_x = \frac{\partial f}{\partial x} \Big|_{x_0, u_0} \cdot \Delta x + \frac{\partial f}{\partial i} \Big|_{x_0, i_0} \cdot \Delta i \quad \text{Equation 5-22}$$

$$\frac{-k_x \cdot i_0^2}{x_0^3} \cdot 2 \cdot 0.63 \cdot \Delta x + \frac{2 \cdot k_x \cdot i_0^2}{x_0^2} \cdot V_{tol} \cdot 0.63 \cdot \Delta i = m \cdot \ddot{x}$$

$$G_X = G_Y = \frac{x}{i} = \frac{\frac{2 \cdot k_x \cdot i_0^2}{x_0^2} \cdot V_{tol} \cdot 0.6}{m \cdot s^2 + \frac{k_x \cdot i_0^2}{x_0^3} \cdot 2 \cdot 0.63}$$

To increase the comparability between model and measurement, the closed loop current control is multiplied to the linearized system according to Equation 4-24.

The linearization of the X axis results in the following bode plot. The system has negative spring stiffness. The phase of the system is  $-180^\circ$ . For higher frequencies, the phase drops due to the time delay in the system caused by the sampling rate of 2 kHz.

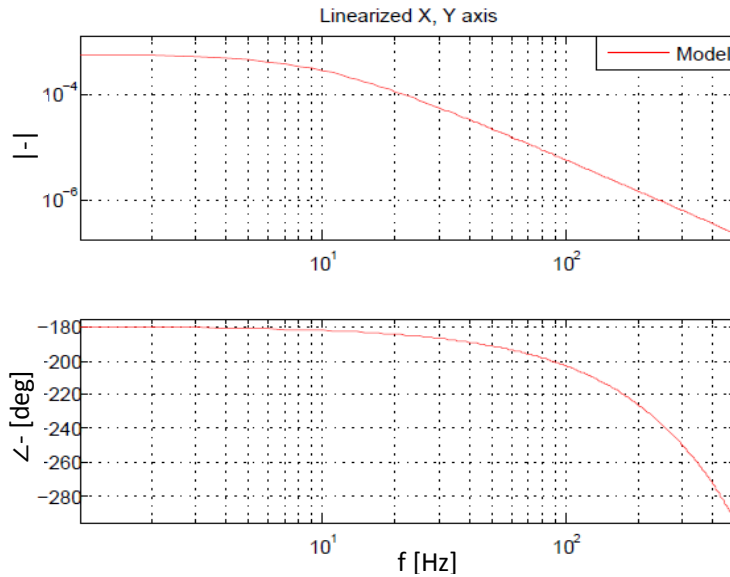


Figure 121 Linearized bode plot of the X-axis

It can be seen, that a crossover frequency between 10 Hz and 100 Hz has to be achieved in the controller design in order to achieve a good phase and gain margin. The linearization of the Y axis is done the same way and results to the same system behavior.

#### 5.4.2.4 Frequency response of the system

The linearized system behavior of the X and Y axis is compared to the measured system behavior. This is done according to the test specified in Table 15 in the appendix. The following section presents the results of these measurements. During the measurement it turned out, that the position controller of the motor axis need to be activated. Otherwise a rotation behavior disturbs the measurement. In the following figure the measured frequency response function of the X axis is shown.

## Magnetic bearing for two additional axes

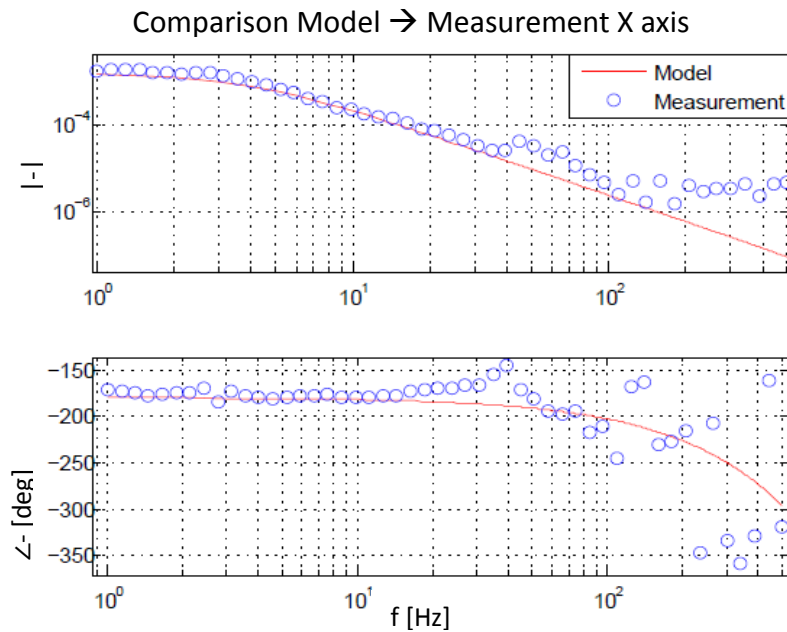


Figure 122 X Axis measured and calculated frequency response

It can be seen, that there is a good comparability between the model prediction and the measurement up to 100 Hz. As the spring stiffness is affected by the current through the actuators which has not been measured. This value is adjusted iteratively and shows a good comparability between model and measurement for 0.2 A which is a resalable value. The measurement and calculation matches quite well with an error of roughly 20%.

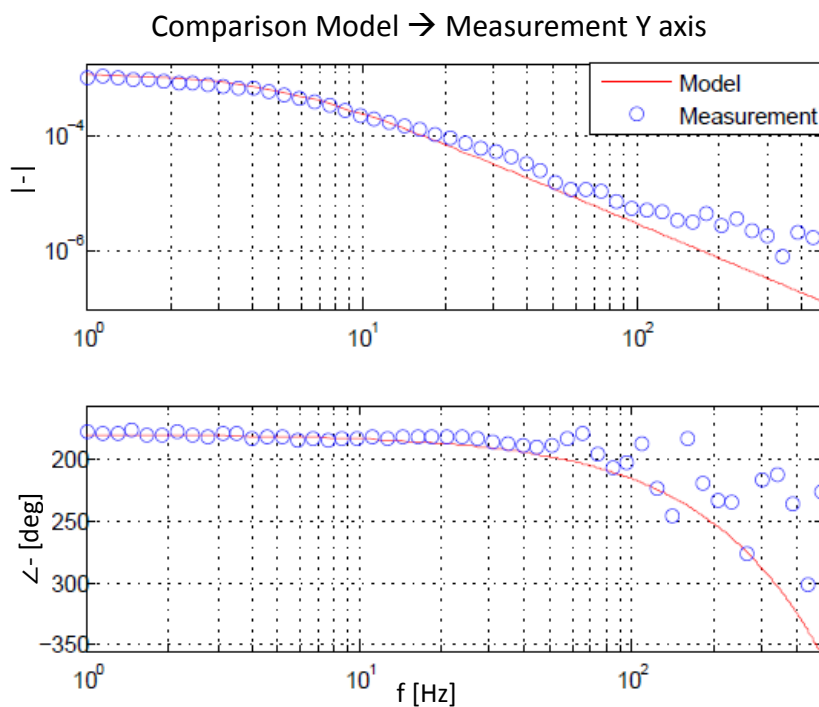


Figure 123 Y Axis measured and calculated frequency response



The frequency response of the Y axis is also been measured. As it can be seen in Figure 123, there is a good comparability between model predictions and measurement.

### 5.4.3 Controller tuning

For the control of the X and Y axis a PI controller combined with a lead-lag compensator is used. The controller is designed to achieve a crossover frequency of 20 Hz with a phase margin of 40°. The equations of the PI controller and the lead-lag compensator are described in the equations Equation 3-48 and Equation 3-49. The lead compensator is designed with the same lead and lag frequencies than the Z controller. Due to the non-linearity of the system the lead compensator is set to be slightly higher than the desired crossover frequency, as the gain of the frequency response magnitude increases for smaller distances. At these distances still a stable control is required.

The integrator frequency is adjusted to 1 Hz, that the phase drop caused by this part of the controller at the crossover frequency is low. The gain of the proportional term is set to 10.000 to achieve a crossover frequency of 30 Hz and a phase margin of 35°.

To verify the stability of the designed controller for both axes, a measurement of the return ratio has been done as it is specified in Table 17 in the appendix and the measurements are compared to the model predictions.

The measured return ratio of the X axis shows a good comparability between the predicted behavior and the actual measurement. It can be seen, that the cross over frequency is slightly higher than expected (30 Hz). A good gain margin of 38° is achieved in the controller.

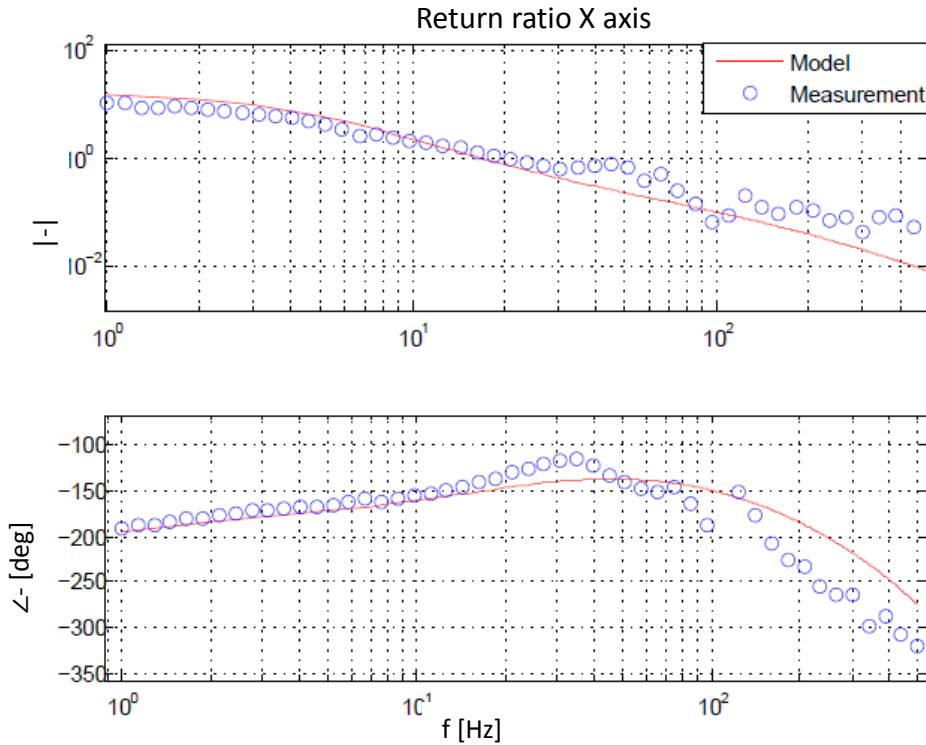


Figure 124 Measurement return ratio X axis

In the measurement of the Y axis also a crossover frequency of 30 Hz and a phase margin of  $40^\circ$  has been achieved, which states a stable control of this axis.

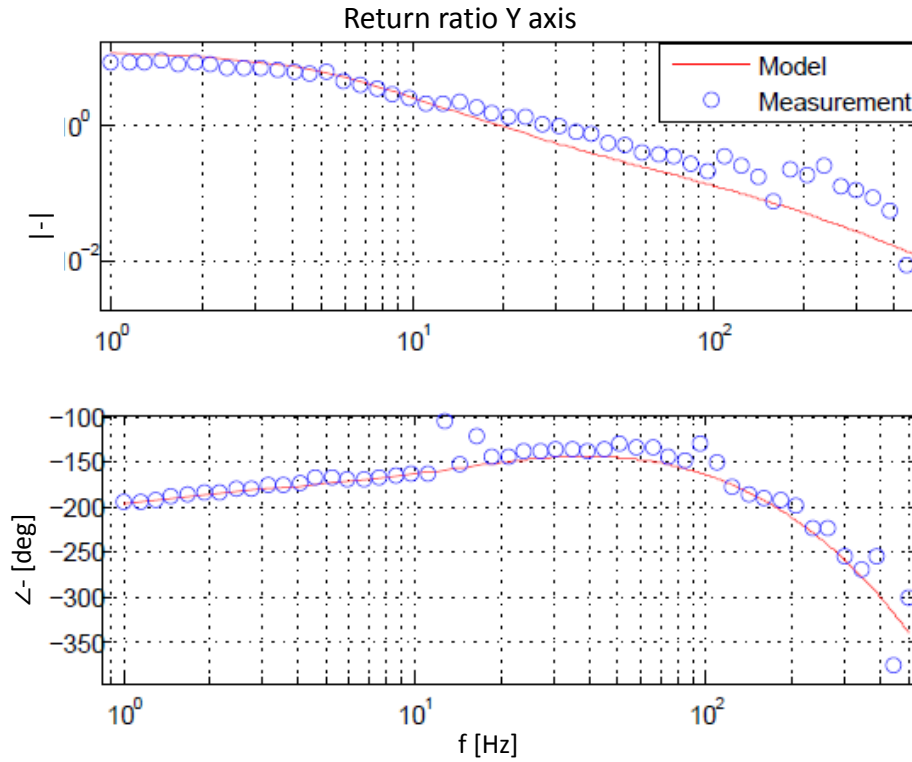


Figure 125 Measurement return ratio Y axis

#### 5.4.4 Measurement of the system behavior for different axes

To verify, that the axes can be adjusted separately by using this control structure the frequency response of the control effort for both axes has been measured for the actuation of one axes according to the specifications of Table 16 in the appendix. Secondly the measured control effort for the actuation of the X and Y axis is compared to the model predictions.

The results are shown in Figure 126 and Figure 127. It can be seen, that the control effort for the unactuated axes is lower than the control effort of the actuated axes. The differences are not that high as in the measurements of the vertical axis, which can be explained with the noise level of the system. The control effort of the unactuated axes is in the same range then in the control effort of the unactuated axes in the vertical axes measurement.

The comparison between measured control effort and model predictions shows a good comparability.

Magnetic bearing for two additional axes

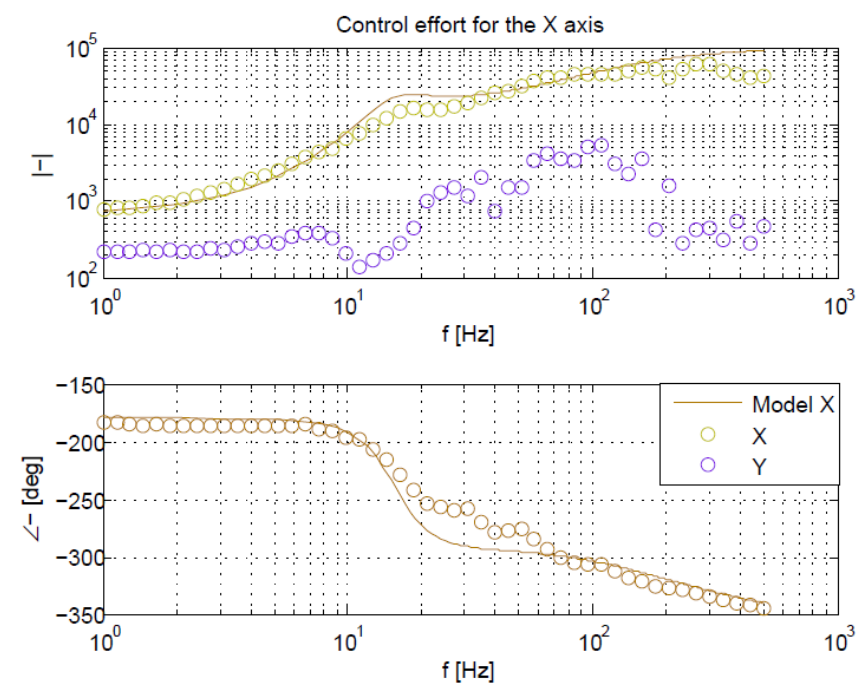


Figure 126 Control effort of the X axis

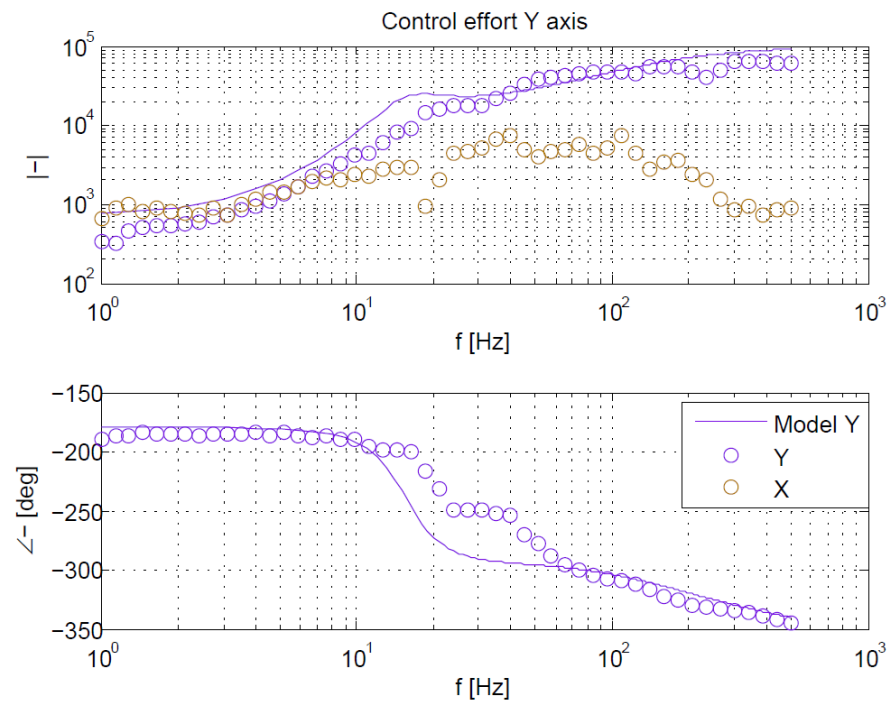


Figure 127 Control effort of the Y axis

## 6 BLDC motor with magnetic bearing

In a last step, the full system has been tested in order to show the functionality of the motor. To verify the full behavior, the different axes in time domain have been measured. The frequency response of the motor is measured by the use of the magnetic bearing. Also the open loop speed steps of the motor are characterized and compared to the former measurement.

### 6.1 System response of the magnetic bearing

The step responses for input changes in the five axes magnetic bearing has been measured in time domain as it is shown in the figure below.

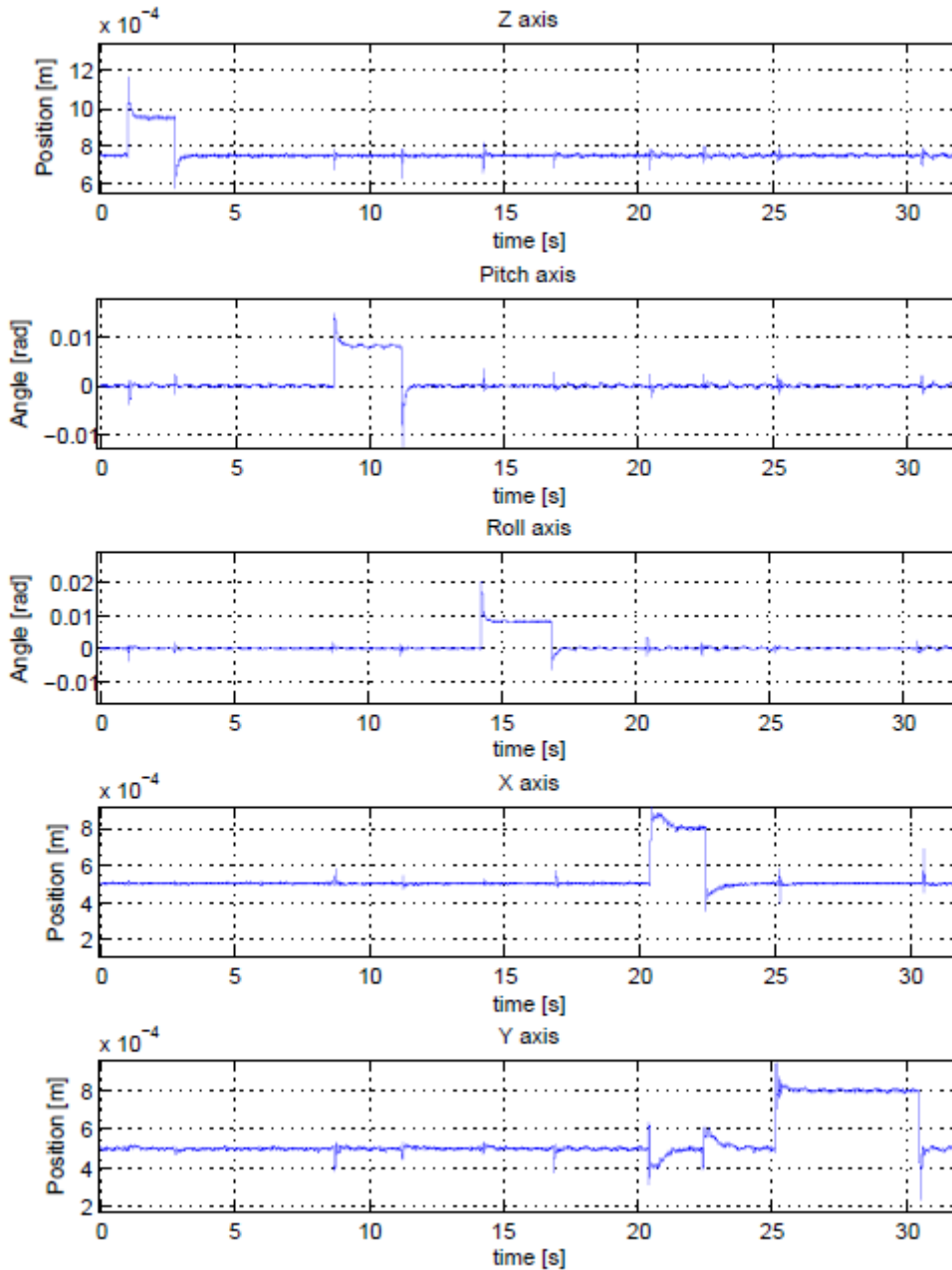


Figure 128 Five axes magnetic bearing measurement in time domain (without rotation)

It can be seen, that there is a stable system behavior in all axes. Changes in one of the Z, Pitch and Roll axis show nearly no coupling to the other axes. Between the X and Y axes the couplings are stronger as it has already seen in the frequency response measurement of these axes.

The next figure shows the step responses for varying inputs in time domain for a rotor speed of 2000 rpm.

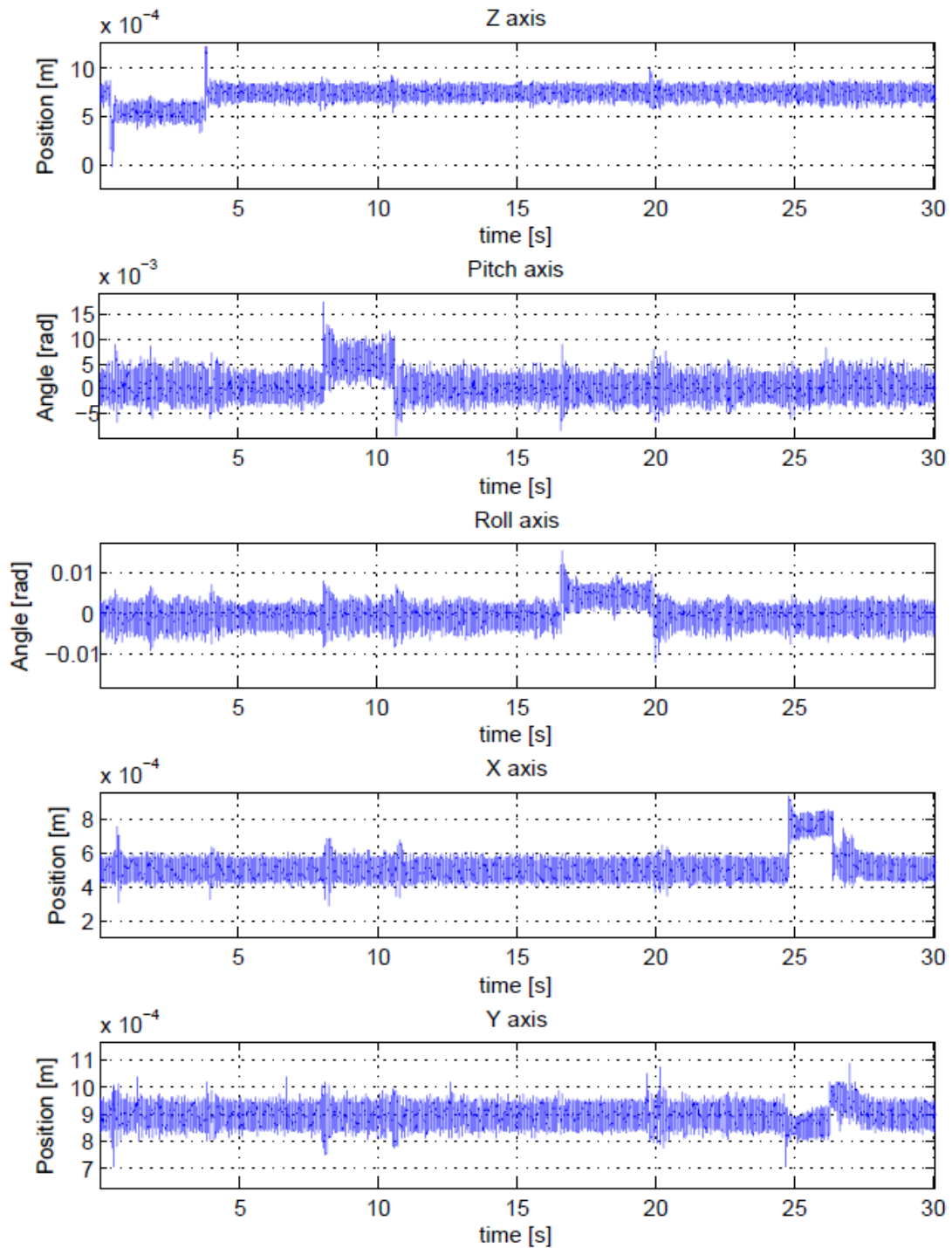


Figure 129 Five axes magnetic bearing measurement in time domain (2000 rpm)

The noise of the sensors can clearly be seen in the figure. Still a stable control of varying inputs of the different axes is possible. The couplings between the vertical axes are low. In the actuation of the horizontal axes, a coupling can be seen.

## 6.2 Motor frequency response

The frequency response of the motor is measured according to Table 11 in the appendix. It can be seen, that there is still a good comparability between the measurement and the model in the relevant frequency range.

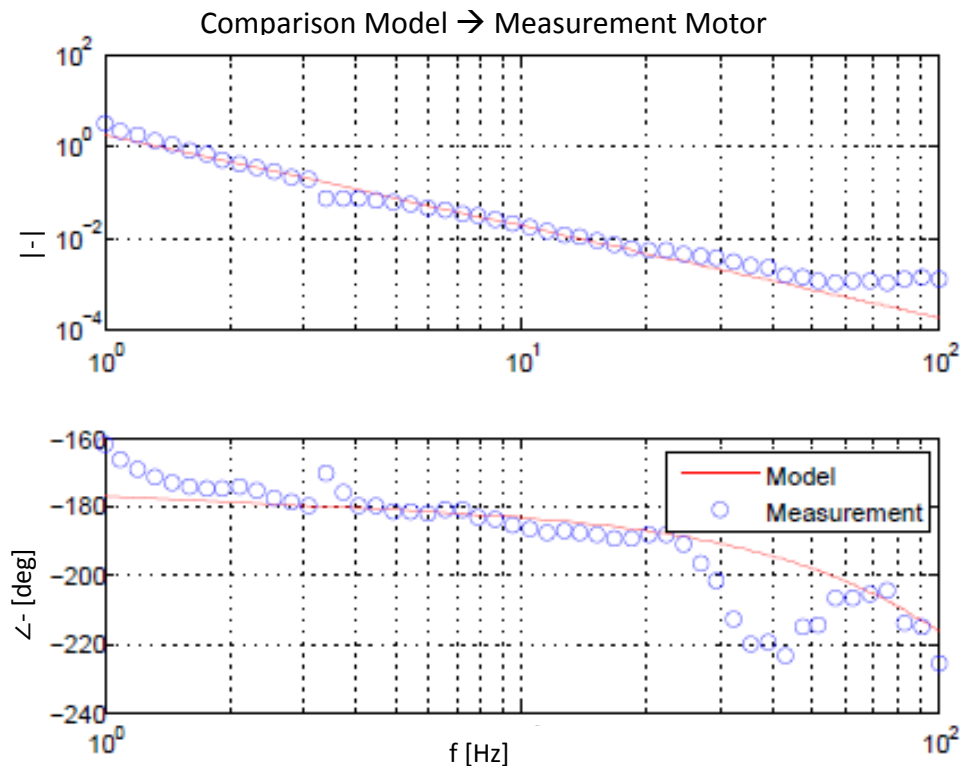
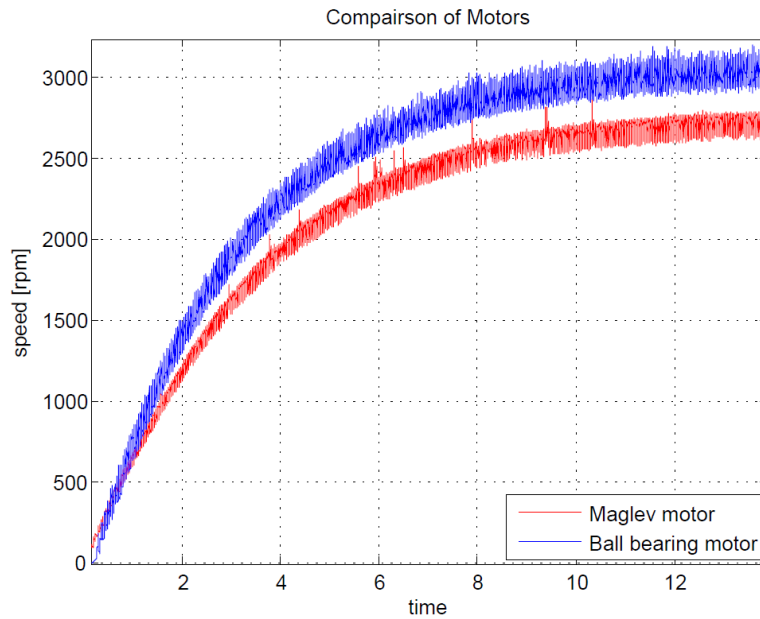


Figure 130 Frequency response measurement of the motor with magnetic bearing

To achieve a good comparability between model and measurement the moment of inertia has been adjusted CAD predicted value of the new rotor which is  $1.5502e-04 \text{ kg}\cdot\text{m}^2$ .

## 6.3 Motor speed

The speed of the motor is measured and compared to the measured open loop step response of the motor with ball bearing. Figure 131 shows the comparison of rotor with magnetic bearing to the conventional motor bearing. It can be seen, that the speed of the motor with magnetic bearing is lower than with magnetic bearing. Possible reasons are the viscous friction due to eddy currents of the magnetic bearing, as well as the coupling between rotor magnets and reluctance actuators.



**Figure 131** Open loop speed step of the maglev BLDC motor

By driving the motor with higher speed, the gyroscope effect of the rotor can be seen. This results in decreasing stability of the rotor for higher speed. The effect could be reduced by readjusting the Pitch and Roll axis controller. The lead-lag compensator is designed to lift the phase over a bigger range of frequencies. Still if the motor has to be driven at higher speed levels than the recent maximum speed the gyroscope effect needs to be compensated by building an analytical model and calculating a proper decoupling of this effect..

## 7 Conclusion and further work

In this thesis, a brushless DC motor with a rotor levitated by reluctance actuators is developed. Because of its modular design, the system can be used in four levels of teaching:

1. In the basic level, the rotor is supported by a ball bearing. The commutation of BLDC motors using block- or sine commutation can be explained. DC motors which are based on the Lorentz principle can be described and modeled as a SISO system. The model based design of position controllers (e.g. PID controller) as well as different methods to compare model and system can be explained.
2. The second level focuses on magnetic levitation of the (not rotating) rotor in three axes. In this level the design and calculation of single acting reluctance actuators and their negative spring stiffness is described. Also the modelling, linearization and control of systems with 3 DOF and the decoupling of different axes in order to achieve independent SISO systems can be shown.
3. At the third teaching level the rotor (not rotating) is magnetically levitated and actively controlled in five degrees of freedom. The modelling and control of an antagonistic (double-acting) reluctance actuator can be shown.
4. The final level is the control of the BLDC motor in six degrees of freedom. Advanced control techniques can be used for the control of the MIMO system in this stage. Also the gyroscopic effect of the spinning rotor can be observed.

As the system is targeted as a teaching tool in universities the primary focus of the project was to keep the costs of the system low. To ensure an easy and cost efficient production many parts were built by 3D printing. The parts which require a magnetic conductivity were manufactured with standard techniques which are available in most workshops. The control of the system is done with two NI myRIO real-time targets (one for controlling the BLDC motor and one for the control of the magnetic bearing).

To ensure a simple and cost efficient production of the motor, an axial field motor with all the windings and sensors placed on a single PCB board was realized. The rotor is made out of steel and round NdFeB magnets. A sine/cosine encoder for the rotary axes of the motor using low cost magnetic fields (Halls sensors) was developed. By using a calculated fitting curve of the sensor reading, a resolution of the encoder which is better than  $0.06^\circ$  was achieved. The sensor reading is implemented on the FPGA of the myRIO to increase the sensor resolution by oversampling and low pass filtering and to reduce time delays.

The characteristic parameters of the motor have been calculated and compared to measured values in order to get an accurate model of the motor. The difference between calculations and measurement is usually in a range between 10 % and 25 %. Particular remarkable is the highly sinusoidal behavior of the back EMF which forms the basics of sine commutation with small torque ripples. Based on a standard model for a DC motor, a PID position controller was tuned to a crossover frequency of 25 Hz using the loop shaping method and



confirmed by experiment. The predicted and measured motor dynamics under closed loop conditions show a high comparability.

The magnetic bearing for the vertical axes (2<sup>nd</sup> teaching level) uses three single acting reluctance actuators for the control of the Z, Pitch and Roll axes. Reluctance actuators were designed based on the analysis of the magnetic flux. The measured actuator force is close to the designed value (i.e. 10 % deviation). To increase the actuator dynamics, an operational amplifier based current controller with a crossover frequency of 1 kHz was developed and implemented. The vertical rotor position is measured in three positions above the rotor using reflective sensors. In order to decouple the MIMO systems into three independent SISO systems, the three axes are controlled in Cartesian coordinates. The sensor values and the forces created by the actuators are transformed into the Cartesian coordinate system. To get a high sampling rate in the real-time target the coordinate transformations of the sensors as well as the force decoupling algorithms are placed on the FPGA of the myRIO board. The magnetic bearing is controlled by a second myRIO real-time target, because of the limitations of D/A channels.

A dynamic model of each axis was built and linearized in order to tune PID controllers for the Cartesian axes Z, Pitch and Roll. Based on the linearized model crossover frequencies for the controllers between 30 Hz and 60 Hz were adjusted. To verify the modeled system, the frequency response of the system and the return ratio for the different axes were measured. Again the difference between the model based on calculated parameters and the measurement is lower than 20 %. In the relevant frequency range a decoupling factor of roughly ten for the vertical axes has been achieved.

The magnetic bearing for the horizontal axis (teaching level 3) uses three reluctance actuators arranged around the rotor at an angle of 120°. The actuators are designed to generate forces up to 0.5 N in the horizontal plane. Again, the measured performance fits well with the expectations (i.e. 0.1 N deviations). For measuring of the horizontal position the same sensor type, as for the vertical axis is used, including a third redundant sensor to reduce measurement errors. The horizontal actuator system is modeled and linearized the same way used for the vertical bearing. PID controllers for the X and Y axis are designed in order to decouple the two axes. Differences between predictions and measurements are again between 10 % and 20 %.

When the BLDC motor is used in combination with the magnetic bearing (teaching level 4), the motor dynamics are very similar to the performance with conventional bearings of teaching level 1. At higher speed of rotation, the gyroscopic effect can be observed. Nevertheless it is possible to use the motor with maximum speed in the present configuration.

## Conclusion and further work

Summarizing, a brushless DC motor including a magnetic bearing which can be used in modular stages of teaching has been developed and successfully tested. Dynamic models of the system have been built which shows a good comparability to the measurements. The system is an effective and cost efficient tool to teach students a wide range of mechatronics.

Works which can be done to increase the performance of the system and to add more teaching features are made in the following:

- In respect of time and resources, the motor has only been tested with an extra PCB where all the sensing and power electronics are placed. A version of a PCB which includes windings and electronics has designed, but still needs to be built and tested.
- When the BLDC motor is used with the magnetic bearing, the gyroscopic effect can be observed which destabilize the rotor. In the configuration of this setup it is still possible to run the motor with maximum speed. Nevertheless this effect can be modeled mathematically and solutions for a stable control for higher speed can be developed. Also the decoupling in the horizontal axes needs to be increased.
- The system can also be used to teach students about advanced techniques in nonlinear controller design and the design for MIMO controllers, as an example flat system based state space control can be shown.

## 8 Bibliography

- [1] A. E. Fitzgerald, C. J. Kingsley und S. D. Uman, Electric Machinery, New York: McGraw-Hill Companies, 2003.
- [2] J. Zhao und Y. Yu, „<https://www.monolithicpower.com>,“ Juli 2001. [Online]. Available: <https://www.monolithicpower.com/Portals/0/Documents/Products/Documents/appnotes/Brushless%20DC%20Motor%20Fundamentals.pdf>. [Zugriff am 11 04 2015].
- [3] S. K. Bhattachary, Electrical Machinery, 2 Hrsg., New Delhi: Tata McGraw-Hill, 1989.
- [4] L. Zhu, „Adaptive control of sinusoidal brushless DC motor actuators,“ Michigan Technological University, MICHIGAN, 2008.
- [5] D. M. Gambetta, „New Design Methodologies for Prontec Circuit Axial Field Brushless DC Motors,“ University of Southern Queensland, Southern Queensland, 2009.
- [6] G. H. Jang und J. H. Chang, „Development of Dual Air Gap Printed Coil BLDC Motor,“ IEEE Transaction on Magnetics, 19999.
- [7] Y. Xie, „Mechatronics Example For Teaching Modelling Dynamics, and Control,“ Massachusetts Institute of Technology, Cambridge, 2003.
- [8] N. M. B., „Modeling of a didactic magnetic levitation system for control education,“ Bd. Telsiks, 2003.
- [9] M. bin Mohad Ab. Halim, M. Sharil bin Yahaya und Z. Bin Ibrahim, „Magnetic levitation Training kit for teaching basic electrical control system courses,“ 2012.
- [10] K. A. Lilenkamp und K. Lundberg, „Low-cost magnetic levitation project kits for teaching feedback system design,“ american control conference, 2004.
- [11] J. Rudolph, „[www.uni-saarland.de](http://www.uni-saarland.de),“ 24 11 2014. [Online]. Available: <http://www.uni-saarland.de/en/campus/faculties/professorial-staff/naturwissenschaftlich-technische-fakultaet-ii/mechatronik/professorial-staff-dept-74-mechatronics-engineering/prof-dr-joachim-rudolph/research/electro-magnetic-bearings/magnetically-support>. [Zugriff am 21 03 2015].
- [12] T. Fukao und A. Chiba, Magnetic bearings and bearingless drives, 2005.
- [13] Orientalmotor, „[www.orientalmotor.com](http://www.orientalmotor.com),“ 2015. [Online]. Available: <http://www.orientalmotor.com/technology/articles/servo-motor-glossary.html>. [Zugriff

am 17 04 2015].

- [14] E. Eitel, „www.machinedesign.com,“ 07 05 2014. [Online]. Available: <http://machinedesign.com/sensors/basics-rotary-encoders-overview-and-new-technologies-0>. [Zugriff am 17 04 2015].
- [15] D. Gerling, K. Mühlbauer und G. Dajaku, „Frisch gewickelt,“ Bd. 12/4, 2012.
- [16] J. F. Gieras, R.-J. Wang und M. J. Kamper, Axial Flux Permanent Magnet Brushless Motors, Springer, 2008.
- [17] D. Gambetta und A. Ahföck, „Designing Printed Circuit Stators for Brushless Permanent Magnet Motors“.
- [18] SEC Electronics inc, „SS49E Linear Hall Effect Sensors“.
- [19] J. Wu, „Design of a Miniature Axial Flux Flywheel Motor with PCB Winding for Nanosatellites,“ International Conference on Optoelectronics and Microelectronics, Changchung Chinga, 2012.
- [20] Sierra Circuits, „www.protoexpress.com,“ [Online]. Available: <https://www.protoexpress.com/NoTouch-pcb/product-specs.jsp>. [Zugriff am 01 03 2015].
- [21] W. Pläßmann und D. Schulz, Handbuch Elektrotechnik: Grundlagen und Anwendungen für Elektrotechniker, Springer Vieweg, 2013.
- [22] Elektronikentwickler-aachen, „www.fs-leiterplatten.de,“ [Online]. Available: [https://www.elektronikentwickler-aachen.de/layouterstellung/layouterstellung\\_43.htm](https://www.elektronikentwickler-aachen.de/layouterstellung/layouterstellung_43.htm). [Zugriff am 02 02 2015].
- [23] D. Trumper, „ASPE Tutorial Notes Precision Mechatronics Part 1: Acutation, Sensing, and Interconnections,“ MIT. Dep. of Mechanical Engineering, Cambridge MA, 2003.
- [24] Fairchild Semiconductors, „L272 / L272A Dual Power Operatonal Amplifier,“ Fairchild Semiconductors, 2013.
- [25] National Instruments, „User Guide and Specifications NI myRIO-1900,“ National Instruments, 2013.
- [26] J. Baur, *Projektbeispiel2\_Zahnriehmenscheibe*, Aalen, 2014.
- [27] J. Baur, „Lecture notes: Modellbasierte Funktionsentwicklung,“ 2014.

## Bibliography

- [28] Texas Instruments, „TI,“ TI, 09 2013. [Online]. Available: <http://www.ti.com/lit/ds/symlink/ldc1000.pdf>. [Zugriff am 04 02 2014].
- [29] Pololu, „Pololu.com,“ Pololu, 2009. [Online]. Available: [https://www.pololu.com/docs/pdf/0J13/QTR\\_application\\_note.pdf](https://www.pololu.com/docs/pdf/0J13/QTR_application_note.pdf). [Zugriff am 04 02 2015].
- [30] Sauter-shop, „Sauter-shop.de,“ sauter-shop, [Online]. Available: <http://www.sauter-shop.de/downloads/technischedrahttabelle.pdf>. [Zugriff am 04 02 2014].
- [31] Vishay, „www.reichelt.de,“ 18 07 2008. [Online]. Available: [https://cdn-reichelt.de/documents/datenblatt/B400/RH\\_NH.pdf](https://cdn-reichelt.de/documents/datenblatt/B400/RH_NH.pdf). [Zugriff am 20 04 2015].
- [32] Texas Instruments, „LM675 Power Operational Amplifier,“ Texas Instruments, Dallas, Texas, 2013.
- [33] Schweiter\_FN, „www.schweizer-fn.de,“ 04 12 2014. [Online]. Available: <http://www.schweizer-fn.de/antrieb/unwucht/unwucht.php>. [Zugriff am 02 03 2015].
- [34] J. Gaukel, „Numerik (ME Master Systems Engineering),“ 2013.
- [35] HKCM, „www.hkcm.de,“ hkcm, 16 12 2014. [Online]. Available: [https://www.hkcm.de/HKCM\\_bh.php?l=de&grade=N52&id=1277&customers\\_article=&products\\_name=](https://www.hkcm.de/HKCM_bh.php?l=de&grade=N52&id=1277&customers_article=&products_name=). [Zugriff am 16 12 2014].
- [36] dextermagnetic, „www.dextermag.com,“ dextermagnetic, 2014. [Online]. Available: <http://www.dextermag.com/resource-center/magnetization-demagnetization-faq#2>. [Zugriff am 16 12 2014].
- [37] wondermagnet, „www.wondermagnet.com,“ 2003. [Online]. Available: <http://www.wondermagnet.com/magfaq.html#q75>. [Zugriff am 16 12 2014].
- [38] cy-magnetics.com, „www.cy-magnetics.com,“ [Online]. Available: <http://www.cy-magnetics.com/CY-Mag-HFerrite.pdf>. [Zugriff am 16 12 2014].
- [39] rubber-magnetic, „www.rubber-magnetic.com,“ 2007. [Online]. Available: <http://www.rubber-magnet.com/NdFeB-flexible-magnets.htm>. [Zugriff am 12 12 2014].
- [40] Dura Magnetics, „www.druamag.com,“ [Online]. Available: <http://www.duramag.com/materials/bonded-magnets/bonded-magnets-technical-information/>. [Zugriff am 16 12 2014].
- [41] rubber-magnetic, „www.rubber-magnetic.com,“ 2007. [Online]. Available:

## Bibliography

- <http://www.rubber-magnet.com/rubber-magnet-strip.htm>. [Zugriff am 16 12 2014].
- [42] K. Lilenkamp, „A Simulink-Driven Dynamic Signal Analyzer,“ Massachusetts Institute of Technology, 1999.
- [43] J. Baur, „Regelungstechnik Einführung (Vorlesungsskript Mechatronik),“ Hochschule Aalen, Hochschule Aalen, 2012.
- [44] K. Lilenkamp und D. Trumper, „Dynamic Signal Analyzer for dSPACE,“ Precision Motion Control Lab, Mass. Ave, Cambridge, MA 02139, 199.
- [45] K&J Magnetic, „[www.kjmagnetics.com](http://www.kjmagnetics.com),“ [Online]. Available: <http://www.kjmagnetics.com/blog.asp?p=halbach-arrays>. [Zugriff am 15 07 2014].
- [46] K&J Magnetic, „K&J Magnetic,“ [Online]. Available: <https://www.kjmagnetics.com/blog.asp?p=homopolar-motors>. [Zugriff am 2015 12 13].
- [47] Linear Technology, „LT1021 Precision Reference“.
- [48] S. D. Umans, 7 Hrsg., Singapore: The MC Graw-Hill Companies, 2014.
- [49] P. F. Kelly, Electricity and Magnetism, Broken Sound Park Nw: Taylor & Francis Group.
- [50] J. Bird, Electrical Circuit Theory and Technology, Burlington: Newnes, 2014.
- [51] Schäffler KG, Technisches Taschenbuch, Würzburg: Schäffler, 2002.
- [52] National Instruments, „[www.ni.com](http://www.ni.com),“ National Instruments, 2014. [Online]. Available: <http://www.ni.com/myrio/>. [Zugriff am 20 12 2014].
- [53] E. Kallenbach, R. Eick, T. Ströhla, K. Feindt, M. Kallenbach, O. Radler und P. Quendt, Elektromagnete, Vieweg+Teubner, 2012.
- [54] G. Conrad, „Rotor Dynamic Testing and Control with Active Magnetic Bearings,“ ETH Zürich, 1998.
- [55] R. Munning Schmidt, G. Schitter und J. Van Eijk, The Design of High Performance Mechatronics, Amsterdam: IOS Press BV, 2011.
- [56] L. Zhou, M. Imani Nejad und D. Trumper, „FlexLab & LevLab: A Portable Solution for Mechatronics Teaching,“ [Online]. Available: [http://web.mit.edu/leizhou/~lei/Poster\\_Flexlab.pdf](http://web.mit.edu/leizhou/~lei/Poster_Flexlab.pdf).
- [57] J. F. Gieras, „Teaching Magnetic Levitation at Graduate Level“.

## Bibliography

- [58] M. Lang, „Berechnung und Optimierung von passiven permanentmagnetischen Lagern für rotierende Maschinen,“ Berlin, 2003.
- [59] S. Earnshaw, „On the Nature of the Molecular Forces which regulate the Constitution of the Luminiferous Ether,“ Transaction of the Cambridge Philosophical Society Vol. VII, Part I, London, 1848.
- [60] J. X. Shen, K. J. Tsen, D. Valathgamuwa und W. K. Chan, „A novel compact PMSM with magnetic bearing for artificial heart application,“ IEEE Transaction on Industrie Application, 2000.
- [61] A. Fernercioglu, „Design and analysis of magnetically levitated axial flux BLDC motor for ventricular assist device (VAD),“ Gaziosmanpasa University, Tokat 60250, Turkey.
- [62] M. Imani Nejad, „Self-Bearing Motor Design & Control,“ Massachusetts Institute of Technology, Cambridge, 2013.
- [63] L. Zhou, M. Imani Nejad und D. L. Trumper, „FlexLab and LevLab: A Portable Lab for Dynamics and Control Teaching,“ Massachusetts Institute of Technology, Cambridge, 2014.
- [64] Honeywell, „SS39ET/SS49E/SS59ET Series Linear Hall-Effect Sensor ICs,“ Honeywell, Golden Valley, 2013.
- [65] S. Walenczewski und E. Wahl, „www.scu.edu,“ 20 02 2014. [Online]. Available: [http://mech208.engr.scu.edu/Homework/HW6/presentations/Walenczewski\\_Wahl\\_BLDCEMotor\\_RevC.pdf](http://mech208.engr.scu.edu/Homework/HW6/presentations/Walenczewski_Wahl_BLDCEMotor_RevC.pdf). [Zugriff am 20 04 2015].
- [66] National Instruments, „www.ni.com,“ National Instruments, 09 08 2013. [Online]. Available: <http://www.ni.com/tutorial/7109/en/>. [Zugriff am 17 04 2015].

## 9 Appendix Motor

### 9.1 Comparison of permanent magnet materials

Table 5 Comparison of magnetic materials

NdFeB	
Br	1.4 T (max) [35]
Hcb	955 kA/m [35]
Bhmax	52 MGOe [35]
Remagnetizability	<ul style="list-style-type: none"> <li>A magnetic field higher 1000 kA/m is needed depending on the grade it can be much higher [36]. For high grades permanent magnets are not strong enough</li> </ul>
Machinability	<ul style="list-style-type: none"> <li>Materials is hard to machine [37]</li> <li>Corrosion appears after removing the safety layer</li> </ul>

Ferrite	
Br	0.4 T (max) [38]
Hcb	300 kA/m [38]
Bhmax	<5 MGOe [38]
Remagnetizability	<ul style="list-style-type: none"> <li>Can be remagnetized using permanent magnets, at average a magnetic field of 100kA/m is needed [36]</li> </ul>
Machinability	<ul style="list-style-type: none"> <li>Material is difficult to machine as the material is hard and brittle</li> </ul>

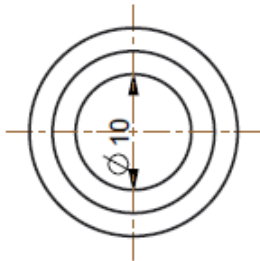
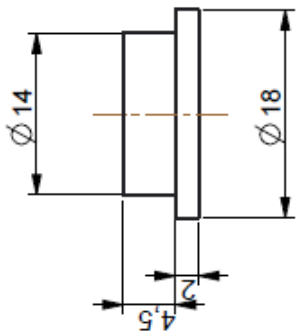
NdFeB flexible Magnets	
Br	0.55 T (max) [39]
Hcb	355 kA/m [39]
Bhmax	5-6 MGOe [39]
Remagnetizability	<ul style="list-style-type: none"> <li>A magnetic field higher 350kA/m is needed depending on the grade it can be much higher [36]. For high grades permanent magnets are not strong enough</li> </ul>
Machinability	<ul style="list-style-type: none"> <li>Easy to manufacture</li> </ul>

Bonded NeFeB Magnets	
Br	0.68 T (max) [40]
Hcb	460 kA/m [40]
Bhmax	10 MGOe [40]
Remagnetizability	<ul style="list-style-type: none"> <li>A magnetic field higher 350kA/m is needed depending on the grade it can be much higher [36]. For high grades permanent magnets are not strong enough</li> </ul>
Machinability	<ul style="list-style-type: none"> <li>Material is machinable, but only used for specific applications which are custom made</li> </ul>

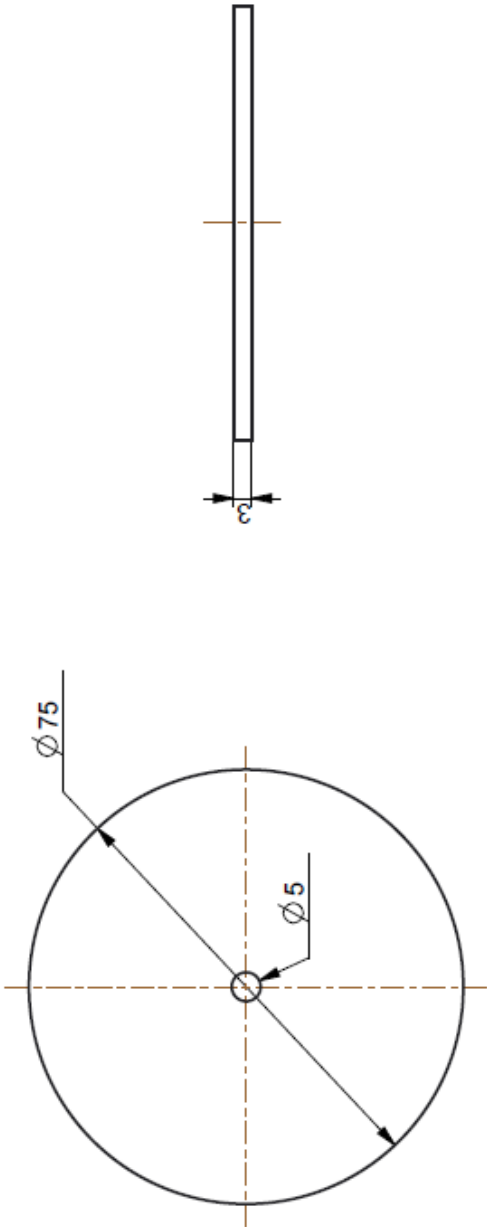
Ferrite flexible Magnets	
Br	0.22 T (max) [41]
Hcb	140kA/m
Bhmax	3-4 MGOe
Remagnetizability	<ul style="list-style-type: none"> <li>Can be remagnetized using permanent magnets. Roughly the same magnetic field which is needed for remagnetizing ferrite magnets is needed</li> </ul>
Machinability	<ul style="list-style-type: none"> <li>Easy to manufacture</li> </ul>



9.2 Mechanical design

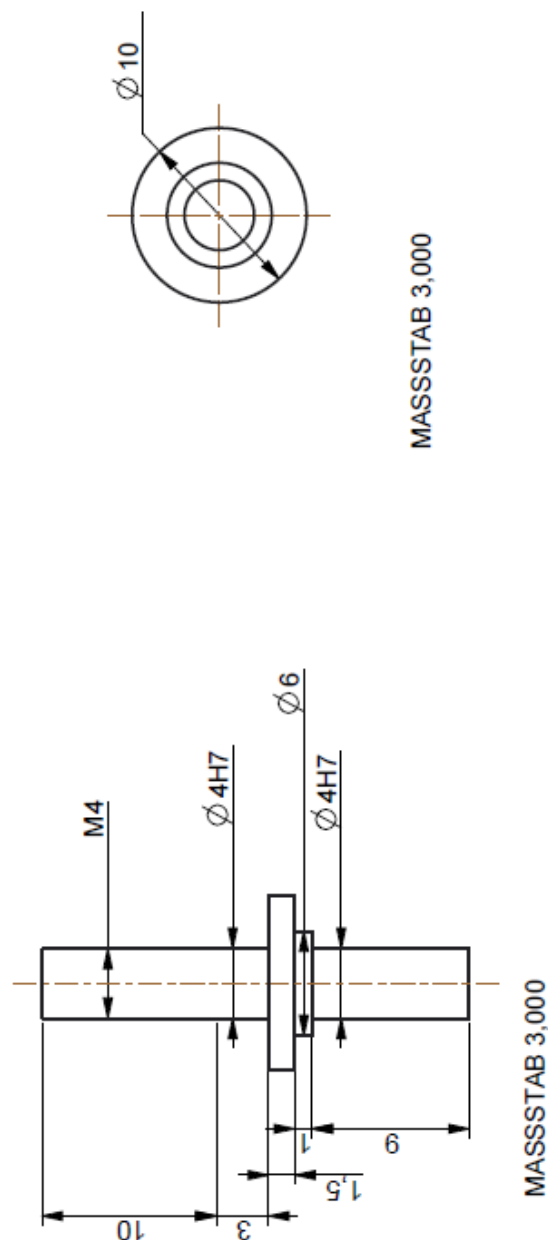


Datenname des Zeichnungsgebietes: MIDDLEPART				Datenname der Zeichnung: MIDDLEPART		Gew.: kg	
				Allgemeintitel: DIN ISO 2768-m-S	Werkstück -baniten DN 6784	Maßstab 2,000	
				Datum	Name	Benennung: Cd 1 Erst. / Nachg. / Rev. Tel. (175) 1880 Erst. / Nachg. / Rev.	
				Bear. #12345678			
				Gepr. #98765432			
				Norm			



Dateiname des Zeichnungsobjektes: ROTOR_IRON				Dateiname der Zeichnung: ROTORIRON		Gew.: kg	
		Algemeintol. DIN ISO 2768-m-S	Werkstoff -leiten DIN 6704	PART	Maßstab 1,000	Berechnung Rotoriron Erstellung: Rotor Iron Tel: 0172 71480 Email: RotorIron@rotor.de	
			Datum	Name		Angezeichnet/checked: Roto Sg i Tel:	Bl.1 1 Bl.
		Bear.	180808EB				
		Gepr.	180808EB				
		Norm					
Zust.	Änderung	Datum	Nam	(Firmenlogo)		(Ers.f.)	(Ers.d.)

Figure 133 CAD drawing motor / rotor iron



Dateiname des Zeichnungsobjektes: SHAFT2		Dateiname der Zeichnung SHAFT2		Gew.: kg	
Allgemeintitel DIN ISO 2768-m-S		Vorstück -arten DIN 6784		Maßstab 2,000	
Datum		Name		Wert 06	
Bear. 000000		Name		Bearbeitung	
Gepr. 000000		Name		Erster Maßstab	
Norm		Name		Teil 000000	
		Name		Endmaßstab 000000	
		(Firmenlogo)		Angegebene Hochschule:	
				Pers. Nr.:	
				Bl. 1	
Zust. Änderung		Datum		(Ers. f.)	
Datum		Name		(Ers. d.)	
				1 Bl.	

Figure 134 CAD drawing motor / rotor shaft

### 9.3 Test specifications

Table 6 Sine/cosine encoder test specification of the motor

Sin/cos encoder test	
<b>1. Aim</b>	Characterizing and adjusting the sensor behavior of the Hall sensor based sine/cosine encoder
<b>2. Specification</b>	<ul style="list-style-type: none"> <li>Measuring and fitting the nonlinearity's of the encoder for different.</li> <li>Verifying the sensor behavior</li> </ul> <p><b>Input:</b></p> <ul style="list-style-type: none"> <li>Rotating rotor with constant speed</li> </ul> <p><b>Measured parameters:</b></p> <ul style="list-style-type: none"> <li>Input value of both Hall sensors</li> <li>Measured rotor position based on the encoder calculations</li> </ul> <p><b>Expectation:</b></p> <ul style="list-style-type: none"> <li>When the rotor is spinning a sine signal with higher harmonics can be seen, which results in differences between measured and actual rotor angle</li> </ul>
<b>3. Test Procedure</b>	<p><b>Preparation:</b></p> <ul style="list-style-type: none"> <li>The motor is connected to the myRIO real-time system. The commutation and the Hall sensor reading is done with this system</li> </ul> <p><b>Test procedure:</b></p> <ul style="list-style-type: none"> <li>The motor is rotating at a constant speed. To achieve a higher accuracy of the measurement as well as for the mapping of the error value, a low speed level is chosen</li> <li>The Hall sensor values are recorded</li> <li>The measured angle values will be compared to an ideal encoder behavior</li> <li>The error between ideal encoder behavior and measured one are fitted with a mathematical function</li> <li>A fitting function is implemented in the real-time program to compensate the nonlinearity's in the measured angle</li> <li>The angle of a rotating motor will be measured and compared to an ideal angle behavior</li> </ul>

Table 7 Coil characterization of the motor

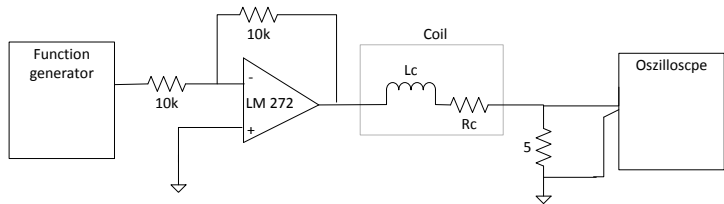
Coil characterization	
<b>1. Aim</b>	Measuring the resistance and inductance of one coil of the motor
<b>2. Specification</b>	<p>The inductance of the coil is measured using an opamp circuit, a function generator and an oscilloscope.</p> <p><b>Input:</b></p> <ul style="list-style-type: none"> <li>Current through the coil driven by a opamp circuit.</li> </ul> <p><b>Measured values</b></p> <ul style="list-style-type: none"> <li>Coils resistance (multimeter)</li> <li>Voltage at the sensing resistance</li> </ul>
<b>3. Test Procedure</b>	<p><b>Preparation:</b></p> <ul style="list-style-type: none"> <li>The coil of the motor is connected to the power amplifier LM272. This amplifier is driven by the function generator</li> <li>To measure the current through the coil, a sensing resistance has been implemented in the system.</li> </ul>  <p><b>Figure 135 Schematic of the inductance measurement circuit</b></p> <p><b>Test Procedure:</b></p> <ul style="list-style-type: none"> <li>The resistance of the coil is measured using a handheld multimeter</li> <li>A square wave signal is applied to opamp</li> <li>The frequency of the signal is adjusted, that the expected PT1 behavior of the coil can be seen</li> <li>The step response of the coil is measured and recorded.</li> <li>The inductance of the coil will be calculated using the time constant of the step response and the measured resistance</li> <li>The measured inductance of the coil is compared to the modeled inductance.</li> </ul>

Table 8 Back EMF measurement of the motor

Back EMF	
<b>1. Aim</b>	Measuring back EMF of the motor to determine the speed and torque constant of the motor
<b>2. Specification</b>	<p>The speed constant of the motor will be measured, therefore the following values have to be measured.</p> <p><b>Input values</b></p> <ul style="list-style-type: none"> <li>• Spinning rotor</li> </ul> <p><b>Measured values</b></p> <ul style="list-style-type: none"> <li>• Back EMF [V]</li> <li>• Rotor speed [Hz] by measuring the zero crossing in the signal</li> </ul>
<b>3. Test Procedure</b>	<p><b>Preparation:</b></p> <ul style="list-style-type: none"> <li>• The motor is disconnected from the power opamp.</li> <li>• The two wires of one coil are connected to a differential input of the myRIO</li> <li>• One Hall sensor is connected to one input of the myRIO</li> <li>• The back EMF value and the Hall sensor value will be measured using the LabVIEW real-time software</li> <li>• The measured values are processed in Matlab</li> </ul> <p><b>Test Procedure:</b></p> <ul style="list-style-type: none"> <li>• To generate back EMF, the motor is rotated by hand</li> <li>• The LabVIEW software records the change in the back EMF depending on the rotor angle position and the speed of the rotor</li> <li>• The rotor speed is measured using the zero crossings of the Hall sensor</li> <li>• Using the speed of the rotor and the amplitude of the back EMF, the speed and torque constant of the motor can be calculated</li> <li>• The shape of the back EMF is discussed in order to verify that the right commutation technique is used.</li> </ul>

Table 9 friction estimation of the motor

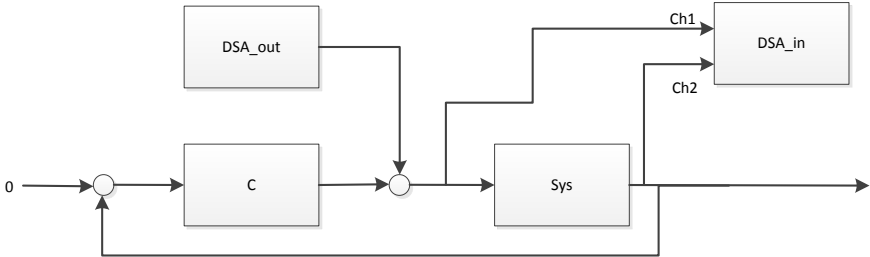
Friction estimation	
<b>1. Aim</b>	Measuring and modeling the friction in the motor
<b>2. Specification</b>	<p>The friction in the motor has to be measured and characterized. Therefore the following value has to be measured:</p> <p><b>Input values</b></p> <ul style="list-style-type: none"> <li>• Spinning rotor [rad/s]</li> </ul> <p><b>Measured values</b></p> <ul style="list-style-type: none"> <li>• Motor speed (derivative of encoder angle) [rad/s] over time</li> </ul>
<b>3. Test Procedure</b>	<p><b>Preparation:</b></p> <ul style="list-style-type: none"> <li>• The motor is connected to the power opamps, in this configuration, the motor can be run in normal mode</li> </ul> <p><b>Test Procedure:</b></p> <ul style="list-style-type: none"> <li>• The motor is accelerated to maximum speed by switching on the motor voltage and commutating the motor using the LabVIEW program. (As an alternative the motor can be accelerated by hand).</li> <li>• When the rotor is spinning with constant speed, the cable between motor and power amp is plugged out. This way no damping due to back EMF is introduced in the system. As an alternative, the voltage in the coils can be switched off. This way it has to be ensured that no electrical current due to back EMF is introduced as this would cause additional damping</li> <li>• The decreasing speed of the rotor is measured using the derivative of the encoder value</li> <li>• A model of the friction is build using coulomb and viscous friction. The model is adjusted iteratively to the measured values.</li> </ul>

Table 10 Open loop speed step of the motor

Open loop speed step	
<b>1. Aim</b>	Measuring the open loop speed steps of the motor for different speed levels to compare the motor behavior to the modeled motor behavior to the measurement
<b>2. Specification</b>	<p>To measure the open loop speed steps of the motor the following parameters have to be measured:</p> <p><b>Input values</b></p> <ul style="list-style-type: none"> <li>• Motor voltage (Amplitude) [V]</li> </ul> <p><b>Measured values</b></p> <ul style="list-style-type: none"> <li>• Motor speed (derivative of encoder angle) [rad/s]</li> </ul>
<b>3. Test Procedure</b>	<p><b>Preparation:</b></p> <ul style="list-style-type: none"> <li>• The motor is connected to the power opamps; in this configuration, the motor can be run in normal mode</li> </ul> <p><b>Test Procedure:</b></p> <ul style="list-style-type: none"> <li>• In the start position, the motor is switched off (speed = 0 rad/s)</li> <li>• A step in the amplitude of the commutation function is given to the motor for the following voltage levels <ul style="list-style-type: none"> <li>○ 2.0 V</li> <li>○ 4.0 V</li> <li>○ 6.0 V</li> <li>○ 8.0 V</li> <li>○ 9.4 V (maximum motor voltage)</li> </ul> </li> <li>• The change of the motor speed in respect of time is recorded in LabVIEW</li> <li>• A Matlab Simulink simulation has been run for the same voltage steps</li> <li>• The simulated and measured open loop step functions are compared</li> </ul>



Table 11 System frequency response of the motor

System frequency response	
<b>1 Aim</b> .	Measuring the frequency response of the system for comparison to the model
<b>2 Specification</b> .	<p>To measure the frequency response of the motor, the following values have to be measured:</p> <p><b>Input values</b></p> <ul style="list-style-type: none"> <li>Sine signal (in LabVIEW after the controller) which is generated in the LabVIEW DSA tool</li> </ul> <p><b>Measured values</b></p> <ul style="list-style-type: none"> <li>Encoder signal of the motor</li> </ul>
<b>3 Test Procedure</b> .	<p><b>Preparation:</b></p> <ul style="list-style-type: none"> <li>The DSA measurement tool is implemented in LabVIEW as shown</li> <li>A stable position controller is implemented. This controller keeps the motor in a controlled position. There are no particular specifications on this controller. It just has to show a stable behavior.</li> </ul>  <p><b>Test Procedure:</b></p> <ul style="list-style-type: none"> <li>The motor and LabVIEW system is started</li> <li>The position controller keeps the system in a stable position</li> <li>For the DSA tool the following values have to be adjusted <ul style="list-style-type: none"> <li>Start frequency 1 Hz</li> <li>Stop frequency 500 Hz</li> <li>Number of frequency bins: 50</li> <li>Setting cycles : 20</li> <li>Calculation cycles 50</li> <li>Sampling time: 0.0005</li> </ul> </li> <li>The DSA measurement is started by starting the start button</li> <li>The frequency response measurement is done automatically</li> <li>The results are compared to the simulated values</li> </ul>

**Table 12 Return ratio measurement of the motor**

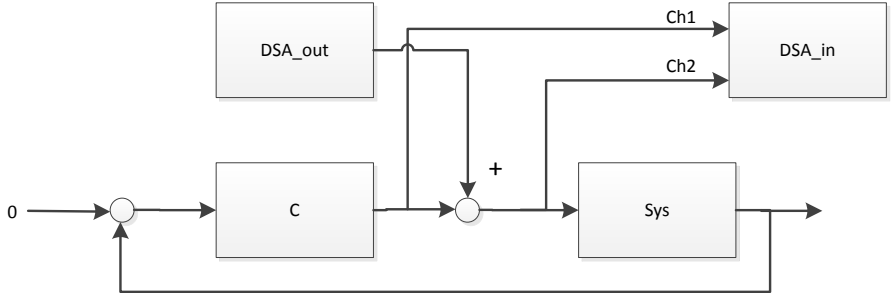
Return ratio measurement	
<b>1 Aim</b> .	Measuring the return ratio of the system to verify the stability of the model based designed controller
<b>2 Specification</b> .	<p>To measure the return ratio, the following values have to be measured:</p> <p><b>Input values</b></p> <ul style="list-style-type: none"> <li>Sine signal (in LabVIEW after the controller) which is generated in the LabVIEW DSA tool</li> </ul> <p><b>Measured values</b></p> <ul style="list-style-type: none"> <li>Encoder signal of the motor</li> </ul>
<b>3 Test Procedure</b> .	<p><b>Preparation:</b></p> <ul style="list-style-type: none"> <li>The motor is connected to the power opamps. In this configuration, the motor can be run in normal mode</li> <li>The DSA measurement tool is implemented in LabVIEW as shown below</li> </ul>  <p><b>Test Procedure:</b></p> <ul style="list-style-type: none"> <li>The motor and LabVIEW system is started</li> <li>The position controller keeps the system in a stable position</li> <li>For the DSA tool the following values have to be adjusted <ul style="list-style-type: none"> <li>Start frequency 1 Hz</li> <li>Stop frequency 100 Hz</li> <li>Number of frequency bins: 50</li> <li>Setting cycles : 10</li> <li>Calculation cycles 100</li> <li>Sampling time: 0.001</li> </ul> </li> <li>The DSA measurement is started by pushing the start button</li> <li>The return ratio measurement is done automatically</li> <li>The return ratio is characterized in relation to phase and gain margin</li> <li>Comparison of measured and modeled return ratio</li> </ul>

Table 13 Step response closed loop of the motor

Step response closed loop	
<b>1 Aim</b> .	Measuring the step function of the system
<b>2 Specification</b> .	To measure the step the following values have to be measured: <b>Input values</b> <ul style="list-style-type: none"> <li>• Input step (LabVIEW)</li> </ul> <b>Measured values</b> <ul style="list-style-type: none"> <li>• Encoder signal of the motor</li> </ul>
<b>3 Test Procedure</b> .	<b>Preparation:</b> <ul style="list-style-type: none"> <li>• The motor is connected to the power opamps, in this configuration, the motor can be run in normal mode</li> </ul> <b>Test Procedure:</b> <ul style="list-style-type: none"> <li>• The motor and LabVIEW system is started</li> <li>• The position controller keeps the system in a stable position</li> <li>• Step functions with different step heights will be applied to the system. The system behavior will be compared to the model predictions.</li> </ul>

Table 14 Trajectory based positioning of the motor

Trajectory based positioning	
<b>1 Aim</b> .	Verifying the trajectory based positioning behavior of the motor
<b>2 Specification</b> .	<p>To measure the step the following values have to be measured:</p> <p><b>Input values</b></p> <ul style="list-style-type: none"> <li>• Position change (LabVIEW)</li> </ul> <p><b>Measured values</b></p> <ul style="list-style-type: none"> <li>• Encoder signal of the motor</li> </ul>
<b>3 Test Procedure</b> .	<p><b>Preparation:</b></p> <ul style="list-style-type: none"> <li>• The motor is connected to the power opamps. In this configuration, the motor can be run in normal mode</li> </ul> <p><b>Test Procedure:</b></p> <ul style="list-style-type: none"> <li>• The motor and LabVIEW system is started</li> <li>• The position controller keeps the system in a stable position</li> <li>• Step functions with different step heights will be applied to the system. The system behavior will be compared to the model predictions.</li> </ul>

## 9.4 Matlab

### 9.4.1 Script for PCB coil printing

```

%% Coildesign of the PCB Board
clear; clc;
%Parameters given for the Coils
Ro      = 37.5; % m outer Radius of the coils
Ri      = 10; % m inner Radius of the coils
w       = 127e-3;% m track with
c       = 152.4E-3;% m inner track clearnce
Ns      = 6; %number of spirals at a layer

%Offset of Layer (where are the coils at the pcb board
xo = 70;
yo = 70;

%Calculating the angle of each coil
alfa=360/(Ns*180)*pi;
sa=sin(alfa);

%Calculation of the distance between two lines
wc=w+c;

%Calculation of the starting points of the coil
x(1)=(Ro-wc)*cos(alfa/2);
y(1)=-(Ro)*sin(alfa/2);
x(2)=Ri*cos(alfa/2);
y(2)=-Ri*sin(alfa/2);
x(3)=Ri*cos(alfa/2);
y(3)=Ri*sin(alfa/2);
x(4)=(Ro-2*wc)*cos(alfa/2);
y(4)=(Ro-2*wc)*sin(alfa/2);
%

% Calculation of the specific points of the coil
i=4; % as the first four points of the coil are given at the starting points
j=1; % Number of turns
M=0; %flag
while(1)
    i=i+1; %Increment the coil points
    ox=0; %The ox Parameter produces the diameter depending elongation...
           %of the coil to get the same clearance between the arcs
    for k=1:j % as the turns increase to the middle the distance has to
               % become bigger
        ox=ox+0.5*0.1905/36*(36-j-1);
    end

    %Calculating the first point of the turn
    % decrease the x by clearance + width of th tracks
    % the ox tho get the clearenc between the arc has to be added
    % there was a x^2 behaviour which is compensated by quadratic equ
    x(i)=x(1)-wc*j*0.65+1*wc+ox+3.9319e-04*(j^2-38*j+37);

    % The cos and tangens behavoir is given by the equ of the triangle
    y(i)=y(1)+(wc/cos(alfa/-10)+wc/tan(alfa/2))*(j)*0.615+1*wc;

    i=i+1; %next point

    x(i)=x(2)+wc*j*1.0; %go w+c to the middle
    % The cos and tangens behavoir is given by the equ of the triangle
    % 0.61 is an adjustment factor
    y(i)=y(2)+0.2135*(wc/cos(alfa/2)+wc/tan(alfa/2))*j;

    i=i+1; %next point

    x(i)=x(3)+wc*j*1.0; %go w+c to the middle
    % The cos and tangens behavoir is given by the equ of the triangle

```

## Appendix Motor

```

y(i)=y(3)-0.2135*(wc/cos(alfa/2)+wc/tan(alfa/2))*j;

i=i+1; %next point

% decrease the x by clearance + width of th tracks
% the ox tho get the clearenc between the arc has to be added
% 0.6338 and 0.13 are adjustment Parameters
x(i)=x(4)-wc*j*0.6338+ox+0.13;
% The cos and tangens behavoir is given by the equ of the triangle
y(i)=y(4)-(wc/cos(alfa/2)+wc/tan(alfa/2))*j*0.615+0.13;

% if the inner radius is equal 2 w+c then hold the inner radius
% constant and adapt the length step to hold the clearance constant
if y(i-1)<y(i-2)+wc;
    M=M+1; %managing the flag b to be set to j in the first time
    if M==1; % moving into the if junktion
        b=j;
    end
    y(i-1)=y(i-1-4); %Making y(i-1) a constant value
    %Increase the x steps to having a constant distance
    x(i-1)=x(i-1)+1.1*wc/cos(alfa/2)*1/tan(alfa/2)*(j-b+1);
    y(i-2)=y(i-2-4); %Making y(i-2) a constant value
    x(i-2)=x(i-2)+1.1*wc/cos(alfa/2)*1/tan(alfa/2)*(j-b+1);
    %Increase the x steps to having a constant distance
end

% if the coil y values getting together stop calculating new coil
% parameters
if y(i)<=y(i-3)+2*wc
    break;
end

% if the coil x parameters getting together stop calculating new coil
% parameters
if x(i) <= 3*wc+x(i-2)
    break;
end

j=j+1;
end

%Remove the last 4 to get a bigger clearance
%in the middle for adding the connector
%pins between two coils on the two layers
x=x(1:end-12);
y=y(1:end-12);

% Rote the coil to get the number of desired coils on one layer
for j = 1:Ns
    for i=1:length(x)
        v_l=sqrt(x(i)^2+y(i)^2); % Calculating the vectorlength of each point
        phi=atan(y(i)/x(i)); % Calculating the angle of each point
        x1(i,j)=v_l*cos(j*alfa+phi);
        y1(i,j)=v_l*sin(j*alfa+phi);
    end
end

%Calculation of the second layer Coil arrangement
%y is mirrored
x2=x1*1;
y2=y1*-1;

%Get the desired offset to the coils to put them on the board where you
%want
x1=(x1)+xo;
y1=(y1)+yo;
x2=x2+xo;
y2=y2+yo;

% Plot the coils to see if the arrangement is alright
for i = 1:Ns
    plot(x1(:,i),y1(:,i));
    hold all
end

```

## Appendix Motor

```
%determine the coil parameters
turncoil=round(length(x)/4); % how many turns has one coil
turnslayer=turncoil*Ns;      % how many turns has on layer
turnthreelayer=turnslayer*3; % how many turns have three layers

%% Script for printing wires
%Opening of a new txt. file
fid = fopen('coil.txt','wt');

fprintf(fid,'procedure CreateCoils();\n') ;
fprintf(fid,'var\n') ;
fprintf(fid,'board : IPCB_Board;\n') ;

%Declaration of the variables

i=1;
while (1)
    fprintf(fid,'track%d : IPCB_Track;\n', i);
    i=i+1;
    fprintf(fid,'arcN_ %d : IPCB_Track;\n', i);

    if i>=length(x1)+5
        break
    end
end

fprintf(fid,'\n');
fprintf(fid,'\n');
fprintf(fid,'begin\n');
fprintf(fid,'board := PCBServer.GetCurrentPCBBoard;\n');
fprintf(fid,'if (board = nil) then exit;\n');
fprintf(fid,'\n');
fprintf(fid,'\n');

%Printing the first Layer

fprintf(fid,'//Printing the first Layer\n');
fprintf(fid,'\n');

%Printing the Coils
for j=1:6

    i=4;
    while (1)

        i=i+1;

        fprintf(fid,'track%d := PCBServer.PCBObjectFactory(eTrackObject, eNoDimension, eCreate_Default);\n',i);
        fprintf(fid,'track%d.x1 := MMsToCoord(%d);\n',i,x1(i,j));
        fprintf(fid,'track%d.y1 := MMsToCoord(%d);\n',i,y1(i,j));
        fprintf(fid,'track%d.x2 := MMsToCoord(%d);\n',i,x1(i+1,j));
        fprintf(fid,'track%d.y2 := MMsToCoord(%d);\n',i,y1(i+1,j));
        fprintf(fid,'track%d.Width := MMsToCoord(%d);\n',i,w);
        fprintf(fid,'track%d.Layer := eTopLayer;\n',i);
        fprintf(fid,'Board.AddPCBObject(track%d);\n',i);
        fprintf(fid,'\n');

        i=i+1;

        fprintf(fid,'track%d := PCBServer.PCBObjectFactory(eTrackObject, eNoDimension, eCreate_Default);\n',i);
        fprintf(fid,'track%d.x1 := MMsToCoord(%d);\n',i,x1(i,j));
        fprintf(fid,'track%d.y1 := MMsToCoord(%d);\n',i,y1(i,j));
        fprintf(fid,'track%d.x2 := MMsToCoord(%d);\n',i,x1(i+1,j));
        fprintf(fid,'track%d.y2 := MMsToCoord(%d);\n',i,y1(i+1,j));
        fprintf(fid,'track%d.Width := MMsToCoord(%d);\n',i,w);
        fprintf(fid,'track%d.Layer := eTopLayer;\n',i);
        fprintf(fid,'Board.AddPCBObject(track%d);\n',i);
        fprintf(fid,'\n');

        i=i+1;

        fprintf(fid,'track%d := PCBServer.PCBObjectFactory(eTrackObject, eNoDimension, eCreate_Default);\n',i);
        fprintf(fid,'track%d.x1 := MMsToCoord(%d);\n',i,x1(i,j));
```

## Appendix Motor

```
fprintf(fid, 'track%d.y1 := MMsToCoord(%d);\n', i, y1(i, j));
fprintf(fid, 'track%d.x2 := MMsToCoord(%d);\n', i, x1(i+1, j));
fprintf(fid, 'track%d.y2 := MMsToCoord(%d);\n', i, y1(i+1, j));
fprintf(fid, 'track%d.Width := MMsToCoord(%d);\n', i, w);
fprintf(fid, 'track%d.Layer := eTopLayer;\n', i);
fprintf(fid, 'Board.AddPCBObject(track%d);\n', i);
fprintf(fid, '\n');

i=i+1;
if i >= length(y1(:,1))-1
    break;
end
fprintf(fid, 'arcN_%d := PCBServer.PCBObjectFactory(eArcObject, eNoDimension, eCreate_Default);\n', i);
fprintf(fid, 'arcN_%d.XCenter := MMsToCoord(%d);\n', i, xo);
fprintf(fid, 'arcN_%d.YCenter := MMsToCoord(%d);\n', i, yo);
radius=sqrt((xo-x1(i, j))^2+(yo-y1(i, j))^2);
fprintf(fid, 'arcN_%d.Radius := MMsToCoord(%d);\n', i, radius);
fprintf(fid, 'arcN_%d.LineWidth := MMsToCoord(0.254);\n', i);
startangle=atan((y1(i+1, j)-yo)/(x1(i+1, j)-xo))/pi*180;
if (x1(i+1, j)-xo) < 0
    startangle=startangle+180;
end

fprintf(fid, 'arcN_%d.StartAngle := %d;\n', i, startangle);
endangle=atan((y1(i, j)-yo)/(x1(i, j)-xo))/pi*180;
if (x1(i, j)-xo) < 0
    endangle=endangle+180;
end

fprintf(fid, 'arcN_%d.EndAngle := %d;\n', i, endangle);
fprintf(fid, 'arcN_%d.Layer := eTopLayer;\n', i);
fprintf(fid, 'arcN_%d.LineWidth := MMsToCoord(%d);\n', i, w);
fprintf(fid, 'Board.AddPCBObject(arcN_%d);\n', i);
fprintf(fid, '\n');

end
end

%Second Layer

fprintf(fid, '//Printing the second Layer\n');
fprintf(fid, '\n');
for j=1:Ns

    i=4;
    while (1)

        i=i+1;

        fprintf(fid, 'track%d := PCBServer.PCBObjectFactory(eTrackObject, eNoDimension, eCreate_Default);\n', i);
        fprintf(fid, 'track%d.x1 := MMsToCoord(%d);\n', i, x2(i, j));
        fprintf(fid, 'track%d.y1 := MMsToCoord(%d);\n', i, y2(i, j));
        fprintf(fid, 'track%d.x2 := MMsToCoord(%d);\n', i, x2(i+1, j));
        fprintf(fid, 'track%d.y2 := MMsToCoord(%d);\n', i, y2(i+1, j));
        fprintf(fid, 'track%d.Width := MMsToCoord(%d);\n', i, w);
        fprintf(fid, 'track%d.Layer := eBottomLayer;\n', i);
        fprintf(fid, 'Board.AddPCBObject(track%d);\n', i);
        fprintf(fid, '\n');

        i=i+1;

        fprintf(fid, 'track%d := PCBServer.PCBObjectFactory(eTrackObject, eNoDimension, eCreate_Default);\n', i);
        fprintf(fid, 'track%d.x1 := MMsToCoord(%d);\n', i, x2(i, j));
        fprintf(fid, 'track%d.y1 := MMsToCoord(%d);\n', i, y2(i, j));
        fprintf(fid, 'track%d.x2 := MMsToCoord(%d);\n', i, x2(i+1, j));
        fprintf(fid, 'track%d.y2 := MMsToCoord(%d);\n', i, y2(i+1, j));
        fprintf(fid, 'track%d.Width := MMsToCoord(%d);\n', i, w);
        fprintf(fid, 'track%d.Layer := eBottomLayer;\n', i);
        fprintf(fid, 'Board.AddPCBObject(track%d);\n', i);
        fprintf(fid, '\n');

        i=i+1;
```



## Appendix Motor

```

fprintf(fid, 'track%d := PCBServer.PCBOBJECTFactory(eTrackObject, eNoDimension, eCre-
ate_Default);\n', i);
fprintf(fid, 'track%d.x1 := MMsToCoord(%d);\n', i, x2(i, j));
fprintf(fid, 'track%d.y1 := MMsToCoord(%d);\n', i, y2(i, j));
fprintf(fid, 'track%d.x2 := MMsToCoord(%d);\n', i, x2(i+1, j));
fprintf(fid, 'track%d.y2 := MMsToCoord(%d);\n', i, y2(i+1, j));
fprintf(fid, 'track%d.Width := MMsToCoord(%d);\n', i, w);
fprintf(fid, 'track%d.Layer := eBottomLayer;\n', i);
fprintf(fid, 'Board.AddPCBOBJECT(track%d);\n', i);
fprintf(fid, '\n');

i=i+1;
if i >= length(y1(:,1))-5
    break;
end
fprintf(fid, 'arcN_%d := PCBServer.PCBOBJECTFactory(eArcObject, eNoDimension, eCre-
ate_Default);\n', i);
fprintf(fid, 'arcN_%d.XCenter := MMsToCoord(%d);\n', i, xo);
fprintf(fid, 'arcN_%d.YCenter := MMsToCoord(%d);\n', i, yo);
radius=sqrt((xo-x2(i, j))^2+(yo-y2(i, j))^2);
fprintf(fid, 'arcN_%d.Radius := MMsToCoord(%d);\n', i, radius);
fprintf(fid, 'arcN_%d.LineWidth := MMsToCoord(0.254);\n', i);
startangle=atan((y2(i, j)-yo)/(x2(i, j)-xo))/pi*180;
if (x2(i, j)-xo) < 0
    startangle=startangle+180;
end

fprintf(fid, 'arcN_%d.StartAngle := %d;\n', i, startangle);
endangle=atan((y2(i+1, j)-yo)/(x2(i+1, j)-xo))/pi*180;
if (x2(i+1, j)-xo) < 0
    endangle=endangle+180;
end

fprintf(fid, 'arcN_%d.EndAngle := %d;\n', i, endangle);
fprintf(fid, 'arcN_%d.Layer := eBottomLayer;\n', i);
fprintf(fid, 'arcN_%d.LineWidth := MMsToCoord(%d);\n', i, w);
fprintf(fid, 'Board.AddPCBOBJECT(arcN_%d);\n', i);
fprintf(fid, '\n');

end
end

% Calculation of the Points for Connection pads
Px1s=94.2-xo;
Py1s=0.0;
Pl1alfa=atan(Py1s/Px1s);
Px2s=95.35-xo;
Py2s=0.0;
P2alfa=atan(Py2s/Px2s);
Px3s=107.7-xo;
Py3s=0;
for i=1:Ns
    Px1(i)=Px1s*cos(alfa*i-Pl1alfa)+xo;
    Px2(i)=Px2s*cos(alfa*i-P2alfa)+xo;
    Py1(i)=Px1s*sin(alfa*i-Pl1alfa)+yo;
    Py2(i)=Px2s*sin(alfa*i-P2alfa)+yo;
    Px3(i)=Px3s*cos(alfa*i)+yo;
    Py3(i)=Px3s*sin(alfa*i)+yo;
    plot(Px1(i), Py1(i), 'o');
    plot(Px2(i), Py2(i), 'o');
    plot(Px3(i), Py3(i), 'o');
end

% % Printing the Pad places
for i=1:Ns
    fprintf(fid, 'track%d := PCBServer.PCBOBJECTFactory(eTrackObject, eNoDimension, eCre-
ate_Default);\n', i);
    fprintf(fid, 'track%d.x1 := MMsToCoord(%d);\n', i, Px1(i));
    fprintf(fid, 'track%d.y1 := MMsToCoord(%d);\n', i, Py1(i));
    fprintf(fid, 'track%d.x2 := MMsToCoord(%d);\n', i, Px1(i)+0.1);
    fprintf(fid, 'track%d.y2 := MMsToCoord(%d);\n', i, Py1(i)+0.1);
    fprintf(fid, 'track%d.Width := MMsToCoord(%d);\n', i, w);
    fprintf(fid, 'track%d.Layer := eTopLayer;\n', i);
    fprintf(fid, 'Board.AddPCBOBJECT(track%d);\n', i);
end

```

## Appendix Motor

```

fprintf(fid, '\n');

fprintf(fid, 'track%d := PCBServer.PCBObjectFactory(eTrackObject, eNoDimension, eCreate_Default);\n', i);
fprintf(fid, 'track%d.x1 := MMsToCoord(%d);\n', i, Px2(i));
fprintf(fid, 'track%d.y1 := MMsToCoord(%d);\n', i, Py2(i));
fprintf(fid, 'track%d.x2 := MMsToCoord(%d);\n', i, Px2(i)+0.1);
fprintf(fid, 'track%d.y2 := MMsToCoord(%d);\n', i, Py2(i)+0.1);
fprintf(fid, 'track%d.Width := MMsToCoord(%d);\n', i, w);
fprintf(fid, 'track%d.Layer := eTopLayer;\n', i);
fprintf(fid, 'Board.AddPCBObject(track%d);\n', i);
fprintf(fid, '\n');

end

% Printing the Pad places outside the coil
fprintf(fid, '//Pads Outside the coils\n');
for i=1:Ns
    fprintf(fid, 'track%d := PCBServer.PCBObjectFactory(eTrackObject, eNoDimension, eCreate_Default);\n', i);
    fprintf(fid, 'track%d.x1 := MMsToCoord(%d);\n', i, Px3(i));
    fprintf(fid, 'track%d.y1 := MMsToCoord(%d);\n', i, Py3(i));
    fprintf(fid, 'track%d.x2 := MMsToCoord(%d);\n', i, Px3(i)+0.1);
    fprintf(fid, 'track%d.y2 := MMsToCoord(%d);\n', i, Py3(i)+0.1);
    fprintf(fid, 'track%d.Width := MMsToCoord(%d);\n', i, w);
    fprintf(fid, 'track%d.Layer := eTopLayer;\n', i);
    fprintf(fid, 'Board.AddPCBObject(track%d);\n', i);
    fprintf(fid, '\n');
end
fprintf(fid, 'end;\n');
fclose(fid);

% Calculation of the wire length of one coil
lcoil=0;
for i = 1:length(x)-1
    lcoil=lcoil+sqrt((x(i+1)-x(i))^2+(y(i+1)-y(i))^2);
end

%Calculation of the maximum tourge per coil
I = 50E-3; %A Current in the Coil
B_air=0.129; %T
Layers=4;
T_coil_layer=0;
Tcoil1=0;
F_turn_g=0;
l_turn_g = 0;
i=1;
j=1;
while(i)
    %length of the n. turn
    % l_turn(j) = sqrt((x(i+1)-x(i))^2+(y(i+1)-y(i))^2);
    lo(j)=sqrt(x(i)^2+y(i)^2)/1000;
    li(j)=sqrt(x(i+1)^2+y(i+1)^2)/1000;
    T_turn(j) = B_air*I*((1/2*lo(j)^2)-(1/2*li(j)^2))*2;

    i=i+4;
    j=j+1;
    if i>=length(x)-1
        break;
    end
end

T_coil = sum(T_turn)*Layers;

T_max = T_coil; %2 Coils have max. tourge

%Motorconstants
Kt=T_max/I
Kn=1/(2*pi*Kt)

%Calculation of the total length of one coil
i=1;
while(i)
    %length of the n. turn
    l_turn(i) = sqrt((x(i+1)-x(i))^2+(y(i+1)-y(i))^2);

```

## Appendix Motor

```

        i=i+1;
        if i>length(x)-1
            break;
        end
    end;
    l_ges=sum(l_turn);

    %Calculation of the resistance of one Coil
    h      = 35.55E-6; %m hith of the wire of the pcb board
    l_turn_ges = sum(l_turn)/1000;
    l_coil   = l_turn_ges*Layers; %!!!! has to be properly calculated
    rohcu    = 1.721E-2; %Ohm*mm^2/m
    R_coil    = rohcu*l_coil/((w)*h*1000); %rohcu [Ohms*mm^2/m]

    %Aproximation of the incutance
    mue0 = 1.2566e-06;
    N=35;
    A=2E-4;
    l=1.5E-3;
    L=mue0*N^2*A/l;

    %Calculation of the Torque constant for round magnets
    dl=20.6/2;
    ds=7.9375/2;
    j=1;
    for i=0:0.001:(2*pi);
        x1(j)=dl*sin(i);
        y1(j)=dl*cos(i);
        xs(j)=ds*sin(i);
        ys(j)=ds*cos(i);
        j=j+1;
    end
    %
    x1=x1+27;
    y1=y1;
    xs=x1+12.5;
    ys=ys;

    % Rotate the magnets
    alfa=45/180*pi;
    for j = 1:8
        for i=1:length(x1)
            v_l=sqrt(x1(i)^2+y1(i)^2); % Calculating the vectorlength of each point
            phi=atan(y1(i)/x1(i)); % Calculating the angle of each point
            x11(i,j)=v_l*cos(j*alfa+phi);
            y11(i,j)=v_l*sin(j*alfa+phi);
        end
    end
    for j = 1:8
        for i=1:length(x1)
            v_l=sqrt(xs(i)^2+ys(i)^2); % Calculating the vectorlength of each point
            phi=atan(ys(i)/xs(i)); % Calculating the angle of each point
            xs1(i,j)=v_l*cos(j*alfa+phi);
            ys1(i,j)=v_l*sin(j*alfa+phi);
        end
    end
    x11=x11+xo;
    y11=y11+yo;
    xs1=xs1+xo;
    ys1=ys1+yo;
    plot(x11,y11,'k',xs1,ys1,'k')

```

### 9.4.2 Motormodell parameter script

```
%% Comparasion Model speed Step to Measured speed step
close all;

%% Model
R=59.5; %Ohms (Measured Multimeter)
L=4E-4; %H (fitted in inductance_measurement_model)
J = 1.15e+02/1000^2; %out of CAD
Fr=8e-6;
Fc=0.15E-3;
Kt=0.0233;
    %0.0297
G=1.5;
V=10;

%% Controller

kp=190; %648.0348
Ir=10;

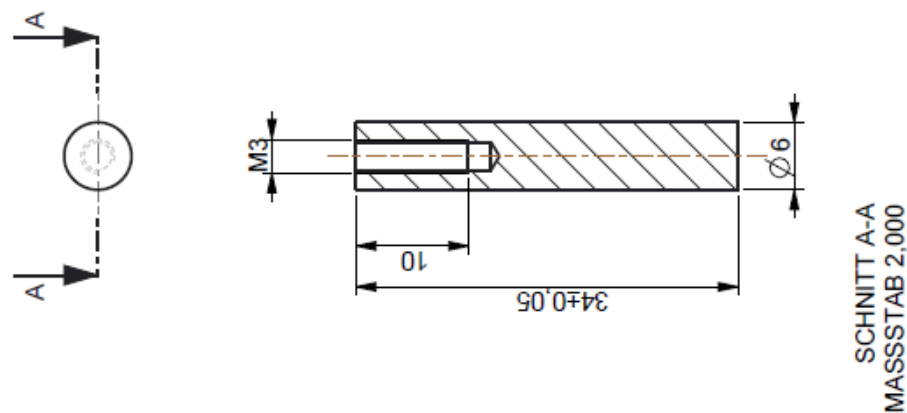
lag=tf([1 Ir], [1 0]);

%Lead2
alpha2=18;
f_lead2=30;
w0_lead2=f_lead2*2*pi;
k_lead2=sqrt(alpha2);
a_lead2=w0_lead2/sqrt(alpha2);
b_lead2=w0_lead2*sqrt(alpha2);
lead2=k_lead2*tf([1 a_lead2],[1 b_lead2]);

C=(kp*lag*lead2);
figure()
bode(C)
```

10 Appendix magnetic bearing

10.1 Mechanical design



Bauteil 4x fertigen

Dateiname des Zeichnungsobjektes: COIL_1				Dateiname der Zeichnung: COIL_1		Gew.: kg	
PART				Maßstab 1,000		Werkstoff 1.6	
Allgemeintol. DIN ISO 2768-m-S				Werkstoff -anforderung DN 6784		Benennung Coil 1 Ersteller: Markus Rab Tel. 0171/14880 Email: markus.rab@drb.de	
				Datum		Name	
				Bearb. 09.02.04		09.02.04	
				Gepr. 09.02.04		09.02.04	
				Norm			

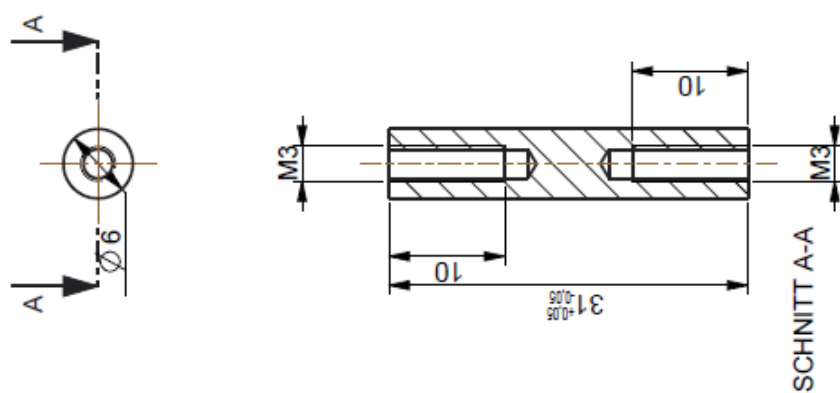
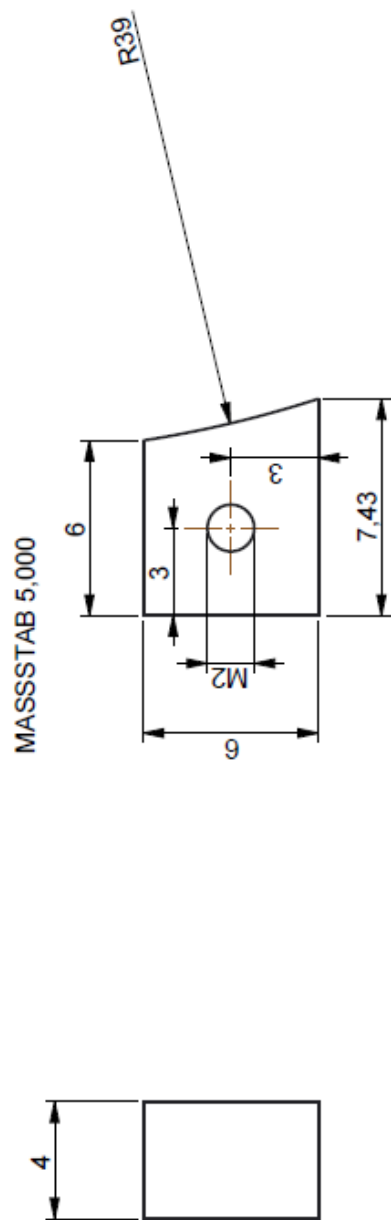


**Figure 137 CAD drawing bearing / reluctance actuator X-Y core**

Bauteil 4x fertigen

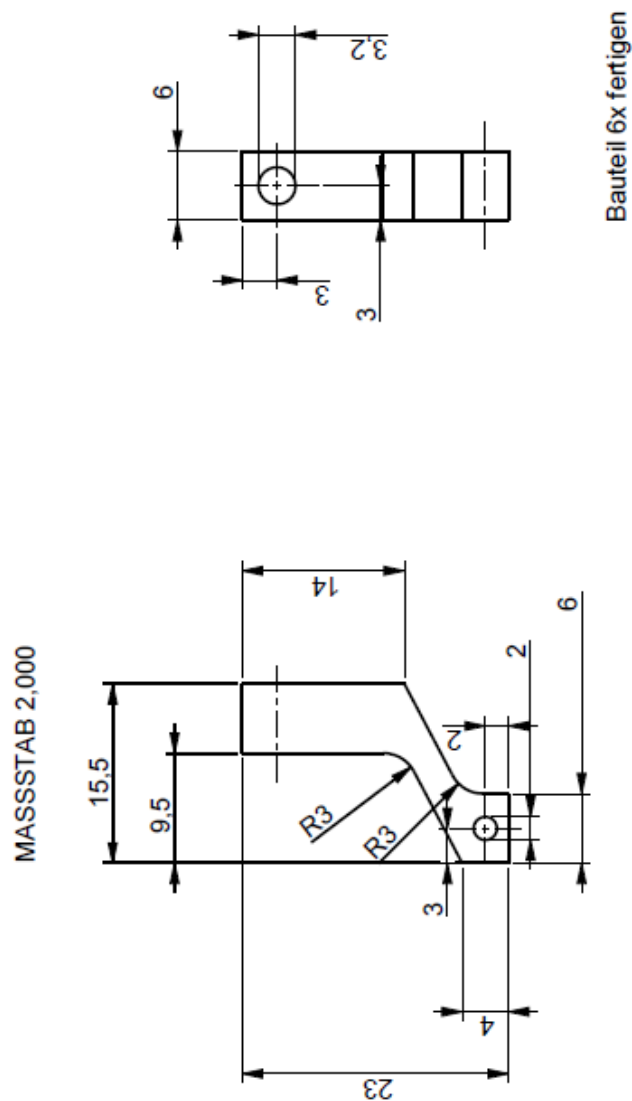
[illegible]



Bauteil 6x fertigen

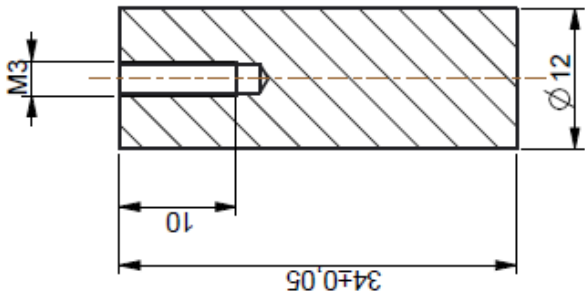
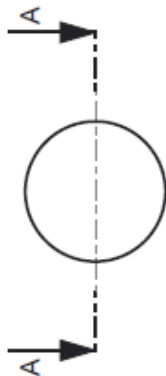
Dateiname des Zeichnungsobjekts: COILPARTXY				Dateiname der Zeichnung: COILPARTXY		Gew.: kg	
Allgemeintol. DIN ISO 2768-m-S				Vorstück -leiten DN 6784		Maßstab 2,000	
				Name			
				Bear. 8098/01			
				Gepr. 8098/01			
Datum				Name		Bemerkung: Qualität Fertiger Nachschub Tel. 0172/1980 Email: Michael.Feig@vde.de	
Bear. 8098/01				8098/01			
Gepr. 8098/01				8098/01			
Norm							
(Firmenlogo)						Angebotgeber/Endabnehmer: Peter Berg Tel.	
Datum				Name		8098/01	
Änderung						1 Bl.	
Zust.				Nam. (Urspr.)		(Ers.d.)	

Figure 138 CAD drawing bearing / X-Y part for actuator



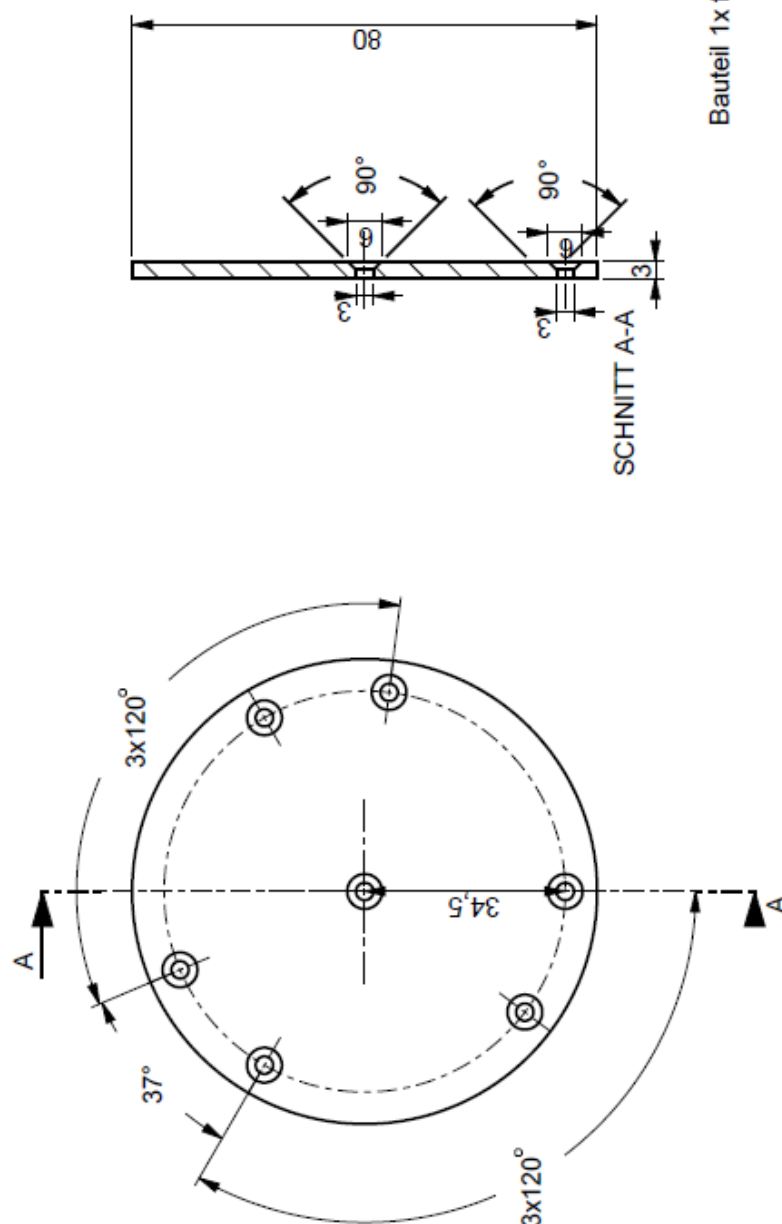
Dateiname des Zeichnungsobjektes: COILPARTXY2				Dateityp: PART		Dateiname der Zeichnung: COILPARTXY2		Gew.: kg	
				Allgemeintitel: DIN ISO 2768-m-S		Werkstoff: -Jantian DN 6784		Maßstab 1,000  Werkstoff (Stahl (unverfestet))	
				Datum:		Name:			
				Bear. 88888888		88888888			
				Gepr. 88888888		88888888			
				Norm:					





Bauteil 1x fertigen

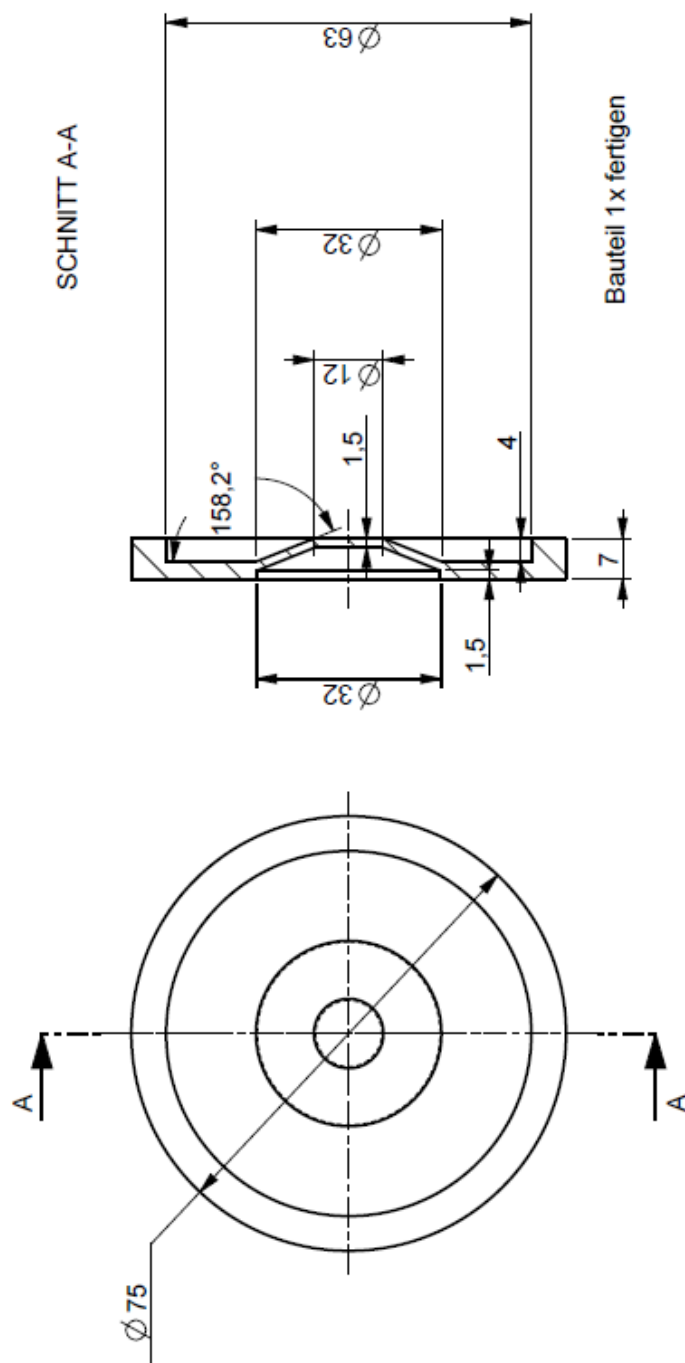
Dateiname des Zeichnungsobjektes: MIDDLERRETURN				Dateiname der Zeichnung: MIDDLERRETURN		Gew.: kg	
				Allgemeintol. DIN ISO 2768-m-S	Werkstück -Anfert. DN 6704	Maßstab 1,000	
						Werkstoff: 06	
						Benennung: Mädelchen	
						Eckler-Miller-Prob	
						Id 01721488	
					End-Materialprüfung		
					Aquaquadrachide: 1 Bl.		
					1 Bl.		
					(Ers.f.)		
					(Ers.d.)		



Bauteil 1x fertigen

[illegible]

**Figure 141 CAD drawing bearing / return iron**



Dateiname der Zeichnung:		Dateiname der Zeichnung:	
ROTORIRON		ROTORIRON	
Allgemeintol. DIN ISO 2768-m-S		Maßstab 1,000	
Bear. 800000		Gew.: kg	
Gepr. 800000		Werkstoff	
Norm		Bemerkung: Rotor Gebrauch: Rotor Id (17011488) End (17011488)	
(Firmenlogo)		Angezeichnete/r Firma/ig/	
Datum		Blatt	
Zust.		2 Bl.	
Änderung		(Ers.f.)	
Datum		(Ers.d.)	
Namf.(Urspr.)			

Figure 142 CAD drawing bearing / rotor iron

## 10.2 Test specifications

Table 15 System frequency response magnetic bearing

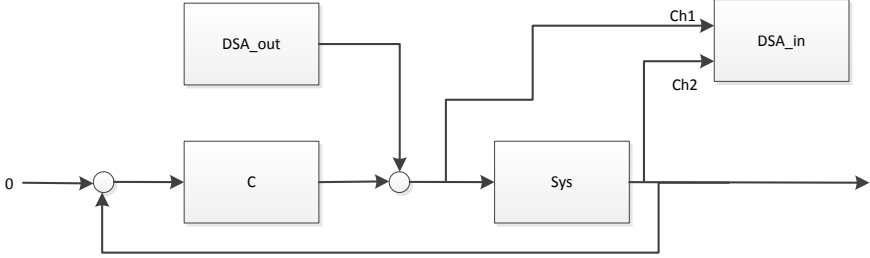
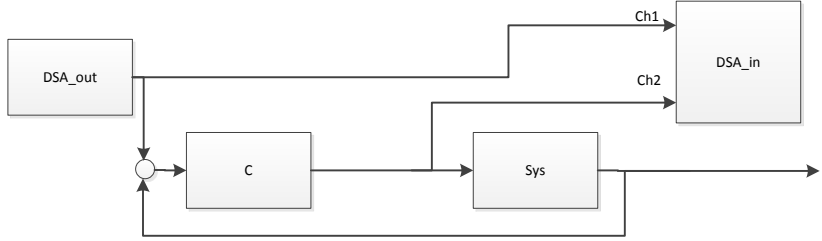
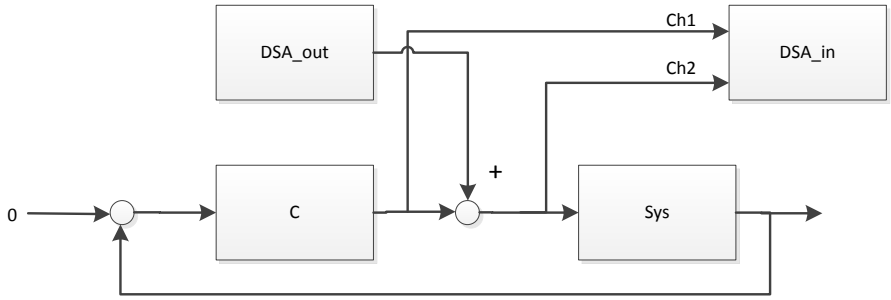
System frequency response	
<b>1 Aim</b> .	Measuring the frequency response of the system for comparison to the model
<b>2 Specification</b> .	<p>To measure the frequency response of the motor, the following values have to be measured:</p> <p><b>Input values</b></p> <ul style="list-style-type: none"> <li>Sine signal (in LabVIEW after the controller) which is generated in the LabVIEW DSA tool</li> </ul> <p><b>Measured values</b></p> <ul style="list-style-type: none"> <li>Rotor position</li> <li>Control effort</li> </ul>
<b>3 Test Procedure</b> .	<p><b>Preparation:</b></p> <ul style="list-style-type: none"> <li>The DSA measurement tool is implemented in LabVIEW as shown</li> <li>A stable position controller is implemented. This controller keep the motor in a controlled position. There are no particular specifications on this controller. It just has to show a stable behavior.</li> </ul>  <p><b>Test Procedure:</b></p> <ul style="list-style-type: none"> <li>The motor and LabVIEW system is started</li> <li>The position controller keeps the system in a stable position</li> <li>For the DSA tool the following values have to be adjusted             <ul style="list-style-type: none"> <li>Start frequency 1 Hz</li> <li>Stop frequency 500 Hz</li> <li>Number of frequency bins: 50</li> <li>Setting cycles : 20</li> <li>Calculation cycles 50</li> <li>Sampling time: 0.0005</li> </ul> </li> <li>The DSA measurement is started by starting the start button</li> <li>The frequency response measurement is done automatically</li> <li>The results are compared to the simulated values</li> </ul>

Table 16 Decoupling verification magnetic bearing

Decoupling verification	
<b>1 Aim</b> .	Measuring the control effort in the different axis when one axis is actuated in order to verify the decoupling of the system
<b>2 Specification</b> .	<p>To measure the control effort using the DSA tool, the following values have to be measured:</p> <p><b>Input values</b></p> <ul style="list-style-type: none"> <li>Sine signal (in LabVIEW after the controller) which is generated in the LabVIEW DSA tool</li> </ul> <p><b>Measured values</b></p> <ul style="list-style-type: none"> <li>DSA input (desired position)</li> <li>Control effort</li> </ul>
<b>3 Test Procedure</b> .	<p><b>Preparation:</b></p> <ul style="list-style-type: none"> <li>The DSA measurement tool is implemented in LabVIEW as shown</li> <li>A stable position controller is implemented.</li> </ul>  <p><b>Test Procedure:</b></p> <ul style="list-style-type: none"> <li>The motor and LabVIEW system is started</li> <li>The position controller keeps the system in a stable position</li> <li>For the DSA tool the following values have to be adjusted <ul style="list-style-type: none"> <li>Start frequency 1 Hz</li> <li>Stop frequency 500 Hz</li> <li>Number of frequency bins: 50</li> <li>Setting cycles : 20</li> <li>Calculation cycles 50</li> <li>Sampling time: 0.0005</li> </ul> </li> <li>The DSA measurement for the actuated and unactuated axis is done</li> <li>The differences between actuated and unactuated axes are compared and rated regarding their decoupling</li> <li>The control effort of the actuated axis is compared to the predicted model behavior</li> </ul>

**Table 17 Return ratio measurement magnetic bearing**

Return ratio measurement	
<b>1 Aim</b> .	Measuring the return ratio of the system to verify the stability of the model based designed controller
<b>2 Specification</b> .	<p>To measure the return ratio, the following values have to be measured:</p> <p><b>Input values</b></p> <ul style="list-style-type: none"> <li>Sine signal (in LabVIEW after the controller) which is generated in the LabVIEW DSA tool</li> </ul> <p><b>Measured values</b></p> <ul style="list-style-type: none"> <li>Loop transition in front and after the excitation signal</li> <li>(Rotor position)</li> </ul>
<b>3 Test Procedure</b> .	<p><b>Preparation:</b></p> <ul style="list-style-type: none"> <li>The DSA measurement tool is implemented in LabVIEW as shown below</li> </ul>  <p><b>Test Procedure:</b></p> <ul style="list-style-type: none"> <li>The motor and LabVIEW system is started</li> <li>The position controller keeps the system in a stable position</li> <li>For the DSA tool the following values have to be adjusted <ul style="list-style-type: none"> <li>Start frequency 1 Hz</li> <li>Stop frequency 500 Hz</li> <li>Number of frequency bins: 50</li> <li>Setting cycles : 20</li> <li>Calculation cycles 50</li> <li>Sampling time: 0.0005</li> </ul> </li> <li>The DSA measurement is started by pushing the start button</li> <li>The return ratio measurement is done automatically</li> <li>The return ratio is characterized in relation to phase and gain margin</li> <li>comparison of measured and expected return ratio</li> </ul>

### 10.3 DSA Tool Test

The DSA tool has been tested to verify the accuracy in the magnitude and phase measurement. In this test, the system has been connected to a programmed low pass filter with a frequency of 100 Hz. The DSA tool is connected in the following configuration:

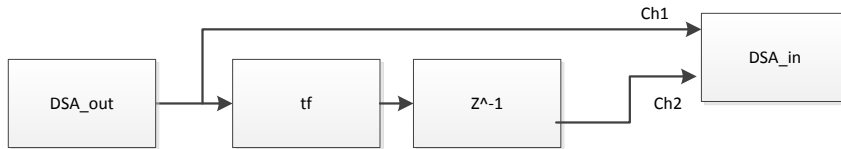


Figure 143 Implementation DSA tool test

The measured frequency response with a comparison to the model is shown in the figure below. It can be seen, that there is a good comparability in the magnitude of the plot even to high frequencies. In the measurement of the phase there is an extra phase lag which cannot be described. This extra phase lag effects the phase negatively for frequencies higher 100 Hz.

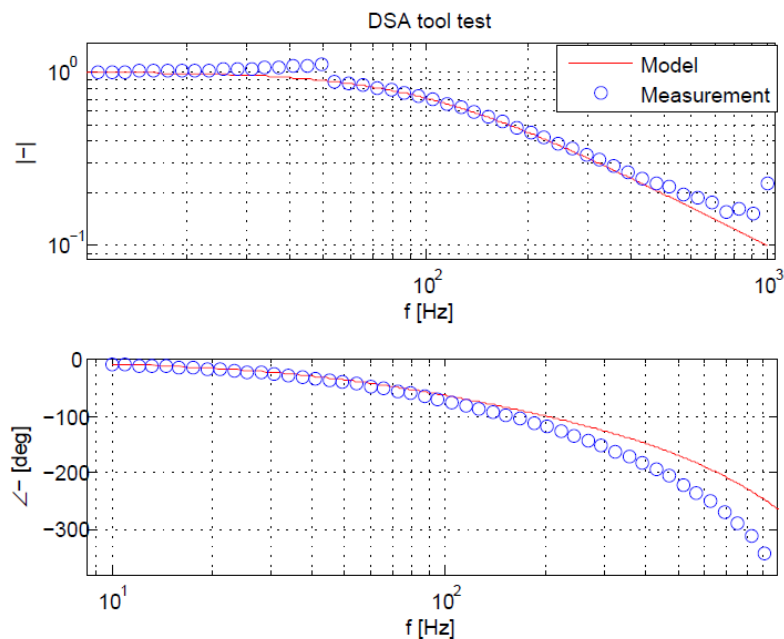


Figure 144 DSA tool test

## 10.4 Simulink model

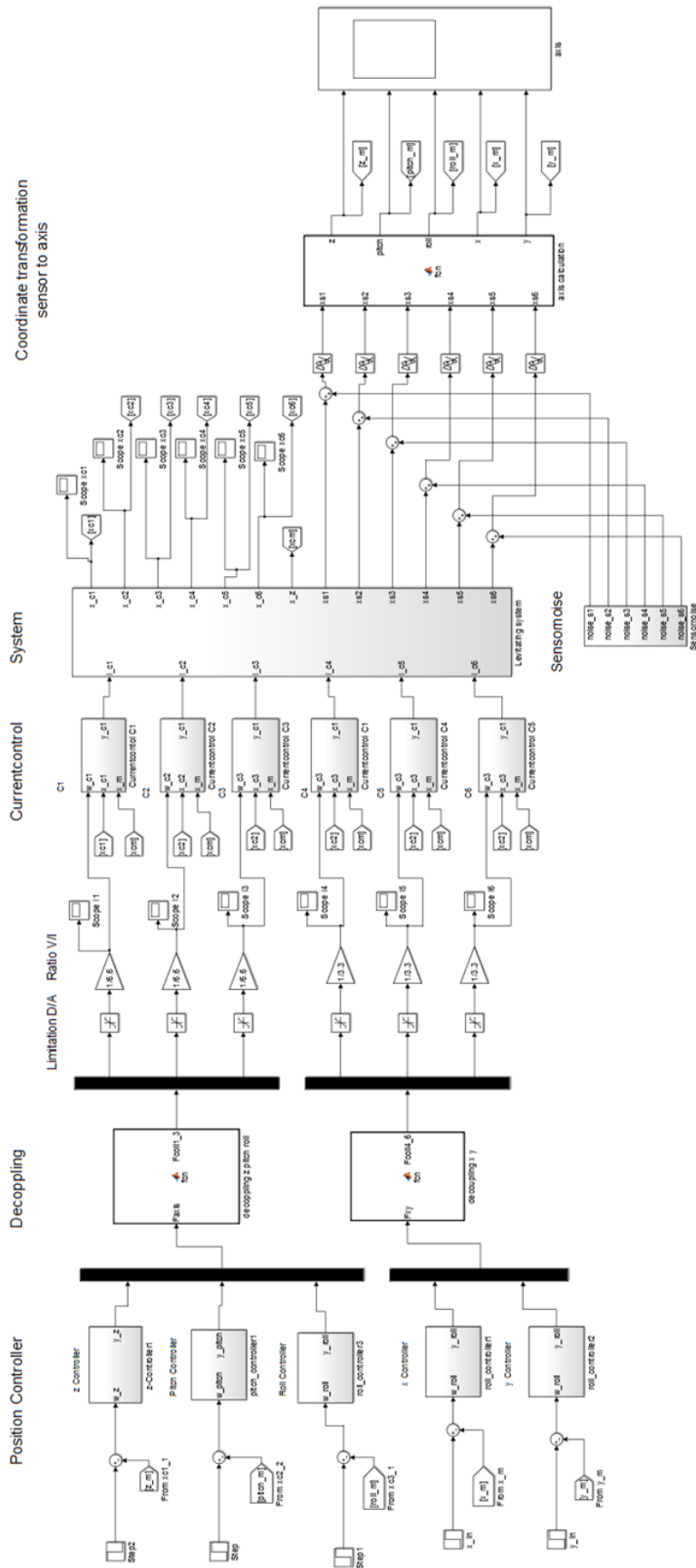


Figure 145 Simulink model top view



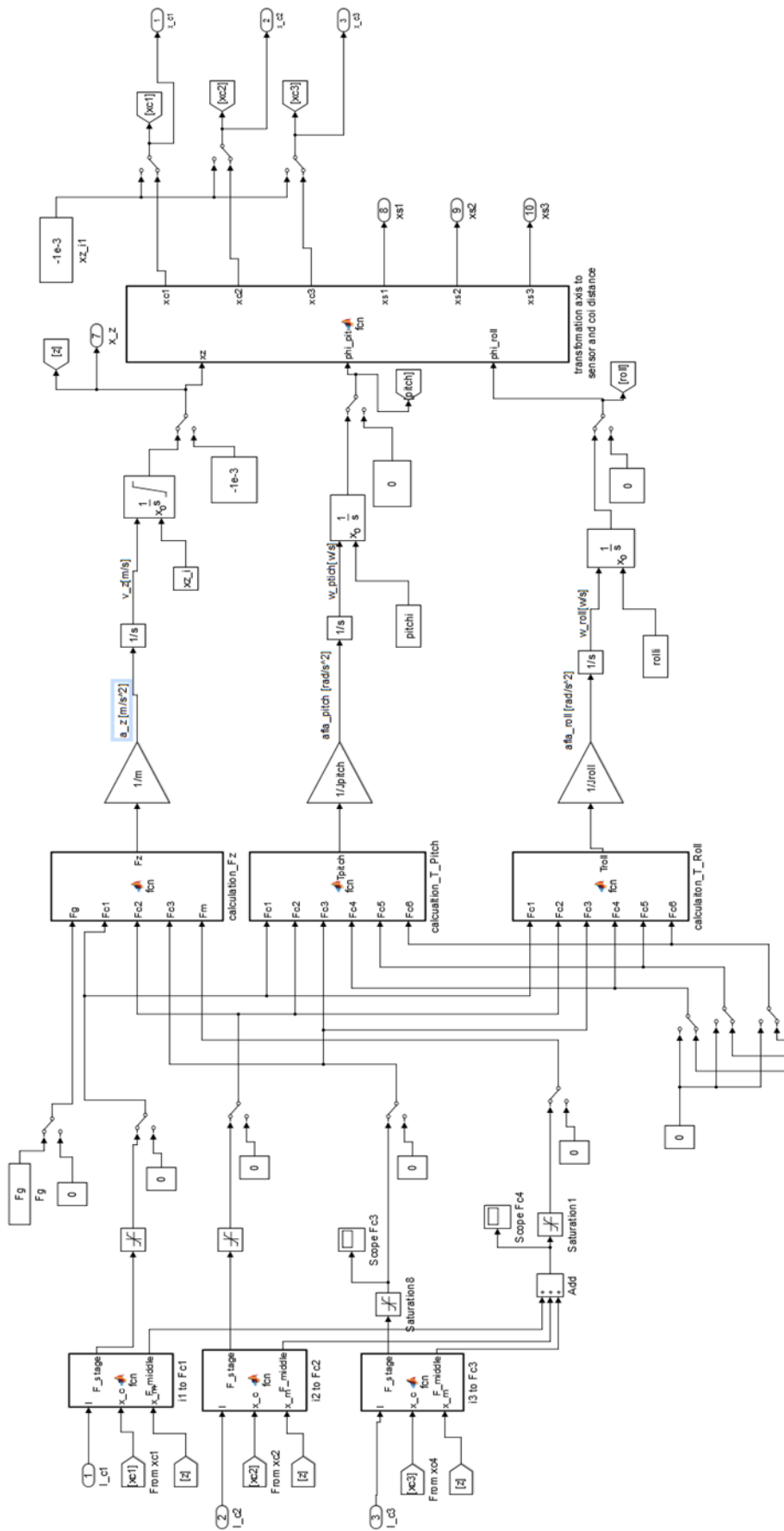


Figure 146 Simulink model Z, Pitch and Roll axis

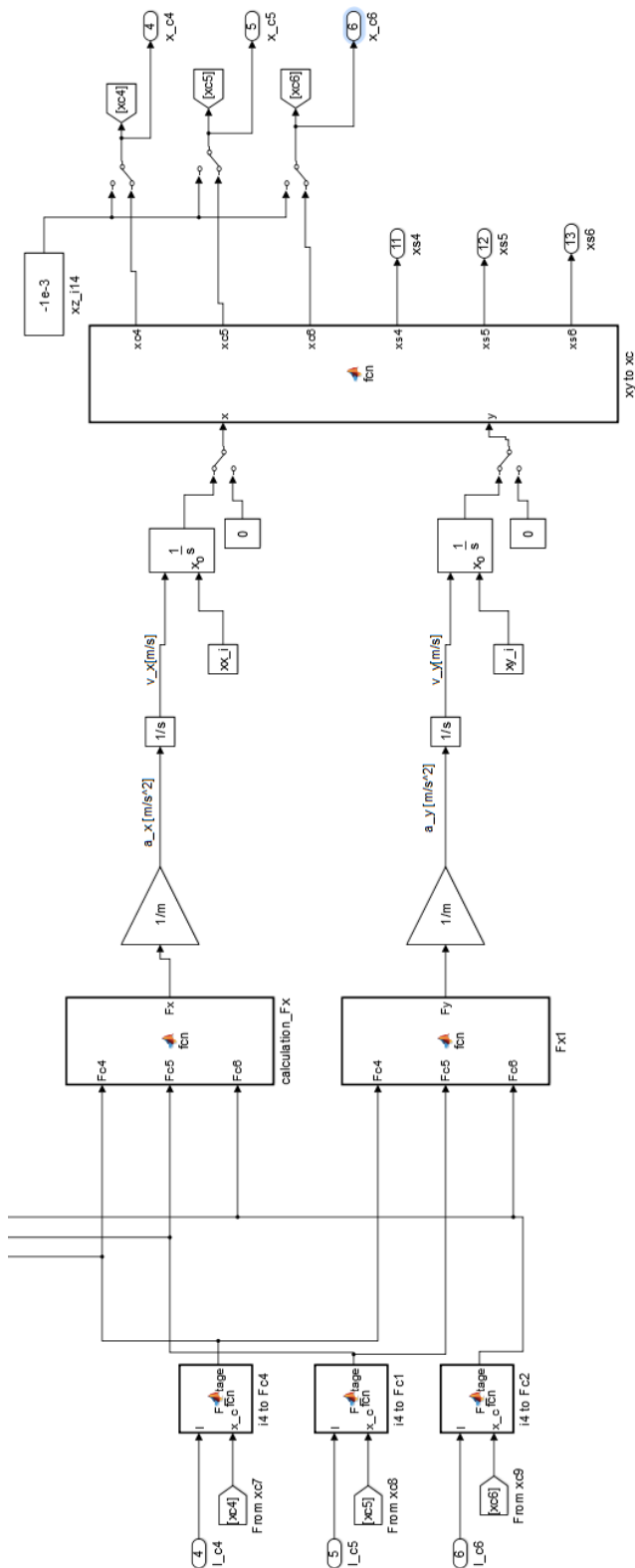


Figure 147 Simlink model of the X and Y axis

current control for one coil

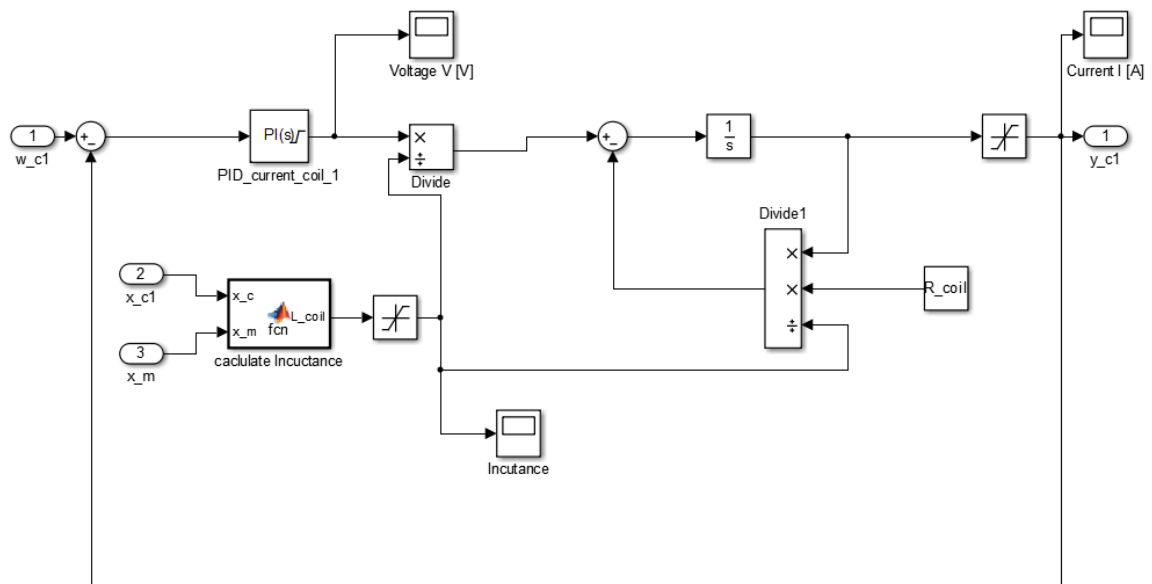


Figure 148 Simulink model current control

### Magnetic bearing parameters:

```
clear; clc;

%Initial Conditions
xz_i=-2E-3;
rolli=0.005;
pitchi=0.005;
xx_i=0.0e-3;;
xy_i=0.0e-3;
timed=5e-4;

% Gravity Force
m=0.186; %kg
g=9.81;
Fg=m*g;
```

### Decoupling Z, Pitch, Roll

```
function Fcoil1_3 = fcn(Faxis)

A=[1/3 -0.33 -0.57;
  1/3 -0.33 0.57;
  1/3 0.66 0];
```

## Appendix magnetic bearing

```
Fcoil1_3=A*Faxis;
```

### Decoupling X,Y

```
function Fcoil4_6 = fcn(Fxy)

phicc=37*pi/180;
B=[cos(-phicc) sin(-phicc);
   cos(120*pi/180-phicc) sin(120*pi/180-phicc);
   cos(240*pi/180-phicc) sin(240*pi/180-phicc)];

Fcoil4_6=B*Fxy;
```

### Inductance calculation

```
function L_coil = fcn(x_c,x_m)

x_c=abs(x_c);
x_m=abs(x_m);
N=570;
mue0 = 4*pi*10^-7; %N/A^2
d_stage=6e-3; %m
A_stage=d_stage^2*pi/4;
d_smiddle=12e-3;
A_middle=d_smiddle^2*pi/4;
muer=500;

R_stage = x_c/(mue0*A_stage);
R_middle = x_m/(mue0*A_middle);

R_tot=R_stage+R_middle;

L_coil=(N)^2/R_tot;
```

### Force calculation

```
function [F_stage,F_middle] = fcn(I,x_c,x_m)
x_c=x_c*-1;
if x_c<=1e-4
    x_c=1e-4;
end
x_m=x_m*-1;
if x_m<=1e-4
    x_m=1e-4;
end
mue0=4*pi*10^-7;
N=570;

d_stage=6e-3; %m
A_stage=d_stage^2*pi/4;
d_smiddle=12e-3;
A_middle=d_smiddle^2*pi/4;

R_stage = x_c/(mue0*A_stage);
```

## Appendix magnetic bearing

```
R_middle      = x_m/(mue0*A_middle);

R_tot=R_stage+R_middle;
Sigma        = N*I; %A
% Magnetic Flux
Phi          = Sigma/R_tot; %Vs (kg*m^2/(A*s^2) (T*m^2)
% Flux density
B_stage      = Phi/A_stage;
B_middle     = Phi/A_middle;
%Actuator specific parameter

F_stage=B_stage^2*(A_stage)/(2*mue0);
F_middle=B_middle^2*(A_middle)/(2*mue0);

end
```

## Forces in the Z axis

```
function Fz = fcn(Fg,Fc1,Fc2,Fc3,Fm)

Fz=-Fg+Fc1+Fc2+Fc3+Fm;

end
```

## Torque Pitch

```
function Tpitch = fcn(Fc1,Fc2,Fc3,Fc4,Fc5,Fc6)

alfa=cos(1.0472);
R=35e-3; %m
R1=4e-3;
phicc=37*pi/180;
Fpitch=-Fc2*alfa-Fc1*alfa+Fc3;
Fdis=Fc4*cos(-phicc)+Fc5*cos(120*pi/180-phicc)+Fc6*cos(240*pi/180-phicc);
Tpitch=Fpitch*R+Fdis*R1;
end
```

## Torque Roll

```
function Troll = fcn(Fc1,Fc2,Fc3,Fc4,Fc5,Fc6)

R=35e-3;%m
R1=4e-3;
alfa=sin(1.0472);
phicc=37*pi/180;
Froll=-Fc1*alfa+Fc2*alfa;
Fdis=Fc4*sin(-phicc)+Fc5*sin(120*pi/180-phicc)+Fc6*sin(240*pi/180-phicc);
Troll=Froll*R+Fdis*R1;
end
```

## Appendix magnetic bearing

### Force in the X axis

```
function Fx = fcn(Fc4,Fc5,Fc6)

phicc=37*pi/180;
Fx=Fc4*cos(-phicc)+Fc5*cos(120*pi/180-phicc)+Fc6*cos(240*pi/180-phicc);

end
```

### Force in the Y axis

```
function Fy = fcn(Fc4,Fc5,Fc6)

phicc=37*pi/180;
Fy=Fc4*sin(-phicc)+Fc5*sin(120*pi/180-phicc)+Fc6*sin(240*pi/180-phicc);

end
```

### Axis Z, Pitch and Roll to sensor values

```
function [xc1,xc2,xc3,xs1,xs2,xs3] = fcn(xz,phi_pitch,phi_roll)

R=35E-3; %m
a30=0.5000;
a60=0.8660;

xc1=xz-R*sin(phi_pitch)*a30-R*sin(phi_roll)*a60;
xc2=xz-R*sin(phi_pitch)*a30+R*sin(phi_roll)*a60;
xc3=xz+R*sin(phi_pitch);

axis=[xz,sin(phi_pitch),sin(phi_roll)]';

phisens=16.5*pi/180;
phi120=120*pi/180;
phi240=240*pi/180;
e=R*cos(-phisens);
f=R*sin(-phisens);
c=R*cos(phi120-phisens);
d=R*sin(phi120-phisens);
a=R*cos(phi240-phisens);
b=R*sin(phi240-phisens);

A=[1 a b;
   1 c d;
   1 e f];

xs=A*axis;
xs1=xs(1);
xs2=xs(2);
xs3=xs(3);

end
```

## Appendix magnetic bearing

### Axis X,Y to sensor value

```
function [xc4,xc5,xc6,xs4,xs5,xs6] = fcn(x,y)

phicc=37*pi/180;

xc4=x*cos(-phicc)+y*sin(-phicc);
xc5=x*cos(120*pi/180-phicc)+y*sin(120*pi/180-phicc);
xc6=x*cos(240*pi/180-phicc)+y*sin(240*pi/180-phicc);

xc4=xc4+1e-3;
xc5=xc5+1e-3;
xc6=xc6+1e-3;

phics=26*pi/180;
phi120=120*pi/180;
phi240=240*pi/180;

a=cos(-phicc-phics);
b=sin(-phicc-phics);
c=cos(phi120-phicc-phics);
d=sin(phi120-phicc-phics);
e=cos(phi240-phicc-phics);
f=sin(phi240-phicc-phics);

axis=[x,y]';
A=[a,b;
   c,d;
   e,f];

xs=A*axis;
xs4=xs(1)+1e-3;
xs5=xs(2)+1e-3;
xs6=xs(3)+1e-3;

end
```

### Sensor values to axis

```
function [z,pitch,roll,x,y] = fcn(xs1,xs2,xs3,xs4,xs5,xs6)

%z, pitch, roll calculation
R=35E-3; %m
phisens=16.5*pi/180;
phi120=120*pi/180;
phi240=240*pi/180;
e=R*cos(-phisens);
f=R*sin(-phisens);
c=R*cos(phi120-phisens);
d=R*sin(phi120-phisens);
a=R*cos(phi240-phisens);
b=R*sin(phi240-phisens);

A=[1    a    b;
   1    c    d;
```

## Appendix magnetic bearing

```
1 e f];

axis=A^-1*[xs1,xs2,xs3]';
z=axis(1);
pitch=(axis(2));
roll=(axis(3));

%x, y calculation
phicc=37*pi/180;
phics=26*pi/180;
phi120=120*pi/180;
phi240=240*pi/180;

a=cos(-phicc-phics);
b=sin(-phicc-phics);
c=cos(phi120-phicc-phics);
d=sin(phi120-phicc-phics);
e=cos(phi240-phicc-phics);
f=sin(phi240-phicc-phics);

A=[a,b;
   c,d;
   e,f];

xs=[xs4-1e-3;
    xs5-1e-3;
    xs6-1e-3];

b=A'*xs;
An=A'*A;

axis=An^-1*b;
x=axis(1);
y=axis(2);
```